

NASA Contract Report CR182247

Elevated Temperature Crack Growth

Final Report

**K.S. Kim, R.H. Vanstone,
S.N. Malik, J.H. Laflen
GE Aircraft Engines
Cincinnati, Ohio 45215**

November 1988

**Prepared for
National Aeronautics and Space Administration
Lewis-Research Center
21000 Brookpark Road
Cleveland, Ohio 44135**



(NASA-CR-182247) ELEVATED TEMPERATURE CRACK
GROWTH Final Report (OF) 293 p CSCL 20K

N90-26355

Unclass

63/39 0291103



Report Documentation Page

1. Report No. CR182247	2. Government Accession No.	3. Recipient's Catalog No.	
4. Title and Subtitle Elevated Temperature Crack Growth		5. Report Date November 1988	
		6. Performing Organization Code	
7. Author(s) K.S. Kim, R.H. Van Stone, S.N. Molik, J.H. Laflen		8. Performing Organization Report No. R89AEB-325	
		10. Work Unit No.	
9. Performing Organization Name and Address GE Aircraft Engines 1 Neumann Way Cincinnati, OH 45215		11. Contract or Grant No. NAS3-23940	
		13. Type of Report and Period Covered Final Report	
12. Sponsoring Agency Name and Address NASA Lewis Research Center 21000 Brookpark Road Cleveland, Ohio 44135-3191		14. Sponsoring Agency Code	
15. Supplementary Notes			
16. Abstract A study was performed to examine the applicability of path-independent (P-I) integrals to crack growth problems in hot section components of gas turbine aircraft engines. Alloy 718 was used in this study, and the experimental parameters included combined temperature and strain cycling, thermal gradients, elastic-plastic strain levels, and mean strains. A literature review was conducted of proposed P-I integrals, and those capable of analyzing hot section component problems were selected and programmed into the postprocessor of a finite element code. Detailed elastic-plastic finite element analyses were conducted to simulate crack growth and crack closure of the test specimen, and to evaluate the P-I integrals. It was shown that the selected P-I integrals are very effective for predicting crack growth for isothermal conditions.			
17. Key Words (Suggested by Author(s)) Elastic-Plastic Fracture Mechanics, Thermomechanical Fatigue, Fatigue Crack Growth, Alloy 718, Finite Element, Crack Closure		18. Distribution Statement	
19. Security Classif. (of this report) UNCLASSIFIED	20. Security Classif. (of this page) UNCLASSIFIED	21. No. of pages 272	22. Price*
"NATIONAL SECURITY INFORMATION" Unauthorized Disclosure Subject to Criminal Sanctions		CLASSIFIED BY: _____	
		DECLASSIFY ON: _____	
WHEN SEPARATED FROM ENCLOSURES, HANDLE THIS DOCUMENTATION PAGE AS: UNCLASSIFIED			

ABSTRACT

A study was performed to examine the applicability of path-independent (P-I) integrals to crack growth problems in hot section components of gas turbine aircraft engines. The Alloy 718 was used in this study, and the experimental parameters included combined temperature and strain cycling, thermal gradients, elastic-plastic strain levels, and mean strains. A literature review was conducted of proposed P-I integrals, and those capable of analyzing hot section component problems were selected and programmed into the post-processor of a finite element code. Detailed elastic-plastic finite element analyses were conducted to simulate crack growth and crack closure of the test specimen, and to evaluate the P-I integrals. It was shown that the selected P-I integrals are very effective for predicting crack growth for isothermal conditions.

KEY WORDS

Elastic-plastic fracture mechanics, Path-independent integrals, Thermomechanical fatigue, Elastic-plastic finite element method, Crack closure, Gap element, Fatigue Crack Growth, Nickel-base Superalloys, Alloy 718

ACKNOWLEDGMENTS

The authors of this report would like to acknowledge the assistance of D.S. Miller, R.C. Volmer, T.L. Richardson, and E.D. Deaton for developing the CMOD gage, thermal gradient, and TMF crack growth techniques as well as instrumenting and performing the crack growth tests during this investigation. We also deeply appreciated the help of J.F. Yau during the initial stages of this investigation. W.V. Ross was instrumental in performing the microscopy during the material characterization studies. We also appreciated the many helpful comments provided by T.W. Orange from the NASA-Lewis Research Center.

TABLE OF CONTENTS

	<u>Page</u>
1.0 INTRODUCTION	1
2.0 REVIEW OF PATH-INDEPENDENT INTEGRALS	5
2.1 Review of P-I Integrals	5
2.2 Numerical Implementation of P-I Integrals	11
2.2.1 P-I Integral Computation Algorithm	11
2.2.2 Computation of P-I Integrals	13
3.0 ANALOG MATERIAL	27
3.1 Material Selection	27
3.2 Material Processing and Microstructure	29
3.3 Determination of Alloy 718 Constitutive Properties	31
3.3.1 Tensile Properties	40
3.3.2 Cyclic Properties	56
3.3.3 Creep Tests	69
4.0 SPECIMEN EVALUATION	81
4.1 Buttonhead Single Edge Notch Specimen	81
4.1.1 J-integral Validation	83
4.1.2 SEN Specimen Buckling Experiments	85
4.2 Triple Extensometer Boundary Condition Test	87
4.3 Specimen Analysis	89
4.3.1 3D Specimen Analysis	91
4.3.2 2D Full Specimen Model	96
4.3.3 2D Gage Section Model	103

	<u>Page</u>
5.0 EXPERIMENTAL AND DATA ANALYSIS TECHNIQUES	107
5.1 Test Frequency	107
5.2 Crack Closure	109
5.3 Buttonhead Single Edge Notch Specimen	110
5.5 Data Acquisition	112
5.5 Data Analysis	113
5.6 Thermal Gradient SEN Technique	122
5.7 Thermal Mechanical Fatigue (TMF) Technique	124
5.8 Modified Compact Specimen	126
6.0 EXPERIMENTAL RESULTS OF ISOTHERMAL SEN CRACK PROPAGATION TESTS	131
6.1 Test Matrix	131
6.2 Crack Morphology	133
6.3 Fracture Mechanics Analysis	138
6.3.1 Results of Zero Mean Strain ($A_{\epsilon}=\infty$) Tests	144
6.3.2 Results of Non-zero Mean Strain Tests	144
6.3.3 Influence of Test Temperature	155
7.0 ISOTHERMAL FINITE ELEMENT ANALYSIS	167
7.1 Literature Survey	167
7.2 Finite Element Method	169
7.3 Crack Growth and Crack Closure Analysis	173
7.3.1 Finite Element Model	173
7.3.2 Analysis Procedure	175
7.3.3 Crack Growth Simulation	176
7.3.4 Crack Closure Analysis	178
7.3.5 Boundary Conditions	180
7.4 Results of Analysis	185
7.4.1 Crack Growth Simulation	185
7.4.2 Crack Closure Analysis	193

	<u>Page</u>
7.5 Computation of P-I Integrals	201
7.5.1 Crack Growth Simulation	201
7.5.2 Crack Closure Analysis	207
7.6 Prediction of Crack Growth with P-I Integrals	222
7.7 Discussion	227
8.0 CRACK PROPAGATION WITH THERMAL GRADIENT	235
8.1 Test Matrix	235
8.2 Monotonic Tests and Finite Element Analysis	235
8.3 Cyclic Temperature Gradient Tests	239
9.0 RESULTS OF VERIFICATION EXPERIMENTS	247
9.1 TMF Experiments	247
9.1.1 TMF Test Matrix	247
9.1.2 Crack Morphology	250
9.1.3 Fracture Mechanics Analysis	250
9.2 Compact Specimen Results	253
9.2.1 Modified Compact Displacement Results	257
9.2.2 Fracture Mechanics Analysis	259
10.0 RESULTS AND DISCUSSION	263
11.0 REFERENCES	267

LIST OF TABLES

	<u>Page</u>
Table 1: Summary of P-I Integrals	6
Table 2: Variation of Alloy 718 Elastic Modulus and Creep Properties with Temperature.	28
Table 3: Composition of Alloy 718 Plate	30
Table 4: Constitutive Property Test Matrix	39
Table 5: Summary Of Alloy 718 Tension Tests	42
Table 6: Alloy 718 Tension Stress-Strain Curve Constants	53
Table 7: Alloy 718 Tensile Stress-Strain Curve Values	54
Table 8: Summary Of Alloy 718 Cyclic Tests	58
Table 9: Alloy 718 Cyclic Stress-Strain Curve Constants	68
Table 10: Alloy 718 Tensile Stress-Strain Curve Values	74
Table 11: Summary of Estimated Values of J, δ , and δ_t for Alloy 718 at 649°C	84
Table 12: Variation of Cycle Period and Cycle Accumulation in Strain Rate Controlled Tests with Strain Rate and Range	108
Table 13: Isothermal SEN Crack Propagation Test Matrix	132

	<u>Page</u>
Table 14: Summary of Isothermal SEN Crack Propagation Tests	134
Table 15: P-I Integral Values at Different Crack Lengths of SEN Specimen N4-31 (538°C, $A_{\epsilon}=\infty$, 0.50% Strain Range)	203
Table 16: P-I Integral Values at Different Crack Lengths of SEN Specimen N4-3 (538°C, $A_{\epsilon}=\infty$, 1.15% Strain Range)	204
Table 17: P-I Integral Values at Different Crack Lengths of SEN Specimen N5-33 (538°C, $A_{\epsilon}=\infty$, 1.70% Strain Range)	205
Table 18: Values of P-I Integrals from Crack Closure Analysis of SEN Specimen N4-31 (538°C, $A_{\epsilon}=\infty$, 0.50% Strain Range)	224
Table 19: Values of P-I Integrals from crack Closure Analysis of SEN Specimen N4-3 (538°C, $A_{\epsilon}=\infty$, 1.15% Strain Range)	225
Table 20: Values of P-I Integrals from crack Closure Analysis of SEN Specimen N5-33 (538°C, $A_{\epsilon}=\infty$, 1.70% Strain Range)	226
Table 21: Region II Crack Growth Rate Constants for Path-Independent Integrals	232
Table 22: Summary of Temperature Gradient Crack Propagation Tests	243
Table 23: TMF Crack Propagation Test Matrix	248
Table 24: Summary of TMF Crack Propagation Tests	251
Table 25: Results of Modified Compact Specimen Crack Propagation Tests	260

LIST OF FIGURES

	<u>Page</u>
Figure 1: Integration Paths and Areas.	8
Figure 2: Flow Chart of Postprocessor for Path-Independent Integral Computations.	12
Figure 3: Geometry of an ASTM Standard Compact Specimen and its Finite Element Model.	14
Figure 4: Near Crack-Tip Mesh Refinement and Circular Paths for the Compact Specimen.	16
Figure 5: Path-independence of J-Integral Along Various Paths for Each Load Step.	17
Figure 6: Blackburn J^* -Integral for the Four Load Steps for the Compact Specimen.	19
Figure 7: Kishimoto \hat{J} -Integral for the Four Load Steps for the Compact Specimen.	20
Figure 8: Comparison of Area and Line Integral Term Contributions to (a) Blackburn (J^*) and (b) Kishimoto (\hat{J}) Integrals.	21
Figure 9: Load Versus Load Point Displacement for the Compact Specimen at Various Load Steps.	22
Figure 10: Atluri T_p^* -Integral ($= \sum \Delta T_p^*$) Along Various Integration Paths for Loading and Unloading Steps.	23

	<u>Page</u>
Figure 11: Atluri T_p -Integral ($= \Sigma \Delta T_p$) Along Various Integration Paths for Loading and Unloading Steps.	24
Figure 12: Cyclic Stress-Strain Curves for Linear Thermal Gradient Problem.	25
Figure 13: P-I Integrals for Thermo-Mechanical Loadings and Temperature-Dependent Material Properties.	26
Figure 14: Optical Micrograph of Alloy 718 with the Longitudinal Direction Displayed Horizontally and the Thickness Direction Displayed Vertically.	32
Figure 15: Optical Micrograph of Alloy 718 with the Longitudinal Direction Displayed Horizontally and the Transverse Direction Displayed Vertically.	33
Figure 16: Optical Micrograph of Alloy 718 with the Transverse Direction Displayed Horizontally and the Thickness Direction Displayed Vertically.	34
Figure 17: Optical Micrograph of Alloy 718 Showing the Elongation of the Banded Inclusions with the Longitudinal Direction Displayed Horizontally and the Thickness Direction Displayed Vertically.	35
Figure 18: Drawing of the Test Specimen Used to Evaluate the Tensile and Creep Properties of Alloy 718.	37
Figure 19: Drawing of the Test Specimen Used to Evaluate the Cyclic Properties of Alloy 718.	38

	<u>Page</u>
Figure 20: Stress-Strain Response of Alloy 718 Specimen under Monotonic Tensile Loading at 427°C (800°F) at a Strain Rate of 0.2%/sec which Exhibited Extensive Serrated Yielding.	41
Figure 21: Variation of Tension Stress-Strain Response of Alloy 718 at 538°C (1000°F) for Three Different Strain Rates.	44
Figure 22: Experimental Data and Multi-linear Curve for the Alloy 718 Tension Tests Performed at 21°C (70°F).	46
Figure 23: Experimental Data and Multi-linear Curve for the Alloy 718 Tension Tests Performed at 427°C (800°F).	47
Figure 24: Experimental Data and Multi-linear Curve for the Alloy 718 Tension Tests Performed at 482°C (900°F).	48
Figure 25: Experimental Data and Multi-linear Curve for the Alloy 718 Tension Tests Performed at 538°C (1000°F).	49
Figure 26: Experimental Data and Multi-linear Curve for the Alloy 718 Tension Tests Performed at 593°C (1100°F).	50
Figure 27: Experimental Data and Multi-linear Curve for the Alloy 718 Tension Tests Performed at 649°C (1200°F).	51
Figure 28: Multi-linear Tension Stress-Strain Curve for Alloy 718 at 538°C (1000°F) for Strains up to 0.50.	52
Figure 29: Variation of the Alloy 718 Tension Stress-Strain Curves with Test Temperature.	55

	<u>Page</u>
Figure 30: Variation of the Plastic Strain Range with the Total Strain Range during a Block Strain Cyclic Test of Alloy 718 at 538°C (1000°F) and a Strain Rate of 0.02% / sec.	57
Figure 31: Variation of the Maximum and Minimum Stresses as a Function of Cycles for a Cyclic Tests of Alloy 718 at 538°C (1000°F) and Strain Ranges of 0.017 but with Different Strain Rates.	60
Figure 32: Variation of the Maximum and Minimum Stresses as a Function of Cycles for a Cyclic Tests of Alloy 718 at 427°C (800°F) with Strain Ranges of (a) 0.0115, (b) 0.0170, and (c) 0.035.	61
Figure 33: Variation of the Maximum and Minimum Stresses as a Function of Cycles for a Cyclic Tests of Alloy 718 at 538°C (1000°F) with Strain Ranges of (a) 0.0115, (b) 0.0170, and (c) 0.035.	62
Figure 34: Variation of the Maximum and Minimum Stresses as a Function of Cycles for a Cyclic Tests of Alloy 718 at 593°C (1100°F) with Strain Ranges of (a) 0.0115, (b) 0.0170, and (c) 0.035.	63
Figure 35: Variation of the Maximum and Minimum Stresses as a Function of Cycles for a Cyclic Tests of Alloy 718 at 649°C (1200°F) with Strain Ranges of (a) 0.0115, (b) 0.0170, and (c) 0.035.	64

	<u>Page</u>
Figure 36: Hysteresis Loops from Cyclic Tests of Alloy 718 at 538°C (1000°F) at Approximately 20, 50, and 80% of Life for Strain Range 0.0170 Illustrating the Absence of Strain Rate Sensitivity.	65
Figure 37: Variation of Alternating Stress with Alternating Strain Measured in Cyclic Tests on Alloy 718 at 538°C (1000°F).	67
Figure 38: Experimental Alternating Stress - Alternating Strain Data and Multi-linear Curve from Cyclic Alloy 718 Tests at 427°C (800°F).	70
Figure 39: Experimental Alternating Stress - Alternating Strain Data and Multi-linear Curve from Cyclic Alloy 718 Tests at 538°C (1000°F).	71
Figure 40: Experimental Alternating Stress - Alternating Strain Data and Multi-linear Curve from Cyclic Alloy 718 Tests at 593°C (1100°F).	72
Figure 41: Experimental Alternating Stress - Alternating Strain Data and Multi-linear Curve from Cyclic Alloy 718 Tests at 649°C (1200°F).	73
Figure 42: Variation of the Alloy 718 Cyclic Alternating Stress - Alternating Strain Curves with Test Temperature.	75
Figure 43: Comparison of the Alloy 718 Tension and Cyclic Stress Strain Curves at (a) 427°C (800°F) and (b) 649°C (1200°F).	76

	<u>Page</u>
Figure 44: Variation of inelastic Strain with time for Alloy 718 Creep Tests Performed at 538°C (1000°F).	77
Figure 45: Variation of inelastic Strain with time for Alloy 718 Creep Tests Performed at 593°C (1100°F).	78
Figure 46: Variation of inelastic Strain with time for Alloy 718 Creep Tests Performed at 649°C (1200°F).	79
Figure 47: Buttonhead Single Edge Notch (SEN) Specimen.	82
Figure 48: Examples of Control Extensometer Hysteresis Loops in 649°C, 1.7%, $R_{\epsilon}=-1$ SEN Crack Propagation Test after (a) 1 and 2 cycles, (b) 23 cycles, and (c) 55 cycles.	86
Figure 49: Variation of Maximum and Minimum Stress in 649°C (1200°F) SEN and Cyclic Test.	88
Figure 50: Variation of Normal Displacements Measured During Cyclic Loading of a Buttonhead SEN Specimen With $a/W=0.25$ Using 13.97 mm (0.55 inch) Gage Length Extensometers.	90
Figure 51: Buttonhead Specimen 3D Finite Element Model.	92
Figure 52: Prediction of Normal Displacement Variation across Gage Section Predicted from 3D Elastic Analysis of Constant Axial Buttonhead Displacement.	94
Figure 53: Lateral Displacement Profile of the Buttonhead SEN Specimen Subjected to Uniform Axial Displacement (Dotted Lines Show Undeformed Shape).	95

	<u>Page</u>
Figure 54: Full Specimen 2D Finite Element Model.	97
Figure 55: Comparison of Normal Displacements (u_y) at the End of SEN Specimen as Predicted from 2D and 3D CYANIDE Full Specimen Analyses.	98
Figure 56: Comparison of Normal Displacements (u_y) at the End of SEN Specimen from Experiment and 2D CYANIDE Full Specimen Analysis.	99
Figure 57: Comparison of Experimentally Determined Load-Displacement Hysteresis Loop From Mid-width Extensometer with 2D CYANIDE Full Specimen Analysis.	100
Figure 58: Comparison of Experimentally Determined Load-Displacement Hysteresis Loop from Back Surface Extensometer with 2D CYANIDE Full Specimen Analysis.	101
Figure 59: Comparison of Experimentally Determined Load-Displacement Hysteresis Loop from Front Surface Extensometer with 2D CYANIDE Full Specimen Analysis.	102
Figure 60: Gage Length 2D Finite Element Model with Width of 10.16 mm and Height of 7.94 mm.	104
Figure 61: Predicted Variation of Pseudo K with Vertical Displacement (u_y) in Buttonhead SEN Specimen.	105
Figure 62: Predicted Variation of Pseudo K with Vertical Load in Buttonhead SEN Specimen.	106
Figure 63: Schematic Drawing of Triple Extensometer Buttonhead SEN Test Method.	111

	<u>Page</u>
Figure 64: Variation of Crack Length with Cycles in Displacement Controlled SEN Tests Performed at 538°C (1000°F).	114
Figure 65: Stress-Displacement Hysteresis Loops of (a) Controlling Extensometer, (b) Back Face Extensometer, and (c) CMOD gage from Cycle 195 of Specimen N4-3.	116
Figure 66: Variation of Maximum, Minimum, Crack Closure, and Crack Opening Stress with Cycles for Specimen N4-3.	118
Figure 67: Variation of Maximum, Minimum, Crack Closure, and Crack Opening Control Displacement with Cycles for Specimen N4-3.	119
Figure 68: Variation of Maximum, Minimum, Crack Closure, and Crack Opening Values of Crack Mouth Opening Displacement (CMOD) with Cycles for Specimen N4-3.	120
Figure 69: Variation of Maximum, Minimum, Crack Closure, and Crack Opening Back Face Displacement with Cycles for Specimen N4-3.	121
Figure 70: Temperature Profile Developed in the Thermal Gradient Experiments.	123
Figure 71: Variation of Thermal Strain during 427 to 649°C (800 to 1200°F) Thermal Cycling of a Buttonhead SEN Specimen.	125

	<u>Page</u>
Figure 72: Comparison of the Thermal Strains Measured with the Controlling and Back Face Extensometers during 427 to 649°C (800 to 1200°F) Thermal Cycling of a Buttonhead SEN Specimen.	127
Figure 73: Drawing of Modified Compact Specimen.	128
Figure 74: Variation of Maximum, Minimum, Crack Closure, and Crack Opening Values of Crack Mouth Opening Displacement (CMOD) with Cycles for Specimen N4-31 Tested at 538°C (1000°F) with 0.50% Strain Range and A_{ϵ} of ∞ .	135
Figure 75: Variation of Maximum, Minimum, Crack Closure, and Crack Opening Values of Crack Mouth Opening Displacement (CMOD) with Cycles for Specimen N5-22 Tested at 593°C (1100°F) with 0.50% Strain Range and A_{ϵ} of ∞ .	136
Figure 76: Variation of Maximum, Minimum, Crack Closure, and Crack Opening Values of Crack Mouth Opening Displacement (CMOD) with Cycles for Specimen N4-15 Tested at 649°C (1200°F) with 1.50% Strain Range and A_{ϵ} of ∞ .	137
Figure 77: Variation of Crack Growth Rate with Cycles in 538°C (1000°F) Displacement Controlled SEN Tests.	140
Figure 78: Variation of K_{max} with Cycles in 538°C (1000°F) Displacement Controlled SEN Tests.	141

	<u>Page</u>
Figure 79: Variation of Crack Growth Rate with ΔK in 538°C (1000°F) Displacement Controlled SEN Tests.	142
Figure 80: Variation of Crack Growth Rate with K_{max} in 538°C (1000°F) Displacement Controlled SEN Tests.	143
Figure 81: Crack Growth Rates Measured in Alloy 718 SEN Specimens Cycled at 427°C (800°F) with $A_{\epsilon}=\infty$ as a Function of K_{max} and Strain Range.	145
Figure 82: Crack Growth Rates Measured in Alloy 718 SEN Specimens Cycled at 538°C (1000°F) with $A_{\epsilon}=\infty$ as a Function of K_{max} and Strain Range.	146
Figure 83: Crack Growth Rates Measured in Alloy 718 SEN Specimens Cycled at 593°C (1100°F) with $A_{\epsilon}=\infty$ as a Function of K_{max} and Strain Range.	147
Figure 84: Crack Growth Rates Measured in Alloy 718 SEN Specimens Cycled at 649°C (1200°F) with $A_{\epsilon}=\infty$ as a Function of K_{max} and Strain Range.	148
Figure 85: Comparison of Crack Growth Rates Measured Alloy 718 SEN Specimens Cycled at 427°C (800°F) with a Strain Range Of 1.15% and A_{ϵ} Ratios of ∞ and 1.0	149
Figure 86: Comparison of Crack Growth Rates Measured Alloy 718 SEN Specimens Cycled at 538°C (1000°F) with a Strain Range Of 1.15% and A_{ϵ} Ratios of ∞ and 1.0.	151

	<u>Page</u>
Figure 87: Comparison of Crack Growth Rates Measured Alloy 718 SEN Specimens Cycled at 593°C (1100°F) with a Strain Range Of 1.15% and A_{ϵ} Ratios of ∞ and 1.0.	152
Figure 88: Comparison of Crack Growth Rates Measured Alloy 718 SEN Specimens Cycled at 649°C (1200°F) with a Strain Range Of 1.15% and A_{ϵ} Ratios of ∞ and 1.0.	153
Figure 89: Comparison of Crack Growth Rates Measured Alloy 718 SEN Specimens Cycled at 427°C (800°F) with Similar Strain Ranges and A_{ϵ} Ratios of ∞ and -2.0.	154
Figure 90: Comparison of Crack Growth Rates Measured Alloy 718 SEN Specimens Cycled at 538°C (1000°F) with Similar Strain Ranges and A_{ϵ} Ratios of ∞ and -2.0.	156
Figure 91: Comparison of Crack Growth Rates Measured Alloy 718 SEN Specimens Cycled at 593°C (1100°F) with Similar Strain Ranges and A_{ϵ} Ratios of ∞ and -2.0.	157
Figure 92: Comparison of Crack Growth Rates Measured Alloy 718 SEN Specimens Cycled at 649°C (1200°F) with Similar Strain Ranges and A_{ϵ} Ratios of ∞ and -2.0.	158
Figure 93: Influence Of Test Temperature on The Crack Growth Rates Measured Alloy 718 SEN Specimens Cycled with a Strain Range Of 0.50% and an A_{ϵ} Ratio of ∞ .	159
Figure 94: Influence of Test Temperature on The Crack Growth Rates Measured Alloy 718 SEN Specimens Cycled with a Strain Range of 0.75% and an A_{ϵ} Ratio of ∞ .	160

	<u>Page</u>
Figure 95: Influence of Test Temperature on The Crack Growth Rates Measured Alloy 718 SEN Specimens Cycled with a Strain Range of 1.15% and an A_c Ratio of ∞ .	161
Figure 96: Influence of Test Temperature on The Crack Growth Rates Measured Alloy 718 SEN Specimens Cycled with a Strain Range of 1.70% and an A_c Ratio of ∞ .	162
Figure 97: Influence of Test Temperature on The Crack Growth Rates Measured Alloy 718 SEN Specimens Cycled with a Strain Range of 1.15% and an A_c Ratio of 1.0.	163
Figure 98: Influence of Test Temperature on The Crack Growth Rates Measured Alloy 718 SEN Specimens Cycled with a Strain Range of 0.93% and an A_c Ratio of -2.0.	164
Figure 99: Single Edge Cracked Plate with Gap Elements on the Crack Face.	171
Figure 100: Finite Element Model of the Gage Section of Single Edge Notch Specimen.	174
Figure 101: Schematic of Loading Steps in Crack Growth Simulation.	177
Figure 102: Stress-CMOD Hysteresis Loop Showing Locations of Finite Element Analysis Load Cases.	179
Figure 103: Crack Length as a Function of Cycle - Interpolated Crack Growth Simulation Analysis.	182
Figure 104: Specimen Displacements at (a) Control and (b) Backface Extensometers Used as Boundary Conditions for Crack Growth Simulation Analysis	183

	<u>Page</u>
Figure 105: Crack Length as a Function of Cycle and Locations of Two Crack Lengths for Crack Closure Analysis.	184
Figure 106: Hysteresis Loops for Crack Lengths of (a) 0.95 mm and (b) 2.54 mm Interpolated for Crack Closure Analysis.	186
Figure 107: Predicted Crack Surface Displacements After Node Release in a SEN Crack Propagation Analysis of a SEN Specimen Cycled at 538°C (1000°F) and 1.15% Strain Range.	187
Figure 108: Predicted Crack Surface Displacement at Tensile Peak in a SEN Crack Propagation Analysis of a SEN Specimen Cycled at 538°C (1000°F) and 1.15% Strain Range.	188
Figure 109: Plastic Zones at the Tensile Peaks for 538°C, 1.15% Strain Range, $A_{\epsilon}=\infty$ for Crack Lengths of (a) 0.3175 mm, (b) 0.95 mm, and (c) 2.54 mm.	190
Figure 110: Comparison of Experimental and Predicted Average Cross Section Stress with Crack Length in a SEN Specimen Cycled at 538°C (1000°F) and 1.15% Strain Range.	191
Figure 111: Comparison of Experimental and Predicted CMOD Range with Crack Length in a SEN Specimen Cycled at 538°C (1000°F) and 1.15% Strain Range.	192
Figure 112: Predicted Variation of Crack Surface Opening During a Loading Cycle of a SEN Specimen with a 2.54 mm Crack Length Cycled at 538°C (1000°F) and 1.15% Strain Range.	194

	<u>Page</u>
Figure 113: Plastic zones at (a) the Closing Point, (b) the Compressive Peak, (c) the Opening Point, and (d) the Tensile Peak for a SEN Specimen Cycled at 538°C, 1.15% Strain Range, $A_{\epsilon}=\infty$ with a Crack Length of 2.54 mm.	195
Figure 114: Comparison of Predicted and Experimentally Measured Average Cross Section Stresses - CMOD Hysteresis Loops in a SEN Specimen Cycled at 538°C (1000°F) and 0.5% Strain Range with Crack Lengths of (a) 0.95 mm and (b) 2.54 mm.	197
Figure 115: Comparison of Predicted and Experimentally Measured Average Cross Section Stress - CMOD Hysteresis Loops in a SEN Specimen Cycled at 538°C (1000°F) and 1.15% Strain Range with Crack Lengths of (a) 0.95 mm and (b) 2.54 mm.	198
Figure 116: Comparison of Predicted and Experimentally Measured Average Cross Section Stress - CMOD Hysteresis Loops in a SEN Specimen Cycled at 538°C (1000°F) and 1.7% Strain Range with Crack Lengths of (a) 0.95 mm and (b) 2.54 mm.	199
Figure 117: Integration Paths for Crack Growth Simulation Analysis.	202
Figure 118: Predicted values of J^* as a Function of Crack Length in a SEN Specimen Cycled at 538°C (1000°F) and 1.15% Strain Range.	206

	<u>Page</u>
Figure 119: Integration Paths for Crack Closure Analysis at a Crack Length of 0.95mm.	208
Figure 120: Integration Paths for Crack Closure Analysis at a Crack Length of 2.54mm.	209
Figure 121: Variation of J^* with Path in a SEN Specimen Cycled at 538°C (1000°F) and 0.5% Strain Range with a Crack Length of 2.54mm.	210
Figure 122: Variation of \hat{J} with Path in a SEN Specimen Cycled at 538°C (1000°F) and 0.5% Strain Range with a Crack Length of 2.54mm.	211
Figure 123: Variation of ΔT_p^* with Path in a SEN Specimen Cycled at 538°C (1000°F) and 0.5% Strain Range with a Crack Length of 2.54mm.	212
Figure 124: Variation of ΔT_p with Path in a SEN Specimen Cycled at 538°C (1000°F) and 0.5% Strain Range with a Crack Length of 2.54mm.	213
Figure 125: Variation of T_p^* with Path in a SEN Specimen Cycled at 538°C (1000°F) and 0.5% Strain Range with a Crack Length of 2.54mm.	214
Figure 126: Variation of T_p with Path in a SEN Specimen Cycled at 538°C (1000°F) and 0.5% Strain Range with a crack Length of 2.54mm.	215

	<u>Page</u>
Figure 127: Variation of J^* with Path in a SEN Specimen Cycled at 538°C (1000°F) and 1.7% Strain Range with a Crack Length of 2.54mm.	216
Figure 128: Variation of \hat{J} with Path in a SEN Specimen Cycled at 538°C (1000°F) and 1.7% Strain Range with a Crack Length of 2.54mm.	217
Figure 129: Variation of ΔT_p^* with Path in a SEN Specimen Cycled at 538°C (1000°F) and 1.7% Strain Range with a Crack Length of 2.54mm.	218
Figure 130: Variation of ΔT_p with Path in a SEN Specimen Cycled at 538°C (1000°F) and 1.7% Strain Range with a Crack Length of 2.54mm.	219
Figure 131: Variation of T_p^* with Path in a SEN Specimen Cycled at 538°C (1000°F) and 1.7% Strain Range with a Crack Length of 2.54mm.	220
Figure 132: Variation of T_p with Path in a SEN Specimen Cycled at 538°C (1000°F) and 1.7% Strain Range with a Crack Length of 2.54mm.	221
Figure 133: Predicted Values of J^* as a Function of Control Displacement During a Cycle in a SEN Specimen Cycled at 538°C (1000°F) and 1.15% Strain Range with a Crack Length of 2.54mm.	223
Figure 134: Variation of Crack Growth Rates Measured in Alloy 718 at 538°C (1000°F) with ΔJ^* .	228

	<u>Page</u>
Figure 135: Variation of Crack Growth Rates Measured in Alloy 718 at 538°C (1000°F) with $\Delta\hat{J}$.	229
Figure 136: Variation of Crack Growth Rates Measured in Alloy 718 at 538°C (1000°F) with ΔT_p^* .	230
Figure 137: Variation of Crack Growth Rates Measured in Alloy 718 at 538°C (1000°F) with ΔT_p .	231
Figure 138: Comparison of Trilinear Approximation and Experimental Data in Alloy 718 Temperature Gradient Tests.	237
Figure 139: Normal Stress Distribution on the Crack Plane for the Trilinear Temperature Distribution and No Applied Load.	238
Figure 140: Variation of the Control and Back Face Displacements in Monotonic Temperature Gradient Tests.	240
Figure 141: Comparison of the Experimental and Predicted Variation of Average Stress (Load / Specimen Area) with Control Displacement in Monotonic Temperature Gradient Tests.	241
Figure 142: Comparison of the Experimental and Predicted Variation of Crack Mouth Opening Displacement (CMOD) with Control Displacement in Monotonic Temperature Gradient Tests.	242
Figure 143: Variation of Crack Growth Rate with K_{max} in the Cyclic Temperature Gradient Tests.	245

	<u>Page</u>
Figure 144: Schematic Figure Showing Variation of Strain with Temperature for In-Phase and Out-of Phase Cycling in 427 to 649°C (800 to 1200°F) TMF Test.	249
Figure 145: Variation of Crack Growth Rates with K_{max} for In-Phase TMF Crack Growth Tests Cycles Cycled between 427 and 649°C (800 to 1200°F).	252
Figure 146: Variation of Crack Growth Rates with K_{max} for Out-of-Phase TMF Crack Growth Tests Cycles Cycled between 427 and 649°C (800 to 1200°F).	254
Figure 147: Variation of Crack Growth Rates with K_{max} for In-Phase TMF Crack Growth Tests Cycles Cycled between 538 and 649°C (1000 to 1200°F).	255
Figure 148: Variation of Crack Growth Rates with K_{max} for Out-of-Phase TMF Crack Growth Tests Cycles Cycled between 538 and 649°C (1000 to 1200°F).	256
Figure 149: Load-Displacement Hysteresis Loops of (a) CMOD, (b) Controlling, (c) Back Face Extensometers from Cycle 131 of Modified Compact Specimen Test N3-16 (538°C, 2.4% Strain Range, $A_{\epsilon}=\infty$).	258
Figure 150: Comparison on Crack Growth Rates in Alloy 718 Measured in Modified Compact (large triangles) and SEN Specimens for $A_{\epsilon}=\infty$ Cycling at 427°C.	261
Figure 151: Comparison on Crack Growth Rates in Alloy 718 Measured in Modified Compact (large triangles) and SEN Specimens for $A_{\epsilon}=\infty$ Cycling at 427°C.	262

1.0 INTRODUCTION

Critical gas turbine engine hot section components such as blades, vanes, and combustor liners tend to develop minute cracks during the early stages of operation. These cracks may then grow under conditions of fatigue and creep to critical size. Current methods of predicting growth rates or critical crack sizes are inadequate, which leaves only two extreme courses of action. The first is to take an optimistic view with the attendant risk of an excessive number of service failures. The second is to take a pessimistic view and accept an excessive number of "rejections for cause" at considerable expense in parts and downtime. Clearly it is very desirable to develop reliable methods of predicting crack growth rates and critical crack sizes.

To develop such methods, it is desirable to relate the processes that control crack growth in the immediate vicinity of the crack tip to parameters that can be calculated from the remote field data, such as stresses and displacements. The most likely parameters appear to be certain path-independent (P-I) integrals, several of which have already been proposed for application to inelastic problems involving nonuniform temperature distribution. A thorough analytical and experimental evaluation of these parameters needs to be made under conditions including elevated temperature cyclic and thermomechanical fatigue loading, both with and without thermal gradients.

The purpose of this investigation was to investigate the ability of currently available P-I integrals to correlate fatigue crack propagation under conditions that simulate the turbojet engine combustor liner environment. This was accomplished through a multi-year, combined experimental and analytical program.

Rice's J-integral⁽¹⁾ has received much attention among researchers since its introduction to fracture mechanics. It is a measure of severity of the deformation field at the crack tip and has proven to be a viable parameter for prediction of crack initiation and growth under monotonic

tensile loading in the nonlinear regime. The path-independence of the J-integral is valid only within the deformation theory of plasticity. Hence, it cannot be defined for unloading after plastic deformation; however some workers have used operational definitions of ΔJ to correlate crack growth data under cyclic loading(2). The J-integral is not path-independent in the presence of a temperature gradient or material inhomogeneity.

Among the newly proposed P-I integrals which can consider cyclic and non-isothermal loadings are the Blackburn(3), Kishimoto(4), and Atluri(5) integrals. The utility of these P-I integrals for fatigue crack growth analysis under large cyclic plasticity was investigated by performing elastic-plastic finite element analysis of a single edge notch (SEN) specimen. Gap elements were used to predict the occurrence of crack closure and opening under cyclic loading conditions. A post-processor was developed to compute the P-I integrals from the results of finite element analyses. The P-I integrals were computed at the loading steps in the fatigue cycles in the analyses. The computed results of the P-I integrals were used to correlate the experimental crack growth data.

Alloy 718, a nickel-base superalloy, was selected as the analog material to simulate a combustor liner material. Experiments were performed to determine the monotonic and cyclic constitutive response of this material over the temperature range from 427 to 649°C (800 to 1200°F). Fatigue crack growth experiments under isothermal, temperature gradient, and thermal mechanical conditions were performed over this same temperature range. These tests were performed on buttonhead SEN specimens and a modified compact specimen geometries under elastic-plastic displacement control conditions. Most of the tests were performed using the SEN geometry. It was shown that linear elastic fracture mechanics could not adequately model the fatigue crack growth behavior for elastic-plastic cycling. The trends observed for isothermal conditions with strain range and temperature were very similar to those observed for the temperature gradient and TMF crack growth tests. This indicates that if P-I integrals can model isothermal conditions, then they

also may be able to predict the growth of cracks for non-isothermal loading conditions.

Experimental data and finite element analyses of the entire SEN specimen has shown that the deformation within the gage section can be modeled using a two-dimensional analysis of the gage section with a linear variation of axial displacements across the end of the gage section. The crack growth experiments were performed with three extensometers - two to experimentally establish the remote displacement gradient and a crack mouth opening displacement (CMOD) gage. The remote displacements gradient was used as the boundary conditions for simulations of the 538°C (1000°F) crack growth tests. There was excellent agreement between the analytically and experimentally determined load, CMOD, and occurrence of crack closure. It was shown that the elastic and elastic-plastic crack growth behavior can be predicted using several of the P-I integrals over a range of crack lengths and cyclic plasticity.

It is noted that the detailed finite element analysis simulating the crack growth and crack closure behavior was performed only for the isothermal conditions. Therefore, the ability of the P-I integrals studied here still remains to be investigated for other situations. Also, the geometry dependence of the ability of the P-I integrals as nonlinear fracture parameters was not addressed in this report. These subjects are currently under investigation in a separate study(6).

2.0 REVIEW OF PATH-INDEPENDENT INTEGRALS

2.1 Review of P-I Integrals

As a parameter for predicting crack growth in the elastic-plastic regime, the utility of the J-integral is limited. The theoretical basis of the J-integral does not allow the extension of its usage to nonproportional loading and unloading in the plastic regime, nor can it be used in the presence of a temperature gradient and material inhomogeneity. A typical example where all these limiting factors are operative would be the hot section components of a gas turbine in mission cycles.

In recent years there has been considerable effort to modify or reformulate the P-I integral. Consequently, a number of new P-I integrals have emerged. These include the J^* -integral of Blackburn(3), the \hat{J} -integral of Kishimoto, et. al.(4), the J_θ -integral of Ainsworth, et. al.(10), the ΔT_p^* - and ΔT_p -integrals of Atluri, et. al.(5), and two thermoelastic P-I integrals, J_w of Wilson and Yu(8), and J_G by Gurtin(9). These P-I integrals have been critically reviewed in this program. In this report, only a brief synopsis of the review is presented. A detailed discussion of the available P-I integrals is given as a result of the review performed during the present investigation and was reported elsewhere(7). The theoretical background has been examined with particular attention to whether or not the path-independence is maintained in the presence of (1) nonproportional loading, (2) unloading in the plastic regime, and (3) a temperature gradient and material inhomogeneity. The relation among the P-I integrals, salient features, and limitations were investigated. The physical meaning, the possibility of experimental measurement, and the computational ease were also examined. The summary of the review is presented in Table 1. In view of the requirements associated with performing crack growth analysis tasks in this program, the following conclusions were made:

Table 1: Summary of P-I Integrals

(1) P-I Integral	Measure of Crack Tip Severity	Physical Meaning (2)		Capability to Handle			Computation (Integrals Involved)	Experimental Measurement (5)
		Elastic	Thermo- elastic	Plastic	Prop. & Loading (plastic regime)	Thermal Strain	Material Inhomogeneity	
J	Yes	$-\frac{\partial P}{\partial a}$	-	$-\frac{\partial P}{\partial a}$	Yes	No	No	Line
J _w	Yes	$-\frac{\partial P}{\partial a}$	$-\frac{\partial \phi}{\partial a}$ (3)	-	No	Yes	No	Line + Area
J _G	Yes	$-\frac{\partial P}{\partial a}$	$-\frac{\partial \phi}{\partial a}$	-	No	Yes	No	Line
J _{\theta}	Yes	$-\frac{\partial P}{\partial a}$	$-\frac{\partial \phi}{\partial a}$	$-\frac{\partial P}{\partial a}$	Yes	Yes	No	Line + Area
J*	Yes	$-\frac{\partial P}{\partial a}$	$-\frac{\partial \phi}{\partial a}$	Unknown	Yes	Yes	Yes	Line + Area
\bar{J}	Yes	Rate of work done to crack tip by surrounding material (4)			Yes	Yes	Yes	Line + Area
ΔT_p^*	Yes	$-\frac{\Delta \Pi}{\partial a}$ for prop. loading			Yes	Yes	Yes	Line + Area
ΔT_p	No	Unknown for nonprop. loading			Yes	Yes	Yes	Line + Area

- Note: (1) $J = J_w = J_G = J_\theta = J^* = \bar{J}$ for elastic and thermoelastic deformation of homogeneous materials,
 $J = \Sigma \Delta T_p^* = \Sigma \Delta T_p$ for monotonic proportional loading.
- (2) P = Potential energy, ϕ = Global thermodynamic potential, $\Delta \Pi$ = Incremental energy
(3) Provided that the internal energy is identical to the strain energy at the crack tip
(4) With the assumption of a rigid fracture process zone at the crack tip independent of the crack size
(5) Yes if it can be expressed as the rate of a potential, or if it can be expressed as a line integral along the boundary
(6) Yes if the loading is proportional

1. The J^* , \hat{J} , ΔT_p , and ΔT_p^* integrals maintain path-independence under the thermomechanical cycles used in tests in this program. Although the physical meaning of these P-I integrals needs to be pursued further, they were selected for continued evaluation in this program.
2. The J , J_w , J_G , and J_θ integrals have limited capabilities. The J_w and J_G integrals are usable only for thermoelastic cases with homogeneous material properties. These integrals may be helpful in predicting crack growth in a small temperature gradient field and under small-scale yielding conditions. The J_θ integral is a modified version of J (modified to include the thermal strain). Thus, it cannot be used with substantially nonproportional loading and unloading in the plastic regime. However, it would be worthwhile to investigate the utility of operationally defined ΔJ and possibly ΔJ_θ for the test cycles in this program, if the selected four P-I integrals are not useful.

The P-I integrals reviewed in this program are shown here. The index notation was used. The common variables are:

σ_{ij} = stress tensor
 ϵ_{ij} = strain tensor
 u_i = displacement vector
 t_i = traction vector
 θ = relative temperature
 α = thermal expansion coefficients
 μ, λ = Lamé's constants

Figure 1 shows the integration paths and areas used in the following P-I integrals:

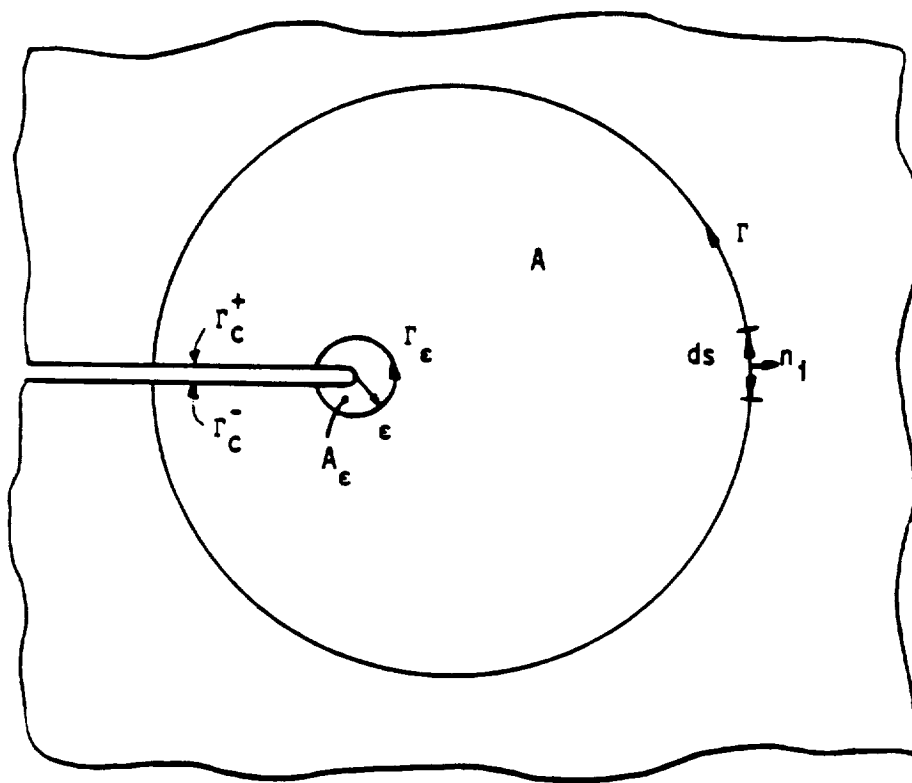


Figure 1: Integration Paths and Areas.

Rice's J-Integral⁽¹⁾

$$J = \int_{\Gamma} (n_1 W - t_i u_{i,1}) ds \quad (2.1)$$

$$\text{where } W = \int_0^{\epsilon_{ij}} \sigma_{ij} d\epsilon_{ij}$$

Wilson and Yu's Thermoelastic Integral⁽⁸⁾

$$J_W = \int_{\Gamma} (n_1 W - t_i u_{i,1}) ds - \alpha(3\lambda+2\mu) \int_A \{(\theta \epsilon_{ii})_{,1/2} - \epsilon_{ii} \theta_{,1}\} dA \quad (2.2)$$

$$\text{where } W = \sigma_{ij} \epsilon_{ij} / 2$$

Gurtin's Thermoelastic Integral⁽⁹⁾

$$J_G = \int_{\Gamma} \{n_1 W - t_k u_{k,1} - \frac{\alpha^2 (3\lambda+2\mu)^2}{2(\lambda+\mu)} \theta^2 n_1 + \frac{\alpha\mu(3\lambda+2\mu)}{(\lambda+\mu)} (\theta \frac{du}{dn} - u_1 \frac{d\theta}{dn})\} ds \quad (2.3)$$

$$\text{where } \frac{d}{dn} = n_j \frac{d}{dx_j}$$

$$\text{and } W = \mu \epsilon_{ij} \epsilon_{ij} + \lambda (\epsilon_{kk})^2 / 2$$

Ainsworth, et.al. J_θ-Integral⁽¹⁰⁾

$$J_{\theta} = \int_{\Gamma} (n_1 W - t_i u_{i,1}) ds + \int_A \sigma_{ij} \epsilon_{ij,1} dA \quad (2.4)$$

$$\text{where } W(\epsilon'_{ij}) = \int_0^{\epsilon'_{ij}} \sigma_{ij} d\epsilon'_{ij}$$

$$\text{and } \epsilon'_{ij} = \epsilon_{ij} - \epsilon^{\theta}_{ij}$$

Blackburn's J^* -Integral⁽³⁾

$$J^* = \int_{\Gamma} + \int_C (\sigma_{ij} u_{i,j}/2 \, dx_2 - t_i u_{i,1}) ds + \int_A (\sigma_{ij} u_{i,j}/2 - \sigma_{ij,1} u_{i,j}/2) dA \quad (2.5)$$

Kishimoto, Aoki, and Sakata \hat{J} -Integral⁽⁴⁾

$$\hat{J} = - \int_{\Gamma} + \int_C t_i u_{i,1} ds + \int_A \sigma_{ij} \epsilon_{ij,1} dA \quad (2.6)$$

Atluri, et. al. ΔT -Integrals⁽⁵⁾

$$\begin{aligned} \Delta T_p^* &= \int_{\Gamma} + \int_C \{n_1 \Delta W - (t_i + \Delta t_i) \Delta u_{i,1} - \Delta t_i u_{i,1}\} ds \\ &+ \int_A \{\Delta \sigma_{ij} (\epsilon_{ij,1} + \Delta \epsilon_{ij,1}/2) - \Delta \epsilon_{ij} (\sigma_{ij} + \Delta \sigma_{ij,1}/2)\} dA \end{aligned} \quad (2.7)$$

$$\begin{aligned} \Delta T_p &= \int_{\Gamma} + \int_C \{n_1 \Delta W - (t_i + \Delta t_i) \Delta u_{i,1} - \Delta t_i u_{i,1}\} ds \\ &+ \int_{A_S - A_{\Gamma}} \{(\sigma_{ij,1} + \Delta \sigma_{ij,1}/2) \Delta \epsilon_{ij} - (\epsilon_{ij,1} + \Delta \epsilon_{ij,1}/2) \Delta \sigma_{ij}\} dA \end{aligned} \quad (2.8)$$

where $\Delta W = (\sigma_{ij} + \Delta \sigma_{ij}/2) \Delta u_{i,j}$

A_S = the total area

and A_{Γ} = the area in Γ .

2.2 Numerical Implementation of P-I Integrals

As part of the contract, a postprocessor of finite element analyses for calculating the P-I integrals was developed for use in subsequent tasks of the contract. This section discusses the computational algorithms used in the postprocessor and gives some numerical results for isothermal and linear temperature gradient cases.

2.2.1 P-I Integral Computational Algorithm

Computational algorithms have been developed for numerically implementing various P-I integrals under consideration in the current work. These postprocessor numerical algorithms assume that an accurate inelastic solution is available by using a finite-element model of a specimen geometry containing a crack. In the present work, the two-dimensional (2D) finite element computer code CYANIDE(11), which is a GEAE program, is used for inelastic stress analysis. The CYANIDE program uses the incremental theory of plasticity and accounts for both time-independent plastic flow (plasticity) and time-dependent plastic flow (creep). It uses linearly varying displacements in each triangular element of a model, resulting in constant strains over each element.

A flow chart of the postprocessor P-I integrals computational program is shown in Figure 2. Notice that the J-integral and the J_g -integral are also included in the flow chart, although they were not selected for further evaluation in Section 2.1. The output files from the CYANIDE solution for element stresses and strains, nodal displacements, nodal coordinates, and nodal connectivity for each element are read and stored by the postprocessor program. Paths of integration surrounding the crack tip are chosen so that they consist of sides of the triangular elements. The paths are specified by the user in a subroutine of the program. For each line segment along the integration path, the unit normal vector and its Cartesian components are computed. The quantities, such as σ_{ij} , W , and $u_{i,j}$, that appear in the integrand of P-I integrals are interpolated at the midpoint of the path

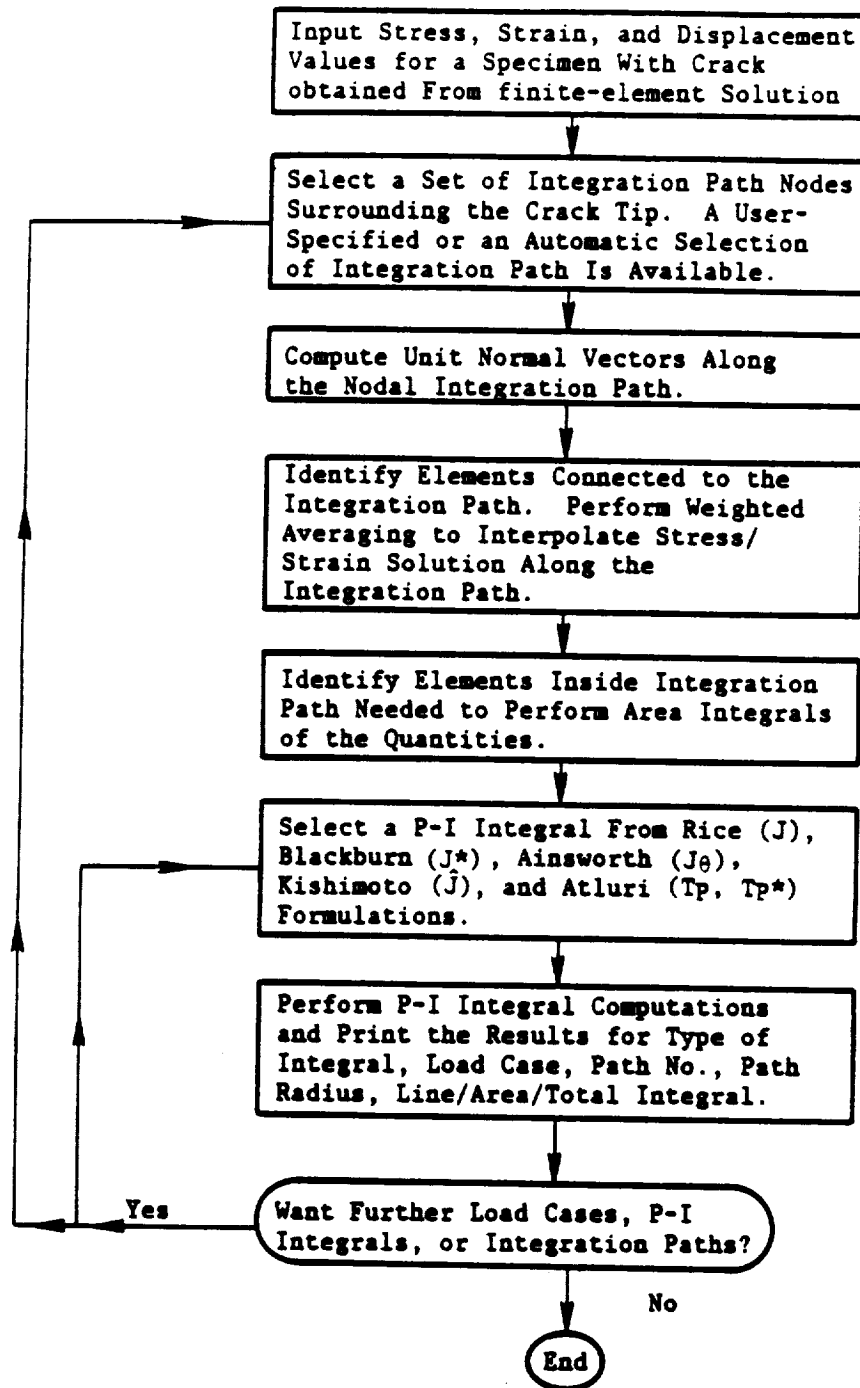


Figure 2: Flow Chart of Postprocessor for Path-Independent Integral Computations.

segment by taking weighted averages of those for the elements containing the segment.

The displacement derivatives for an element are accurately computed from displacement components and coordinates of its vertices (nodes) by using the equations gotten from the shape functions. The shape functions for linear variation of displacements in a triangular element are given by

$$\begin{aligned}u(x,y) &= a_0 + a_1x + a_2y \\v(x,y) &= b_0 + b_1x + b_2y\end{aligned}\tag{2.9}$$

The displacement derivatives for the element are shown to be

$$\frac{du}{dx} = \frac{u_1(y_2 - y_3) + u_2(y_3 - y_1) + u_3(y_1 - y_2)}{x_1y_2 + x_2y_3 + x_3y_1 - x_2y_1 - x_3y_2 - x_1y_3}\tag{2.10}$$

and

$$\frac{dv}{dx} = \frac{v_1(y_2 - y_3) + v_2(y_3 - y_1) + v_3(y_1 - y_2)}{x_1y_2 + x_2y_3 + x_3y_1 - x_2y_1 - x_3y_2 - x_1y_3}\tag{2.11}$$

where the subscripts 1, 2, and 3 represent nodal values at the element vertices. Similar relationships are used for derivatives of element stresses. The stresses at a vertex in the calculations are the weighted average of the element stresses containing the vertex.

2.2.2. Computation of P-I Integrals

To test the implementing of the postprocessor computer program, the P-I integrals were computed for a standard ASTM compact specimen. The geometry of this specimen and the finite element mesh used to model half of the specimen are shown in Figure 3. The model consists of 429 nodes and 782 triangular elements. Dimensions chosen in the study for the width (b) and the crack length (a) are 50.8 and 25.4 mm (2 and 1 inch), respectively. The

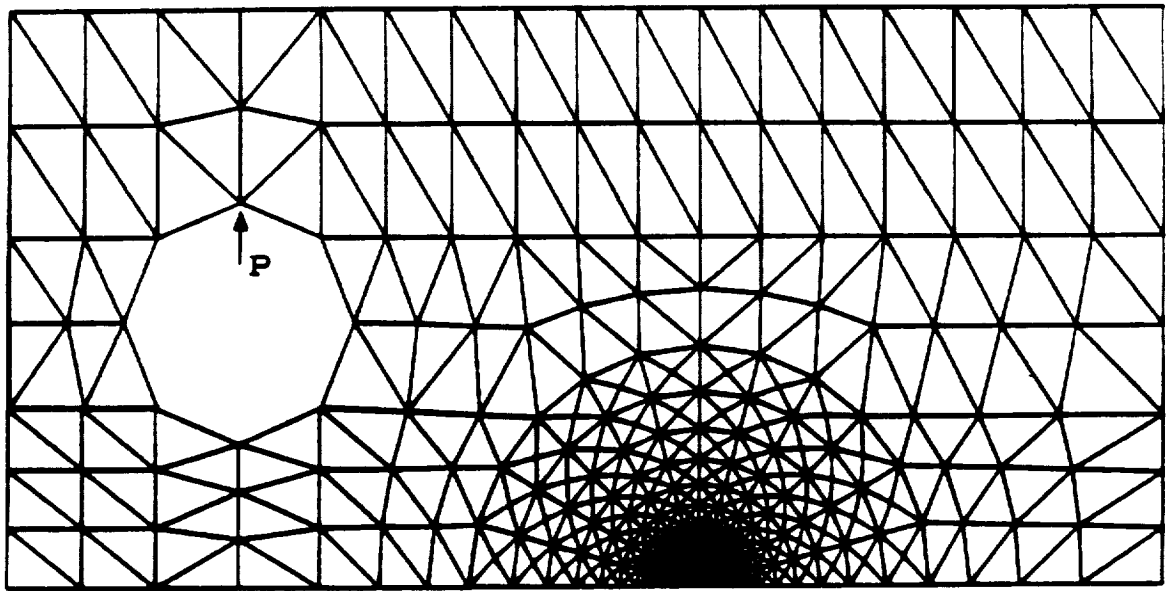
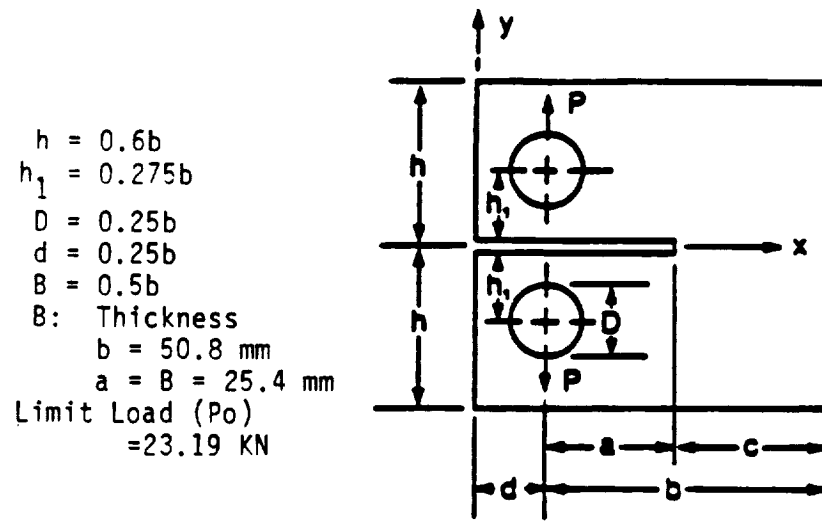


Figure 3: Geometry of an ASTM Standard Compact Tension Specimen and its Finite Element Model.

detailed mesh refinement near the crack tip is shown in Figure 4. There are 12 elements, each subtending a 15° angle and joining at a single vertex point to form the crack tip. Near crack tip mesh refinement, having radial and tangential lines emanating from the crack tip, provides much greater solution accuracy in comparison to models with a uniform distribution of elements in the crack plane.

For elastoplastic analysis, the following Ramberg-Osgood type stress-strain behavior of material was used:

$$\epsilon = (\sigma/E) + \alpha \epsilon_0 (\sigma/\sigma_0)^n$$

with $E = 206.9 \text{ GPa } (30 \times 10^6 \text{ psi})$

$$\alpha = 1.0$$

$$\epsilon_0 = 0.001$$

$$\sigma_0 = 206.9 \text{ MPa } (30 \text{ ksi})$$

$$n = 5$$

$$\text{and } \nu = 0.3$$

The plane stress state of deformation was assumed. Applied load (P) of the compact specimen was increased in steps so that $P/P_0 = 0.25, 0.50, 0.75$, and 1.0 where P_0 is the limit load calculated according to Kumar, et. al.(12).

J-integral results for the four load steps are shown in Figure 5 for each integration path. Integration paths are circular line segments surrounding the crack tip as shown in Figure 4. It can be seen in Figure 5 that for lower values of applied load ($P/P_0 = 0.25$ and 0.50), path-independence is preserved for all paths represented in terms of distances from the crack tip. However, for higher values of load, the J-integral is path-independent for the paths that are away from the crack tip. For paths very close to the crack tip, path-independence was not achieved, perhaps due to nonproportional loading effects or inaccuracies of the field data in close proximity to the crack tip.

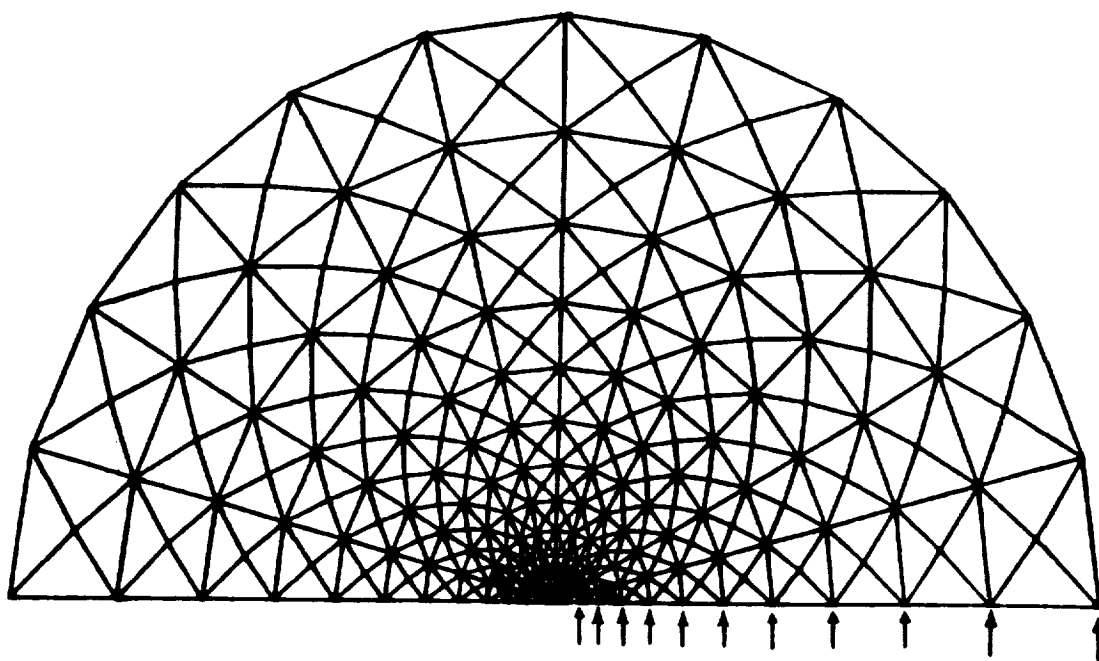


Figure 4: Near Crack-Tip Mesh Refinement and Circular Paths for the Compact Tension Specimen.

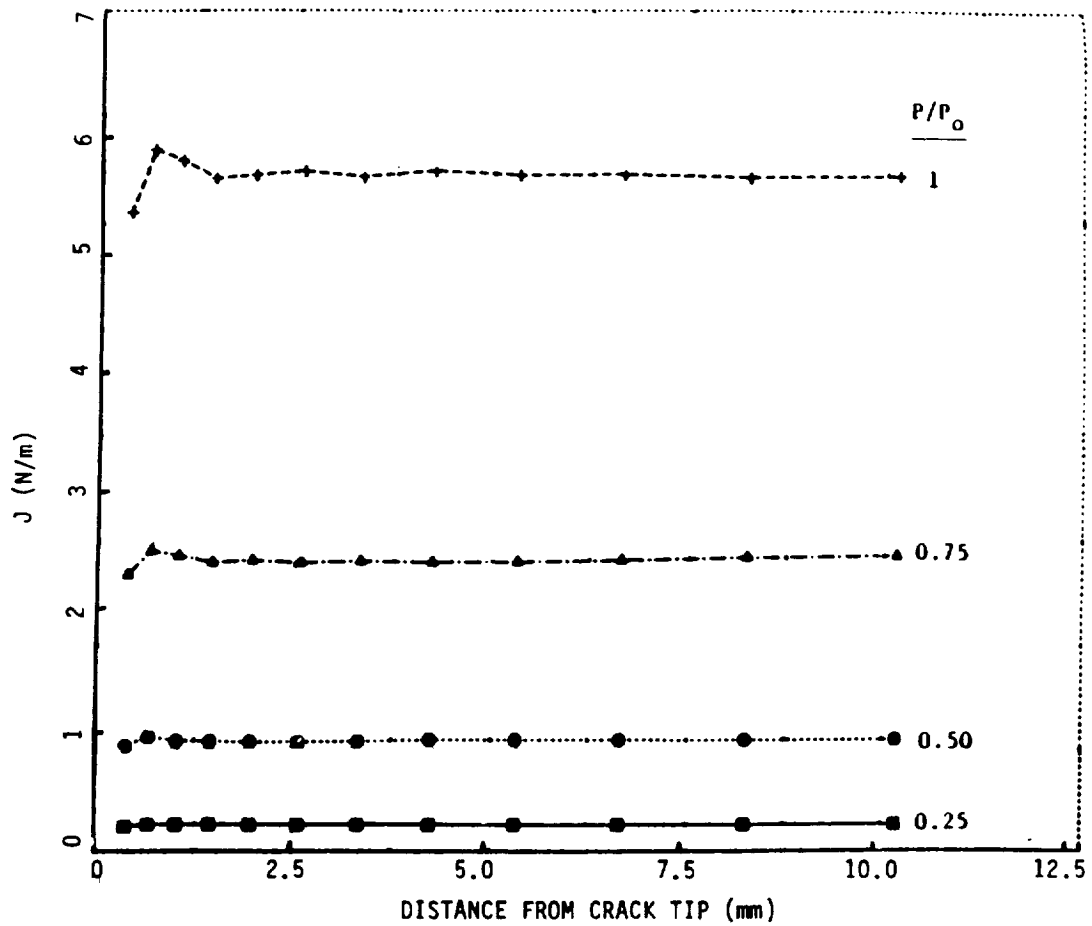


Figure 5: Path-independence of J-integral Along Various Paths for Each Load Step.

The variation of J^* and \hat{J} with the paths are shown in Figures 6 and 7, respectively. It is seen in these figures that the path-independence is maintained to a greater degree for the lower values of applied load. The contribution of line and area integrals is shown in Figure 8. Notice that the relative contribution of the area integral is small for J^* , but is quite significant for \hat{J} .

The Atluri incremental P-I integrals, ΔT_p and ΔT_p^* , were computed for loading to the limit load and unloading to zero load. Figure 9 shows the variation of applied load with load line displacement for this evaluation. For each of the eight incremental load steps, the integrals ΔT_p and ΔT_p^* were computed and then summed to find the total integrals ($T_p = \Sigma \Delta T_p$ and $T_p^* = \Sigma \Delta T_p^*$) at each value of applied load. Figures 10 and 11 show the T_p and T_p^* integrals as functions of distance from the crack tip. Notice that a uniform degree of path-independence is maintained for the four loading steps (1 to 4) up to the specimen limit load. However, for the unloading steps (5 to 8), the path-independence was not as good.

In addition to compact specimen analyses, an elastic-plastic analysis was made on a single edge notch specimen somewhat longer than used to model the experiments in this investigation (Figure 100). The finite element model was subjected to a temperature gradient of 649 to 538°C (1200 to 1000°F) from left to right. The stress-strain curves at these temperatures are shown in Figure 12. The computed P-I integrals are plotted in Figure 13. As expected, the J-integral was path-dependent while the other integrals were nearly path-independent.

In summary, these results show that the finite element postprocessor is working satisfactorily. More detailed presentation of the numerical data in this evaluation has been previously reported(13,14).

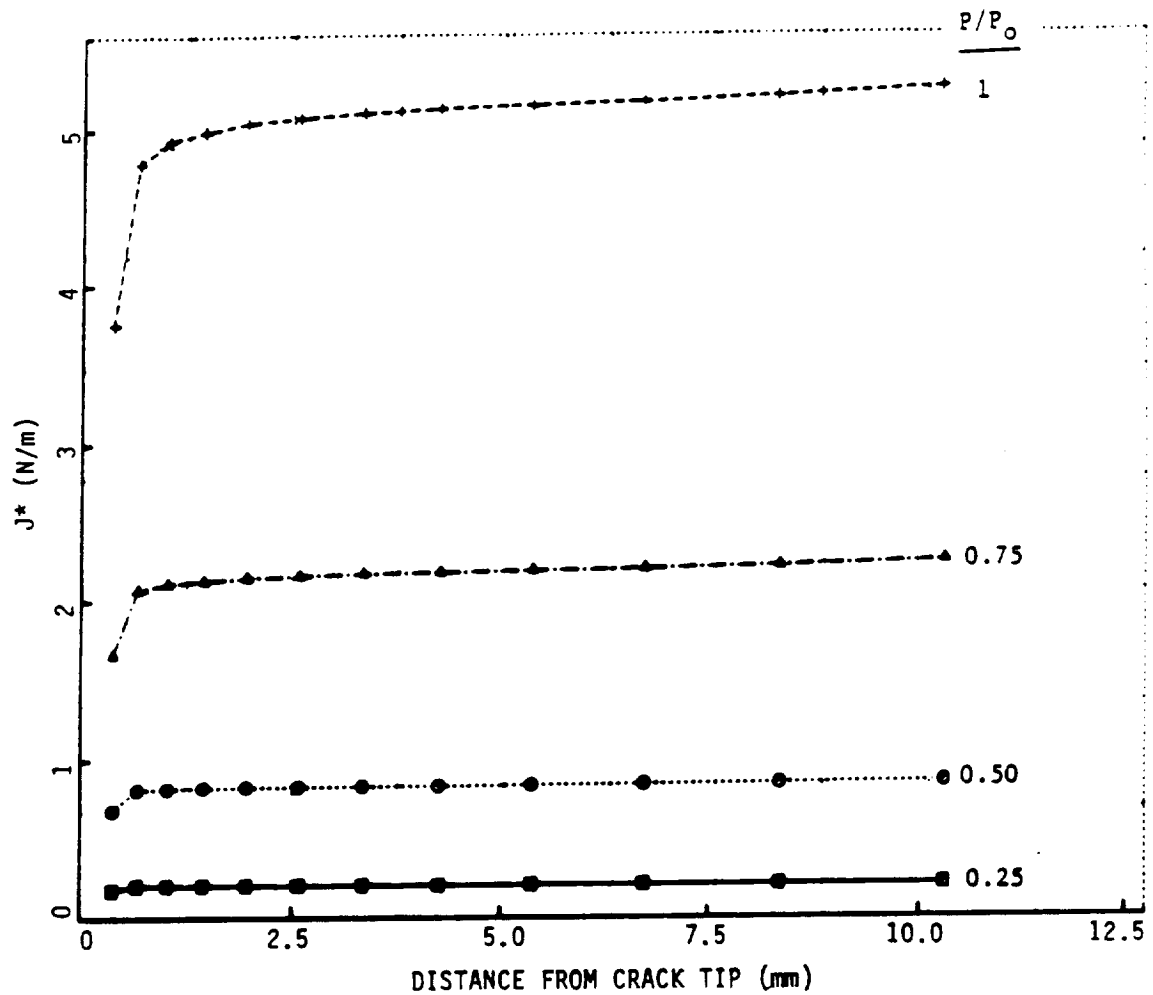


Figure 6: Blackburn J^* -integral for the Four Load Steps for the Compact Tension Specimen.

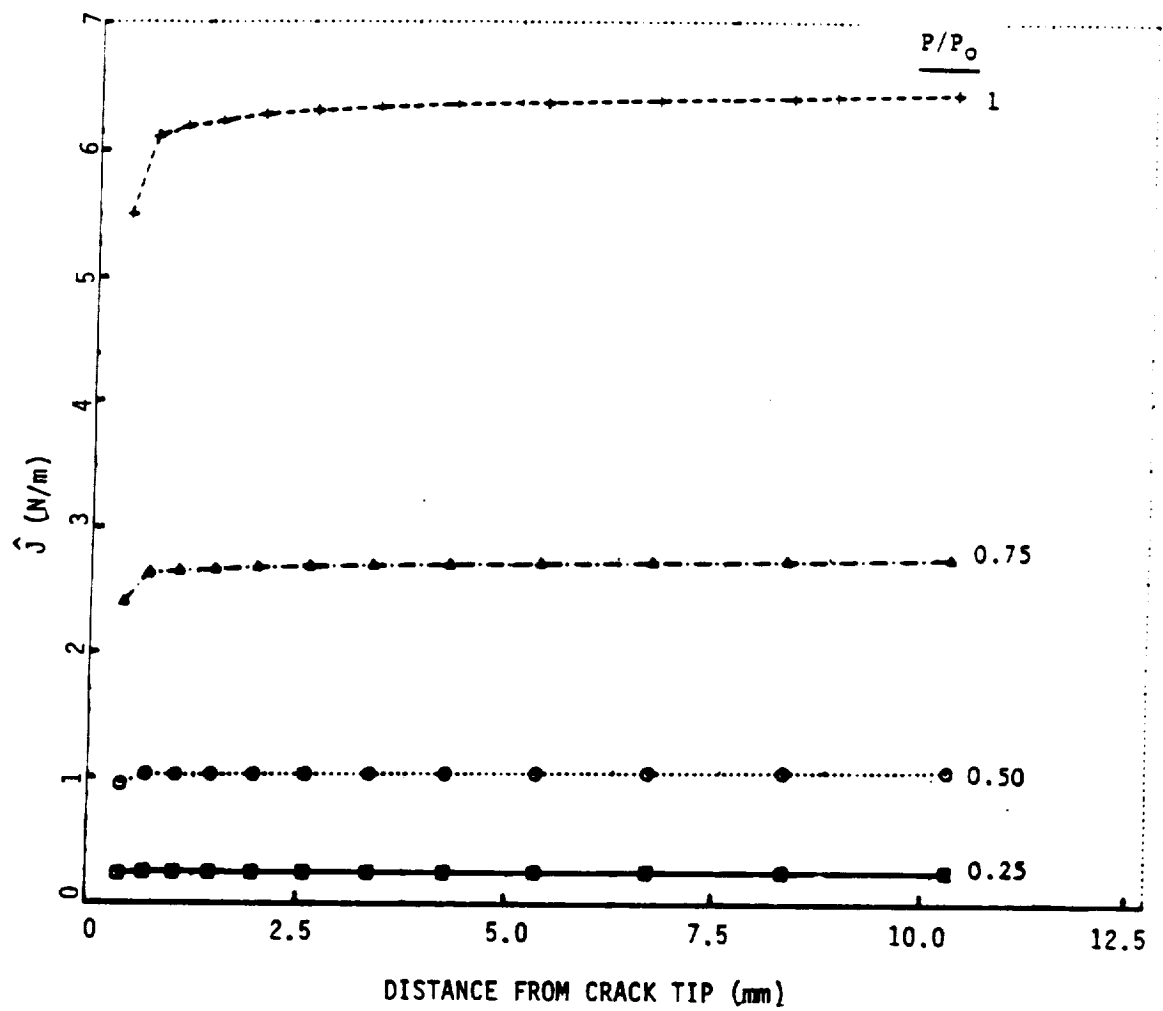
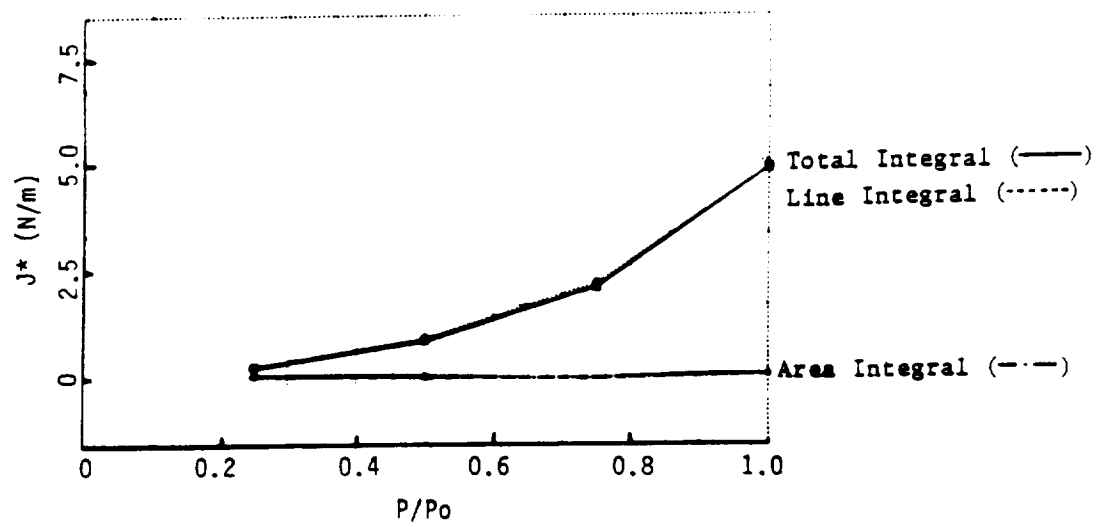
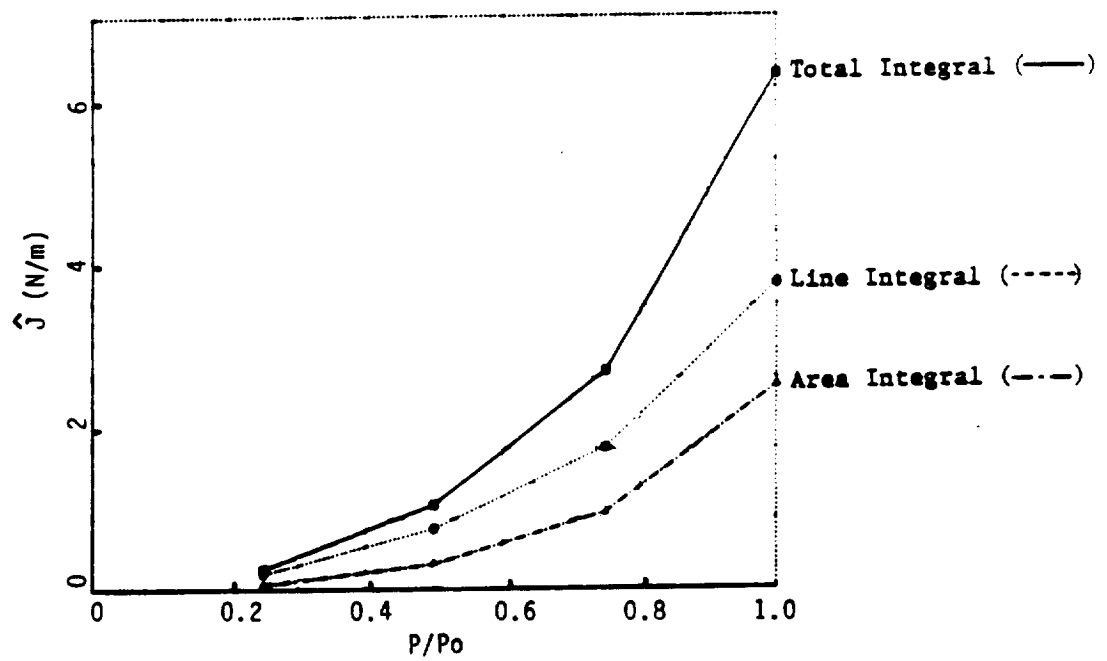


Figure 7: Kishimoto \hat{J} -integral for the Four Load Steps for the Compact Tension Specimen.



(a)



(b)

Figure 8: Comparison of Area and Line Integral Term Contributions to (a) Blackburn (J^*) and (b) Kishimoto (\hat{J}) Integrals.

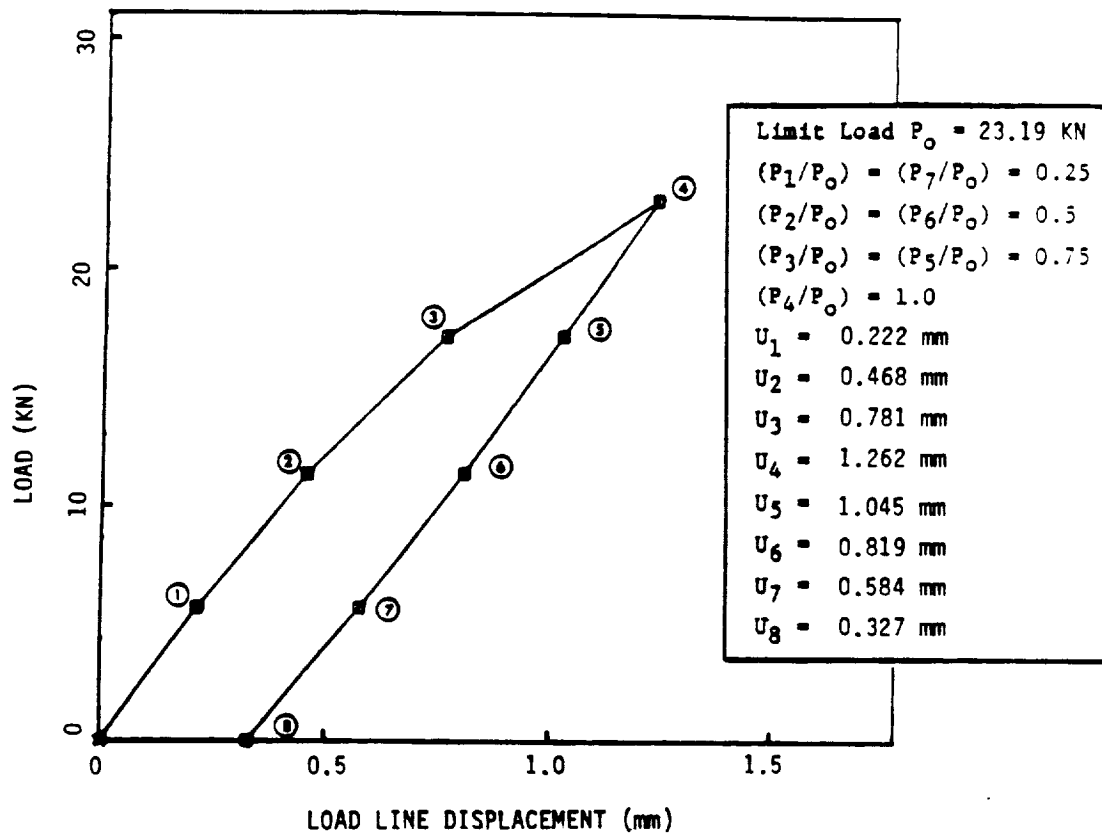


Figure 9: Load Versus Load Point Displacement for the Compact Tension Specimen at Various Load Steps.

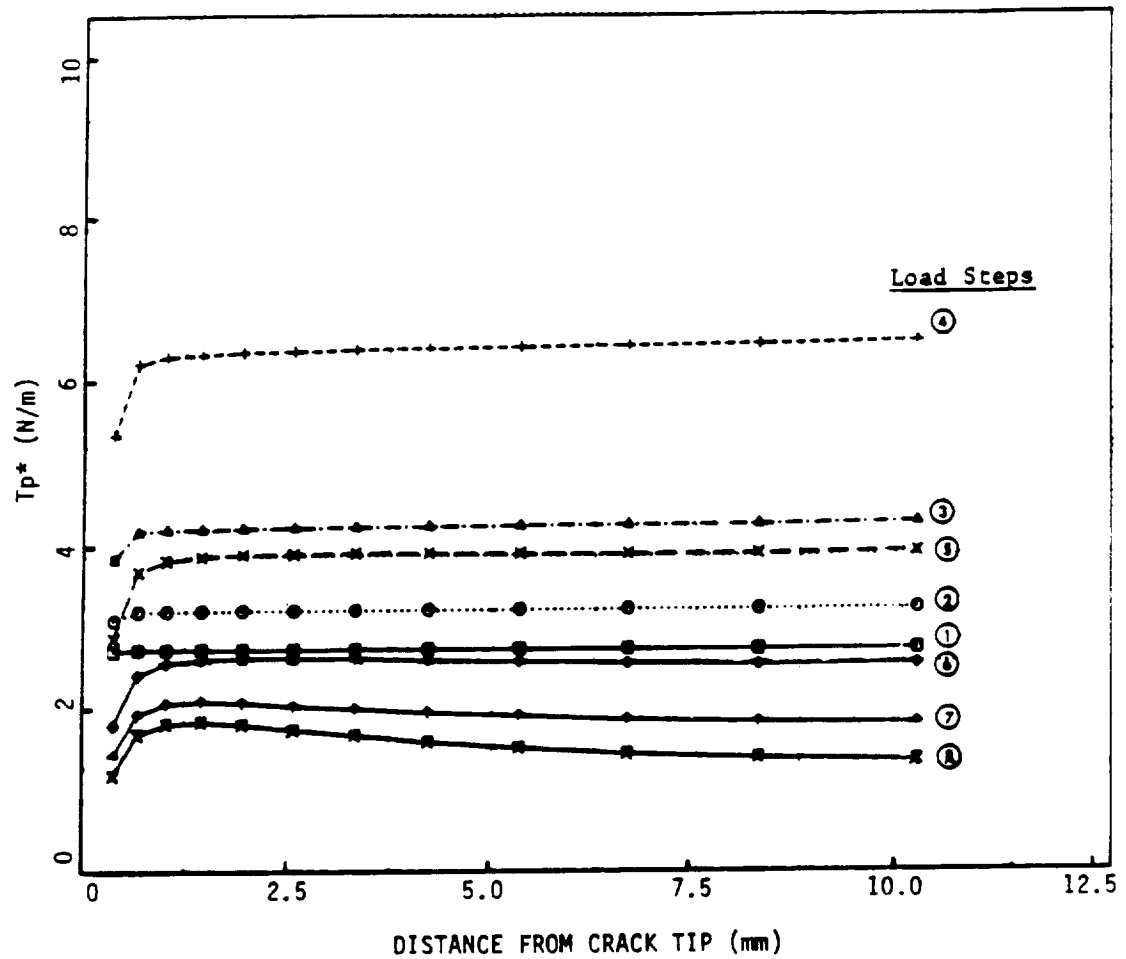


Figure 10: Atluri T_p^* Integral ($= \sum \Delta T_p^*$) Along Various Integration Paths for Loading and Unloading Steps.

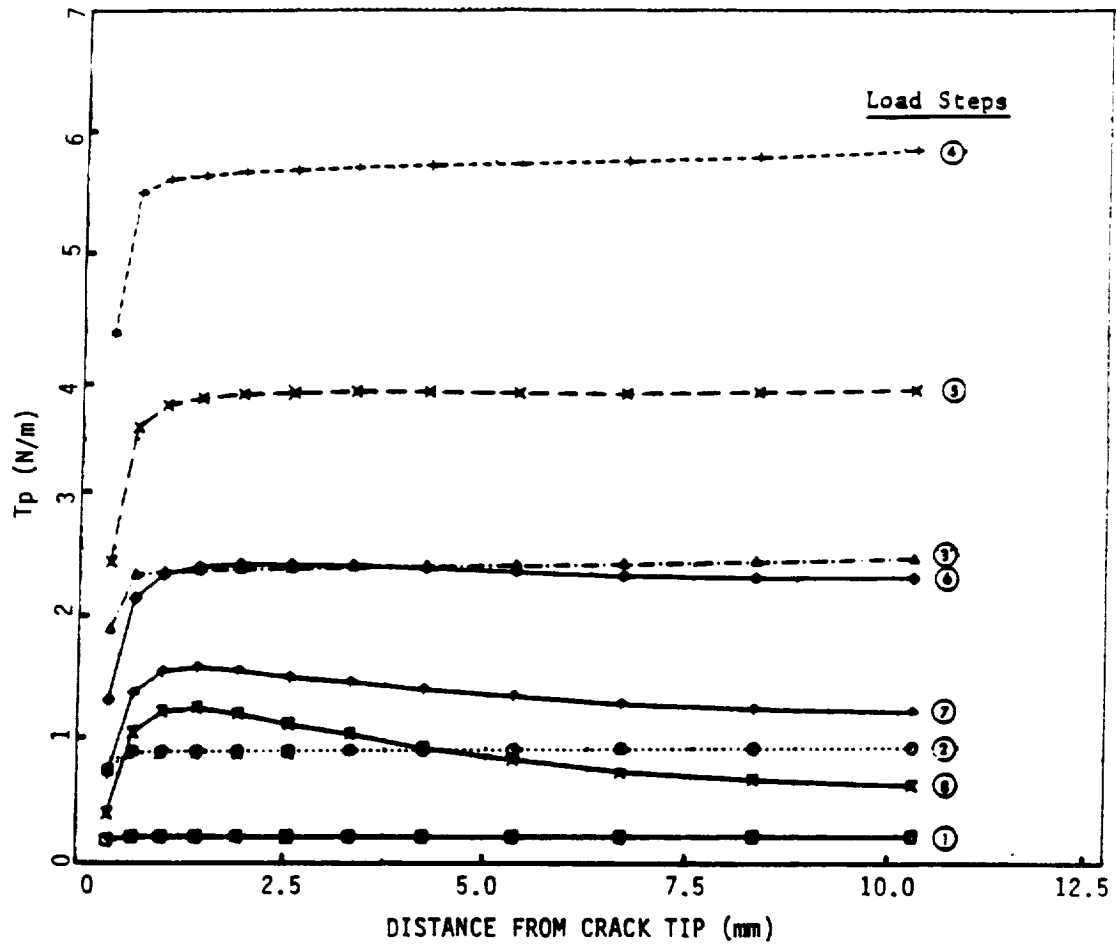


Figure 11: Atluri T_p Integral ($= \sum \Delta T_p$) Along Various Integration Paths for Loading and Unloading Steps.

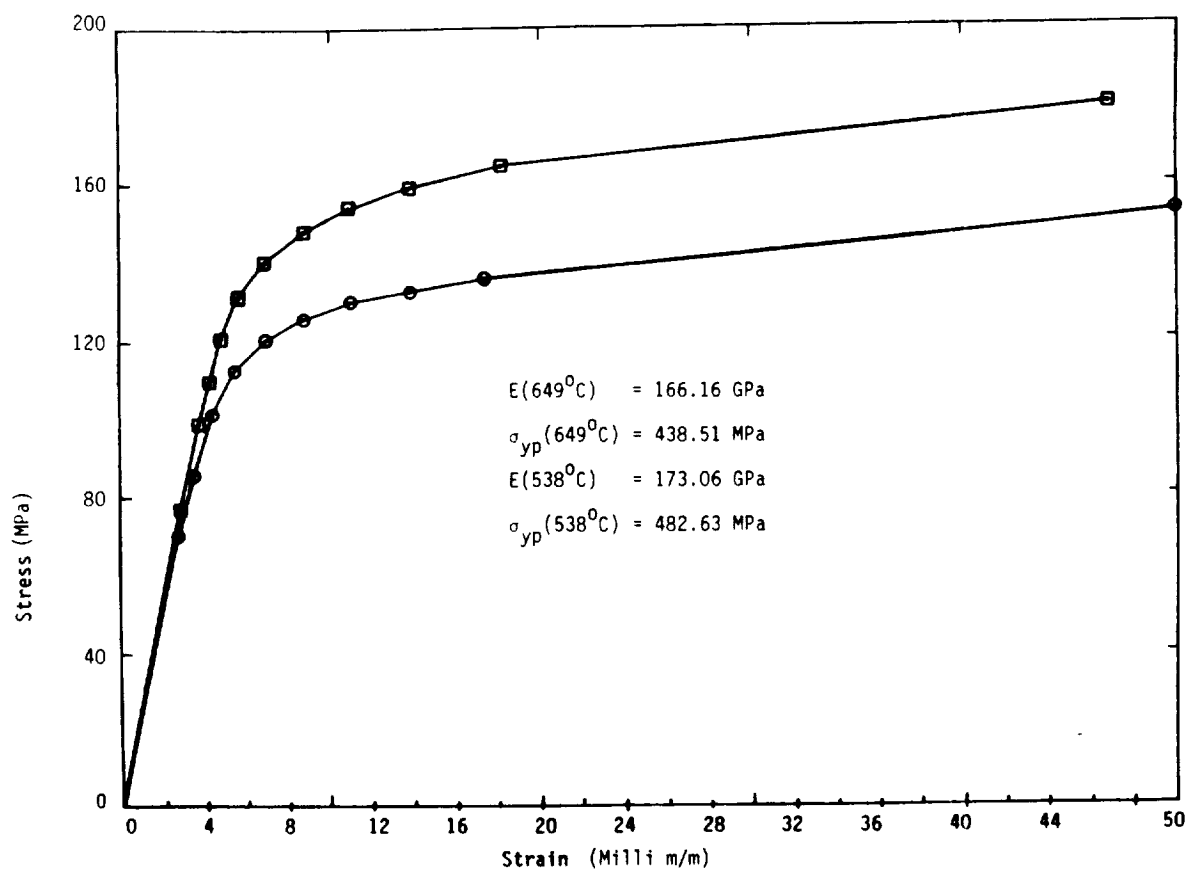


Figure 12: Cyclic Stress-Strain Curves for Linear Thermal Gradient Problem.

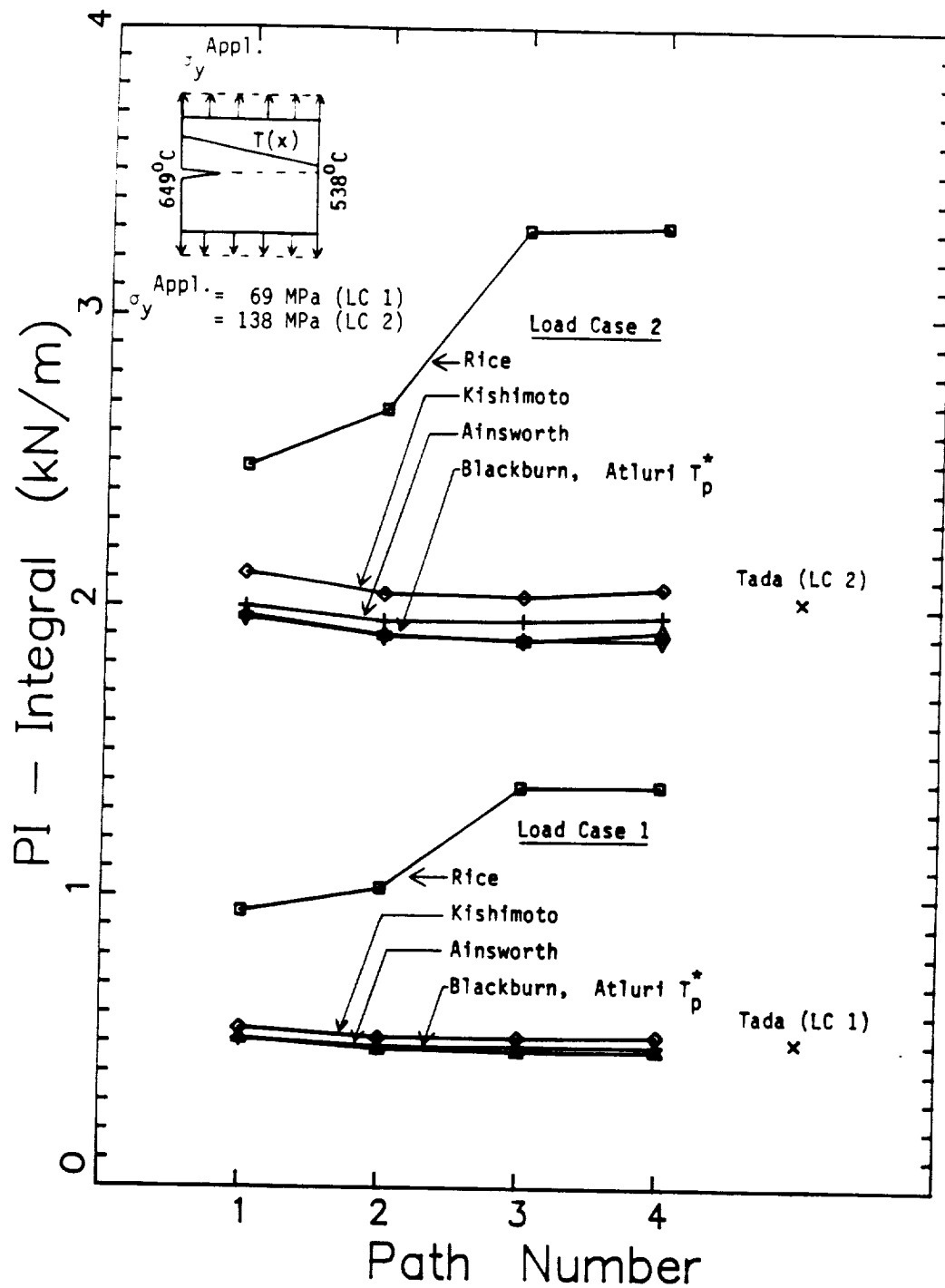


Figure 13: P-I integrals for Thermo-Mechanical Loadings and Temperature-Dependent Material Properties.

3.0 ANALOG MATERIAL

The purpose of the experimental portion of this investigation was to perform experiments to determine the validity of the selected path-independent (P-I) integrals. The "analog" material was selected so that it could be tested at relatively low temperatures while retaining many of the important characteristics of a combustor liner material. Since significant thermomechanical testing was to be performed, the selected alloy must display a range of properties over a significant temperature range. The specific characteristics evaluated include:

- Significant variation in elastic modulus throughout the test temperature range
- Large changes in short-time creep rates throughout the test temperature range
- No metallurgical- or stress-induced phase transformations in the test temperature range
- Thermal conductivity conducive to perform thermal gradient and thermomechanical fatigue (TMF) tests.

3.1 Material Selection

Nickel-Base Alloy 718 was selected for this program, strengthened by γ' . It is metallurgically stable up to temperatures approaching 700°C (1291°F), and has physical properties (thermal expansion and conductivity) similar to nickel-base combustor alloys. In this study it was planned to perform crack growth evaluations over the temperature range from 427°C (800°F) to 649°C (1200°F). Table 2 shows the range of elastic modulus and creep properties throughout this temperature range. The modulus varies by approximately 10%, and the creep rates, estimated by the time to creep 0.2%, vary by at least four orders of magnitude. Thus, Alloy 718 met the

Table 2: Variation of Alloy 718 Elastic Modulus and Creep Properties with Temperature.

	427°C (800°F)	538°C (1000°F)	649°C (1200°F)
Young's Modulus (MPa)	182	175	166
Time to Creep 0.2% at 700 MPa (Hours)	---	30,000	2

requirements for an analog material.

3.2 Material Processing and Microstructure

Alloy 718 plate was procured for use in this program. The plate has a nominal thickness of 22.2 mm (0.875 inch) and was procured in 13 pieces, each measuring 381 mm (15 inches) by 406 mm (16 inches). This plate was produced by Cabot Corporation from heat 2180-1-9836. The ladle composition and specification for Alloy 718 are compared in Table 3. This composition falls within the specified limits.

This material was supplied in a mill-annealed condition. The plates were subsequently solution-treated and aged at the General Electric Engineering Material Technology Laboratory (EMTL) in a vacuum furnace under computer control. The plates were solution-treated at 968°C (1775°F) for one hour at temperature and then cooled to room temperature. They were then aged for eight hours at 718°C (1325°F), cooled at 56°C/hr (100°F/hr) to 621°C (1150°F), where they were held for eight hours. Two plates were heat treated simultaneously. Each heat treatment run was monitored with multiple thermocouples. In the first run (containing only one plate) the aging time exceeded the requested time. For this reason, the plate received a second solution treatment and age cycle. This was not an unusual occurrence. However, to eliminate any potential effects, this plate was used only for specimen development. The remaining plates were heat treated successfully.

The microstructure of one of the plates was characterized using optical metallography during this investigation. Another plate was characterized during the time-dependent crack growth program⁽¹⁵⁾ and similar microstructures were observed. On this basis, the types of microstructures reported here are believed to occur in all of the plates.

Metallographic examination was performed on three faces perpendicular to the longitudinal, width, and thickness directions. Optical micrographs were

TABLE 3: Composition Of Alloy 718 Plate
(Weight Percent)

<u>Element</u>	<u>Specification</u>	<u>Ladle Analysis</u>
C	0.02-0.08	0.06
Mn	0.35 Max	0.17
Si	0.35 Max	0.17
S	0.015 Max	0.002
P	0.015 Max	0.006
Cr	17.0-21.0	17.92
Fe	15.0-21.0	18.32
Co	1.0 Max	0.10
Mo	2.80-3.30	3.03
Nb+Ta	4.75-5.50	5.11
Ti	0.75-1.15	1.12
Al	0.30-0.70	0.45
B	0.006 Max	0.002
Cu	0.30 Max	0.03
Ni	50.0-55.0	53.63

prepared at three magnifications. At the lowest magnification a montage was prepared across the entire specimen, which for two of the specimens was the plate thickness. There did not appear to be any gradients in microstructure through the thickness of the plate.

The microstructure of this plate had a duplex grain size with some large, elongated grains, surrounded by smaller, more equiaxed grains as shown in Figure 14. The larger grains are most likely warm-worked, but unrecrystallized, while the small, uniform grains have been recrystallized during the rolling of the plate. These types of duplex microstructures are quite common in cast and wrought nickel-base superalloys. The elongated shape of the elongated grains was most easily observed in the metallographic section perpendicular to the width direction of the plate confirming that the primary rolling direction of the plate corresponded to the longitudinal direction. Typical microstructures observed on the other two faces are shown in Figures 15 and 16. The large grains were as large as 0.25 mm in width and were up to 0.5 mm long. The small grains had diameters on the order of 0.05 mm.

The evidence of rolling could also be observed in the non-metallic inclusions present in the Alloy 718 plates. These are melt-related and often form in clusters. These clusters are elongated and separated during the rolling of the plates. Figure 17 shows a micrograph of the face perpendicular to the plate width with an inclusion stringer along the rolling direction of the plate.

This microstructural evaluation revealed that the microstructure of the Alloy 718 plates were typical of hot-rolled superalloys.

3.3 Determination of Alloy 718 Constitutive Properties

The purpose of this portion of the testing program was to develop the Alloy 718 mechanical property data for use in the finite-element calculations reported in other sections of this report. The tests included tensile,

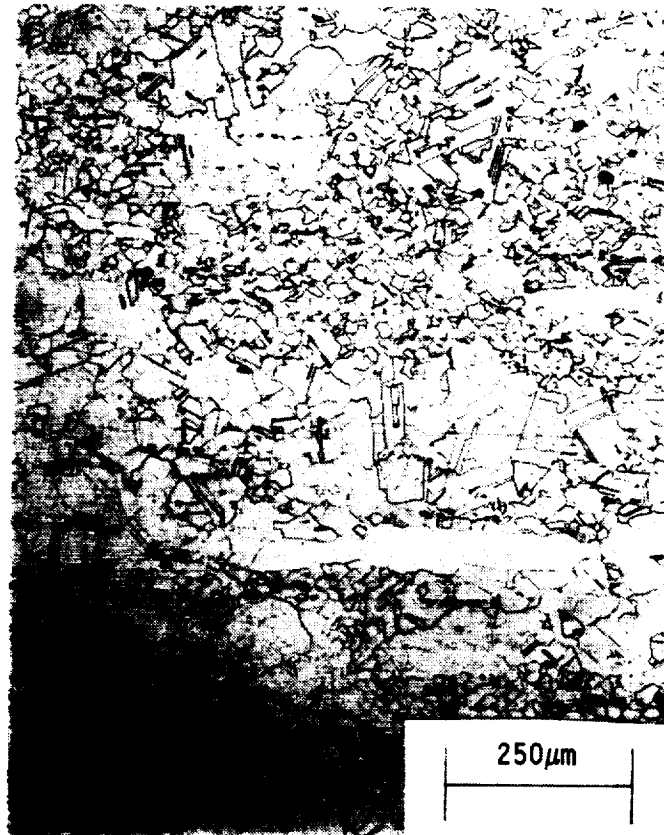


Figure 14: Optical Micrograph of Alloy 718 with the Longitudinal Direction Displayed Horizontally and the Thickness Direction Displayed Vertically.



Figure 15: Optical Micrograph of Alloy 718 with the Longitudinal Direction Displayed Horizontally and the Transverse Direction Displayed Vertically.



Figure 16: Optical Micrograph of Alloy 718 with the Transverse Direction Displayed Horizontally and the Thickness Direction Displayed Vertically.

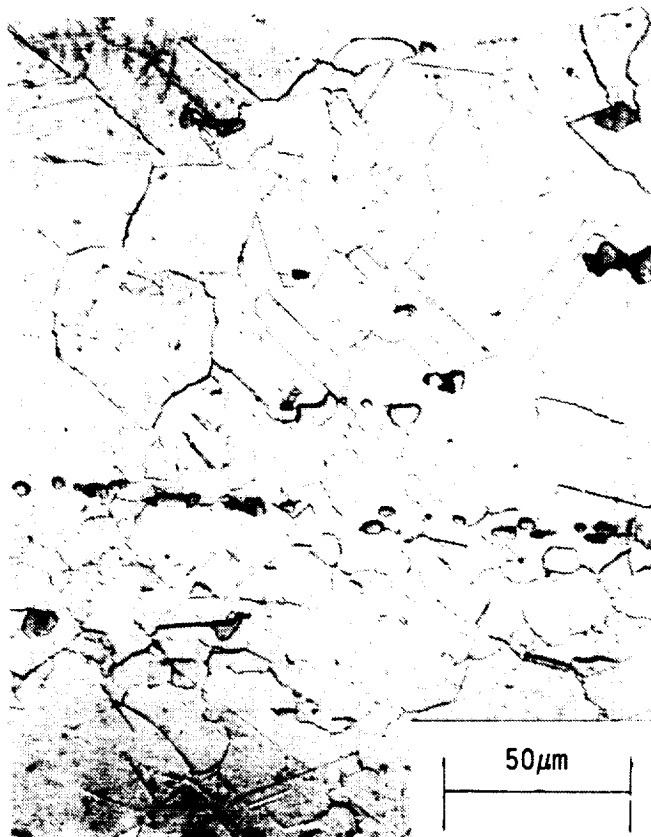


Figure 17: Optical Micrograph of Alloy 718 Showing the Elongation of the Banded Inclusions with the Longitudinal Direction Displayed Horizontally and the Thickness Direction Displayed Vertically.

creep, and cyclic tests. The orientation of all these specimens was so that the tensile axis was parallel to rolling direction of the plate. The fracture surfaces were in the plane containing the width and thickness directions. This corresponded to the fracture plane of the crack growth specimens which will be described in a different section. This plane was selected because it most likely represents the orientation of maximum toughness and thus would permit the largest amount of plasticity during the cyclic constitutive and crack growth tests. This plane is also perpendicular to the axis of the large elongated grains and thus would diminish the opportunity for the large grains to influence the test results.

All the specimens had axisymmetric geometries with a nominal diameter of 6.4mm (0.25 inch) and a nominal gage length of 25.4mm (1 inch). The monotonic (tensile/creep) specimens (Figure 18) had threaded grips, while the cyclic specimens (Figure 19) had buttonhead grips. The buttonhead geometry permits better load reversal and alignment, especially for compressive loads. All tests were performed in closed loop equipment under strain control. The strain was measured using an elevated temperature water cooled extensometer with a gage length of 12.7 mm (0.5 inch). The data from these tests were acquired using an ETS data acquisition system that monitors both the stress-strain hysteresis data at predetermined intervals. The computer software to analyze this data has been described elsewhere⁽¹⁶⁾.

The tensile and cyclic tests were performed at several strain rates to evaluate strain rate sensitivity. Based on previous investigations^(17,18), it is not anticipated that Alloy 718 will show extensive strain rate sensitivity for the conditions used in this program. Table 4 lists the test matrix for these tests. The tensile tests were conducted at three strain rates. The cyclic tests were conducted at three strain ranges and two strain rates. The strain ranges used in the tensile and cyclic tests covered a factor of 25 variations in strain rates. Duplicate creep tests were also performed.

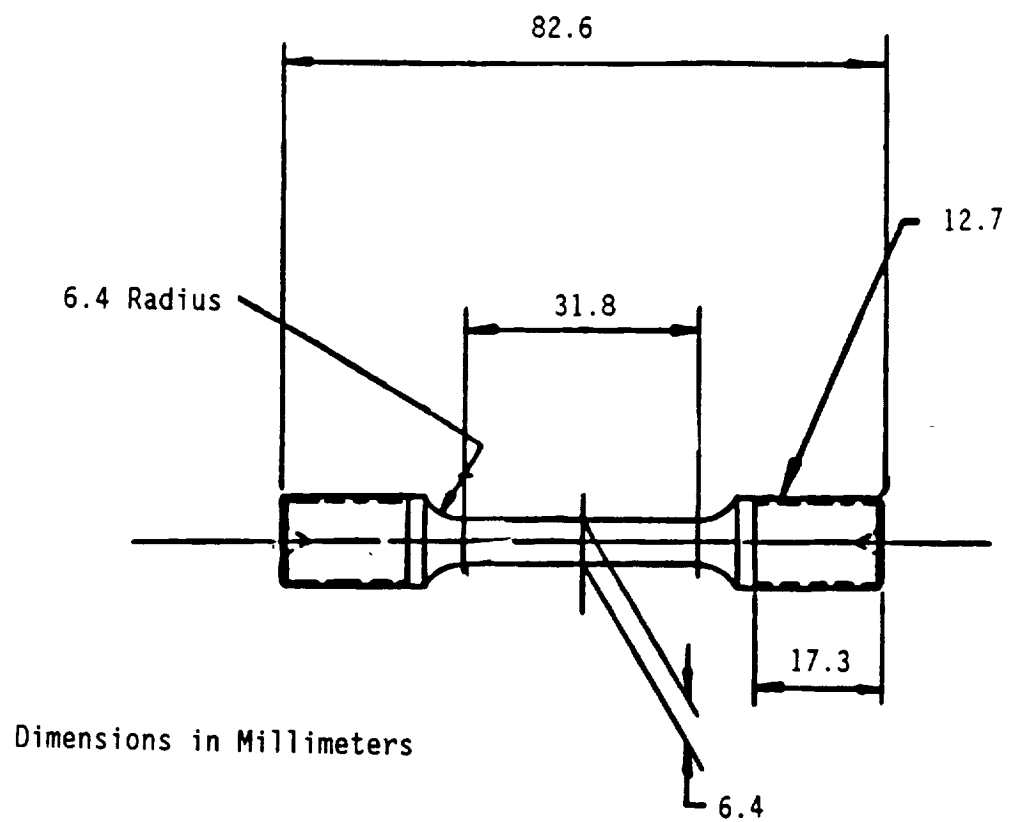


Figure 18: Drawing of the Test Specimen Used to Evaluate the Tensile and Creep Properties of Alloy 718.

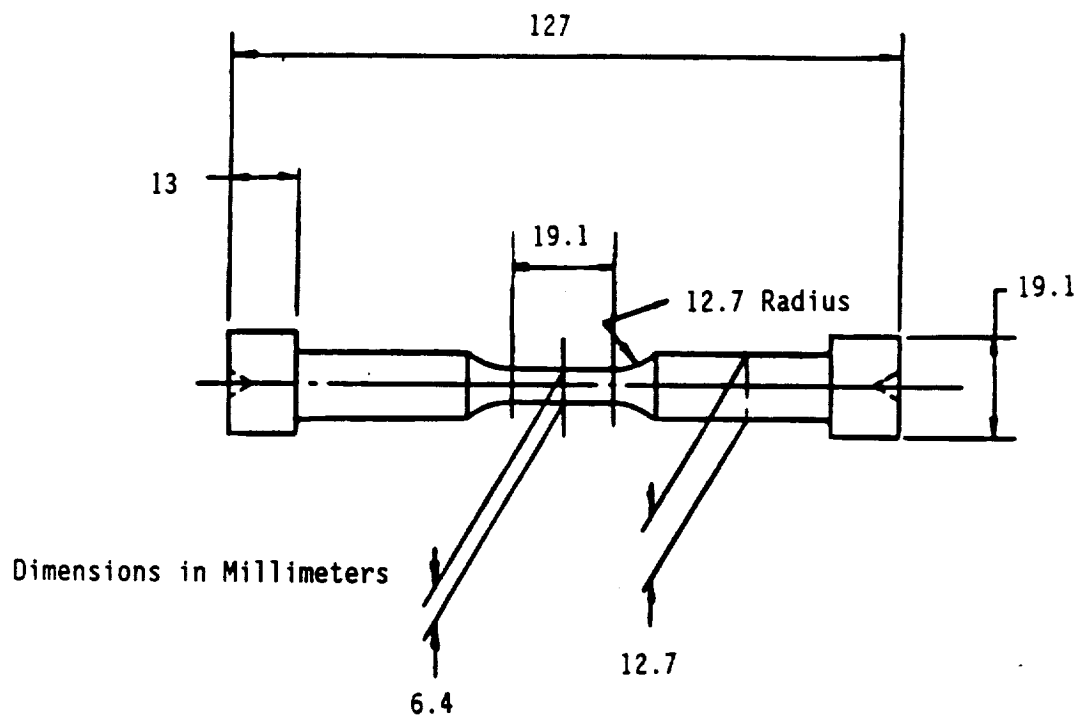


Figure 19: Drawing of the Test Specimen Used to Evaluate the Cyclic Properties of Alloy 718.

TABLE 4: Constitutive Property Test Matrix

TENSION TESTS (strain rate control)

<u>Temperature (°C)</u>	<u>Strain Rates (%/sec)</u>
21	
427	0.02
482	
538	0.10
593	0.50
649	

CREEP TESTS (load control)

<u>Temperature (°C)</u>	<u>Stress Levels (MPa)</u>
538	956, 1003, 1020, 1023, 1058
593	920, 985, 1025, 1059, 1025, 1056
649	751, 761, 815, 821, 956, 958

CYCLIC TESTS (strain control, $A_\epsilon = \infty$, triangular wave shape)

<u>Temperatures (°C)</u>	<u>Strain Rates (%/sec)</u>	<u>Strain Ranges</u>
427		
	0.02	0.0115
538		0.0170
593		
	0.50	0.0350
649		

3.3.1 Tensile Properties

The tensile tests were performed in strain control at a predetermined strain rate. The values of strain rates evaluated were 0.02, 0.10, and 0.50 %/sec. Alloy 718 strains to approximately 10% prior to the onset of specimen necking. The tests were terminated at a total strain of 8% to eliminate the possibility of specimen fracture and damage of the elevated temperature extensometer.

During plastic deformation, Alloy 718, like many other nickel-base superalloys, exhibits serrated yielding. When serrated yielding occurs, there is a small, but rapid, increment in strain. For a displacement controlled test, this results in an elastic unloading of the specimen. The specimen then reloads back to the desired strain and continues loading until this event occurs again. As a result of this behavior, the stress-strain curve is jagged and not the ideally smooth one seen for most materials. Figure 20 shows the stress data obtained for an Alloy 718 tension test performed at 427°C (800°F) with a strain rate of 0.02 %/sec. The data below the maximum stresses resulted from the serrated yielding. Table 5 shows the plastic strain at which serrated yielding was first observed. The serrated yielding data show that, in general, increasing strain rate decreases the plastic strain at which serrated yielding occurs. Serrated yielding was not observed at room temperature. For the five higher temperatures, increasing temperature increased the strain value at the onset of serrated yielding. This conforms to the experience in many nickel-base superalloys where the occurrence of serrated yielding is most severe at approximately 400°C (750°F) and diminishes at both lower and higher temperatures.

Serrated yielding behavior would be extremely difficult to treat in the finite element analysis of the test specimens, so the stress-strain curves were constructed by ignoring data obtained during the unloading associated with serrated yielding.

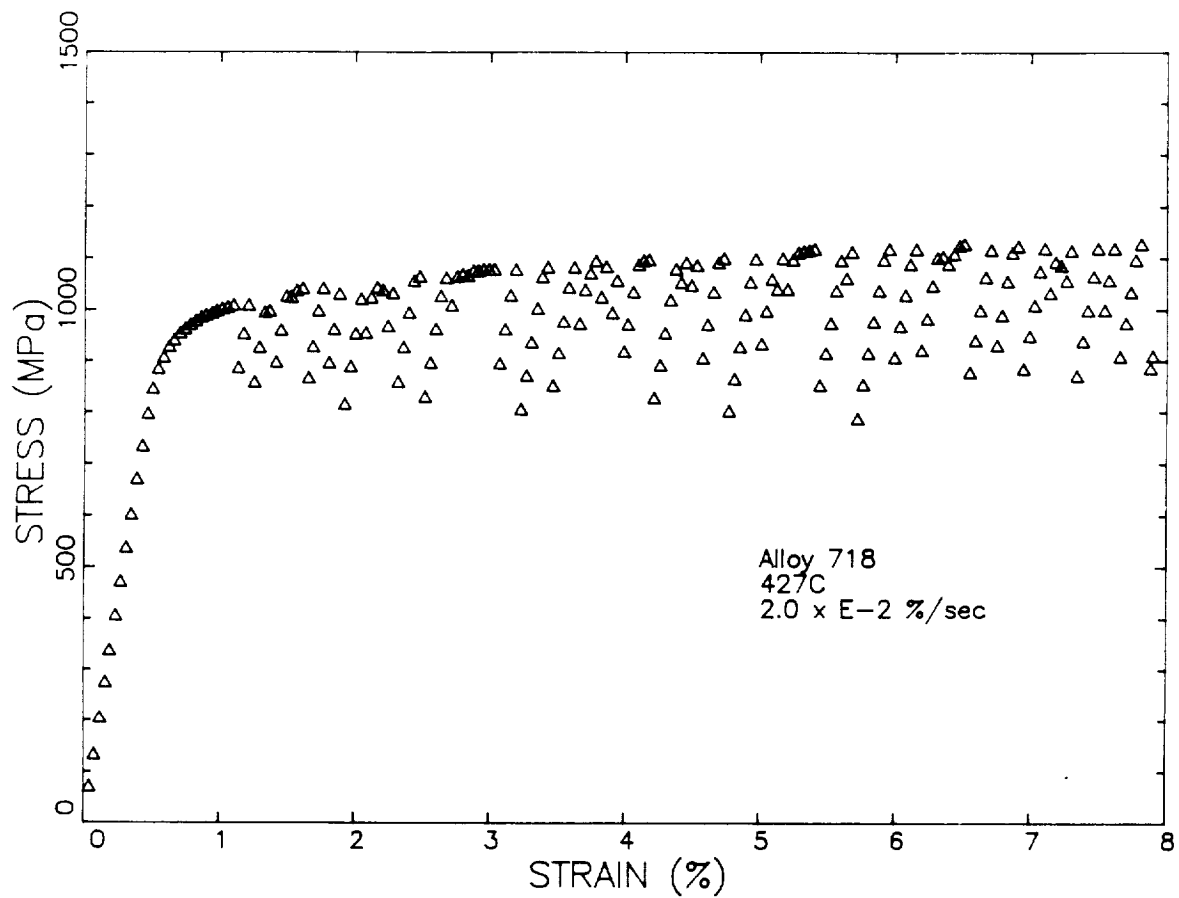


Figure 20: Stress-Strain Response of Alloy 718 Specimen under Monotonic Tensile Loading at 427°C (800°F) at a Strain Rate of 2.0×10^{-2} %/sec Which Exhibited Extensive Serrated Yielding.

TABLE 5: Summary Of Alloy 718 Tension Tests

Test Specimen	Test Temperature (°C)	Strain Rate (%/sec)	0.2% Offset Yield Strength (MPa)	Plastic Strain at Start of Serrated Yielding
N1-2	21	0.02	1095	>0.0716
N1-17	21	0.10	1087	>0.0716
N1-62	21	0.50	1098	>0.0716
N1-59	427	0.02	956	0.0051
N1-4	427	0.10	970	0.0040
N1-20	427	0.10	947	0.0049
N1-21	427	0.50	955	0.0038
N1-23	482	0.02	942	0.0072
N1-57	482	0.10	947	0.0056
N1-6	482	0.50	951	0.0042
N1-8	538	0.02	939	0.0148
N1-26	538	0.10	924	0.0095
N1-55	538	0.50	922	0.0616
N1-53	593	0.02	918	0.0205
N1-10	593	0.10	926	0.0314
N1-29	593	0.50	905	0.0094
N1-32	649	0.02	908	>0.0720
N1-51	649	0.10	903	0.0285
N1-12	649	0.50	925	0.0117

Table 5 also shows the 0.2% offset yield strengths for each of the specimens tested. These data show no indication of a strong strain rate sensitivity. As will be shown later in this section, Alloy 718 showed very little influence of strain rate sensitivity in the tension or cyclic tests.

There was a considerable decrease in yield strength between room temperature and 427°C, however between 427 and 649°C the yield strengths decreased by less than 60 MPa (9 ksi). Figure 21 shows the tensile data obtained at 538°C where different types of points represent the data for different strain rates. As with the yield strength data, the tensile flow curves do not show any significant strain rate sensitivity. As a result, the stress-strain response of Alloy 718 was modeled using classical plasticity rather than a unified constitutive approach.

The crack growth specimens were analyzed using a modified version of the finite element code CYANIDE⁽¹¹⁾. This code requires that the stress-strain curve be introduced by listing the end points of linear segments with the number of segments not to exceed ten. The Alloy 718 stress-strain data determined during this investigation was fit to a Ramberg-Osgood relationship:

$$\epsilon = \sigma/E + (\sigma/A)^{1/n} \quad (3.1)$$

Where ϵ = total longitudinal strain

σ = stress

E = Young's modulus

A, n = material constants

The value of E was determined to be the average of values determined in the tension tests⁽¹⁶⁾. The values of A and n were then determined by regression analysis to the form

$$\epsilon_p = \epsilon - \sigma/E = (\sigma/A)^{1/n} \quad (3.2)$$

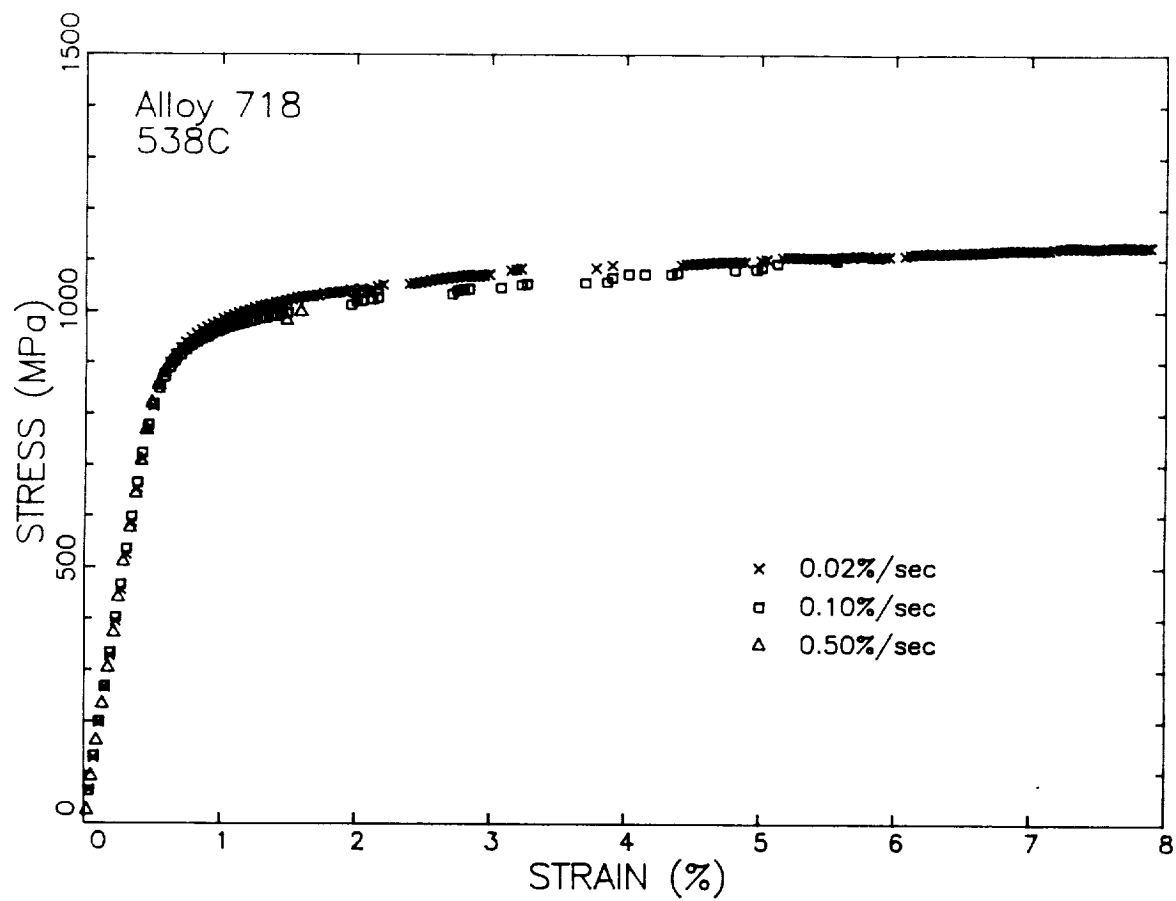


Figure 21: Variation of Tension Stress-Strain Response of Alloy 718 at 538°C (1000°F) for Three Different Strain Rates.

The endpoints of the linear segments on the stress-strain curves were calculated using the appropriate values of E , A , and n in Equation 3.1.

The endpoints were selected to be at predetermined values of strain for the 538°C tests. Some of the early CYANIDE finite element results showed that the elements adjacent to the crack tip required strains in excess of ten percent. To avoid potential inaccuracies associated with extrapolation of the multi-segment stress-strain curve, the strain for the tenth point was selected to be 50%. The ninth value of strain was selected to be 8%, the terminal strain in the Alloy 718 tension tests. The first value of strain was selected to have a value so that the plastic strain was approximately 0.01%, on the order of the strain resolution of the extensometry. The remaining values of strains were selected so that the logarithm of the plastic strains of the endpoints varied linearly. The same values of total strain were used at all temperatures. The value of plastic strain at the first point and the logarithmic linear relationship was not exact for temperatures other than 538°C due to the variation of Young's modulus with temperature.

Figures 22 through 27 show the tension stress-strain data for Alloy 718 at 21, 427, 482, 538, 593, and 649°C (70, 800, 900, 1000, 1100, and 1200°F), respectively. Also shown in these figures are the tension stress-strain curves determined from these data. These curves do not include the final segments starting with a strain of 8% and ending at 50%. Figure 28 shows the entire 538°C curve up to a strain of 50% illustrating that this procedure does not result in a rapid change in slope between the final two segments. The values determined for a Ramberg-Osgood stress-strain curve (E , A , and n) and the endpoints of the multi-linear segment stress-strain curves are listed in Tables 6 and 7, respectively.

Figure 29 shows the stress strain curves for all test temperatures evaluated. There is significant difference between the room temperature curve and those determined for elevated temperature; however, there are relatively small, but consistent differences in tensile response between 427

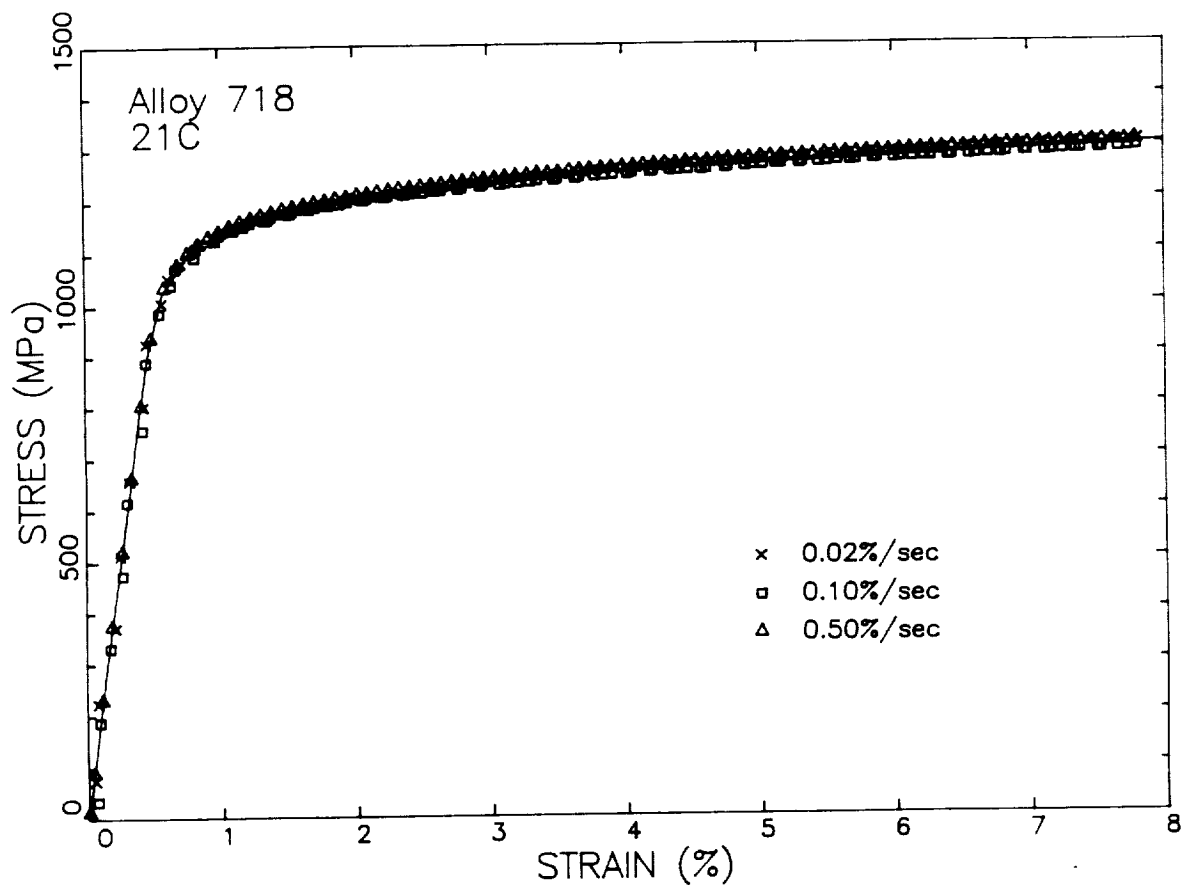


Figure 22: Experimental Data and Multi-linear Curve for the Alloy 718 Tension Tests Performed at 21°C (70°F).

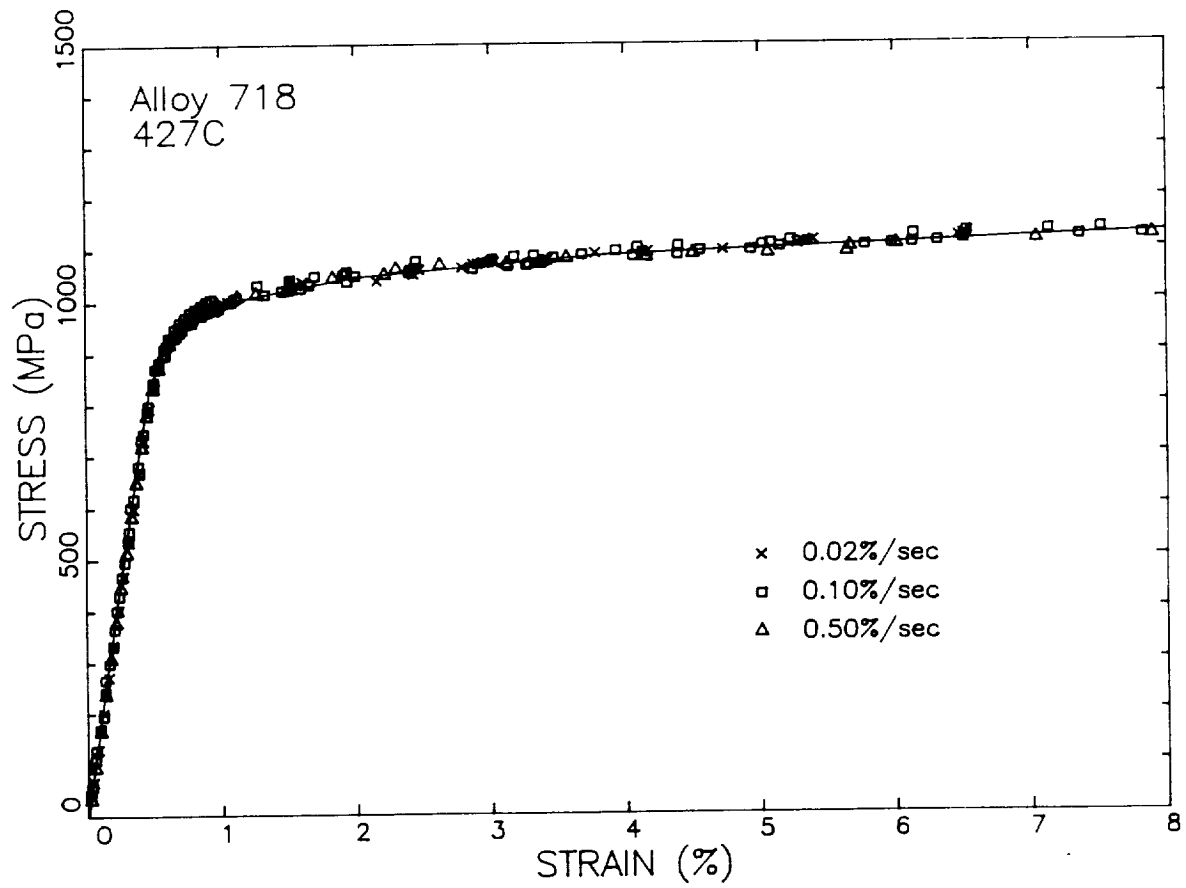


Figure 23: Experimental Data and Multi-linear Curve for the Alloy 718 Tension Tests Performed at 427°C (800°F).

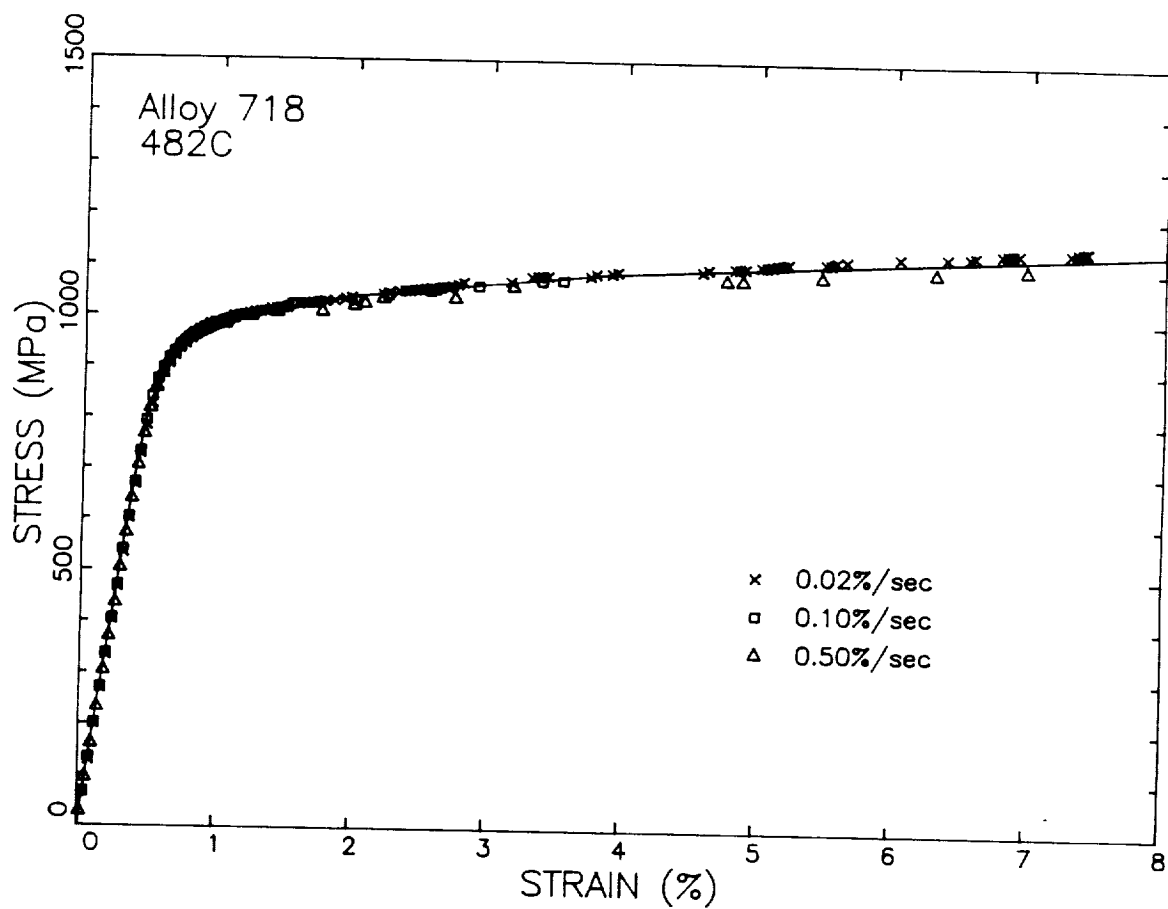


Figure 24: Experimental Data and Multi-linear Curve for the Alloy 718 Tension Tests Performed at 482°C (900°F).

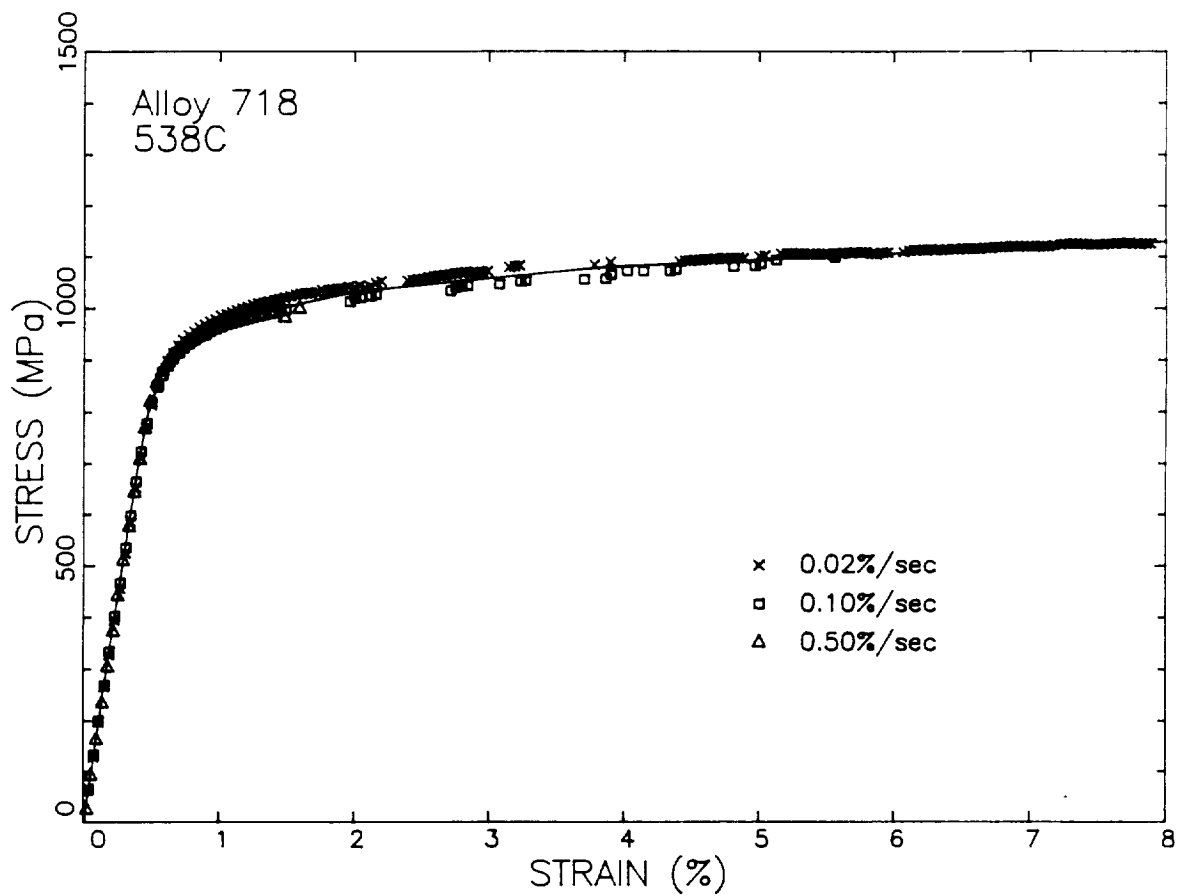


Figure 25: Experimental Data and Multi-linear Curve for the Alloy 718 Tension Tests Performed at 538°C (1000°F).

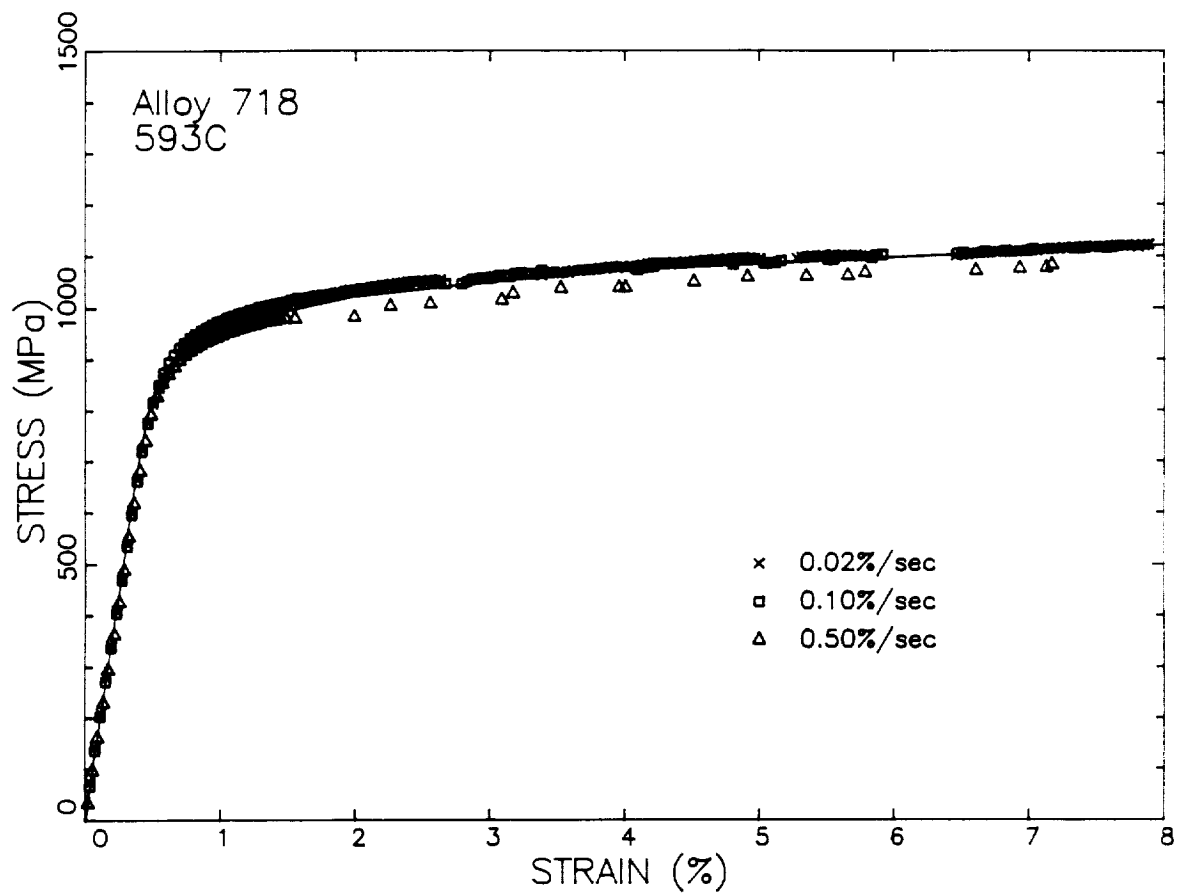


Figure 26: Experimental Data and Multi-linear Curve for the Alloy 718 Tension Tests Performed at 593°C (1100°F).

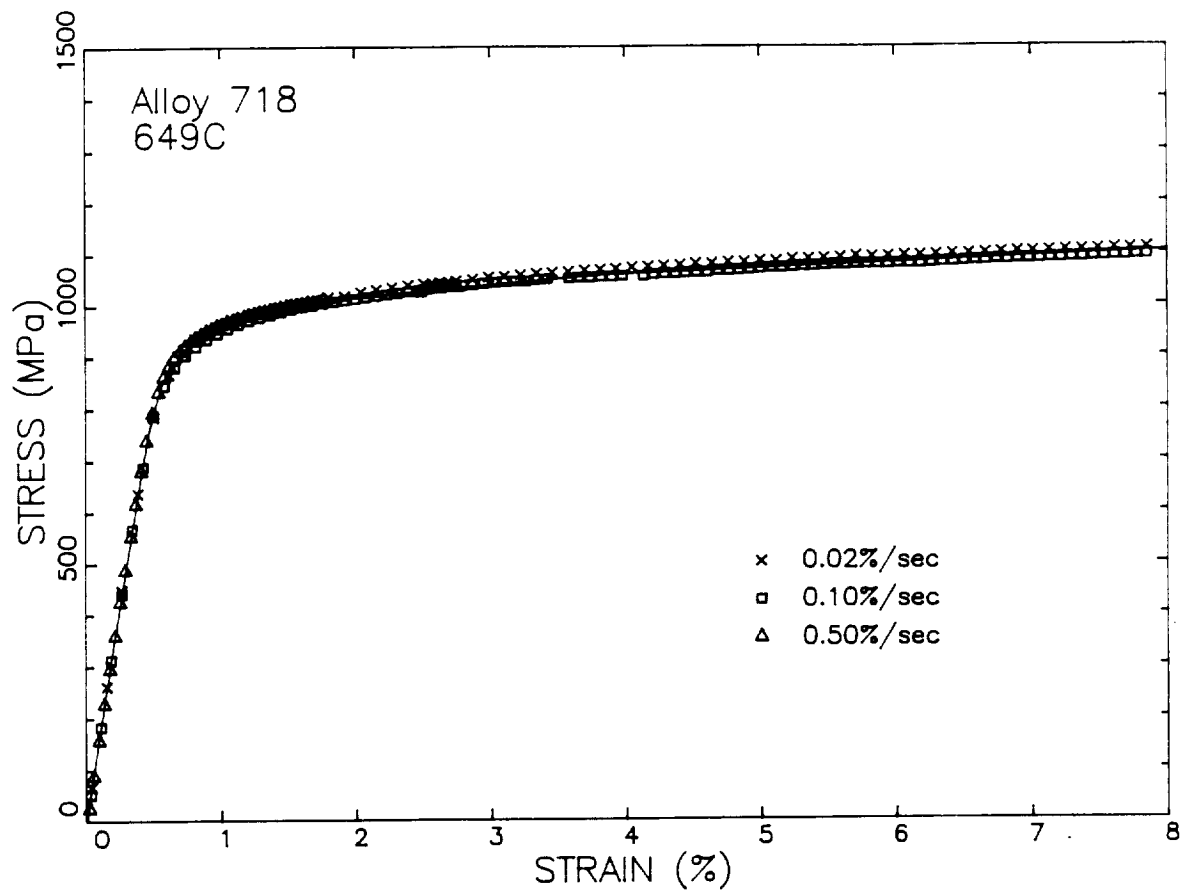


Figure 27: Experimental Data and Multi-linear Curve for the Alloy 718 Tension Tests Performed at 649°C (1200°F).

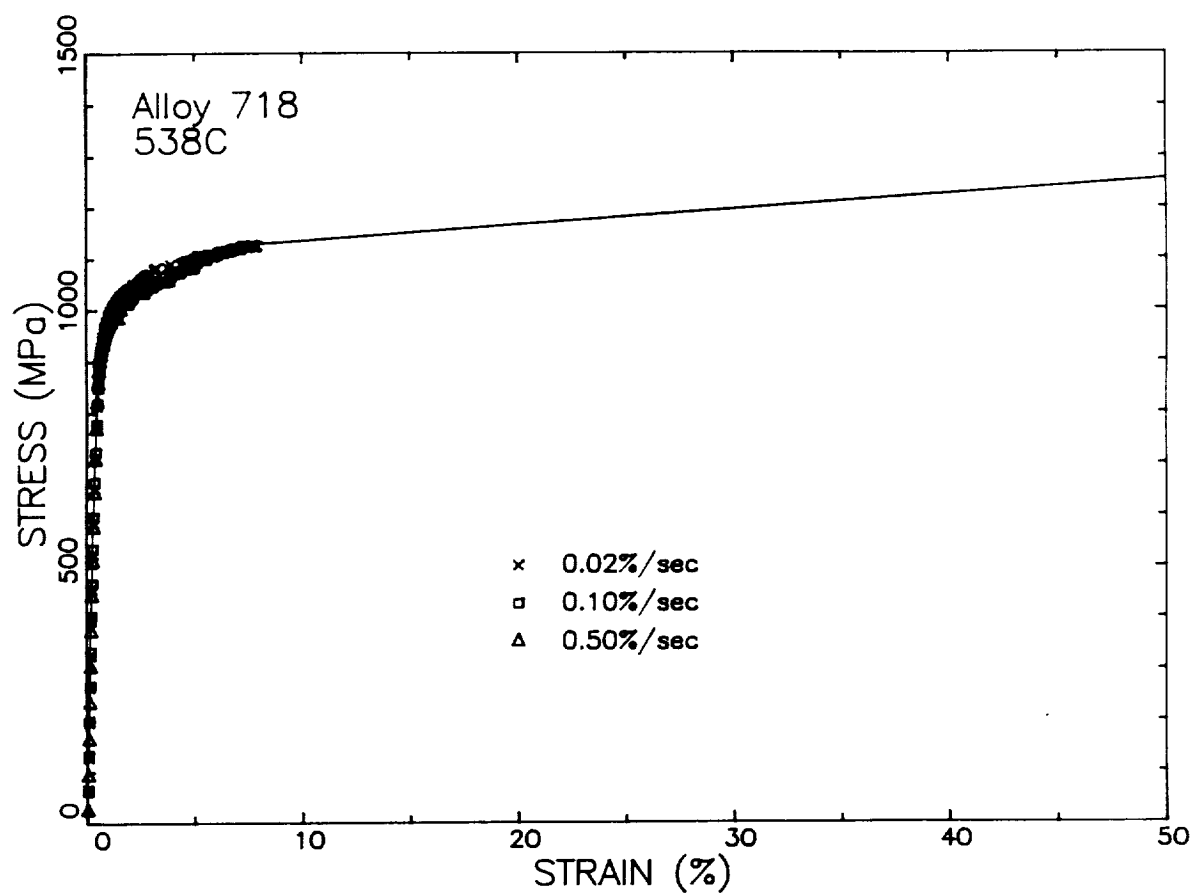


Figure 28: Multi-linear Tension Stress-Strain Curve for Alloy 718 at 538°C (1000°F) for Strains up to 0.50.

Table 6: Alloy 718 Tension Stress-Strain Curve Constants

$$\epsilon = \sigma/E + (\sigma/A)(1/n)$$

Test Temperature (°C)	E (GPa)	A (MPa)	n
21	196.4	1479	0.04828
427	178.5	1276	0.04639
482	177.1	1310	0.05403
538	173.6	1307	0.05537
593	177.1	1299	0.05601
649	162.6	1260	0.05030

Table 7: Alloy 718 Tensile Stress Strain Curve Values

Strain	Flow Stress (MPa)					
	21°C	427°C	482°C	538°C	593°C	649°C
0.0027	530	452	478	469	478	439
0.0041	805	731	723	709	721	666
0.0047	914	824	809	794	801	758
0.0057	1023	906	885	872	870	854
0.0076	1096	961	943	932	926	920
0.0115	1152	1005	993	983	975	970
0.0200	1203	1047	1040	1032	1023	1015
0.0385	1253	1088	1088	1080	1072	1059
0.0800	1304	1130	1137	1131	1122	1104
0.5000	1429	1234	1261	1256	1248	1216

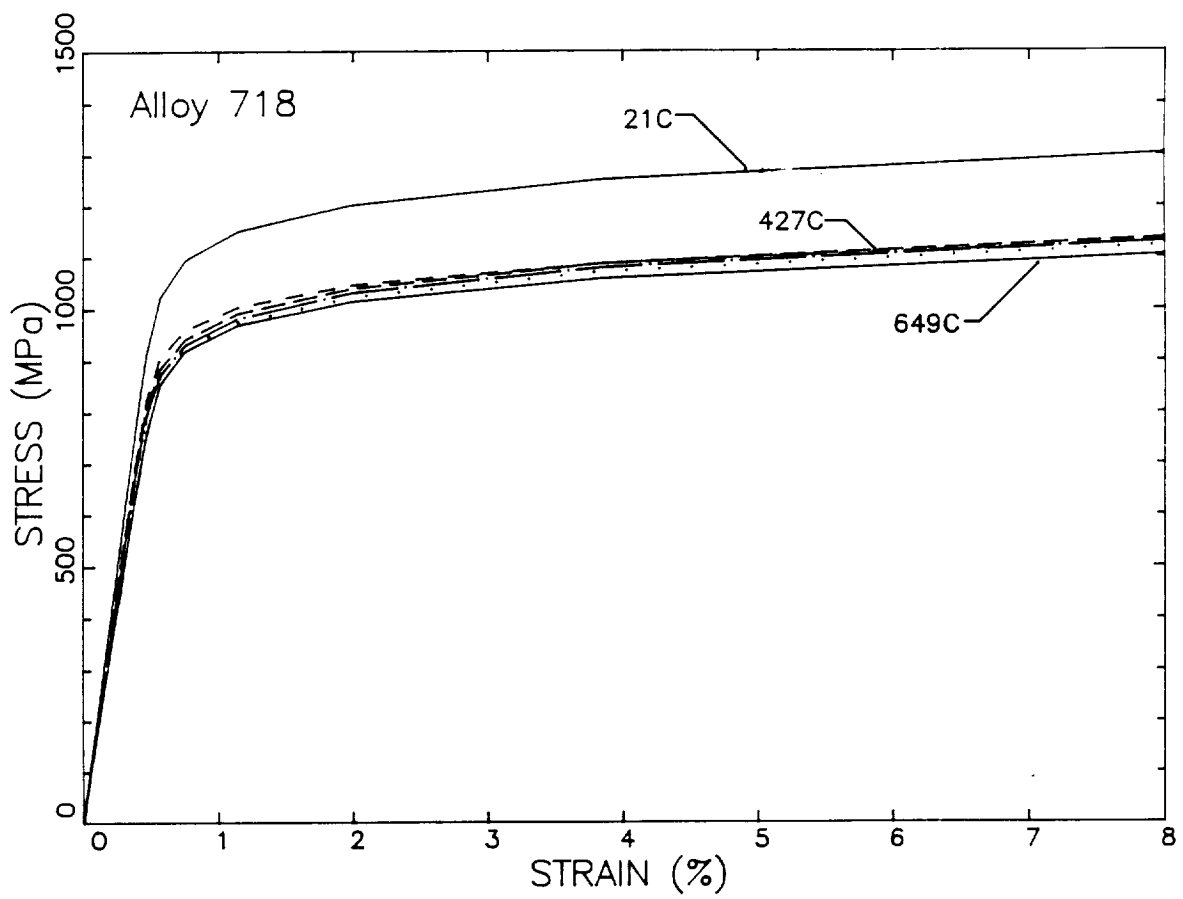


Figure 29: Variation of the Alloy 718 Tension Stress-Strain Curves with Test Temperature.

and 649°C.

3.3.2 Cyclic Properties

The cyclic stress-strain curves were determined in tests performed in strain control with a A_ϵ ratio (alternating strain / mean strain) of infinity or with a mean strain of zero and a constant strain rate (triangular wave shape). The strain rates and temperatures used during these tests were described in Table 4. The three strain ranges for the cyclic tests were determined based on a single 538°C (1000°F) test conducted using a constant strain amplitude block sequence. The test was performed using the A_ϵ ratio and wave shape described above with a strain rate of 0.02%/sec. Each block contained 15 cycles. The strain range in the first block was 0.5%. The strain range in each subsequent block was increased by 0.5%. The test was continued until buckling occurred when the strain range was 4%. Figure 30 shows the variations in plastic strain range with total strain range for this test. Based on these data, the total strain ranges selected for the cyclic constitutive tests were 1.15%, 1.7%, and 3.5%. This corresponds to plastic strain ranges of approximately 0.2, 0.7, and 2.4%. The highest strain range is intended to provide constitutive data which can be used to extrapolate the cyclic stress-strain behavior to the high strain levels anticipated in the finite elements near the crack tip.

Table 8 lists the testing condition and cycles to failure for each of the Alloy 718 cyclic tests performed in this portion of the test program. The highest strain range, fast strain rate tests performed at 427 and 538°C failed early in the tests due to the inability of the test machine to follow the strain during serrated yielding behavior. As expected from the tensile data shown in Table 5, this was only a problem at the lower temperatures and the high strain rates.

As expected, the cycles to failure decreased with increasing test temperature, increasing strain range, and decreasing strain rate. The last behavior corresponds to a lower test frequency (cycles per unit time). Lower

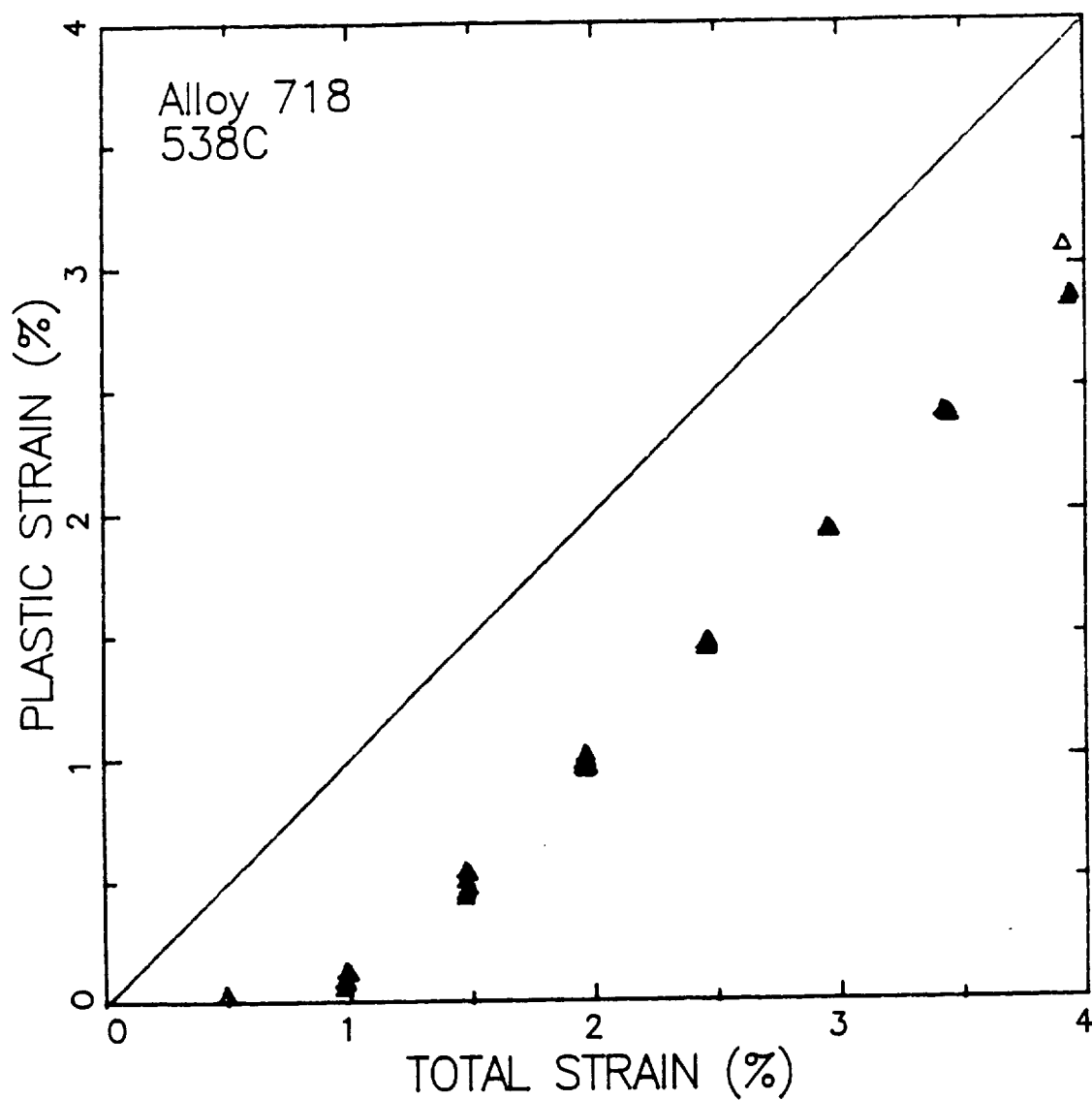


Figure 30: Variation of the Plastic Strain Range with the Total Strain Range during a Block Strain Cyclic Test of Alloy 718 at 538°C (1000°F) and a Strain Rate of 0.02% / sec.

Table 8: Summary Of Alloy 718 Cyclic Tests

Specimen Number	Test Temperature (°C)	Strain Range	Strain Rate (%/sec)	Cycles to Failure	N ₂₀	N ₅₀	N ₈₀
N3-5	427	0.0115	0.02	2228*	425	1125	1725
N3-1	427	0.0115	0.50	4592	910	2310	3710
N1-33	427	0.0170	0.02	1346	260	685	1075
N1-39	427	0.0170	0.50	1666	350	850	1350
N1-42	427	0.0350	0.02	149	32	64	110
N3-10	427	0.0350	0.50	serrated yielding failure			
N3-11	538	0.0115	0.02	2749	525	1325	2125
N1-43	538	0.0115	0.50	3886	760	1960	3110
N3-2	538	0.0170	0.02	801	150	400	650
N1-34	538	0.0170	0.50	1388	275	700	1100
N1-46	538	0.0350	0.02	79	10	40	60
N3-6	538	0.0350	0.50	serrated yielding failure			
N3-7	593	0.0115	0.02	2280	450	1140	1820
N1-40	593	0.0115	0.50	2977	600	1500	2375
N1-44	593	0.0170	0.02	413	75	200	325
N3-12	593	0.0170	0.50	920	175	450	725
N1-35	593	0.0350	0.02	30	6	16	20
N3-3	593	0.0350	0.50	107	20	50	80
N3-4	649	0.0115	0.02	1040	205	515	830
N1-38	649	0.0115	0.50	2327	475	1175	1850
N1-41	649	0.0170	0.02	248	50	125	200
N3-8	649	0.0170	0.50	646	130	325	515
N3-13	649	0.0350	0.02	40	8	20	33
N1-45	649	0.0350	0.50	43	9	20	35

* test terminated prior to failure

test frequency would be expected to diminish fatigue life, particularly at the higher temperatures, due to the degrading effects of creep-fatigue-environment interactions.

Figure 31 shows the maximum and minimum stresses measured during 538°C Alloy 718 cyclic tests as a function of the number of cycles. The results of tests at different strain rates are represented by different types of symbols. As reported previously in the literature⁽¹⁷⁾, Alloy 718 experiences significant cyclic softening early in the tests. This seems to saturate until very late in the test when the stresses again rapidly diminish due to the presence of large cracks in the test specimen. The data in this figure also show, like in the tension tests, little evidence of significant strain rate sensitivity. There is no evidence that the lower cycles to failure observed with lower strain rates was caused by differences in the constitutive response. One possible explanation for this effect is the strong influence of frequency of the crack growth behavior of Alloy 718 at temperatures near 650°C^(15,19-26). One of the plates processed during this program was purchased for use on another program which documented this strong time-dependent crack growth response in this material⁽¹⁵⁾. The cyclic softening and very small strain rate sensitivity behavior shown in Figure 31 was observed for all the temperatures and strain ranges evaluated in this program. This is illustrated in Figures 32 through 35 for the tests performed at 427, 538, 593, and 649°C.

At each data point shown in the previous four figures, a hysteresis loop was recorded using the data acquisition system. In order to sample a significant amount of data, but not be overwhelmed, three hysteresis loops were used from each test. Based on the cyclic softening behavior, the cycles used corresponded to approximately 20, 50, and 80 percent of the fatigue life. Figure 36 shows the data from the six hysteresis loops (two strain rates by 3 loops/test) for the Alloy 718 tests at 538°C with a strain range of 1.70%. These data are the same specimens from which the data in Figure 31 was obtained. There is very little evidence of strain rate sensitivity or influence cyclic softening or hardening between 20 and 80 percent of the

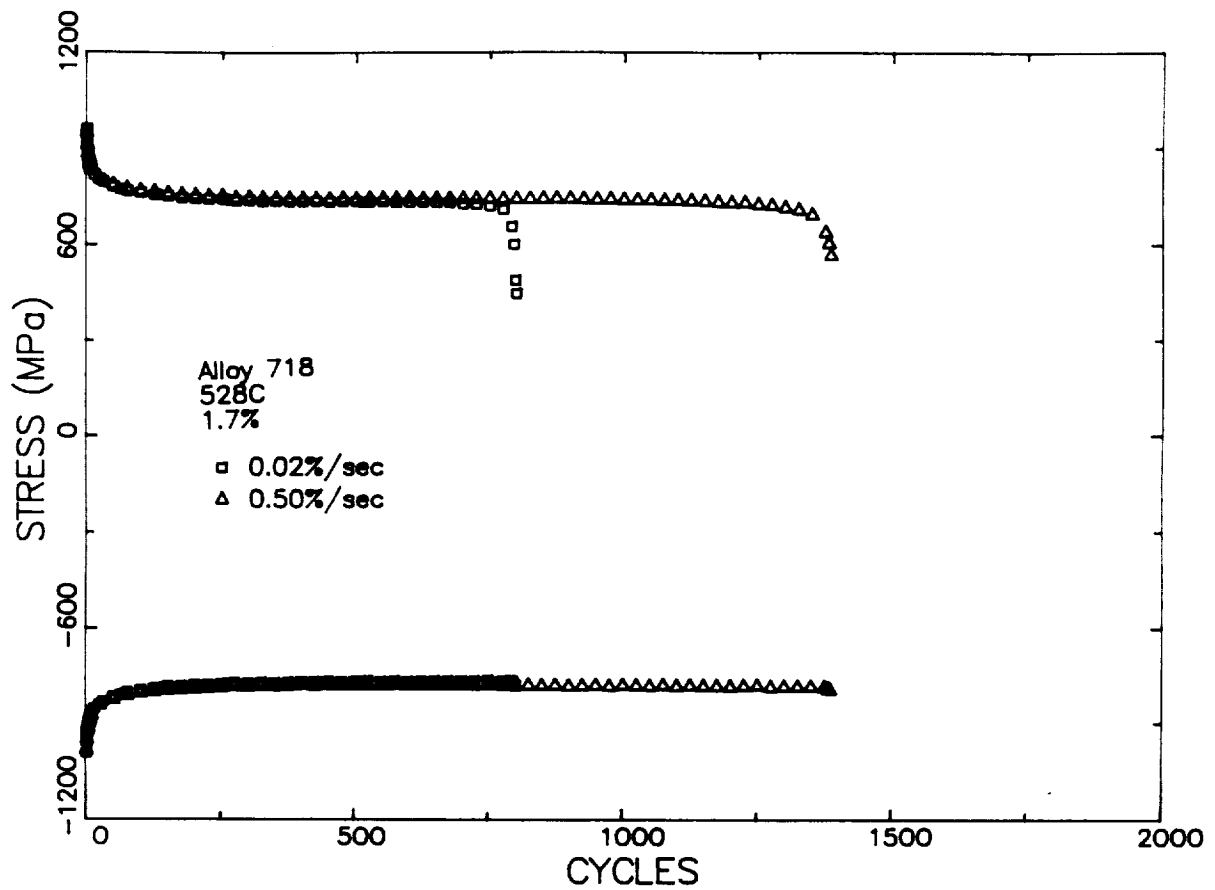


Figure 31: Variation of the Maximum and Minimum Stresses as a Function of Cycles for a Cyclic Tests of Alloy 718 at 538°C (1000°F) and Strain Ranges of 0.017 but with Different Strain Rates.

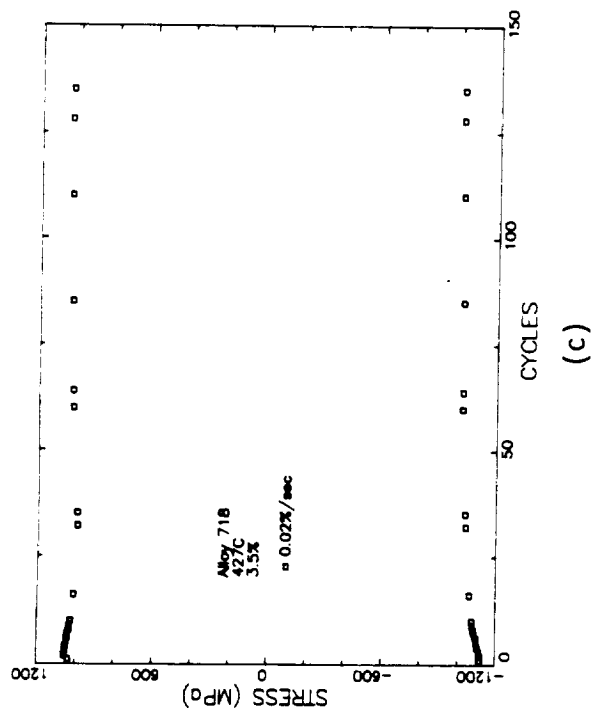
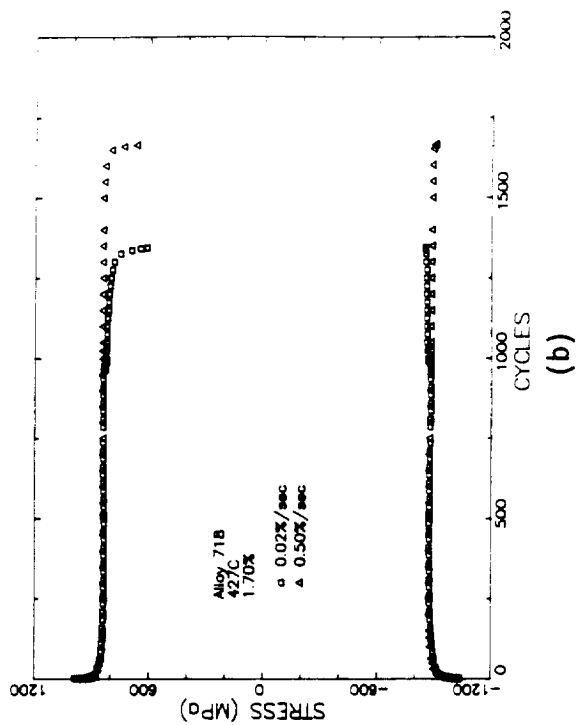
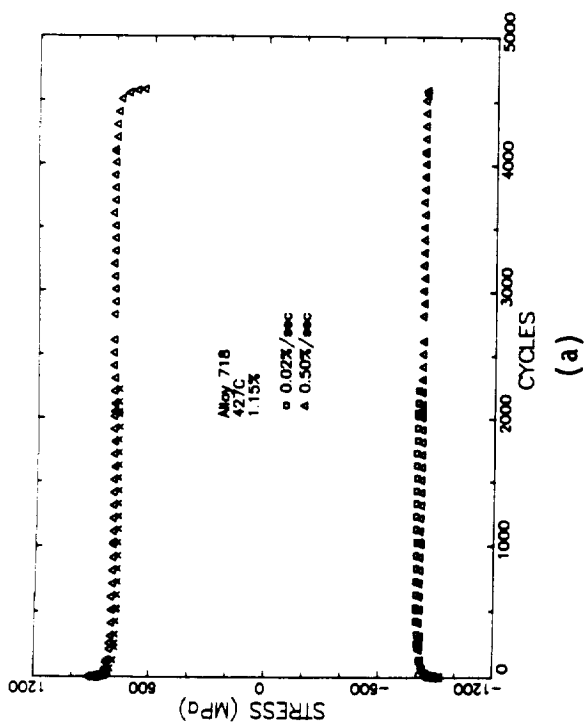


Figure 32:

Variation of the Maximum and Minimum Stresses as a Function of Cycles for a Cyclic Tests of Alloy 718 at 427°C (800°F) with Strain Ranges of (a) 0.0115, (b) 0.0170, and (c) 0.035.

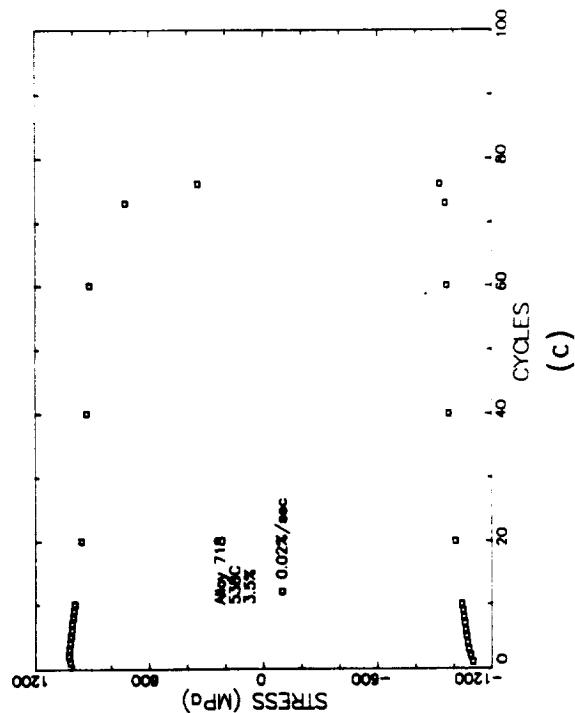
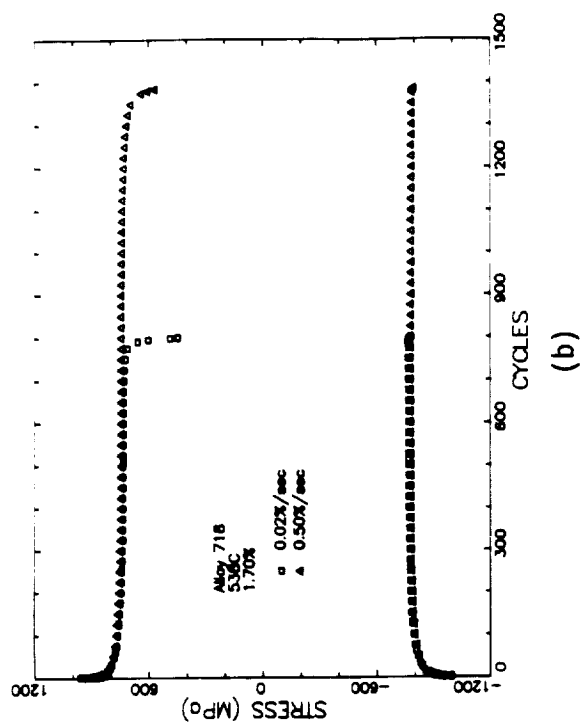
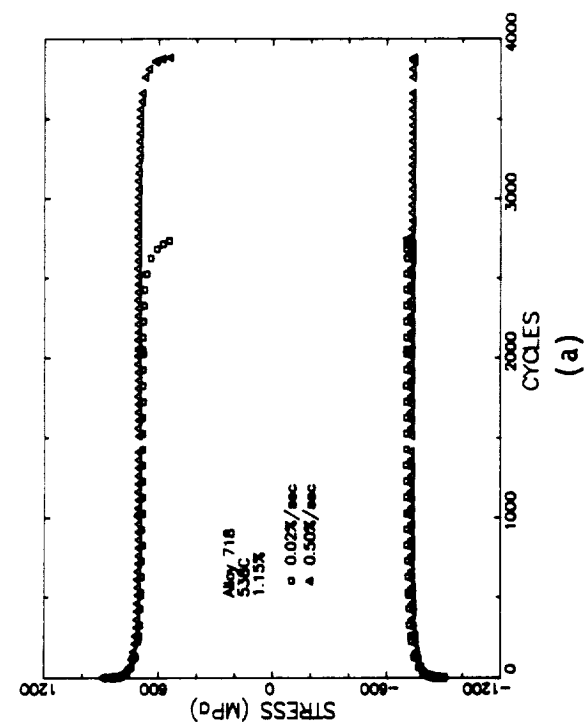


Figure 33:

Variation of the Maximum and Minimum Stresses as a Function of Cycles for a Cyclic Tests of Alloy 718 at 538°C (1000°F) with Strain Ranges of (a) 0.0115, (b) 0.0170, and (c) 0.035.

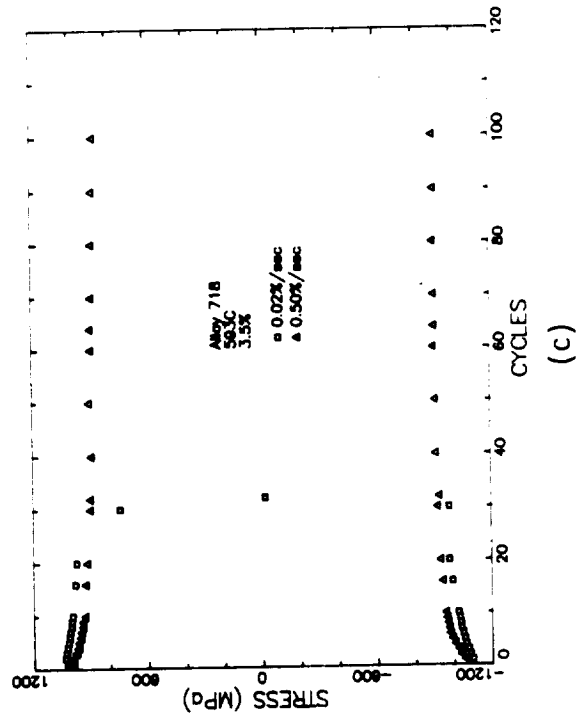
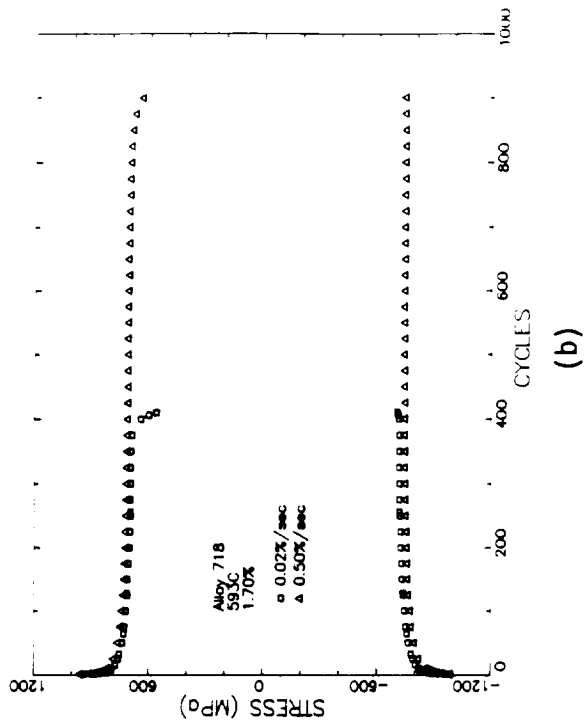
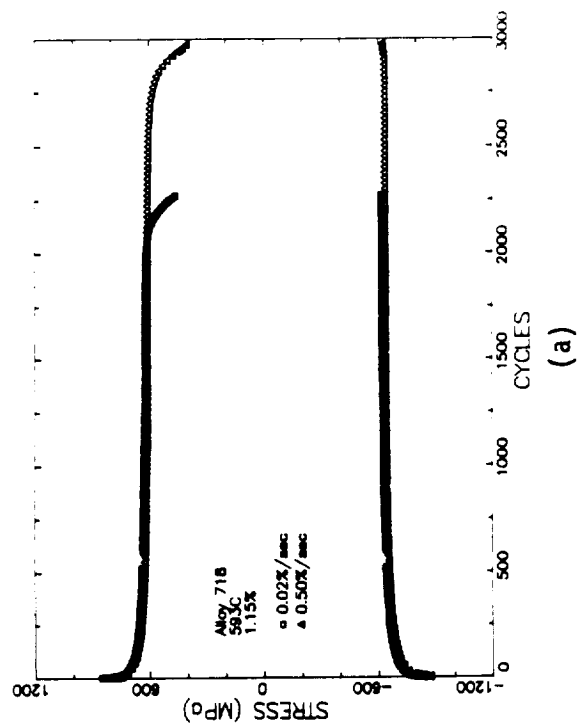


Figure 34:

Variation of the Maximum and Minimum Stresses as a Function of Cycles for a Cyclic Tests of Alloy 718 at 593°C (1100°F) with Strain Ranges of (a) 0.0115, (b) 0.0170, and (c) 0.035.

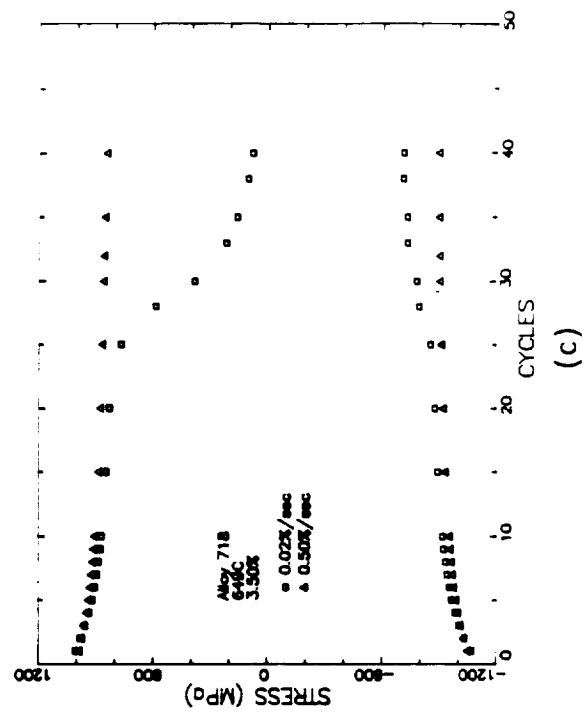
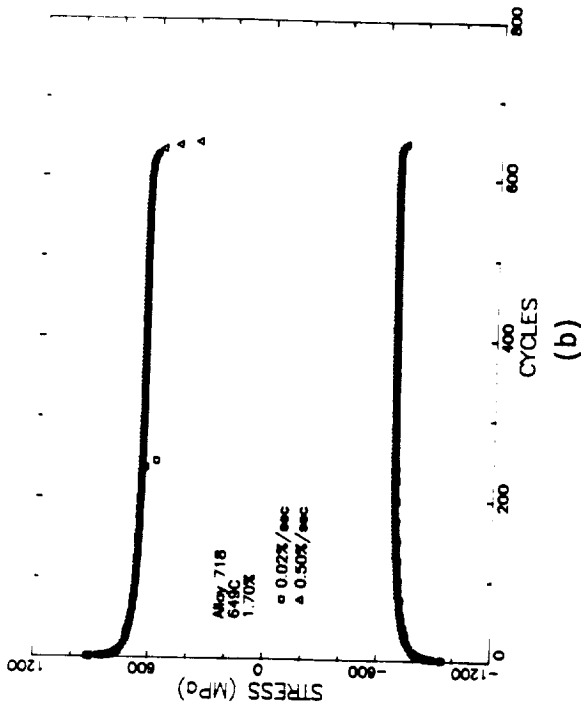
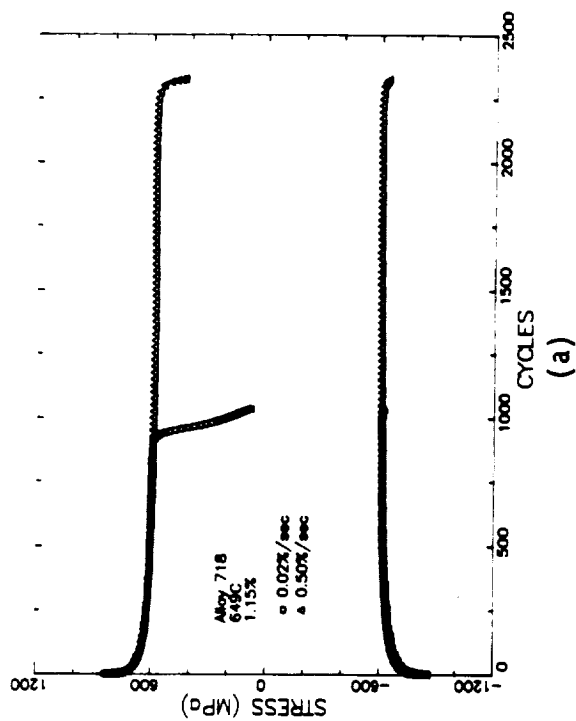


Figure 35:

Variation of the Maximum and Minimum Stresses as a Function of Cycles for a Cyclic Tests of Alloy 718 at 649°C (1200°F) with Strain Ranges of (a) 0.0115, (b) 0.0170, and (c) 0.035.

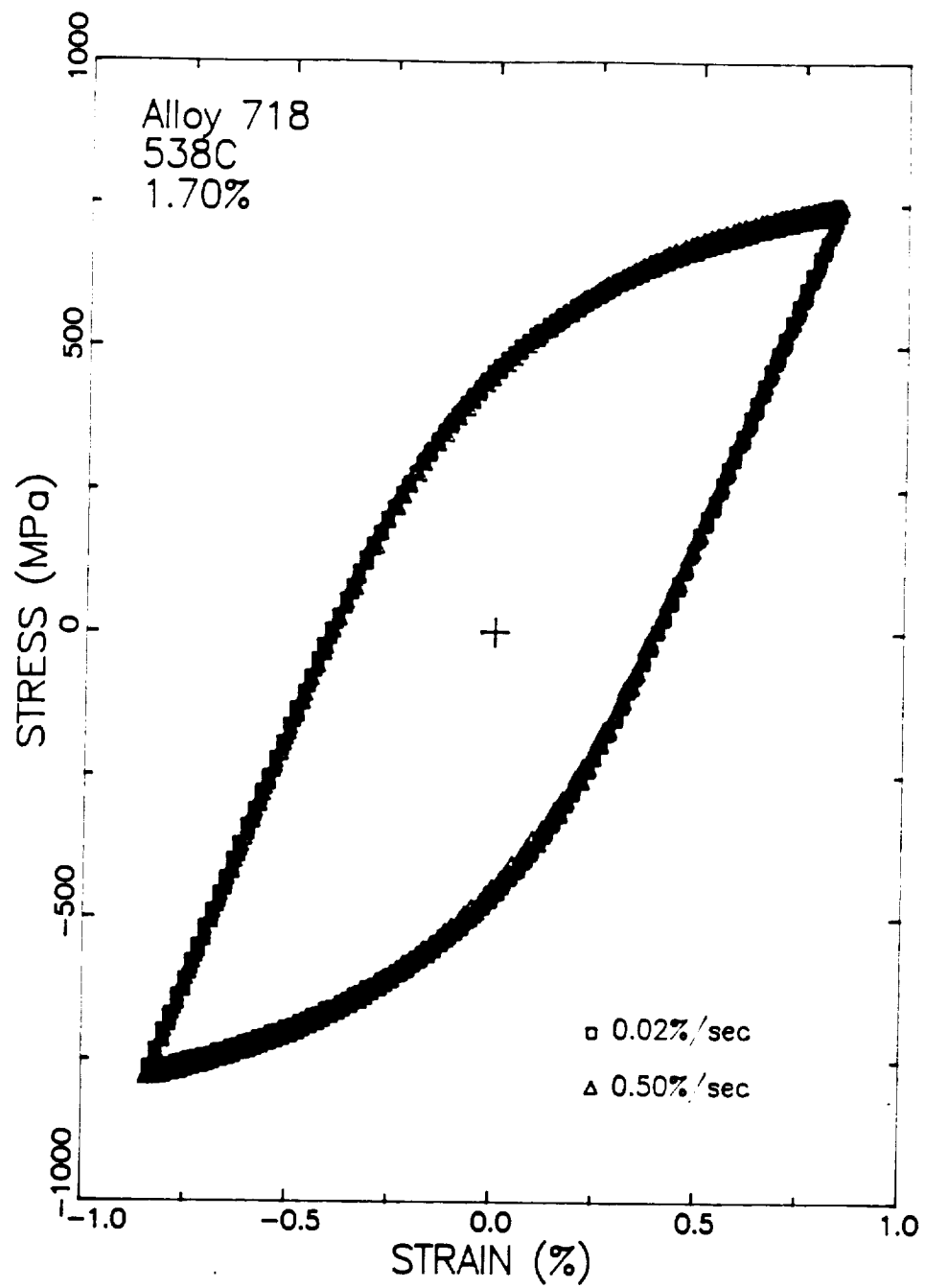


Figure 36: Hysteresis Loops from Cyclic Tests of Alloy 718 at 538°C (1000°F) at Approximately 20, 50, and 80 % of Life for Strain Range 0.0170 Illustrating the Absence of Strain Rate Sensitivity.

fatigue life. This procedure for selecting cyclic hysteresis loops was used on all the cyclic tests. The exact cycle number used are reported in Table 8 and are noted by N₂₀, N₅₀, and N₈₀.

The cyclic fatigue curve used as input for the finite element analysis is the alternating values of stress and strain. The data in each hysteresis loop was divided into an increasing and a decreasing strain part. The alternating values of stress and strain were calculated by taking half of absolute value between a data point and the starting point for that leg (minimum values for increasing strain and maximum values for decreasing strain). For each temperature a total of 36 stress-strain loading patterns were available (3 strain rates x 2 strain ranges x 3 hysteresis loops/test x 2 legs/loop). Figure 37 shows the variations of alternating stress with alternating strain for the Alloy 718 cyclic tests performed at 538°C. The data from the lower two strain ranges are similar, but the data from the 3.5% strain range tests has a higher stress for a given value of strain. This type of constitutive response cannot be modeled exactly using a classical plasticity model. The absence of strain rate sensitivity indicates that it would be difficult to model cyclic softening using a unified constitutive model. It seems likely that the influence of strain range on the cyclic stress-strain curves results from variation in the relative amount of cyclic softening with strain range. Development of a softening model for the CYANIDE finite element code⁽¹¹⁾ is beyond the scope of this investigation, so a classical plasticity model was used to model the constitutive response of Alloy 718 in this investigation. The data from the tests at the lower two strain ranges were used to collapse the data to a Ramsberg-Osgood relationship (Equation 3.1) with the additional restriction that the curve had to pass through a point selected to represent the highest strain values measured in the 3.5% strain range tests. The value of E used in these analyses were identical to the ones determined from the tension tests and listed in Table 6. The values of E, A, and n for the cyclic stress-strain curves are listed in Table 9. These values were converted to a ten segment stress strain curve using the same strain endpoints used in the tensile stress-strain curves. At low strains, the alternating stress is lower than

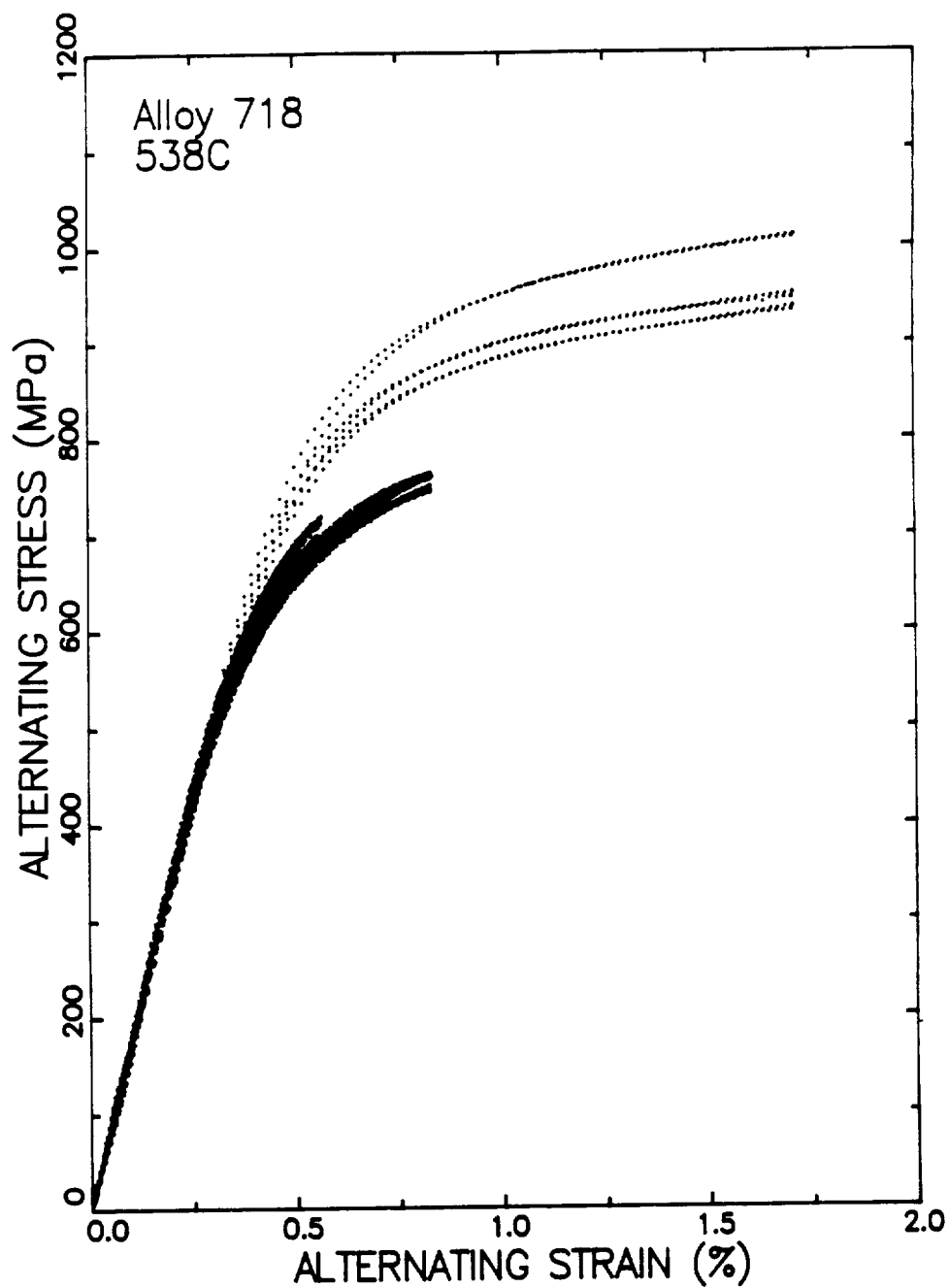


Figure 37: Variation of Alternating Stress with Alternating Strain Measured in Cyclic Tests on Alloy 718 at 538°C (1000°F).

TABLE 9: Alloy 718 Cyclic Stress-Strain Curve Constants

$$\epsilon = \sigma/E + (\sigma/A)^{1/n}$$

Test Temperature (°C)	E (GPa)	A (MPa)	n
427	178.5	1717	0.11598
538	173.6	1877	0.15303
593	177.1	2271	0.19906
649	162.6	1827	0.16723

the tensile flow stress. The cyclic stress strain curve exhibits higher work hardening, so that at high strains, the alternating stress exceeds that in the tension curve. The crossing of the curves occurs beyond the extent of the cyclic data typically at an alternating strain of 2%. It would be expected from the observed cyclic softening behavior that the cyclic stress strain curve could never exceed the monotonic curve. To remedy this situation, the endpoints used for the cyclic stress-strain curve were always the lower of either the tensile or cyclic flow stress. In other words, the cyclic endpoints were used at low strain values and the tension curves were used at high strain values.

Figures 38 through 41 show the cyclic stress strain data from the tests performed at 427, 538, 593, and 649°C, respectively. Also shown in these figures are the multi-linear cyclic stress-strain curves used to model Alloy 718 during finite element analyses of cyclic deformation. The values of the endpoints are given in Table 10.

Figure 42 shows the multi-linear cyclic stress strain curves for these four temperatures. The influence of temperature on the cyclic stress strain curves are much greater than the corresponding tension tests data previously shown in Figure 29. The relative difference between the cyclic and tension flow curves increases with increasing temperature as illustrated in Figure 43 for 427 and 649°C.

3.3.3 Creep Tests

The creep tests were performed according to the test matrix shown in Table 4. These tests have been performed but the data has not yet been analyzed into a constitutive relationship. As a result, the data will be shown in the form of strain versus time plots. A single plot will be shown for each test temperature. The data for tests performed at 538, 593, and 649°C are shown in Figures 44, 45, and 46, respectively.

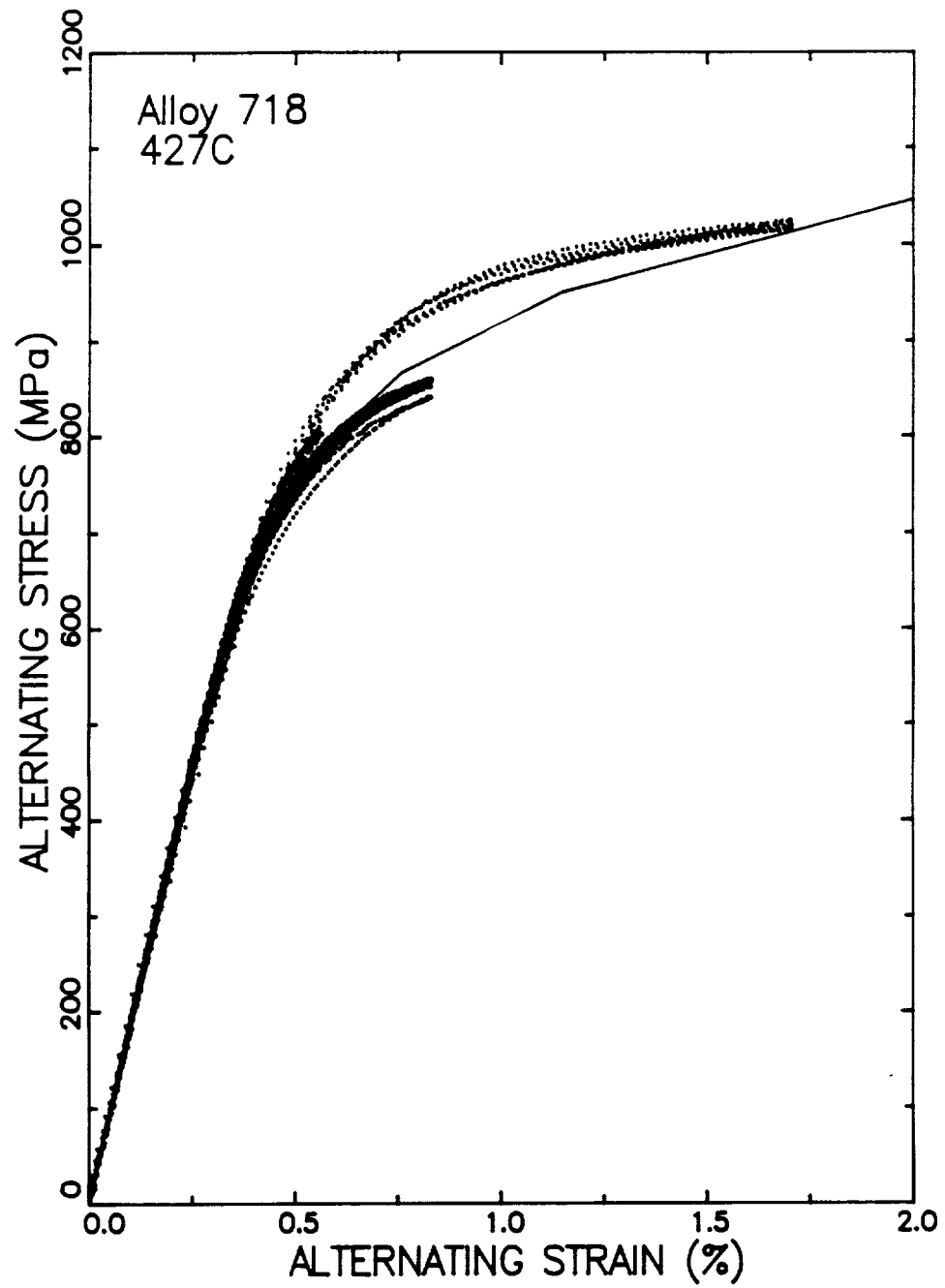


Figure 38: Experimental Alternating Stress - Alternating Strain Data and Multi-linear Curve from Cyclic Alloy 718 Tests at 427°C (800°F).

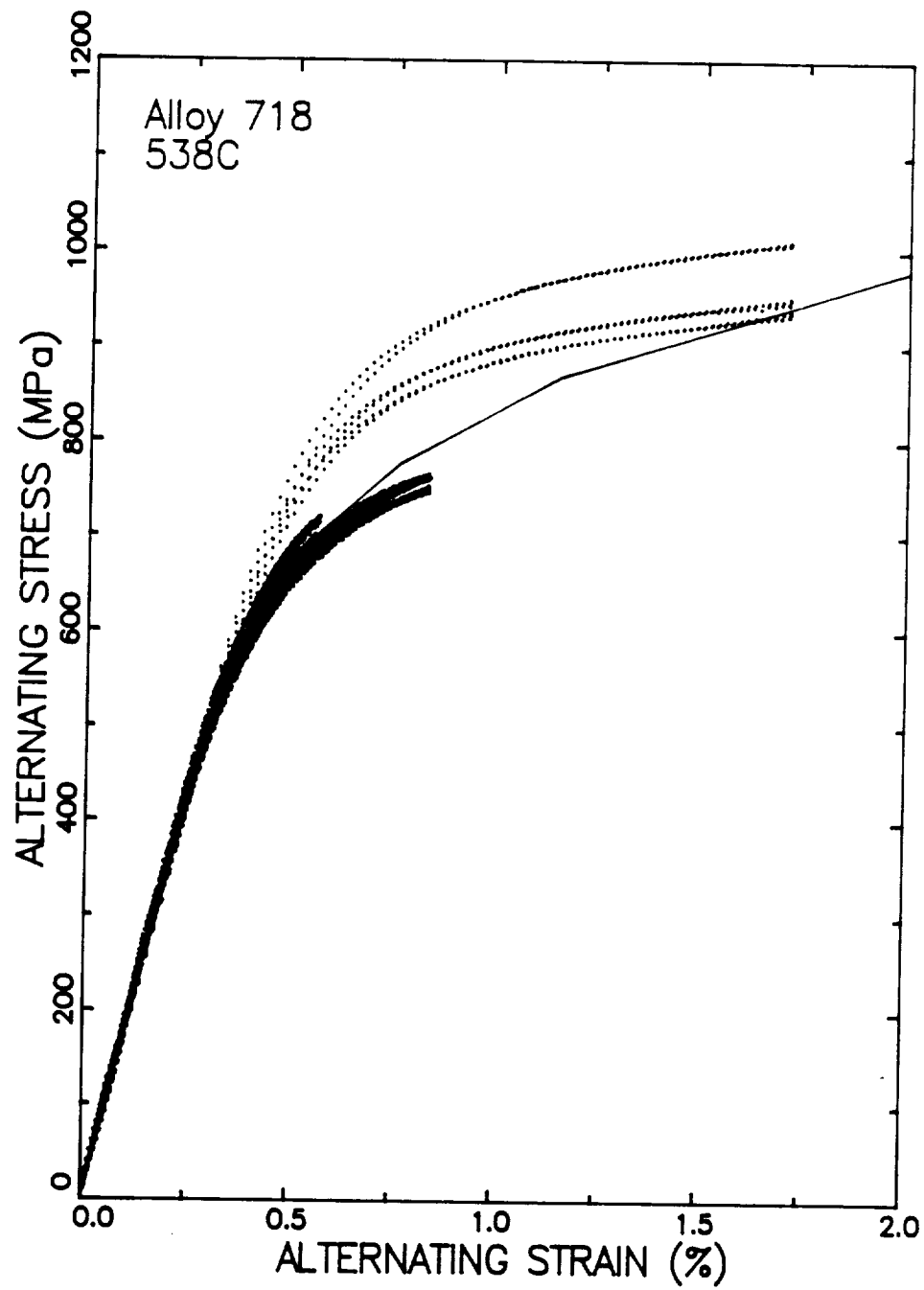


Figure 39: Experimental Alternating Stress - Alternating Strain Data and Multi-linear Curve from Cyclic Alloy 718 Tests at 538°C (1000°F).

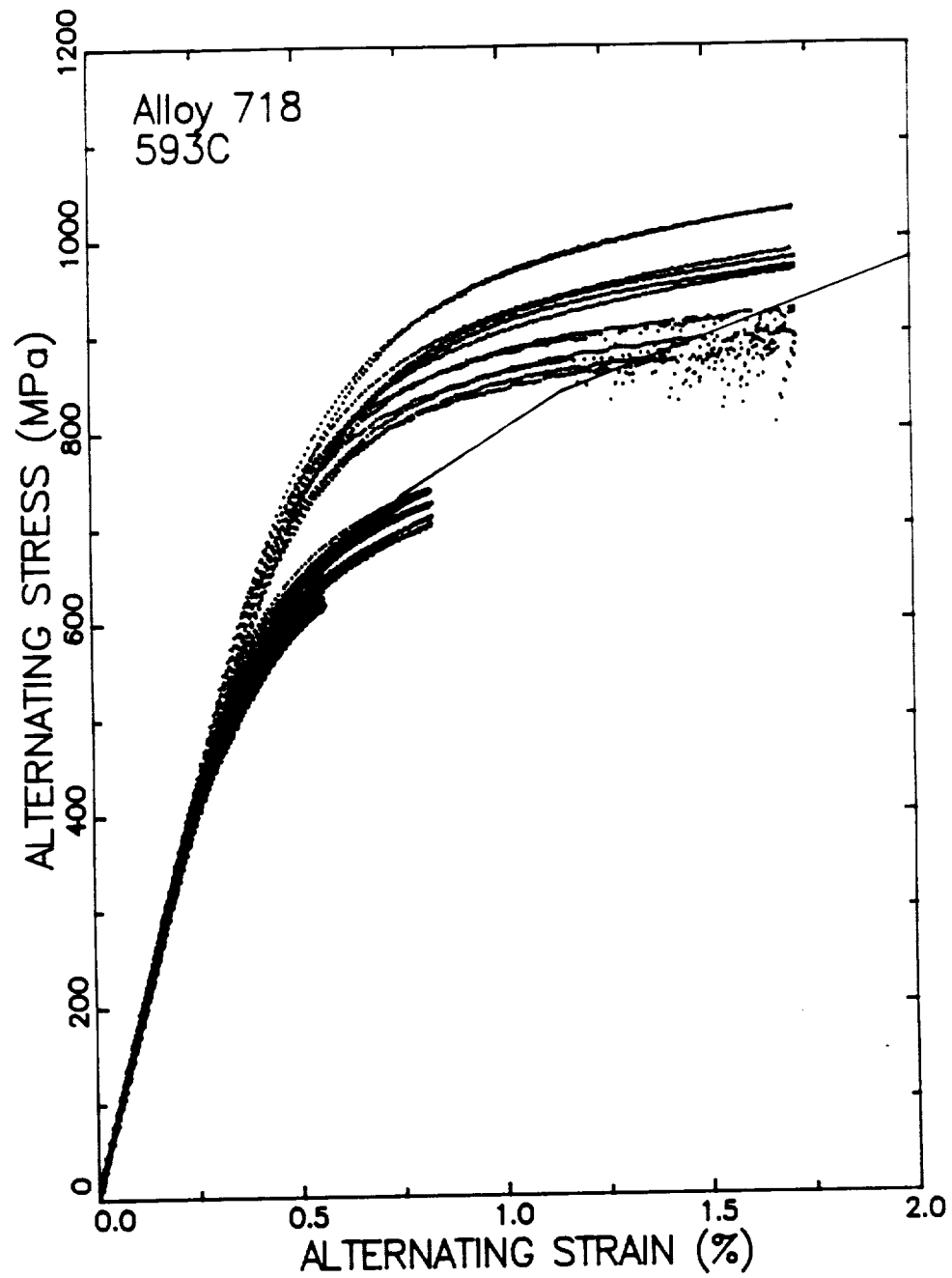


Figure 40: Experimental Alternating Stress - Alternating Strain Data and Multi-linear Curve from Cyclic Alloy 718 Tests at 593°C (1100°F).

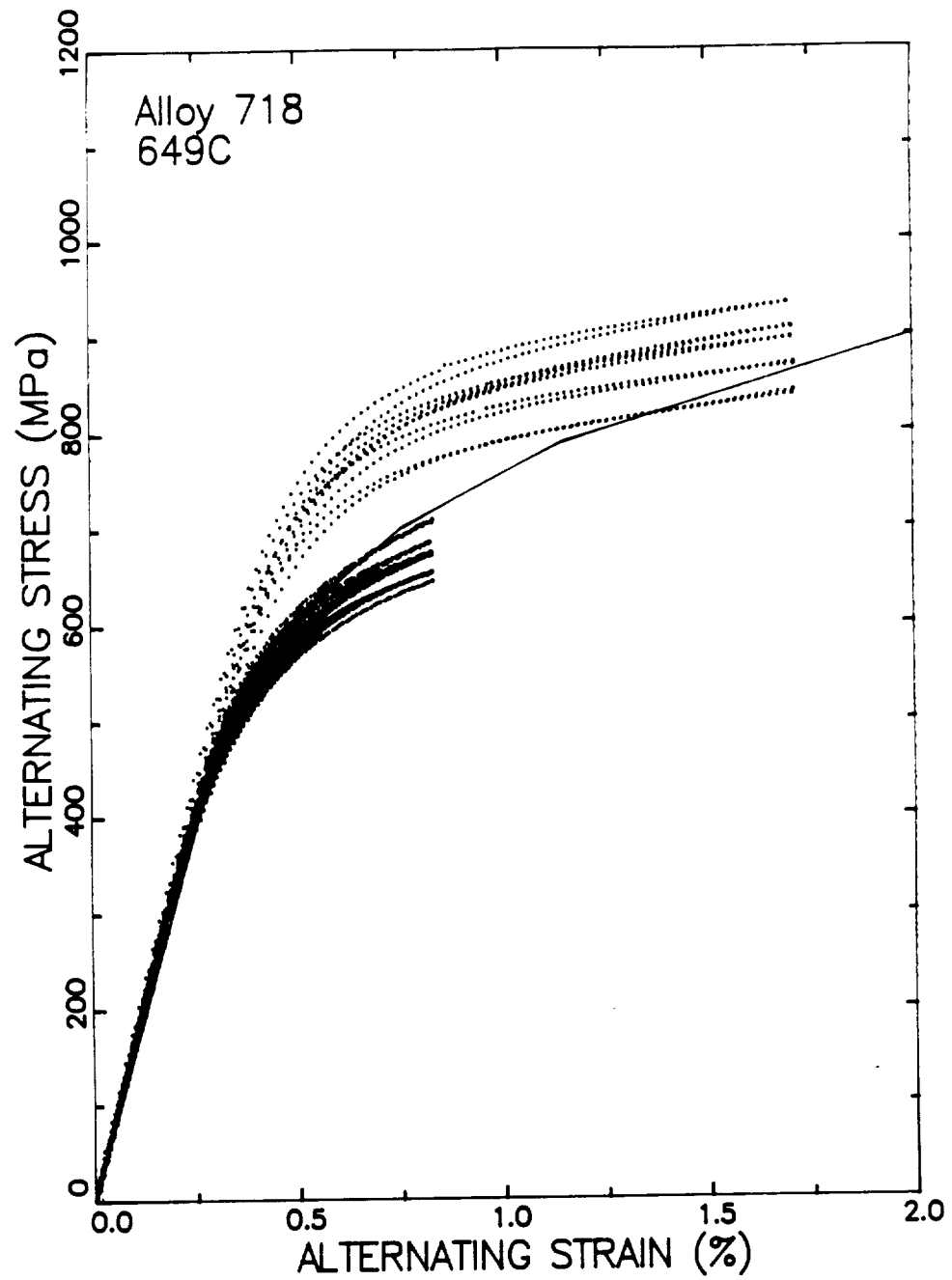


Figure 41: Experimental Alternating Stress - Alternating Strain Data and Multi-linear Curve from Cyclic Alloy 718 Tests at 649°C (1200°F).

TABLE 10: Alloy 718 Tensile Stress Strain Curve Values

Strain	Flow Stress (MPa)			
	427°C	538°C	593°C	649°C
0.0027	479	453	435	416
0.0041	675	605	564	547
0.0047	729	649	604	585
0.0057	792	704	658	635
0.0076	866	777	735	702
0.0115	952	868	840	790
0.0200	1047	980	978	900
0.0385	1088	1080	1072	1029
0.0800	1130	1131	1122	1104
0.5000	1234	1256	1248	1216

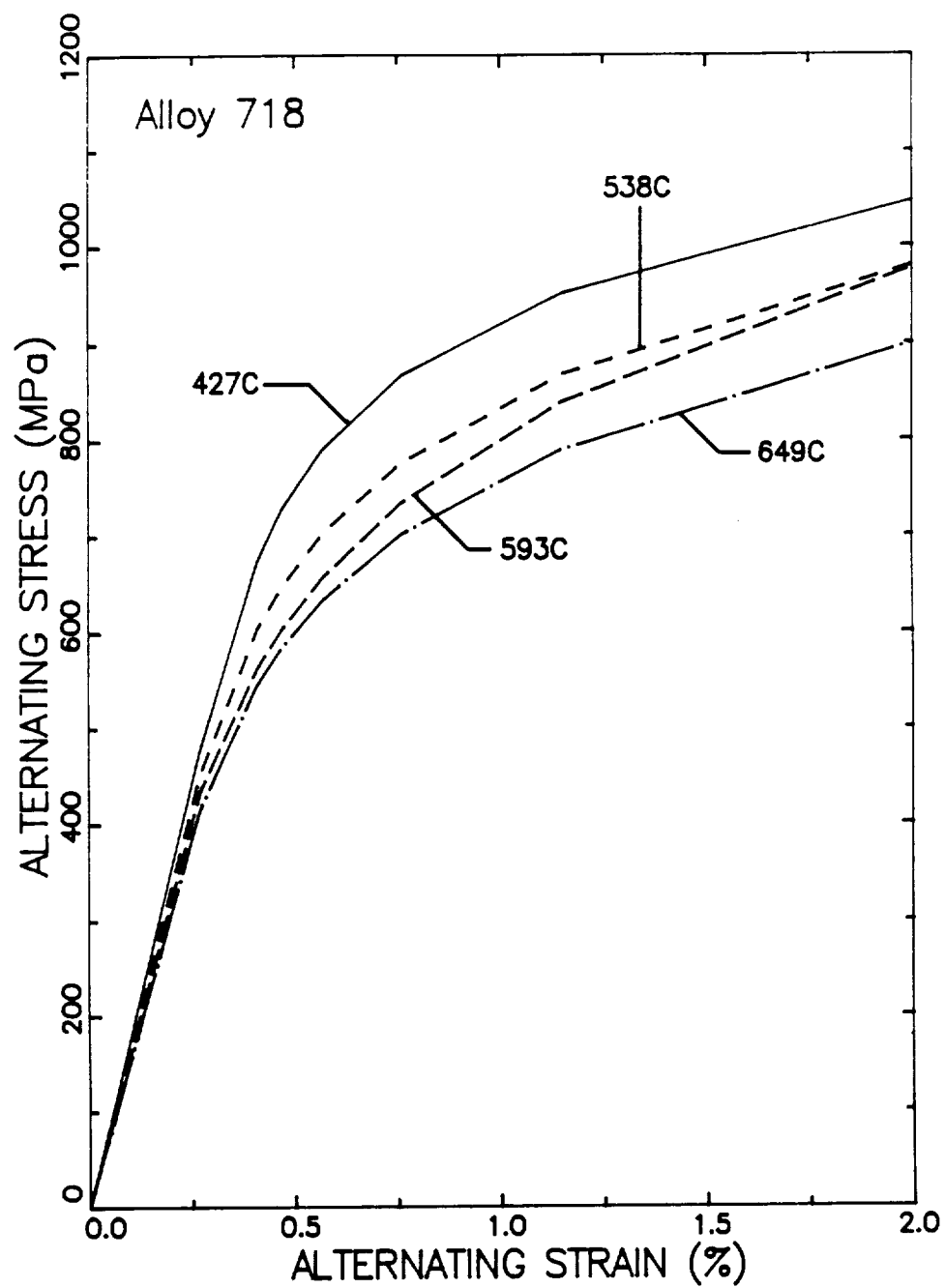
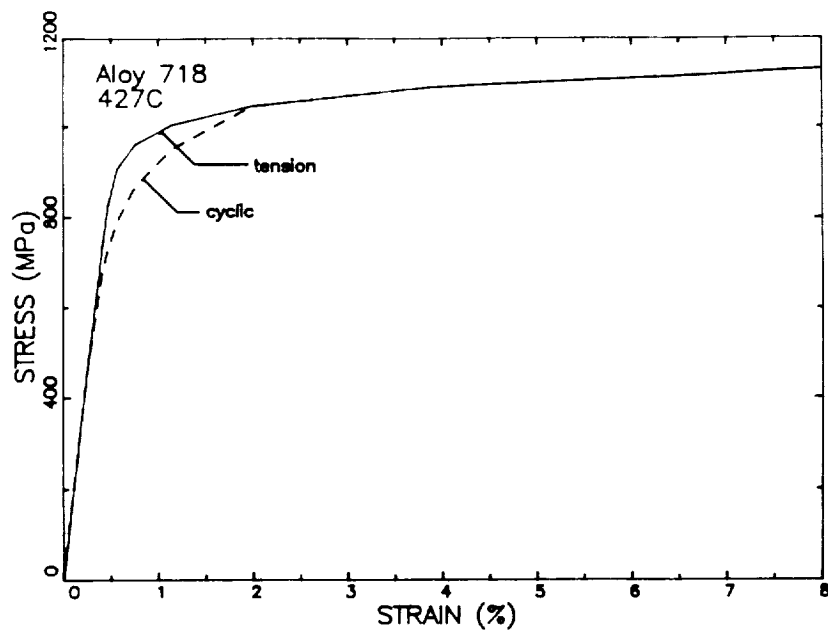
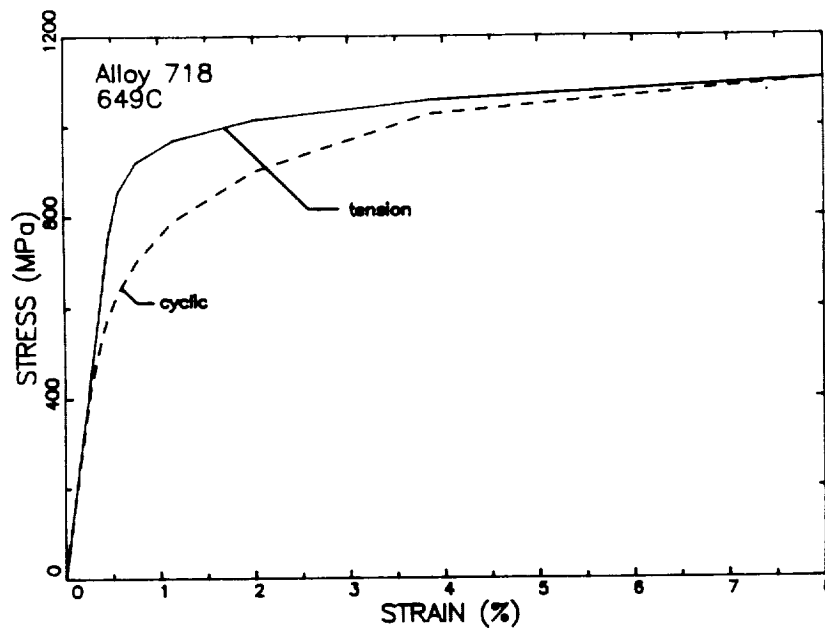


Figure 42: Variation of the Alloy 718 Cyclic Alternating Stress - Alternating Strain Curves with Test Temperature.



(a)



(b)

Figure 43: Comparison of the Alloy 718 Tension and Cyclic Stress Strain Curves at (a) 427°C (800°F) and (b) 649°C (1200°F).

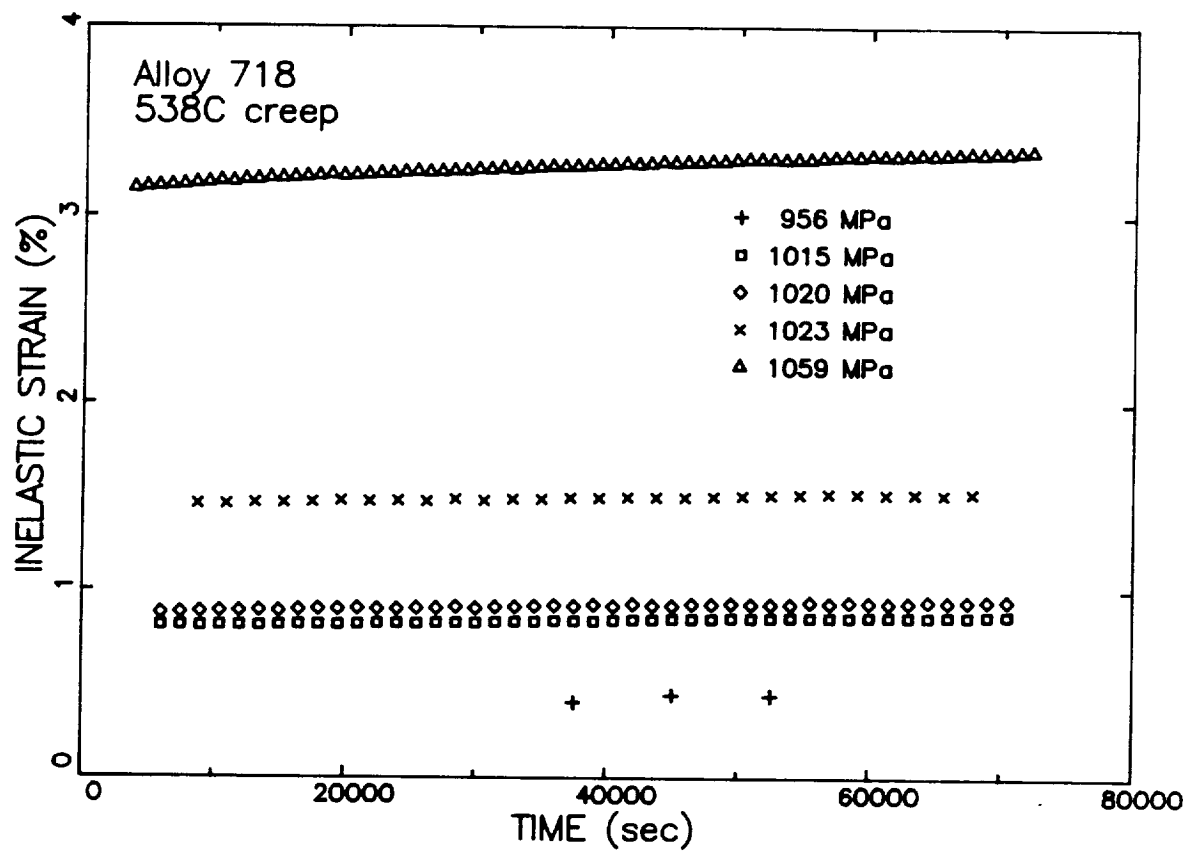


Figure 44: Variation of inelastic Strain with time for Alloy 718 Creep Tests Performed at 538°C (1000°F).

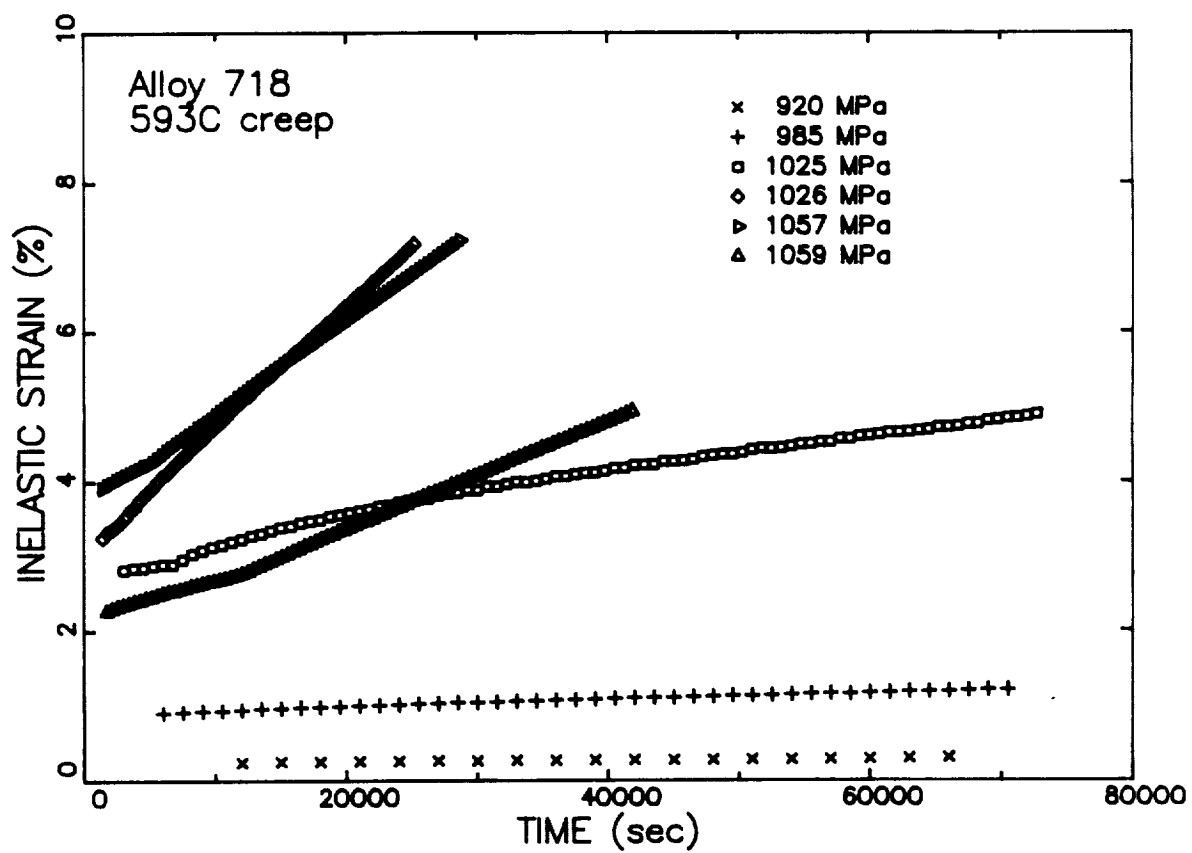


Figure 45: Variation of inelastic Strain with time for Alloy 718 Creep Tests Performed at 593°C (1100°F).

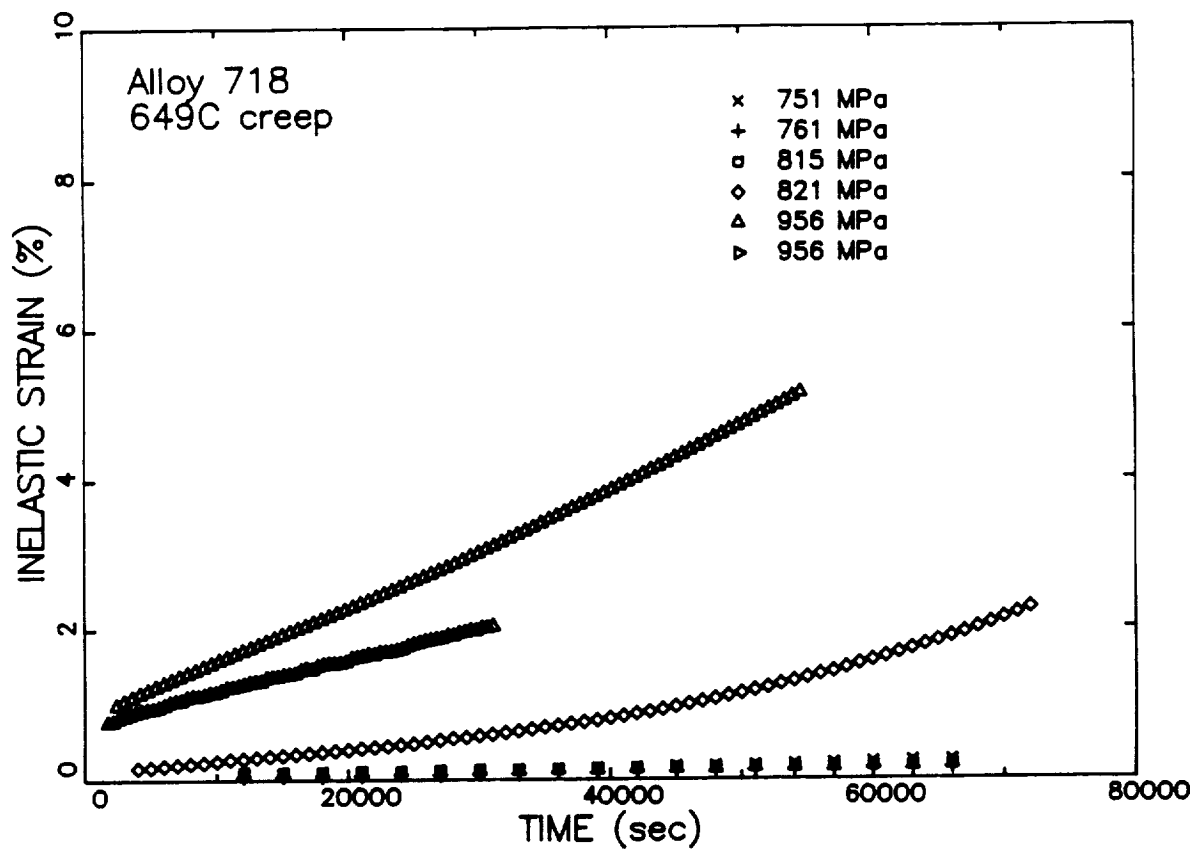


Figure 46: Variation of inelastic Strain with time for Alloy 718 Creep Tests Performed at 649°C (1200°F).

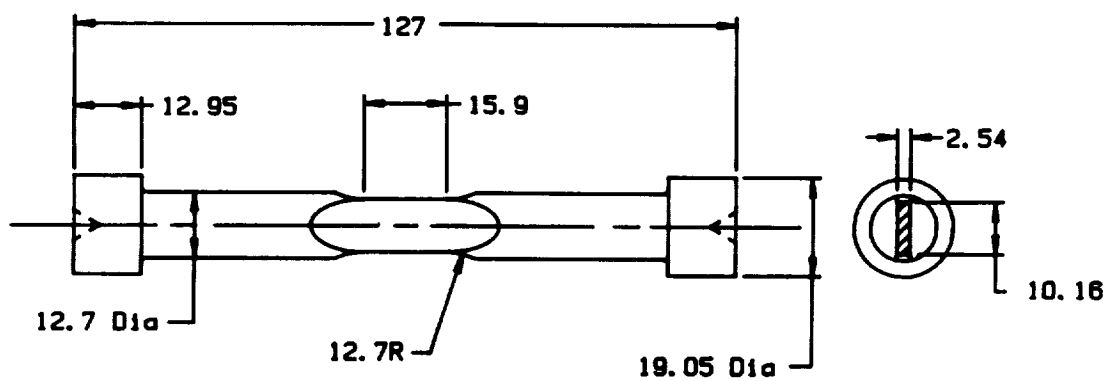
4.0 SPECIMEN EVALUATION

This section of the report will describe a combination of analytical and experimental work on developing the specimens to be used to evaluate P-I integrals in this investigation. Most of the effort in this program was to analytically and experimentally evaluate the crack growth behavior of Alloy 718 in a buttonhead single edge notch (SEN) specimen. Some experiments were also performed using a modified compact specimen so that it could be loaded into compressive stress/strain states. These particular geometries were selected to compare stress states with significantly different combinations of axial and bending stresses. Most of this discussion will be concerned with the development and characteristics of the buttonhead SEN specimen. The issues to be addressed in the following sections are:

1. Validity of specimen dimensions for evaluating P-I integrals
2. Development of specimen gage length to avoid buckling
3. Establishment of specimen control conditions for experiments and boundary conditions for analytical studies.

4.1 Buttonhead Single Edge Notch Specimen

One of the challenges of this program was to design crack growth specimens that were capable of remote strain (displacement) cycling while experiencing bulk cyclic plasticity. The specimen should contain a through crack and have uniform thickness in the gage section so it could be analyzed using two-dimensional finite element modeling. The primary specimen selected for this program was the buttonhead single edge notch (SEN) specimen shown in Figure 47. This specimen has a thickness of 2.54 mm (0.1 inch) and a width of 10.2 mm (0.4 inch). Pin-loaded SEN specimens with this gage section geometry have previously been used by GEAE to determine the linear elastic fracture mechanics crack growth properties of a wide variety of superalloys over a range from room temperature to 980°C (1800°F) (27-29). The modification of the specimen from pin to buttonhead loading was made to accommodate cyclic loading with compressive loads. The dimensions of this



Dimensions are millimeters.

Figure 47: Buttonhead Single Edge Notch (SEN) Specimen.

specimen are sufficiently small to provide a stress/strain intensity for establishing large plasticity and to permit rapid heating and cooling during thermo-mechanical fatigue (TMF) cycling.

4.1.1 J-integral Validation

Another consideration in specimen design was the ASTM-recommended practice for the monotonic J-test requiring that the remaining uncracked ligament be smaller than $25J/\sigma_y$ where σ_y is the yield strength. It was recognized that for primarily tension cases, such as the SEN specimen, this criterion may be a poor estimate. Since it was planned to conduct tests for crack lengths ranging from 0.50 to 3.8 mm (0.02 to 0.15 inch), calculations were performed to evaluate J, crack mouth opening displacement (δ), and crack tip opening displacement (δ_t) using the GE/EPRI Plastic Fracture Handbook⁽³⁰⁾. The 649°C (1200°F) cyclic stress-strain curve for Alloy 718 was determined from the data in the NASA benchmark Program⁽³¹⁾. Using this information, the parameters δ , δ_t , and J, along with \sqrt{EJ} (pseudo-K), were calculated for crack lengths of 1.27, 2.54, and 3.81 mm (0.05, 0.10, and 0.15 inch, respectively) and strain ranges of 0.8, 1.8, and 2.4%. This evaluation was performed for zero mean strain cycling ($A_\epsilon = \infty$) assuming that the crack was open only at positive loads, so the values of J, δ , and δ_t were calculated using the alternating stress range. The calculations were performed for both plane stress and plane strain conditions. The results of these calculations are summarized in Table 11. For the most severe case shown in Table 11, (3.81 mm crack length and 2.4% strain range), the ASTM criteria are exceeded by factors of 6.4 and 3.3 for plane strain and plane stress conditions, respectively.

For cyclic testing conditions, it may be more appropriate that the "process zone size" be smaller than the specimen thickness and remaining ligament. It is generally accepted that the process zone size is on the same order as δ_t . The most severe case listed in Table 11 was δ_t values of less than 0.0127 mm (0.0005 inch). The specimen thickness and remaining ligament are 200 and 500 times larger than δ_t . On this basis, it was anticipated that

TABLE 11: Summary of Estimated Values of J, δ , and δ_t for Alloy 718 at 649°C.

Strain Range	Crack Length (mm)	Plane Stress				Plane Strain			
		J (MPa-m.)	\sqrt{EJ} (MPa/m)	δ (mm)	δ_t (mm)	J (MPa-m)	\sqrt{EJ} (MPa/m)	δ (mm)	δ_t (mm)
0.8%	1.27	0.00194	17.9	0.0023	0.0006	0.00116	13.9	0.0014	0.0005
	2.54	0.00336	23.5	0.0072	0.0011	0.00191	17.7	0.0040	0.0008
	3.81	0.00758	35.4	0.0210	0.0023	0.00399	25.6	0.0112	0.0017
1.6%	1.27	0.00538	29.8	0.0046	0.0017	0.00320	23.0	0.0029	0.0013
	2.54	0.00928	39.2	0.0145	0.0030	0.00527	29.5	0.0081	0.0022
	3.81	0.02100	59.0	0.0419	0.0064	0.01103	42.7	0.0208	0.0046
2.4%	1.27	0.00975	40.2	0.0069	0.0031	0.00583	31.0	0.0043	0.0025
	2.54	0.01684	52.7	0.0217	0.0054	0.00956	39.7	0.0121	0.0040
	3.81	0.03806	79.3	0.0628	0.0116	0.02000	57.5	0.0334	0.0084

this SEN specimen can be used to evaluate P-I integrals under elasto-plastic conditions.

4.1.2 SEN Specimen Buckling experiments

A series of SEN specimens were designed with gage lengths of 28.5, 22.2, and 15.9 mm (1.128, 0.875, and 0.625 inches) to evaluate resistance to buckling. The specimens were cyclically tested under either load or stroke control with the mean value of the control variable at zero. The range of stroke or load was gradually increased until buckling occurred. For the longest gage length geometry, buckling occurred during a room temperature test at approximately 758 MPa (110 ksi). Based on elastic buckling analysis, the gage length was reduced to 22.2 mm. It was estimated that the buckling stress would be 1206 MPa (175 ksi). A room temperature buckling test failed at 1225 MPa (177.8 ksi). This stress level is significantly greater than the yield stress of Alloy 718 so additional tests were performed at 649°C (1200°F), the highest temperature in this program which also has the lowest monotonic and cyclic strength level.

Duplicate 649°C buckling tests were performed on SEN specimens with a 22.2 mm gage length and the specimens buckled at stresses of 856 and 850 MPa (124.3 and 123.3 ksi). This geometry would be marginal for performing tests with cyclic plastic strain. From elastic buckling analysis, it is estimated that gage length must be reduced to 15.9 mm to achieve 649°C buckling stresses of 1206 MPa (175 ksi). Therefore, a crack propagation test was performed with the 15.9 mm gage length geometry at 649°C with the largest strain range (1.7%) planned for use in this program. A 1.27 mm (0.5 inch) extensometer was placed in the center of the 10.2 mm wide face of a SEN specimen with a 0.1 mm deep EDM slot across one side of the 2.5 mm thickness. The specimen was cycled in strain control with A_ϵ of infinity at a strain rate of 0.02 %/sec. A crack nucleated out of the EDM notch and propagated across the entire specimen. The hysteresis loop monitored during the test could be characterized into 3 groups. Very early in the test, perceptible softening was observed on each cycle as shown in Figure 48a. After some 20

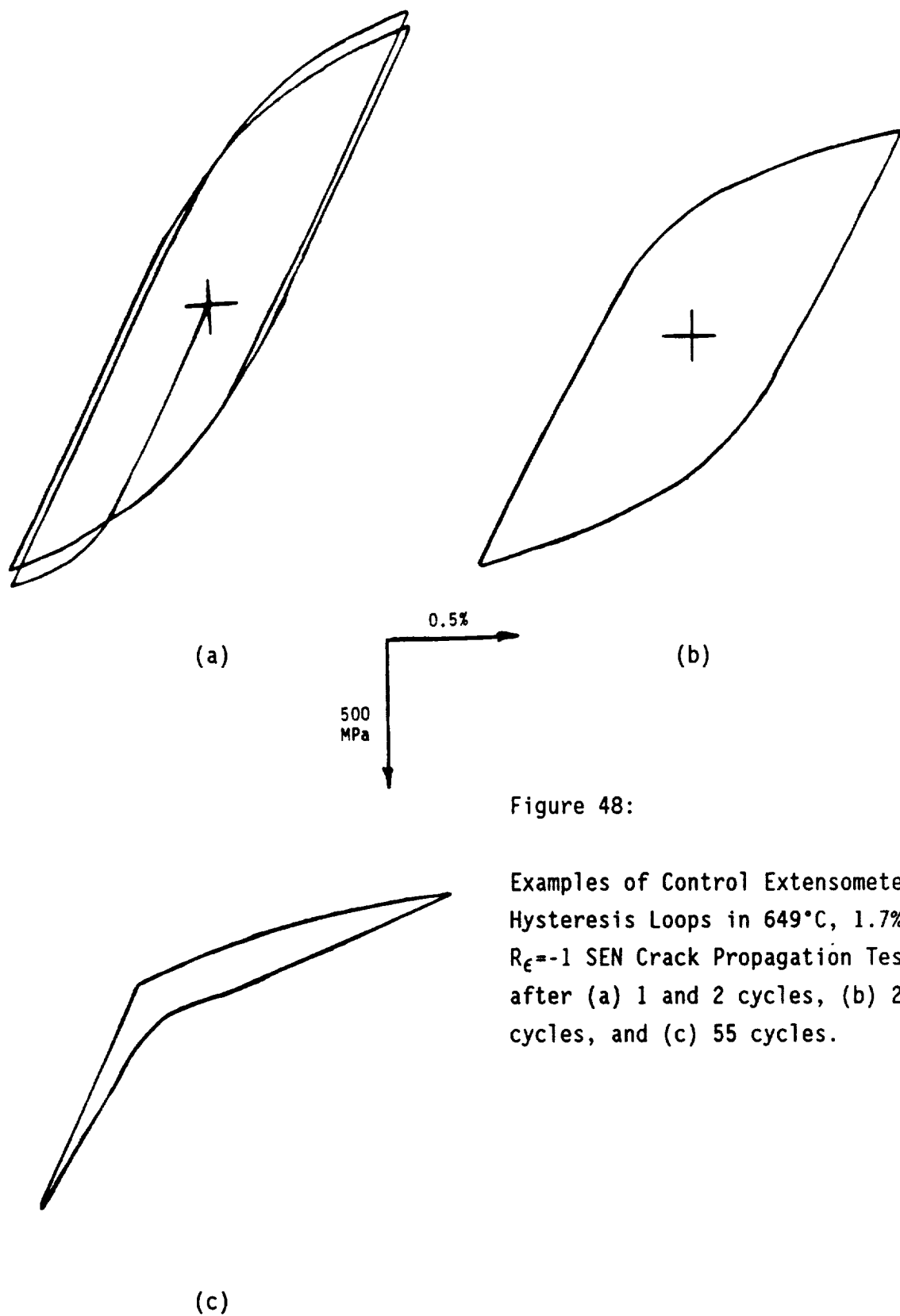


Figure 48:

Examples of Control Extensometer Hysteresis Loops in 649°C, 1.7%, $R_{\epsilon} = -1$ SEN Crack Propagation Test after (a) 1 and 2 cycles, (b) 23 cycles, and (c) 55 cycles.

cycles, the softening was not as rapid, and the loops had the classical appearance shown in Figure 48b. Cusps, indicative of crack closure, started to form as the crack propagated through the specimen, and the maximum stress diminished with each successive cycle. An example of this type of loop is shown in Figure 48c. Visual observation of the crack showed 45° shear bands emanating from the crack tip toward the notched free surface. These were observed over a wide range of crack lengths, but no remnants could be observed after completing the test. The fracture surface of this specimen was extremely flat and showed no evidence of shear lip or crack front tunneling.

Comparison of hysteresis loops from this SEN crack growth test and a companion axisymmetric specimen (notched) cyclic tests showed that early in the test both the SEN and axisymmetric specimen tests had nearly identical hysteresis loops. Figure 49 shows the variation in maximum and minimum stress with cycle number in the SEN and notched specimen cyclic tests. Early in the test, when the crack length in the SEN specimen was short, both specimens showed similar constitutive responses. As the crack length became larger (after approximately 30 cycles), the minimum stress remained constant but the maximum stress started to decrease. At the end of the test (Cycle 68), the maximum stress approached zero. The minimum stress decreased with increasing crack length because of the displacement control at the center of the gage length. The minimum stresses for the two types of tests were similar because the crack closed on itself and both specimens were fully yielded in compression.

These results strongly suggest that the SEN specimen with a gage length of 15.9 mm (Figure 47) would be used as the primary specimen in this program.

4.2 Triple extensometer boundary condition test

A triple extensometer test was performed on an Alloy 718 buttonhead SEN specimen to determine specimen displacements at various locations of the specimen. These data were used for comparison with finite element analyses. These results will be used several times in Section 4.3.

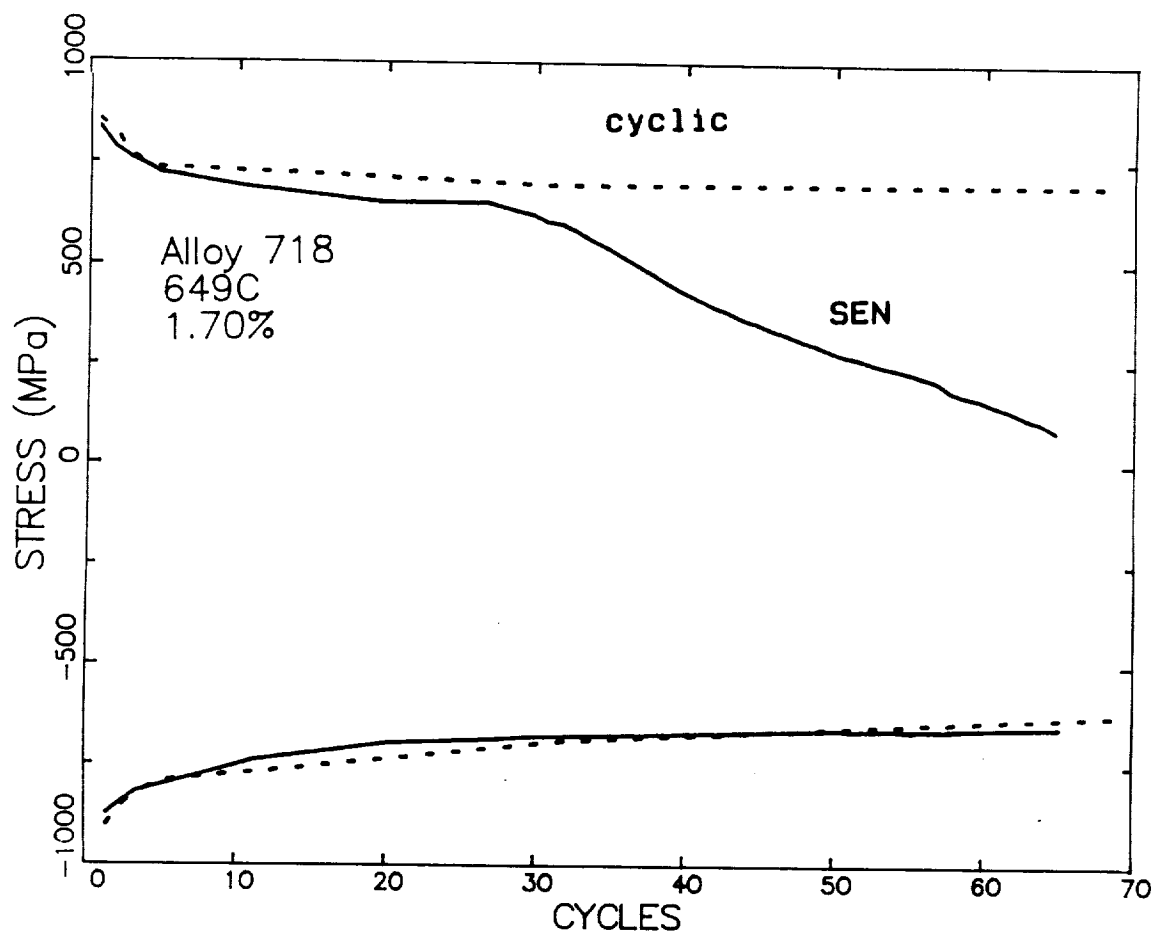


Figure 49: Variation of Maximum and Minimum Stress in 649°C (1200°F) SEN and Cyclic Test.

An Alloy 718 SEN specimen was precracked using low elastic loads. Post-test measurements showed that the crack length was 2.69 mm (0.106 inch). The specimen was then cycled slowly at room temperature with an A_c of infinity and a strain range of 2.4%. The specimen displacements were monitored with three extensometers, one at the center of the gage section ($x/W = 0.5$), one traversing the crack mouth ($x/W = 0$), and one at the back face ($x/W = 1$). All three extensometers had a gage length of 13.97 mm (0.55 inch) to correspond to a nodal points in the finite element meshes. The test was controlled using an extensometer located in the center of the gage section. At the maximum value of strain (1.2%), all three extensometers had non-linear variation of displacements with load, indicative of appreciable inelastic strains. Alloy 718 exhibits significant cyclic softening which has also been observed during cyclic crack growth (Figure 49). Most of the finite element analyses were performed prior to determining the cyclic stress strain curve of Alloy 718, so the tension properties were used to predict the behavior of the buttonhead SEN specimens. The loading on the first cycle should obey the monotonic response rather than the cyclically softened response.

Figure 50 shows the variation of displacement along the specimen width with applied load. For both loading and unloading, the normal displacements vary in an almost linear fashion with distance across the specimen width. The dashed lines show the extrapolated crack face displacement from the control and back face extensometers. These data support the use of two extensometers to determine the linear displacement boundary conditions across the top of the gage section.

4.3 Specimen analysis

In order to use this linear displacement approach, it was necessary to examine the distribution of boundary displacements by finite element analyses for the buttonhead SEN specimen. The results of analyses were also used to provide guidelines for experimental set-up and data measurement. These analyses included four different finite element meshes starting with a full three-dimensional (3D) model which included the specimen buttonhead and ended

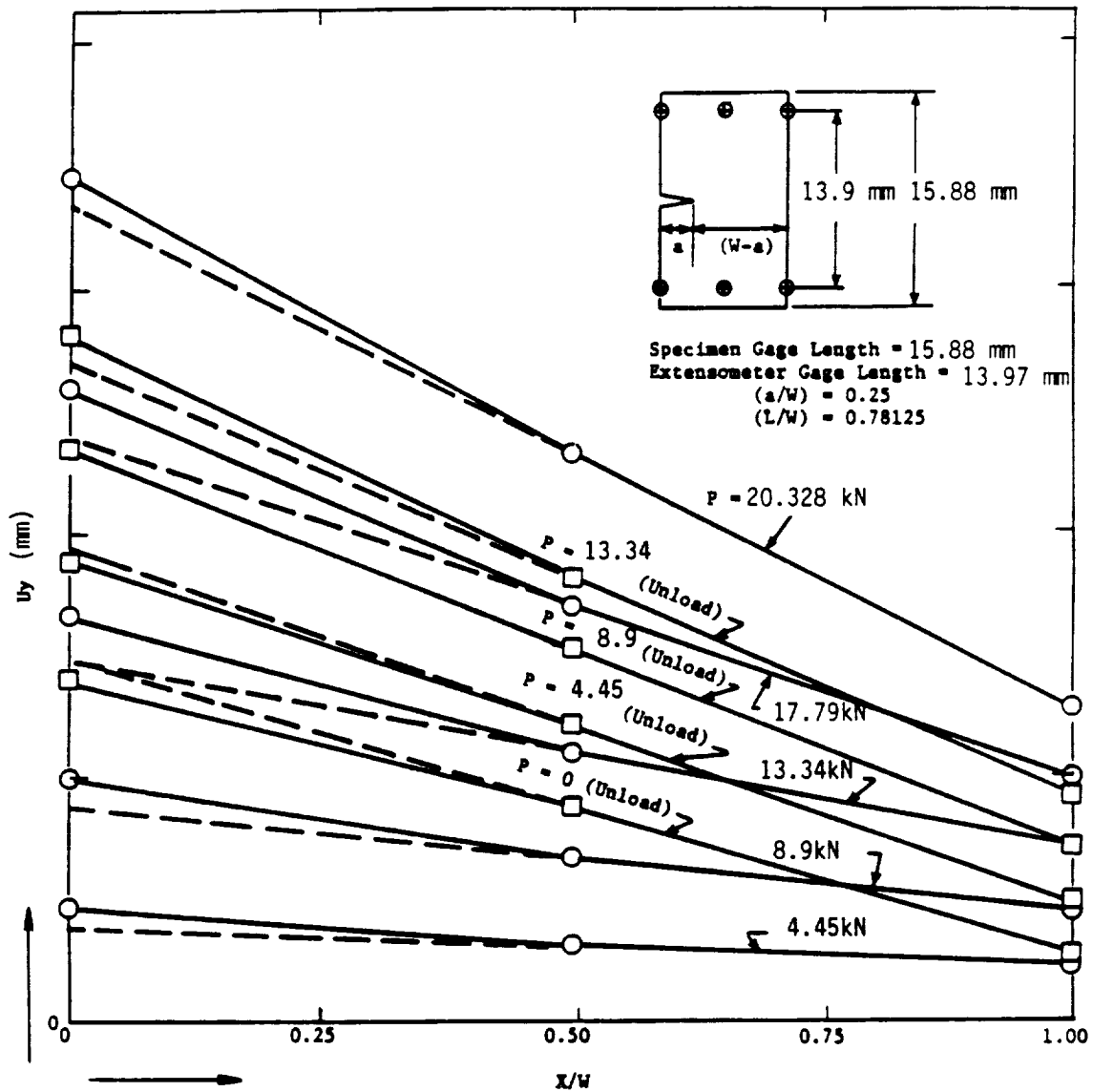


Figure 50: Variation of Normal Displacements Measured During Cyclic Loading of a Buttonhead SEN Specimen With $a/W=0.25$ Using 13.97 mm (0.55 inch) Gage Length Extensometers.

with a two-dimensional (2D) model of just the specimen gage section.

All the analyses were performed using the room temperature properties of Alloy 718. The elasto-plastic analyses were performed using the 21°C (70°F) tension stress-strain curve of Alloy 718. This approach was taken because these finite element results were compared to the load and displacements measured during the first loading cycle which should obey the monotonic response rather than the cyclic-softened constitutive behavior.

4.3.1 3D Specimen Analysis

The first analysis performed was a 3D finite element analysis for the entire specimen. Figure 51 shows the three-dimensional mesh of the buttonhead specimen consisting of eight-noded isoparametric brick elements. The model had 1107 nodes and 720 elements. It had a finer mesh in the gage section relative to the mesh size in the shank and buttonhead regions to improve the accuracy of the prediction of stresses and displacements in the more highly stressed gage section. This grid has a gage length (L) of 1.14 mm (0.45 inch). This is slightly longer than the specimen geometry shown in Figure 47 because the analysis was performed prior to completion of the buckling tests. The analysis was performed for a single crack length of 2.5 mm (0.10 inch) or $a/W = 0.25$. This crack length represents an upper bound for the maximum a/W evaluated analytically in this program.

Elastic analyses were performed using two different ways of applying prescribed end displacements. In the first case, a constant axial displacement was applied to the buttonhead, while in the second case, constant displacement was applied on the top portion of the specimen shank circumference adjacent to the buttonhead. These two boundary conditions were used to evaluate the uncertainty in the actual displacements induced by the laboratory gripping fixtures. By equating the resulting elastic axial displacement (u_y) at a given node point in the gage section, it was found that the two end displacement cases have a maximum of 3 percent difference in stresses and displacements across the width of the gage section. Therefore,

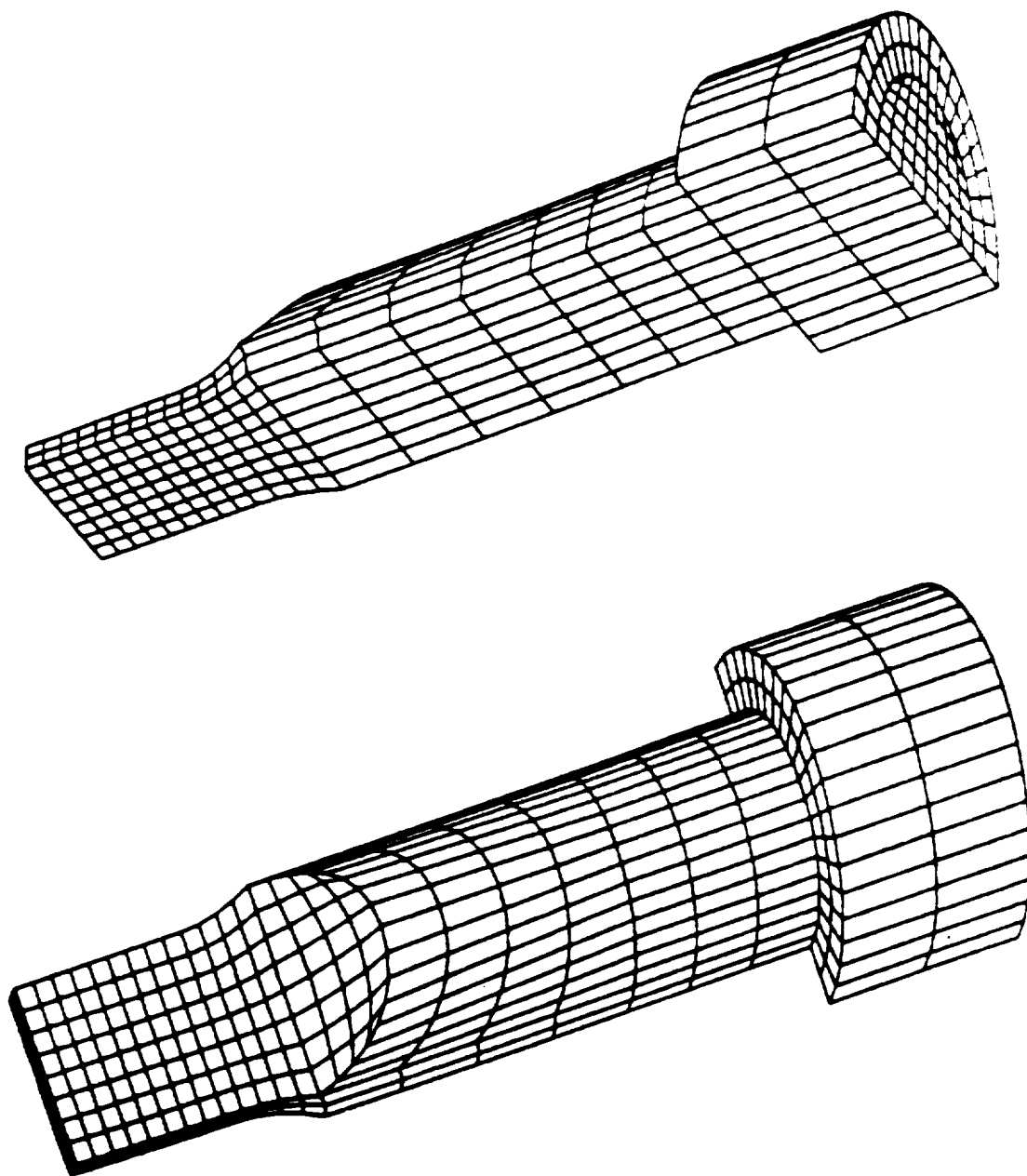


Figure 51: Buttonhead Specimen 3D Finite Element Model.

it was concluded that for elastic response the application of constant end displacement to either the buttonhead or to the shank leads to almost identical results in the gage section.

Figure 52 shows the elastic axial displacement (u_y) along the gage section width for different planes parallel to that of the crack (y/L ratios). These results show that for a constant axial displacement of 0.25 mm (0.01 inch) applied at the shank top of a test specimen, the u_y displacement varies linearly across the gage section width near the end of the gage length.

In addition to the normal displacement, the 3D finite element analysis also shows that the gage section experiences significant lateral displacement (u_x). Figure 53 shows the deformed shape of the SEN specimen. The specimen's lateral displacement in the crack plane is of the same order (0.089 mm or 0.0035 inch) as the crack mouth opening displacement (CMOD). The lateral deflection is mainly due to the fact that the buttonhead is fixed against lateral movement and the bending moment due to the presence of the crack causes the specimen to move laterally in the crack plane where it has the lowest stiffness.

Some additional 3D elastic-plastic analyses were performed on the smaller gage section specimen which also confirmed the basic linear nature of displacement near the end of the gage section. This work which utilized 20 noded brick elements did not have sufficient mesh refinement for accurate elastic-plastic comparison with the experimental results. In all the 3D analyses, there was little variation of the stresses through the thickness of the specimen. Accordingly, 2D analyses could be performed with little loss in accuracy, but with much finer mesh size and at lower costs relative to the 3D analysis.

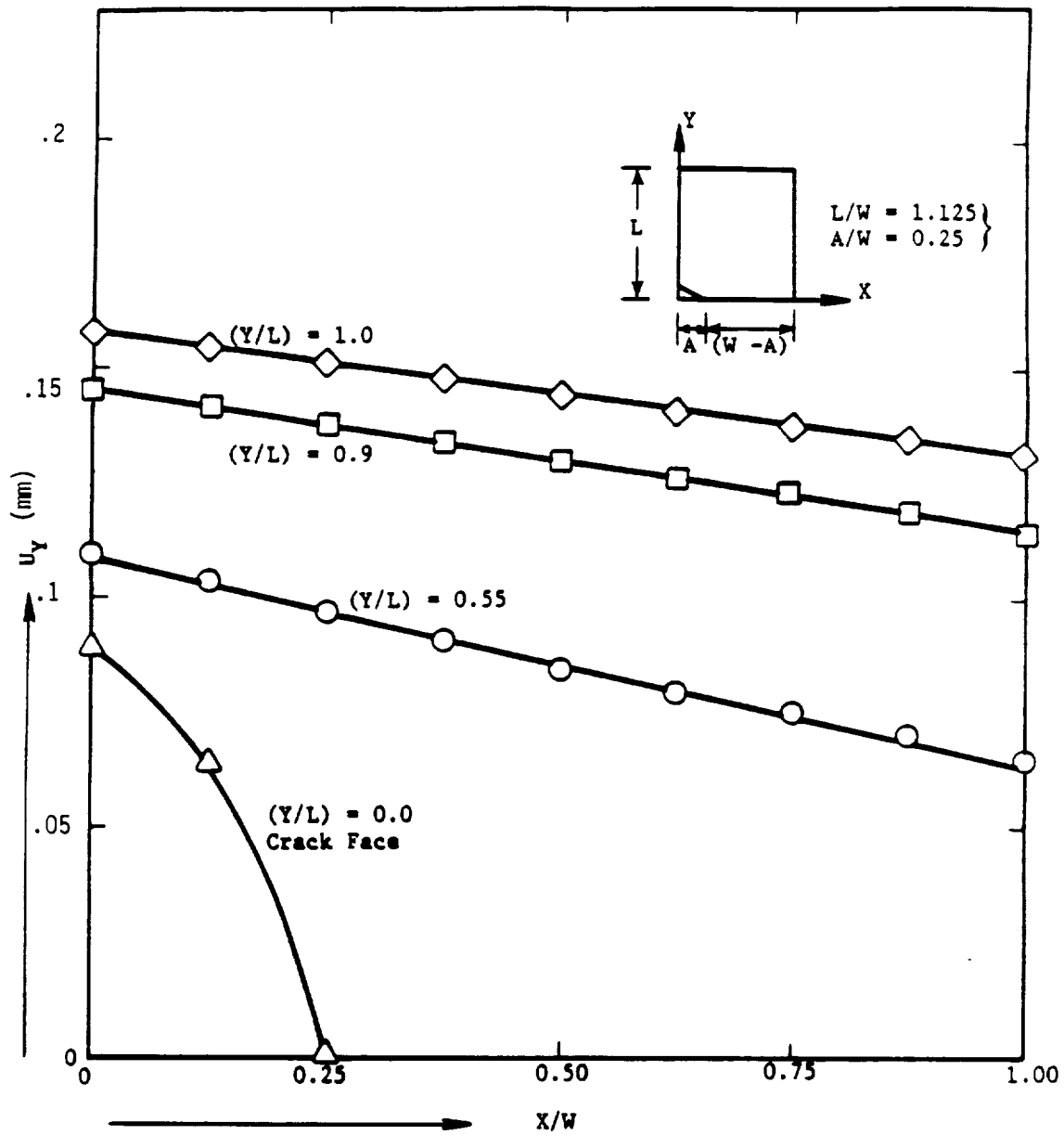


Figure 52: Prediction of Normal Displacement Variation across Gage Section Predicted from 3D Elastic Analysis of Constant Axial Buttonhead Displacement.

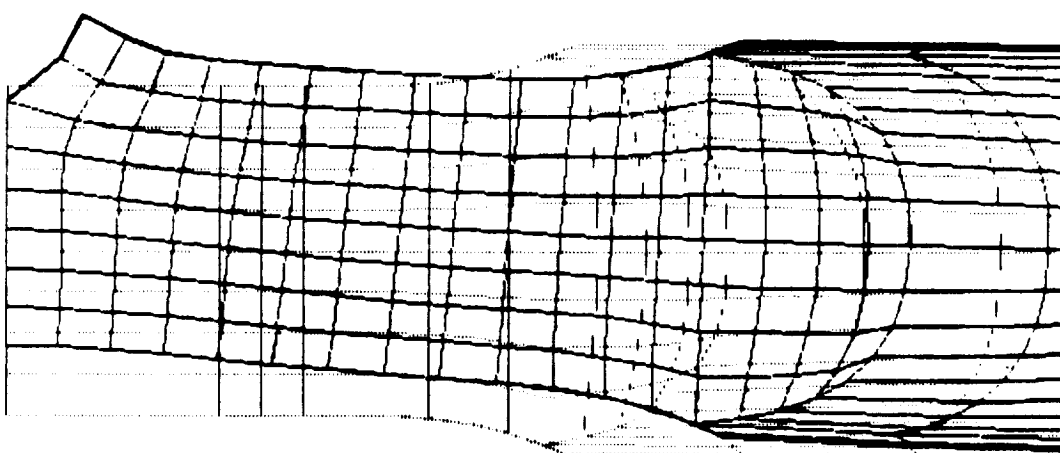
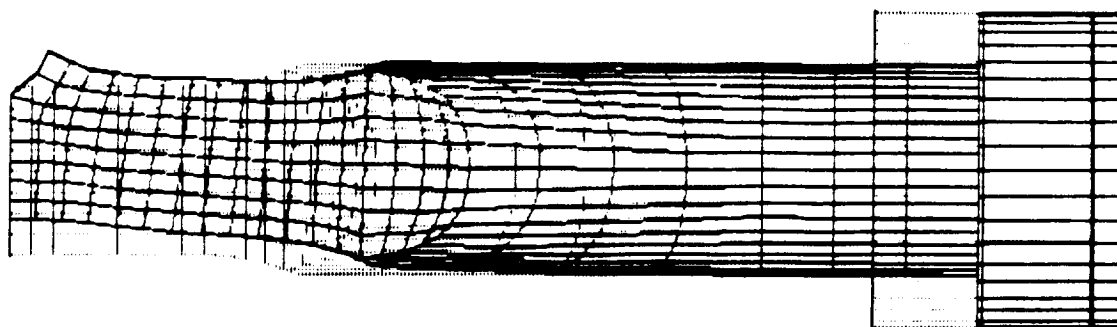


Figure 53: Lateral Displacement Profile of the Buttonhead SEN Specimen Subjected to Uniform Axial Displacement (Dotted Lines Show Undeformed Shape).

4.3.2 2D Full Specimen Model

The 2D full specimen model is shown in Figure 54. It has 566 nodes and 1002 elements. In the gage length portion all 634 elements have a constant thickness of 2.54 mm (0.1 inch). The elements in the shank portion of the specimen had variable thickness depending on their location within the circular cross-section of the shank. The near crack tip mesh size for the 2D model is 0.15 mm (0.006 inch), whereas for the 3D model it is 1.27mm (0.05 inch).

Plane stress elasto-plastic analyses were performed for various applied normal displacements at the shank end. A comparison of the normal displacement u_y at the end of the gage length ($y = 7.11$ mm or 0.28 inch) obtained from 2D and 3D full specimen models is shown in Figure 55 for various values of the applied buttonhead displacement. For lower values of applied displacement, where the response is essentially elastic, the 2D and 3D analyses agree quite well. As the plasticity spreads from the gage section into the radius and shank, with increasing buttonhead displacement, the level of agreement diminishes. The results of the 2D elasto-plastic solution are believed to more realistically represent the specimen behavior for the large plastic strains because the 3D 20-node brick mesh is significantly coarser than the 2D mesh in the crack plane region.

Figure 56 shows the good agreement between the predicted displacement gradient at the end of the gage section and that measured in the triple extensometer experiment previously described. This analysis also showed that the use of a linear variation in displacement across the specimen width is a reasonable approximation. Another way of comparing the CYANIDE predictions and the experimental results is to compute the load for a given end displacement, and compare the predictions with the experimental results. This has been done in Figures 57, 58, and 59 for the mid-width, back surface, and front surface extensometers, respectively. These comparisons demonstrate that the behavior of the specimen is well understood and can be described by the finite element method assuming full constraint at the

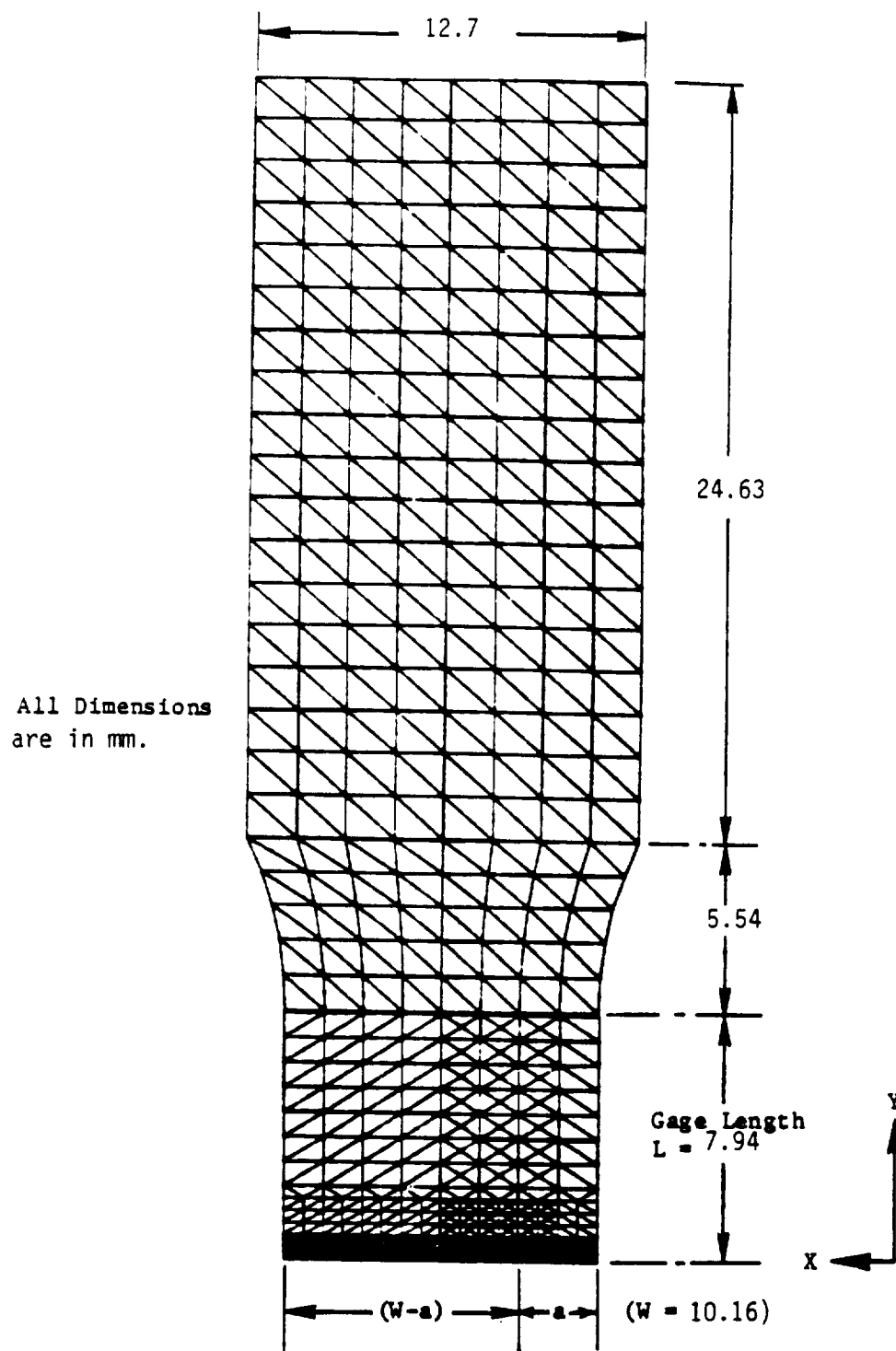


Figure 54: Full Specimen 2D Finite Element Model.

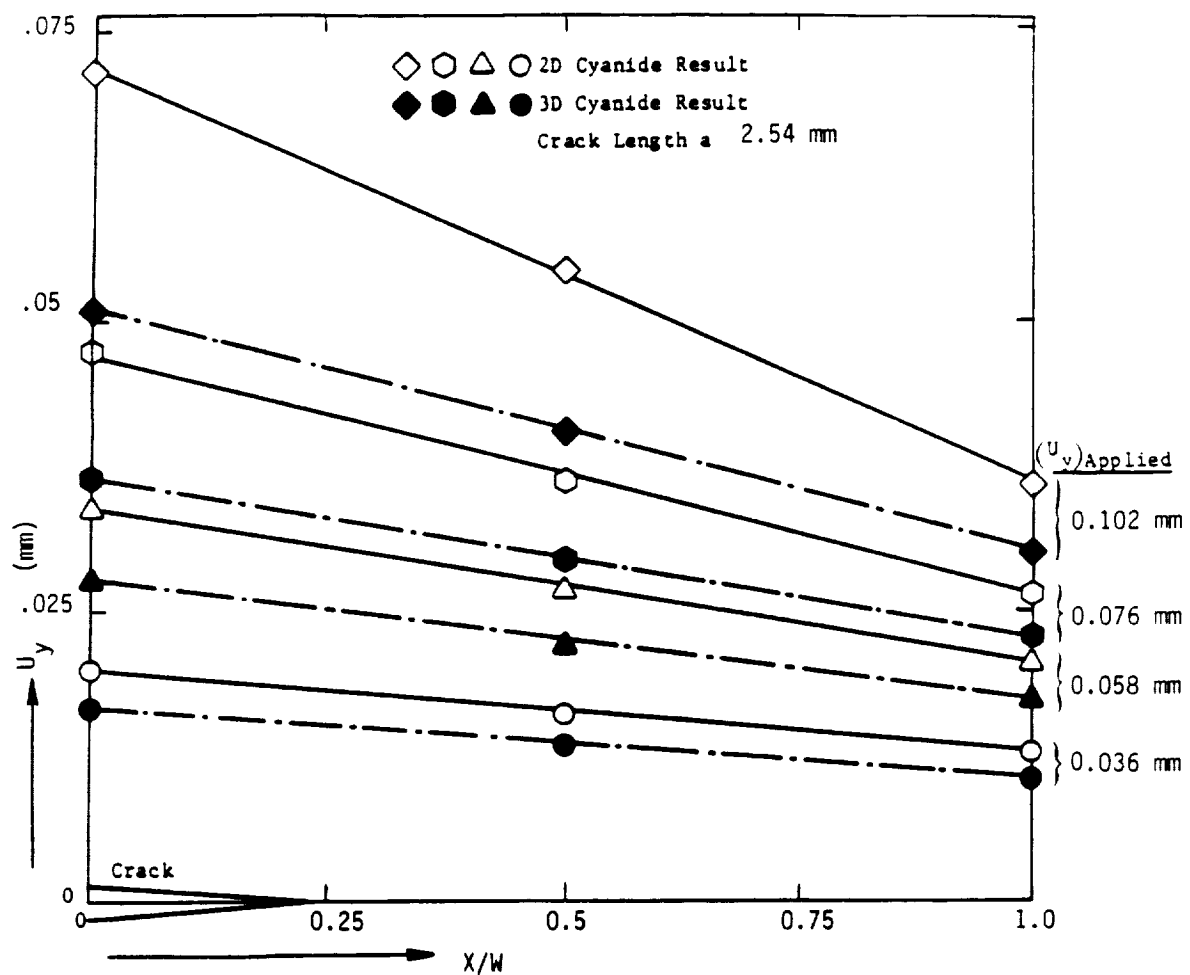


Figure 55: Comparison of Normal Displacements (u_y) at the End of SEN Specimen as Predicted from 2D and 3D CYANIDE Full Specimen Analyses.

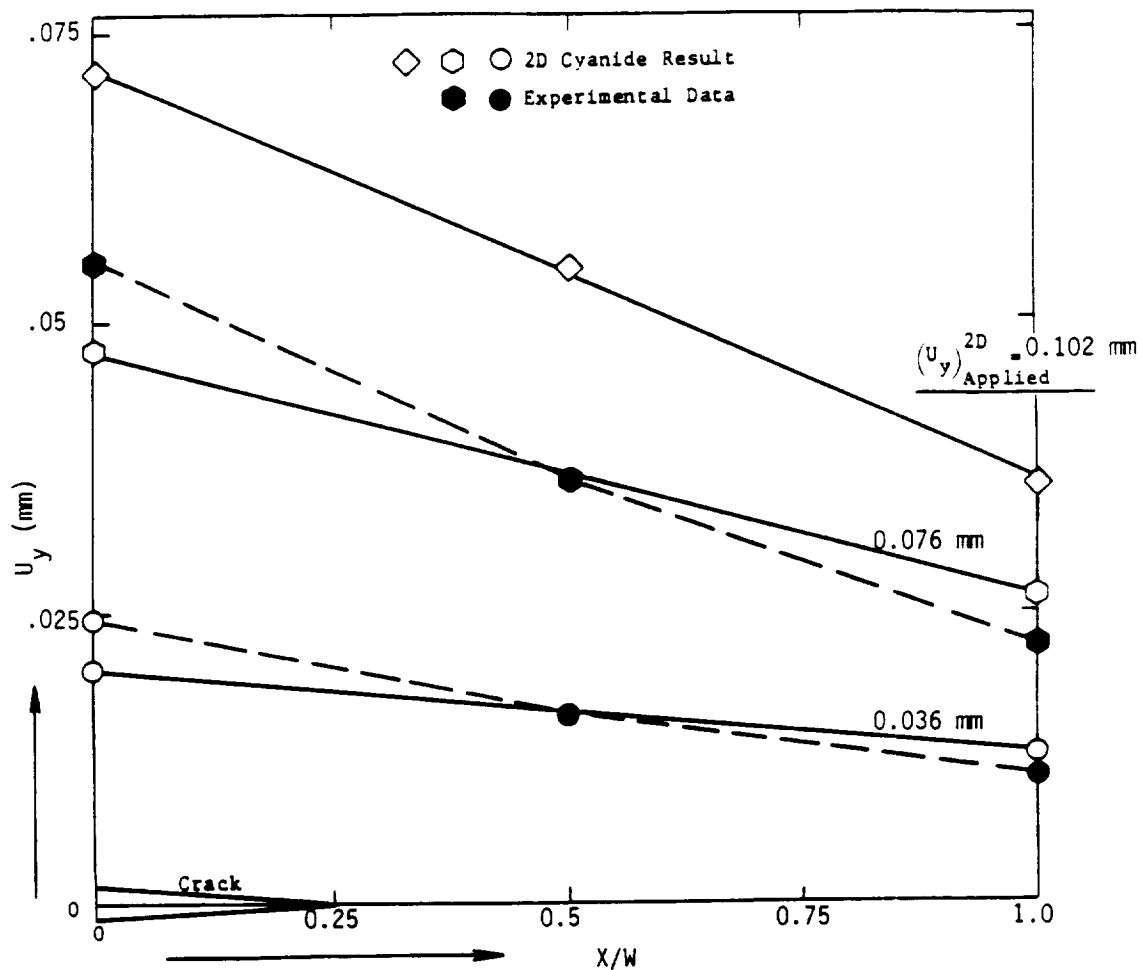


Figure 56: Comparison of Normal Displacements (u_y) at the End of SEN Specimen from Experiment and 2D CYANIDE Full Specimen Analysis.

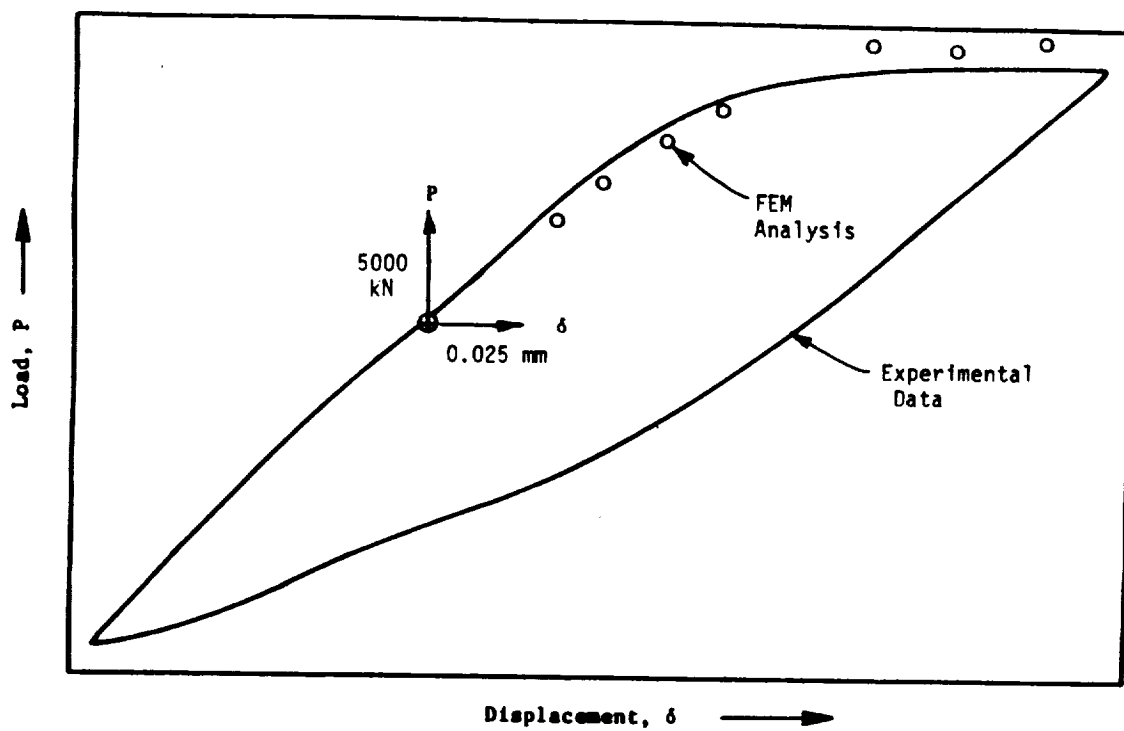


Figure 57: Comparison of Experimentally Determined Load-Displacement Hysteresis Loop from Mid-width Extensometer with 2D CYANIDE Full Specimen Analysis.

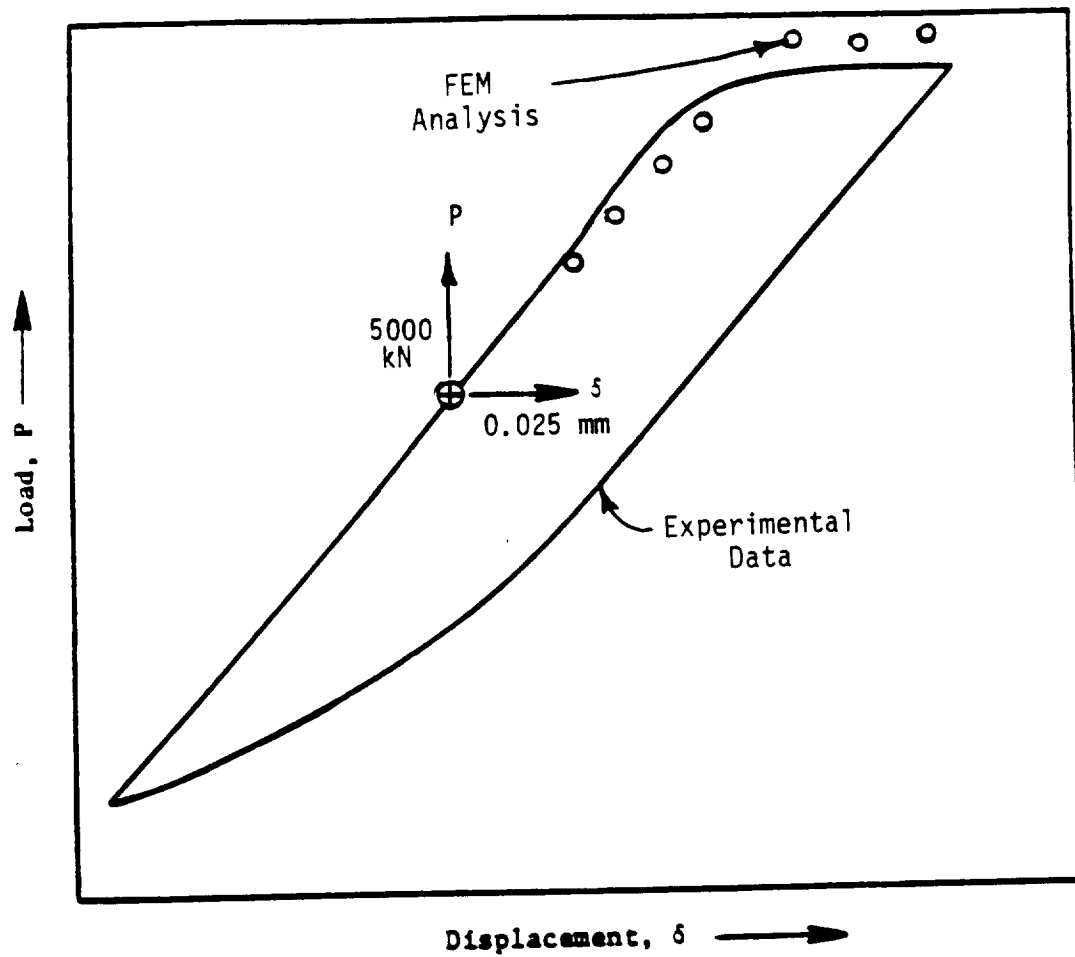


Figure 58: Comparison of Experimentally Determined Load-Displacement Hysteresis Loop from Back Surface Extensometer with 2D CYANIDE Full Specimen Analysis.

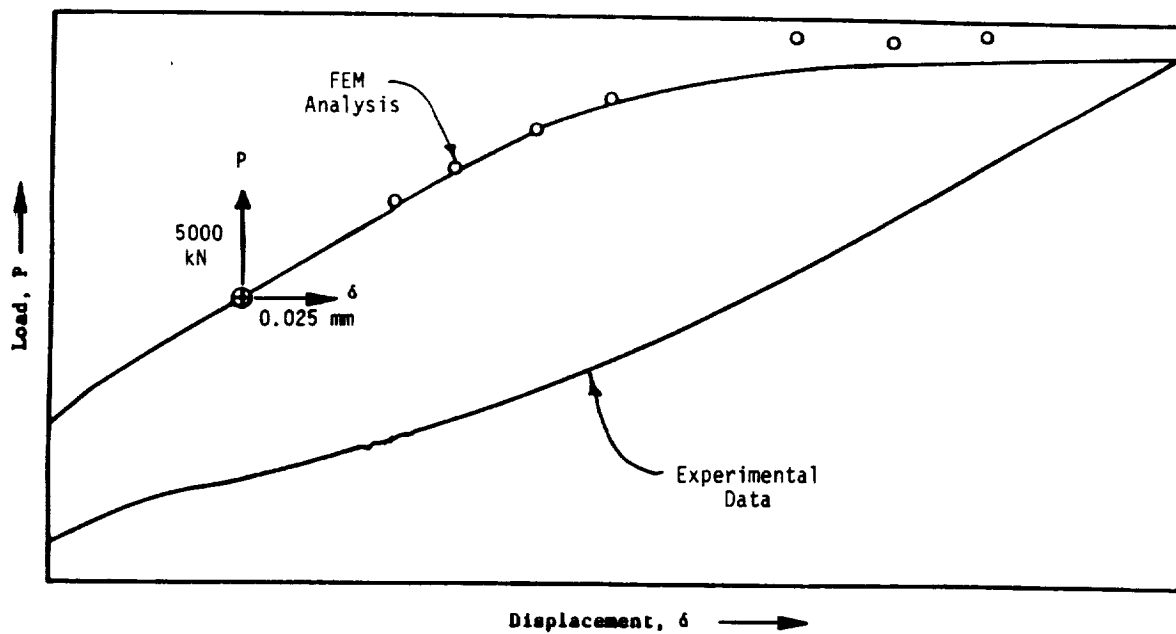


Figure 59: Comparison of Experimentally Determined Load-Displacement Hysteresis Loop from Front Surface Extensometer with 2D CYANIDE Full Specimen Analysis.

specimen end.

While these results were encouraging, the test specimens were controlled by the mid-width displacement and not the shank displacement. Therefore, it was desirable to experimentally measure the displacements in the gage section to determine the boundary conditions for a refined finite element mesh gage section model. This would save computational costs and eliminate the need to determine displacements in the shank of the specimen. Both the experiments and the analysis showed the displacements varies approximately linearly across the specimen width at the end of the gage section. Thus the back surface and mid-width extensometers can be used to completely describe the displacement boundary conditions in a gage section model.

4.3.3 2D Gage Section Model

As a final verification of this procedure, finite element analyses were performed on a reduced section model having a crack length of 2.54mm (0.1 inch). The finite element mesh used in these analyses are shown in Figure 60. An analysis was performed assuming the proposed approach of using a linear displacement variation as determined from the displacements measured experimentally at the mid-width and back surface locations. A second analysis was performed using the displacements from the full specimen model to analyze the gage section model. Pseudo-stress intensity factors were determined from the J-integral calculated using the P-I integral post-processor. These results as well as those from the full 2D specimen analysis are plotted in Figures 61 and 62 as a function of the mid-width displacement and nominal load, respectively. These results show that the J-integral results are not sensitive to the analysis scheme. Therefore, the experimental displacements can be used directly to determine the linear displacement boundary conditions for the reduced section model. The adequacy of this approach is demonstrated in Section 7.0 which analyzes the isothermal data determined in this program.

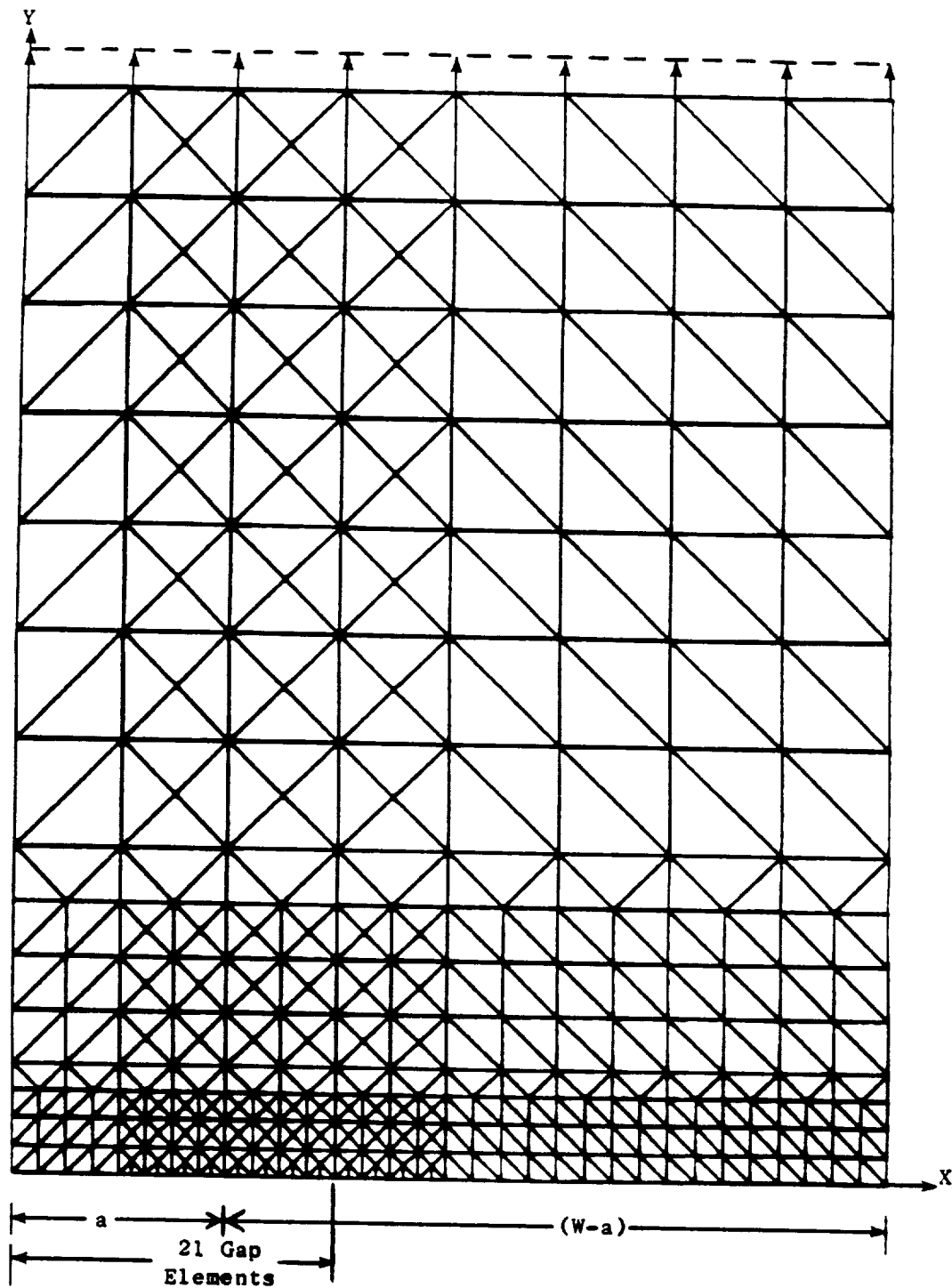


Figure 60: Gage Length 2D Finite Element Model with Width of 10.16 mm and Height of 7.94 mm.

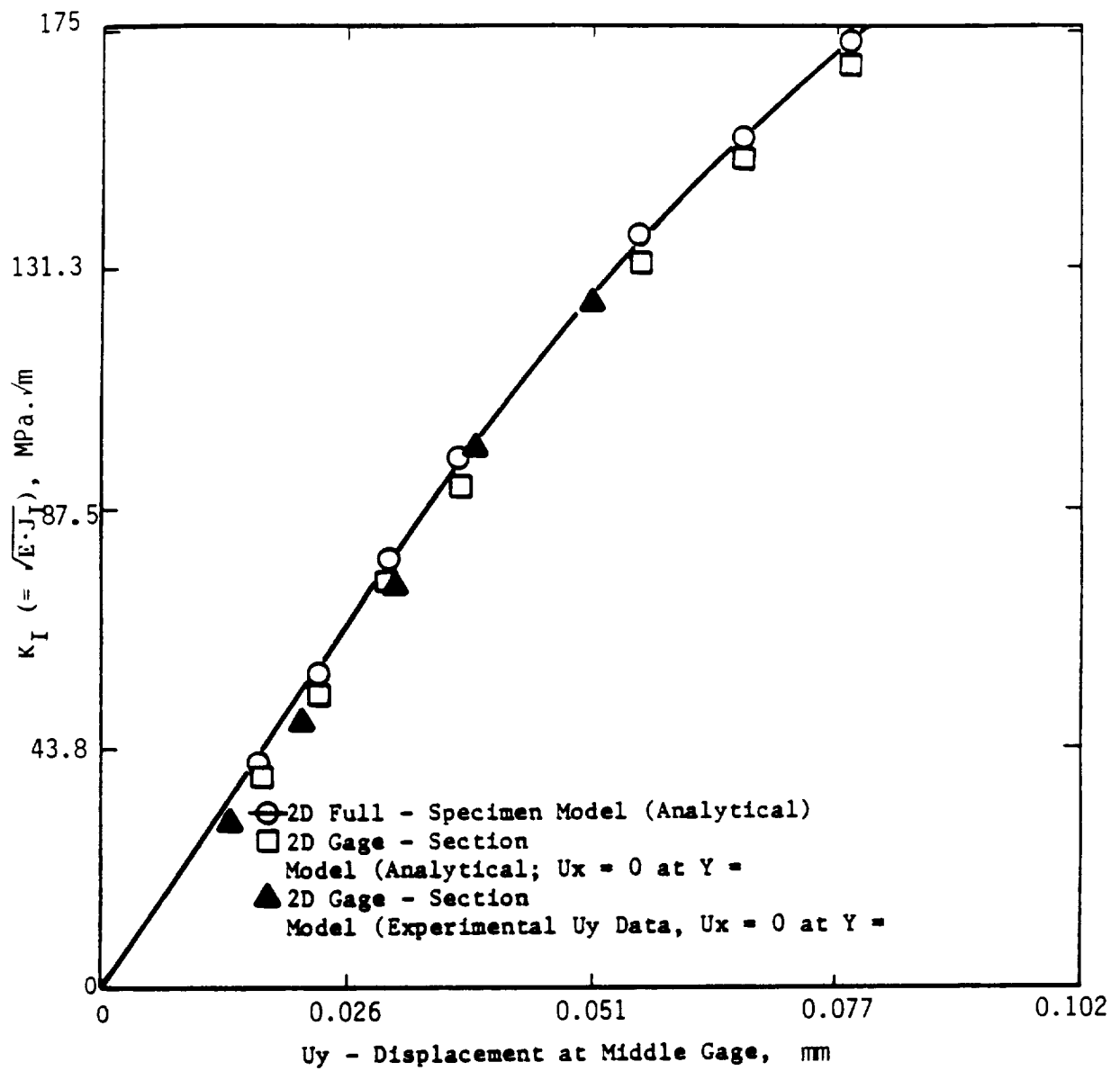


Figure 61: Predicted Variation of Pseudo K with Vertical Displacement (u_y) in Buttonhead SEN Specimen.

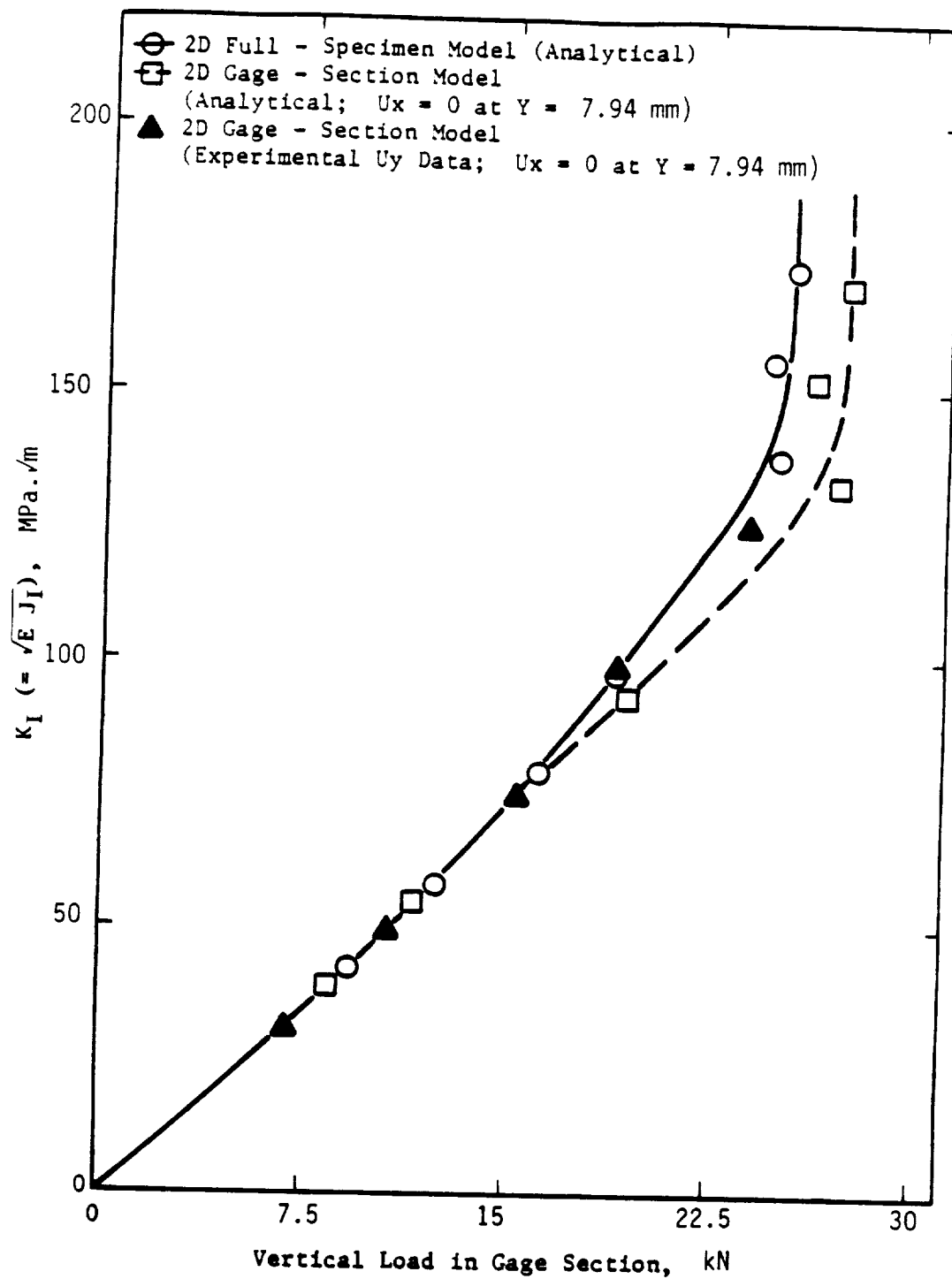


Figure 62: Predicted Variation of Pseudo K with Vertical Load in Buttonhead SEN Specimen.

5.0 EXPERIMENTAL AND DATA ANALYSIS TECHNIQUES

The purpose of the crack growth tests performed in this program was to provide data to (1) describe the growth of the cracks and (2) determine specimen boundary conditions necessary for finite element analyses. The test matrices were designed to use a single specimen geometry to perform crack growth tests under net section elastic and elasto-plastic deformation. This same geometry was to be used for thermal gradient and thermal-mechanical fatigue (TMF) tests. The primary specimen selected was the buttonhead single edge notch (SEN) specimen with some additional verification tests performed using a modified compact specimen.

This portion of the report describes the experimental techniques and data reduction procedures used to analyze these data. A detailed description of the experimental results will appear in other sections.

5.1 Test Frequency

One of the considerations in this testing program is whether to conduct crack propagation tests under strain rate or under frequency control. Table 12 shows the cycle period and rate of cycle accumulation as a function of strain rate and strain range. For strain range conditions to be used in this program, the cycle period can vary by a factor of 3.4 which might induce various amounts of environmental time-dependent crack growth, particularly at the more elevated temperatures(15,19-26). It was most desirable to perform all types of crack growth tests (isothermal, thermal gradient, and TMF) under nearly identical cycling conditions to avoid difficulties associated with time-dependent crack growth. The most limiting type of test was the TMF tests where the specimen size, to a large extent, controls the time necessary to cool the specimen during each TMF cycle. The time required to cool a buttonhead specimen was evaluated by instrumenting a specimen with multiple thermocouples. The specimen was heated with a RF (radio frequency) induction coil which heated the gage length to temperature variations of less than 3°C (5°F). The specimen was thermally cycled from 427 to 649°C (800 to 1200°F) by

TABLE 12: Variation of Cycle Period and Cycle Accumulation in Strain Rate Controlled Tests With Strain Rate and Range

Strain Rate (%/sec)	Strain Range	Cycle Period (sec)	Cycles/day
0.02	0.0050	50	1,728
	0.0115	115	751
	0.0170	170	508
0.50	0.0050	2	43,200
	0.0115	4.6	18,783
	0.0170	6.8	12,706

turning the RF generator on and off. The temperature variation was almost linear with time and required approximately 30 seconds to change the temperature by 220°C (400°F), the largest range to be used in the TMF tests. Based on this result and previous experience with these types of tests, a desirable temperature ramp time was selected to be no smaller than 45 seconds (90 second cycle) so that the temperature would be well controlled and uniform along the gage length. The test frequency selected for this program was 0.01 Hz (100 seconds/cycle or 864 cycles/day). This results in different strain rates for different strain ranges, but was judged not to be significant because of the lack of strain rate sensitivity observed in the Alloy 718 tensile and cyclic constitutive tests.

5.2 Crack Closure

An important part of the crack growth experiments are the detection of the opening and closing of the crack. A variety of techniques have been used to measure the closure behavior in cracks. Almost all of those studies were performed on tests specimens cycled in a nominally elastic fashion. One common conclusion reached from experimental closure studies is that the detection of closure is highly dependent on the measurement technique. For the purpose of this investigation, where large plastic strains will be experienced over a large section of the specimen gage length, the use of non-displacement techniques, such as potential drop or acoustic emission, may experience experimental difficulties or introduce experimental artifacts during the testing program. Experience with displacement techniques has shown that the ability to detect the occurrence of crack closure is dependent on where the displacement is measured relative to the crack tip and on the gage length of the device. The smaller gage lengths and hence the smaller amount of bulk material displacement increases the ability to accurately detect crack closure. For the purpose of this test program, it is not known exactly which test data was to be used for evaluation of the P-I integrals prior to conducting the tests. This placed the restriction that the CMOD gage should be able to operate over a wide variety of crack lengths without frequent interruption of the test to reposition the gage or to perform other

instrumentation. This restriction rules out the use of the laser interferometric gage developed by Sharpe and co-workers(32-34) because of its limited gage length and necessity to be near the crack tip. The remaining techniques would monitor the crack mouth opening or measure of the strain on the back face of the specimen. The CMOD approach was selected because of experimental ease and uncertainties about the interpretation of back face strain in a specimen which is experiencing a combination of cyclic plasticity and significant amount of bending, particularly when the crack has grown to a large size.

A CMOD gage was developed by modifying a standard 12.7 mm (0.5 inch) elevated temperature extensometer to have a gage length of approximately 0.76 mm (0.03 inch). The reduced gage length was used to improve the sensitivity to the closure and still be relatively easy to use. The electronics were also altered resulting in significantly improved resolution relative to the standard extensometer configuration. This CMOD gage extensometer was calibrated using both differential and high sensitivity micrometers to a displacement sensitivity of 0.0076 mm/volt (0.0003 inch/volt) which has sufficient resolution for the subsequent experimental activities. The strain measured with this CMOD gage on an uncracked and unnotched SEN specimen was the same as that measured with the conventional extensometer having a gage length of 12.7 mm (0.5 inch), more than 16 times larger.

5.3 Buttonhead Single Edge Notch Specimen

A drawing of the buttonhead SEN specimen was previously shown in Figure 63. The basic test matrix includes tests with a total strain ranges from 0.50% to 1.70% with A_ϵ of infinity. The 0.50% strain range should result in nominally elastic cycling while the higher strain ranges should result in significant cyclic plasticity. The highest strain range for the crack propagation tests corresponds to the intermediate strain range used to determine cyclic constitutive properties. All specimens contained a 0.25 mm (0.01 inch) deep electric discharge machined (EDM) crack starter notch centered along the gage length traversing the thickness of the gage length.

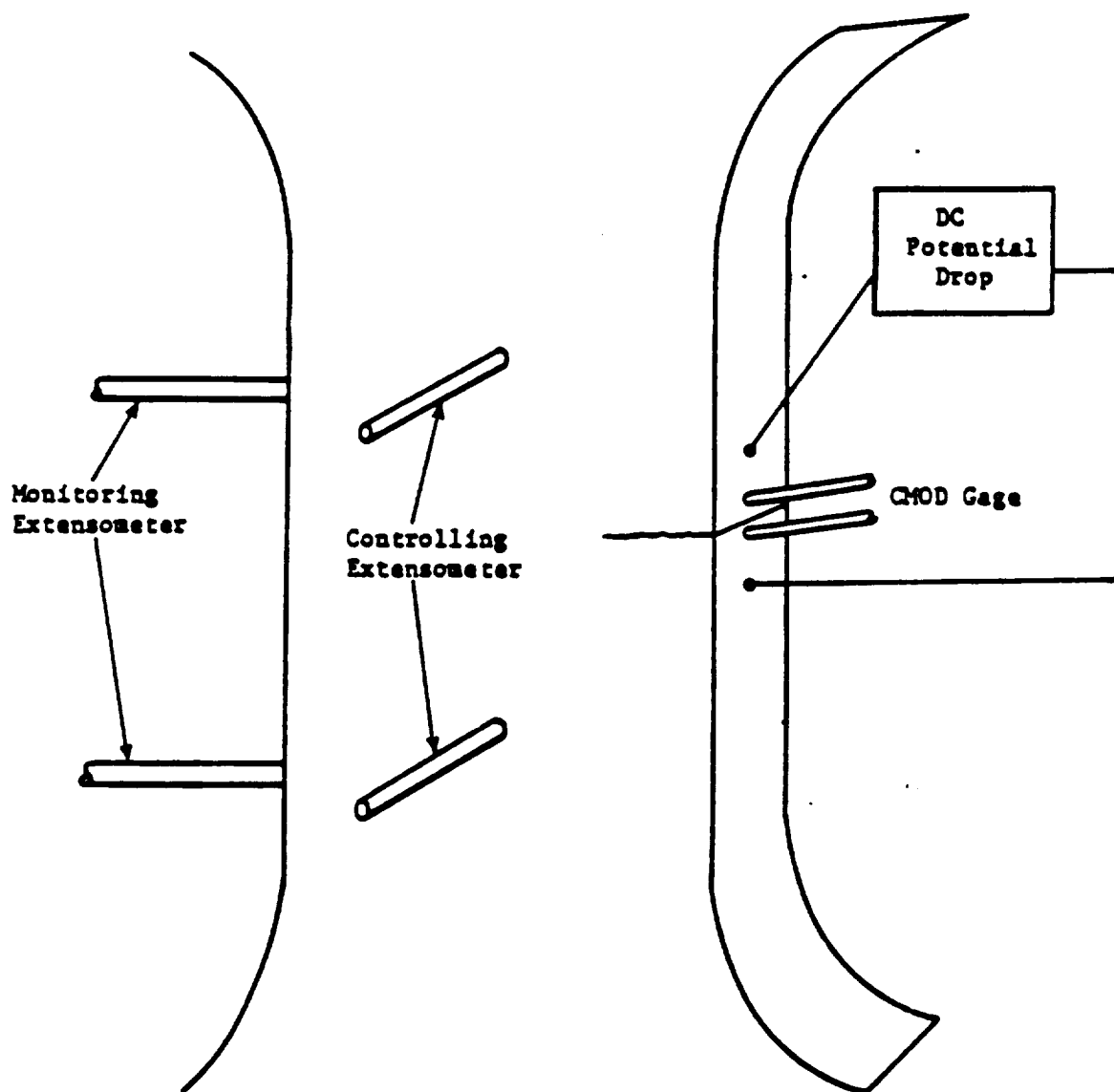


Figure 63: Schematic Drawing of Triple Extensometer Buttonhead SEN Test Method.

The higher strain range tests were performed without a precrack, but some of the lower temperature, low strain range crack propagation tests were precracked to have a initial crack length of approximately 0.5 mm (0.02 inch). The intent of these tests was to provide data to evaluate the P-I integrals at crack length to specimen width ratios (a/W) not exceeding 0.25. The crack propagation tests were stopped with a/W ratios between 0.50 and 0.75.

All SEN tests were performed in a strain (displacement) control mode in order to eliminate the problems associated with load controlled tests (ratcheting or excessive plasticity). The experimental setup shown schematically in Figure 63. The specimen displacement was controlled using an extensometer with a gage length of 12.7 mm (0.5 inch) mounted at the center of the 10.2 mm wide gage section. The small gage length CMOD gage was positioned across the mouth of the notch. A third extensometer was required to experimentally determine the linear displacement boundary conditions for the finite element analyses. It was positioned on the back face of the specimen (opposite the notch) so that it would not collide with the other extensometers. The controlling and back face extensometers had the same gage lengths and established the linear displacement gradient 6.35 mm (0.25 inch) above and below the plane of the crack.

5.4 Data Acquisition

The crack length was monitored using a direct current, on-off potential drop technique used extensively in linear elastic fracture mechanics characterization of materials with a pin-loaded SEN specimen⁽²⁷⁻²⁹⁾. The apparatus used was originally developed by Gangloff⁽³⁵⁾ and adapted to the SEN geometry by Wilcox and Henry⁽³⁶⁾. The potential probe spacing was increased from approximately 0.82 mm (0.032 inch) to 1.6 mm (0.064 inch) so that the potential probes did not interfere with the CMOD gage. The potential is averaged over a predescribed number of cycles and converted to crack length using the potential solution developed by Johnson⁽³⁷⁾ which considers the influence of potential probe spacing. A detailed description of the data analysis procedure is described elsewhere⁽³⁸⁾. This technique permitted the

tests to be performed without the requirement for visual monitoring of the crack length.

These tests were further automated using an ETS test control and data acquisition system to monitor load and displacements. This equipment was very similar to that used to measure the Alloy 718 constitutive properties except that it was modified to monitor five channels rather than just the two used during the isothermal constitutive tests. The five channels were used to monitor the three different types of displacements (control, back face, and CMOD) and the load on the specimen. The ETS was also configured so that it could provide the cycle pulse necessary to trigger the current switching used in the on-off direct current potential drop system. As in the Alloy 718 constitutive tests, the load-displacement hysteresis loops were recorded at preselected cycles. That data was stored off on floppy disks for subsequent data analysis.

5.5 Data Analysis

This section will describe and show examples of the types of data determined using the potential drop and data acquisition system. The interpretation of this data will be given in other sections. The data reductions procedures will be illustrated using data from 538°C (1000°F) Alloy 718 SEN crack growth tests with a mean strain of zero ($A_{\epsilon} = \infty$). These include a single tests with a strain range of 0.5 percent and duplicate tests with strain ranges of 1.15 and 1.7 percent. Figure 64 shows the crack lengths as measured with a DC potential drop technique plotted as a function of the number of cycles. These data show the excellent reproducibility of the test method. The cracks for the highest strain range grew extremely rapidly. The number of cycles used to propagate the cracks from a 0.25 mm (0.01 inch) deep EDM slot to over 7.6 mm (0.3 inch) in length required 95 and 100 cycles for the two 1.7 percent strain range tests.

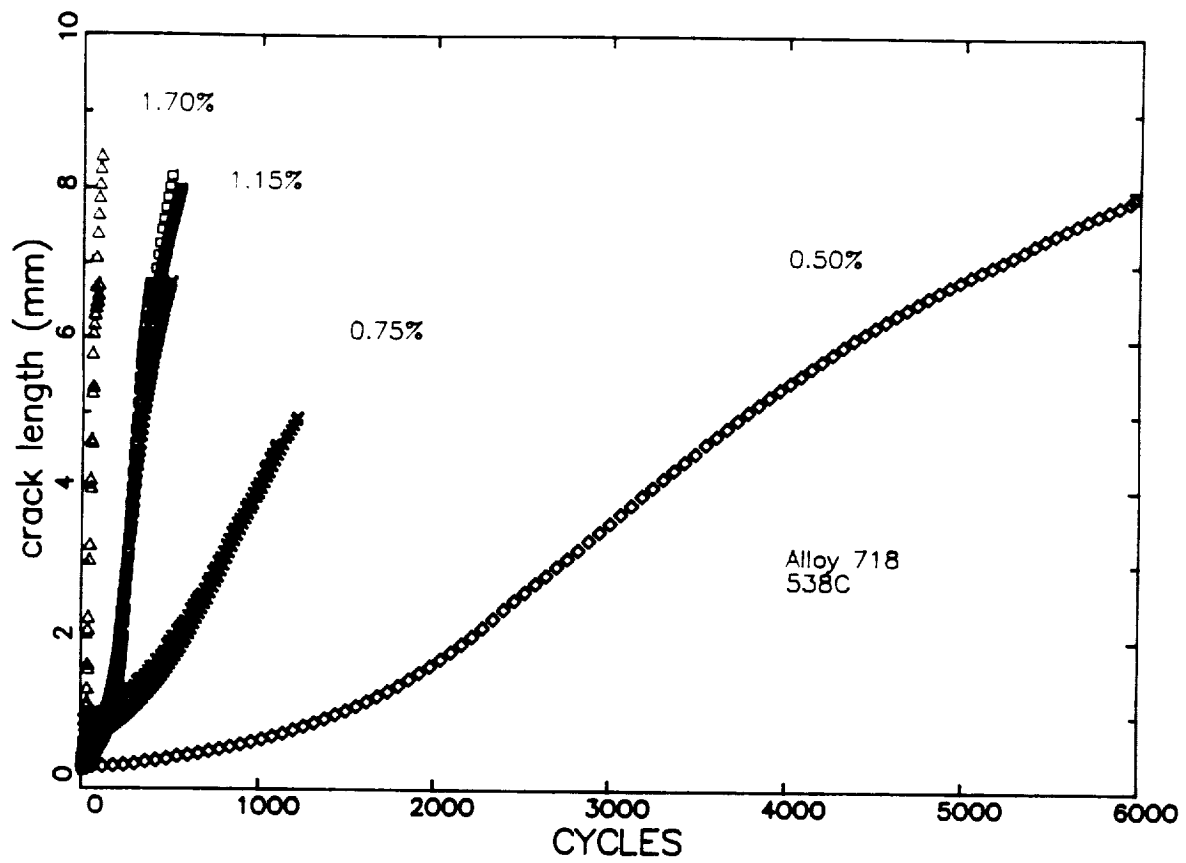


Figure 64: Variation of Crack Length with Cycles in Displacement Controlled SEN Tests Performed at 538°C (1000°F).

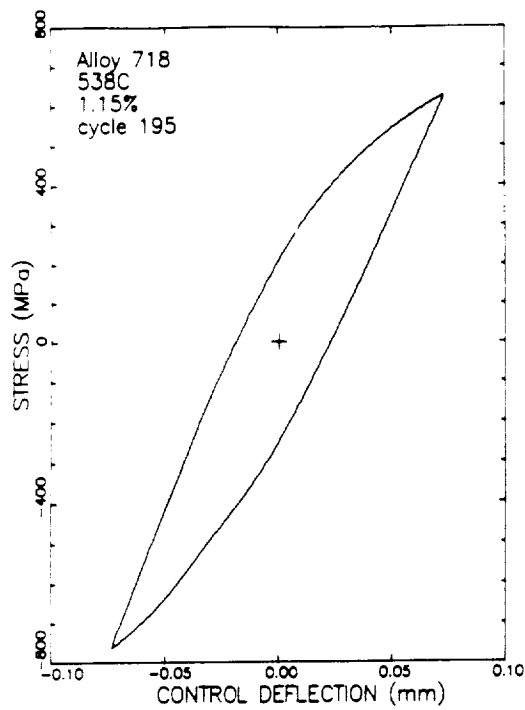
The crack growth rates were analyzed using linear elastic fracture mechanics. The crack growth rates were calculated using a seven point sliding polynomial technique⁽³⁹⁾. The value of K was calculated using the solution developed by Harris⁽⁴⁰⁾ for restrained bending in a single edge notch specimen.

$$K = \sigma_{avg} \sqrt{\pi a \{5/\sqrt{(20-13(a/W)-7(a/W)^2)}\}} \quad (5.1)$$

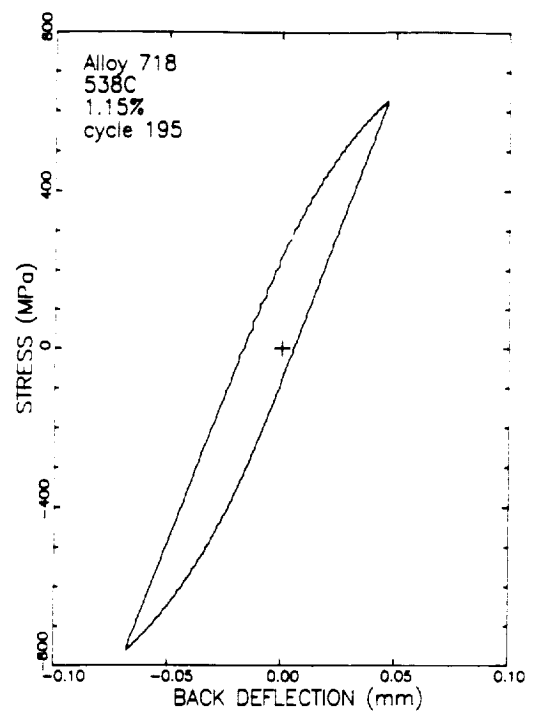
The validity of this relationship was verified by Malik and Gilbert⁽⁴¹⁾ who calculated K-values using both influence functions and J-integrals from the elastic 2D full specimen finite element analysis of the buttonhead SEN specimen. They found that their results were very close to those calculated using the equation developed by Harris.

The analysis of the load-displacement data will be illustrated using the results from specimen N4-3, a buttonhead single edge notch (SEN) specimen tested at 538°C (1000°F) with a strain range of 1.15% and A_c of ∞ . The crack length measurements of this test were included in Figure 64.

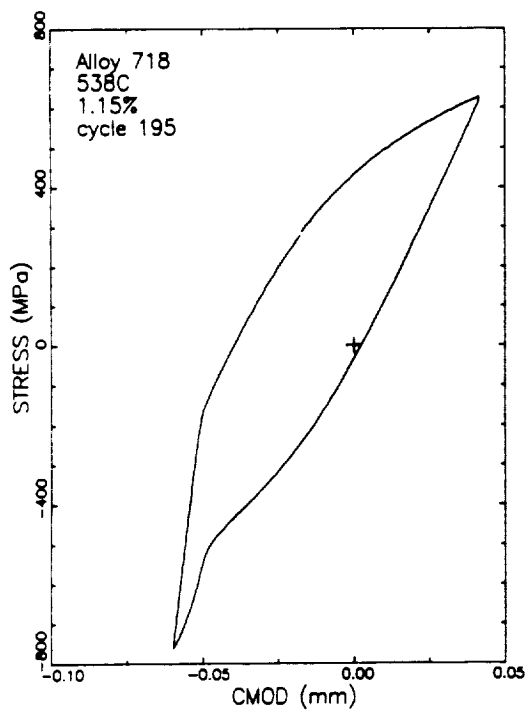
Figure 65 shows the hystereses loops from the control, crack mouth, and back face extensometers from cycle 195. The crack mouth opening displacement (CMOD) data clearly shows the cusping in the hysteresis loop indicating the presence of crack closure. This test program is one of the first to simultaneously use different displacement measurements to detect closure. These loops illustrate that the ability to detect closure is highly dependent on the location and gage length of the displacement gage. Of the greatest significance is the apparent absence of cusping in the back face displacements. This occurs because this SEN specimen geometry is primarily a tension specimen relative to geometries like the compact specimen. This may also suggest that back face deflection is not a very sensitive technique to detect crack closure for this specimen geometry. Additional work with a smaller gage length back face extensometer is necessary to investigate this possibility.



(a)



(b)



(c)

Figure 65:

Stress-Displacement Hysteresis Loops of (a) Controlling Extensometer, (b) Back Face Extensometer, and (c) CMOD gage from Cycle 195 of Specimen N4-3.

The occurrence of crack closure was detected from a change in the slope of the load-CMOD curve at the point where the crack opens or closes. In nominally elastic tests, the loading and unloading curves are virtually identical and crack closure is often detected by subtracting an apparent elastic slope from the measured displacements. Closure is determined to occur when that difference exceeds a given value. The use of this technique becomes more difficult for hysteresis loops like that shown in Figure 65 where there is not a distinct linear region due extensive plasticity. The technique used in this study to determine closure was to search for a change in slope rather than some offset value from nominally elastic behavior. The change in slope corresponds to a discontinuity in the second derivative of load and CMOD. A seven point sliding polynomial technique(16,39) was used to calculate the second derivative of load with respect to CMOD for both increasing and decreasing load portions of each available load-CMOD hysteresis loop. The points of the crack closure (decreasing load) and crack opening (increasing load) were determined to occur when the absolute value of the second derivative reached a maximum value. This technique accurately determined the closure/opening points in the available load-CMOD loops with readily apparent cusps. By knowing these locations, the values of the specimen displacements at the controlling and back face extensometer locations when crack opening and closure occurred were also known.

Figure 66 show the variation on maximum load (+), minimum load (x), closure load (square), and opening load (triangle) with cycle number for specimen N4-3. At the beginning of the test the CMOD loop does not show much cusping and it is difficult to reliably detect the presence of closure as indicated by the large amount of scatter in the opening and closure loads. As the crack grows, the cusping increases and the detection of closure becomes much more reproducible. Figures 67 through 69 show the variation in the control, crack mouth, and back face deflections at maximum load, minimum load, crack closure, and crack opening as a function of cycle number in the same test. These figures show that the specimen displacements are almost identical at the crack opening and closing events.

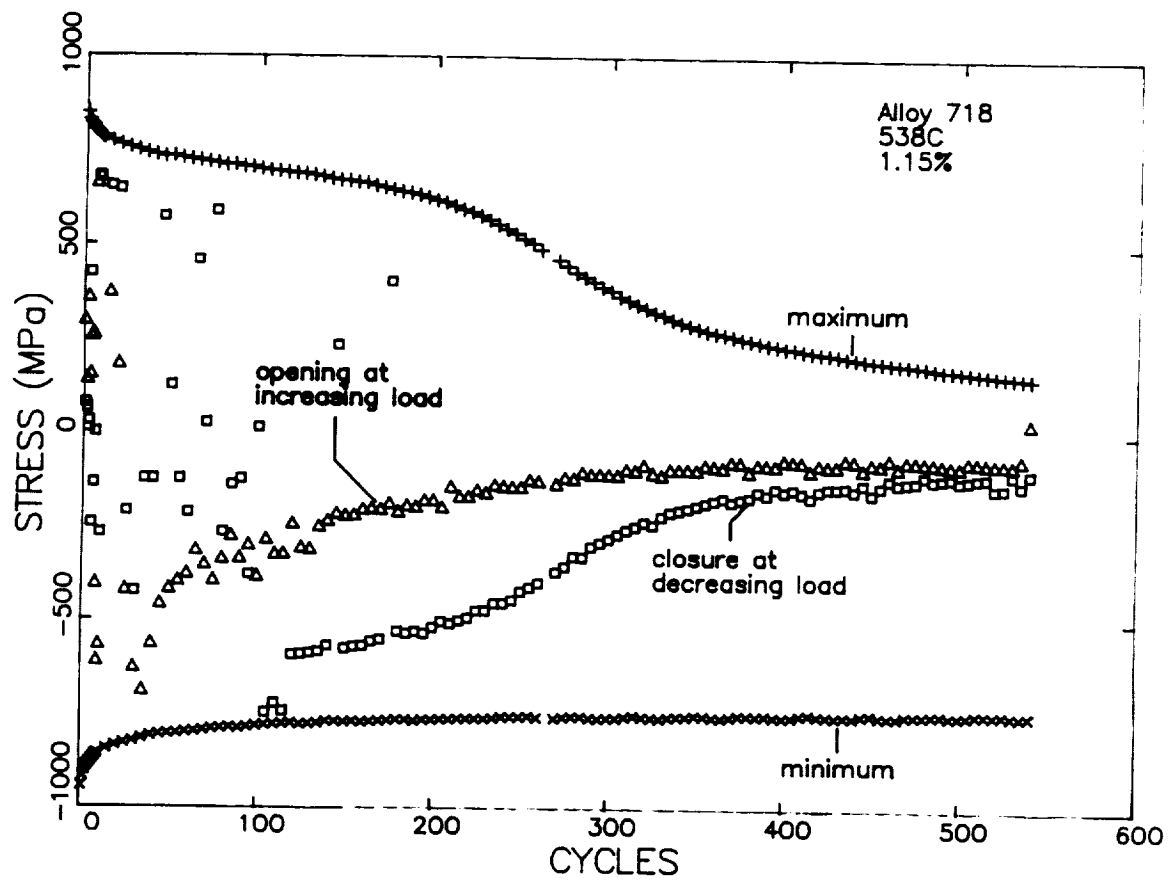


Figure 66: Variation of Maximum, Minimum, Crack Closure, and Crack Opening Stress With Cycles For Specimen N4-3.

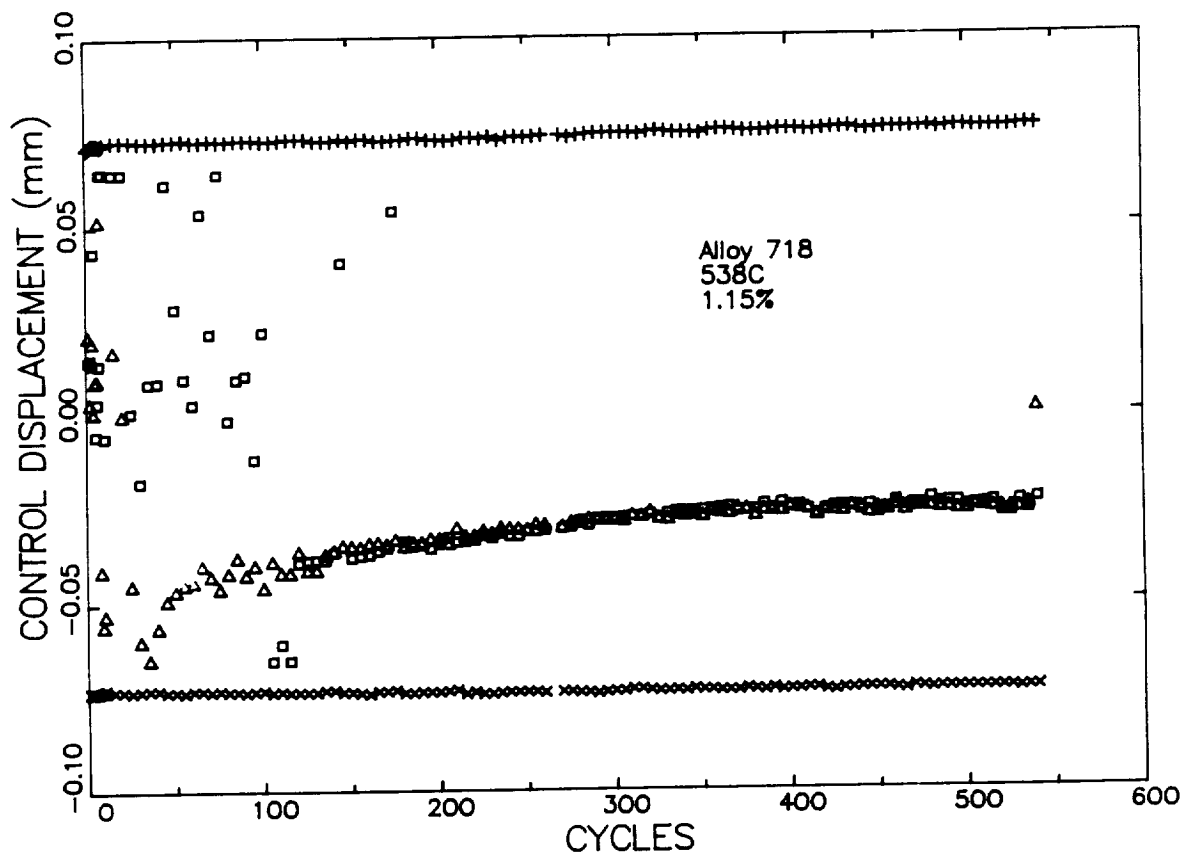


Figure 67: Variation of Maximum, Minimum, Crack Closure, and Crack Opening Control Displacement With Cycles For Specimen N4-3.

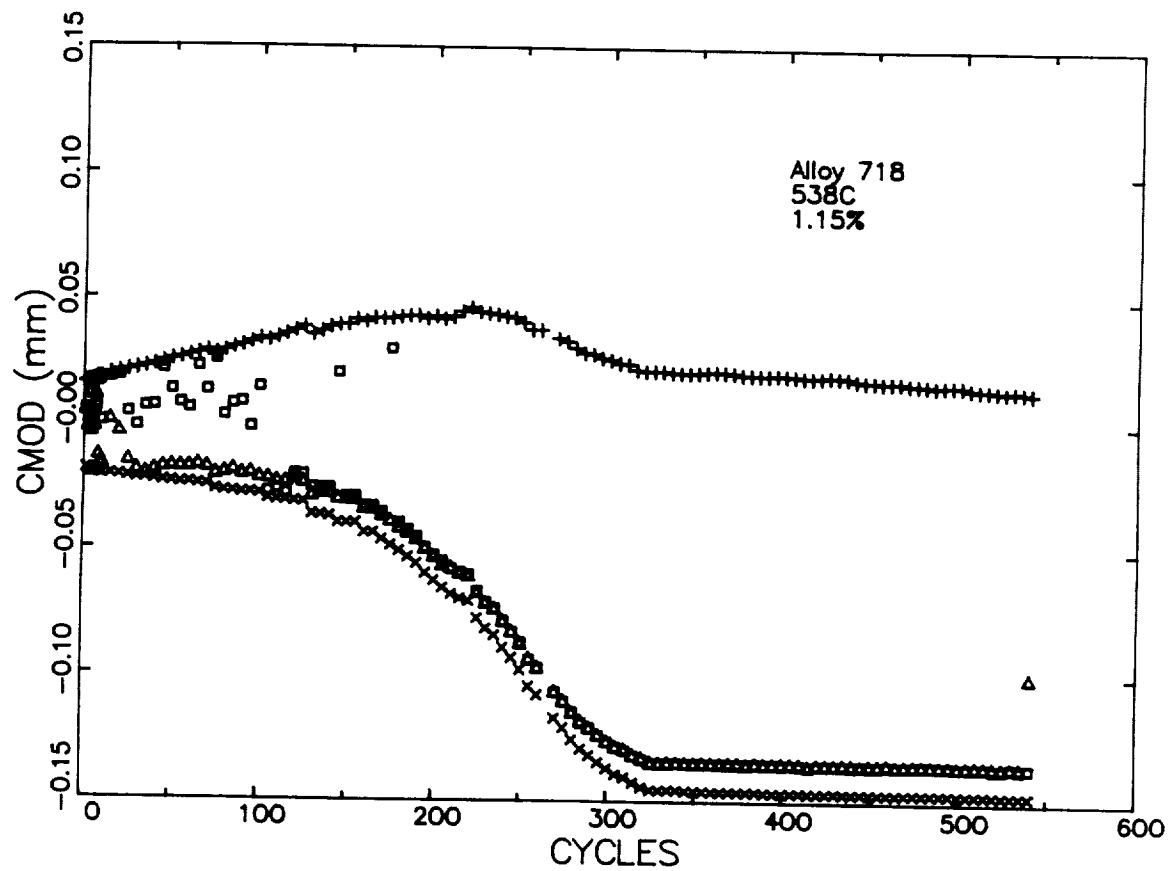


Figure 68: Variation of Maximum, Minimum, Crack Closure, and Crack Opening Values of Crack Mouth Opening Displacement (CMOD) With Cycles For Specimen N4-3.

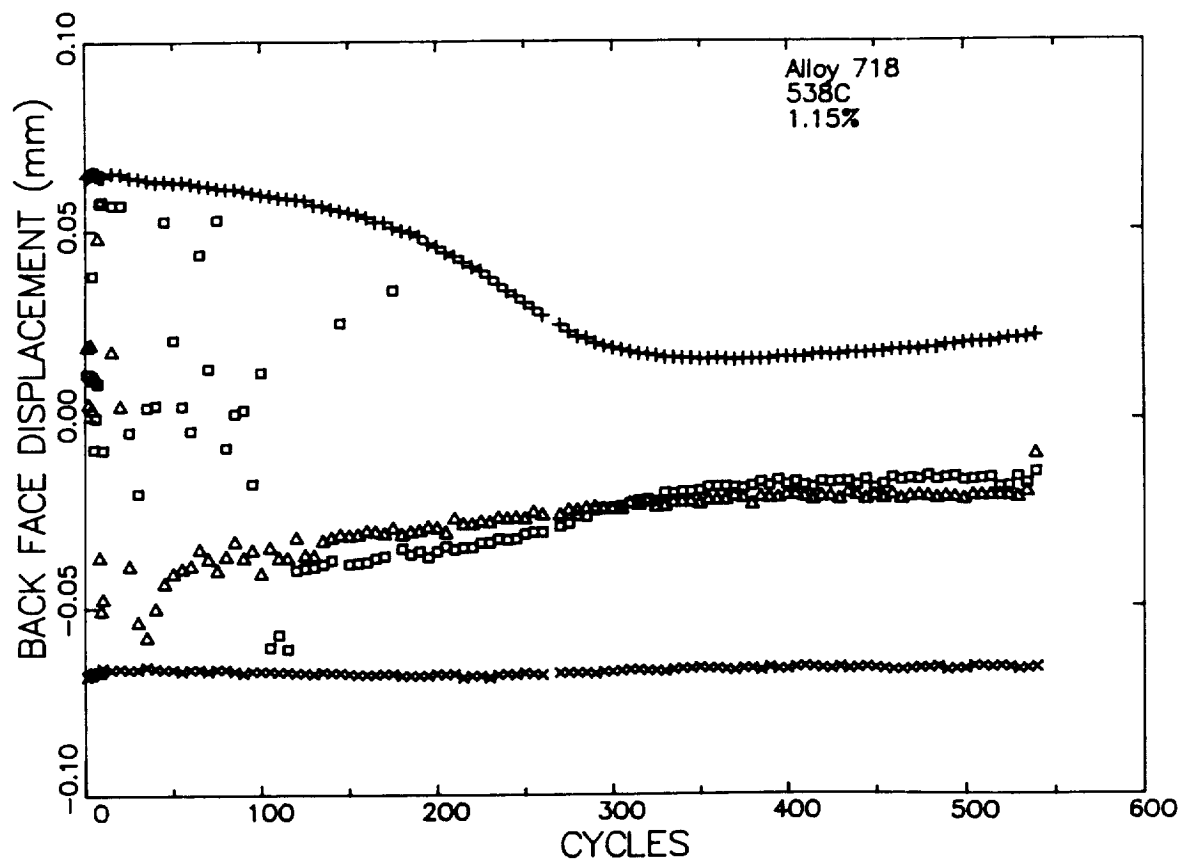


Figure 69: Variation of Maximum, Minimum, Crack Closure, and Crack Opening Back Face Displacement With Cycles For Specimen N4-3.

5.6 Thermal Gradient SEN Technique

The thermal gradient tests were performed identically to the isothermal tests just described except that the temperature was varied across the width of the specimen. A technique to introduce a thermal gradient was developed using a combination of induction heating and forced air cooling. The potential sensitivity of the CMOD extensometer to vibration due to its small gage length prevented the use of cooling air on the crack mouth side of the specimen, so the crack was grown from the high temperature to the low temperature. The specimen was heated by an induction coil which was offset toward the crack mouth side of the specimen. Cooling air was also introduced between the extensometer arms of the back face extensometer. This gradient technique was developed on a specimen which was monitored with fifteen thermocouples. Three sets of five thermocouples were attached to the specimen along the crack plane and at planes 6.4 mm (0.25 inch) above and below the crack plane. The two latter locations correspond to the positions where the arms of the two large gage length extensometers contact the specimen. On all three planes, a thermocouple was located at each edge of the 10.2 mm (0.4 inch) wide specimen and at intervals of 2.54 mm (0.1 inch). The presence of the thermocouples prevented the attachment of the three extensometers, so the temperatures were monitored along the plane of the crack in another specimen using an optical pyrometer attached to a travelling microscope. The results of the temperature measurements are shown in the Figure 70. The line connecting the "X" symbols represent the optical pyrometry measurements. These results show a small amount of temperature difference from specimen-to-specimen and along the gage length. This variation is within an acceptable range.

This technique was used to perform both monotonic and cyclic temperature gradient tests.

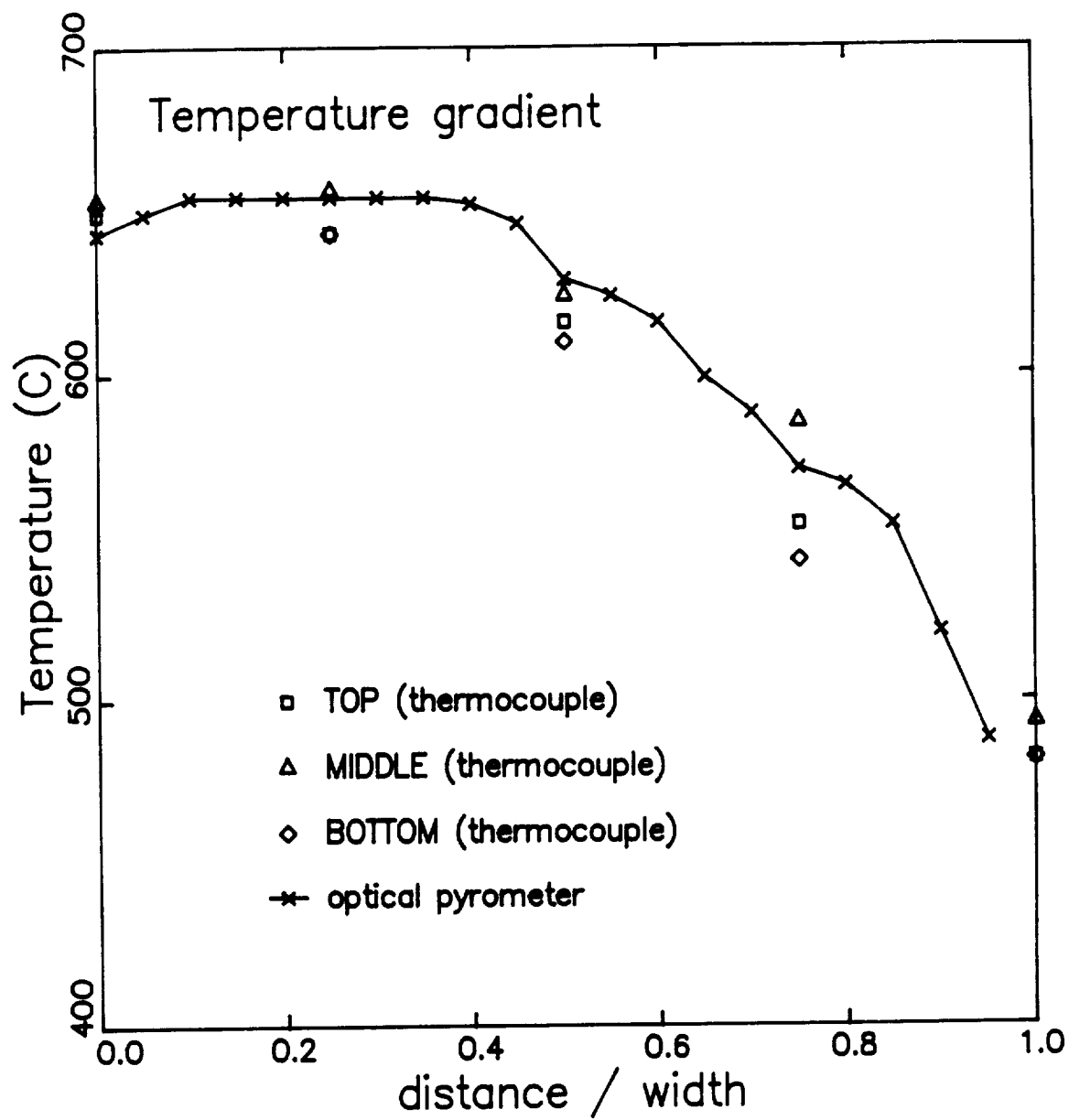


Figure 70: Temperature Profile Developed in the Thermal Gradient Experiments.

5.7 Thermal Mechanical Fatigue (TMF) Technique

The TMF crack propagation tests were performed using a computer-controlled TMF test facility at the General Electric EMTL Testing Laboratory. The test were controlled by a PDP-1123 computer which provided the command signal for the test machine, the pulse signal necessary to run the potential drop system, and the information necessary to use the data acquisition capabilities of the ETS system. The first step in the testing procedure was to program the desired thermal cycle into the memory of the PDP-1123 computer, which permits 300 control steps during a cycle with a constant time increment between each control point. For these 0.01 Hz tests, there would be a control point each 0.33 second. The specimen was then thermally cycled at zero load until a stabilized strain-temperature hysteresis loop is obtained. The 300 thermal strain values from the stabilized loop are automatically stored in the PDP-1123 memory. The desired mechanical strain profile is then programmed into the memory. The mechanical strain at each of the 300 control points is then calculated and added to the thermal strain to obtain the total strain at each control point. The 300 total strain values are used as the command signal for the testing machine. The temperature signal is used to control the RF generator.

While running either the thermal cycle only (at zero load) or the thermal-mechanical test, the ETS data acquisitions system monitored the load and the displacements on each of the three extensometers. The difference between the two types of displacement data were used to calculate the mechanical displacements. The software used to analyze the data from the TMF tests is identical to that used for the isothermal tests except that the analysis can be done for either total or mechanical displacements.

Examples of a typical thermal displacement cycle will be shown for specimen N5-45, a SEN specimen cycle from 427 to 649°C (800 to 1200°F). A total of nine (9) thermal cycles were monitored prior to the start of the TMF test. Figure 71 shows the thermal strains measured with the control extensometer. The small dots indicate individual measurements and the solid

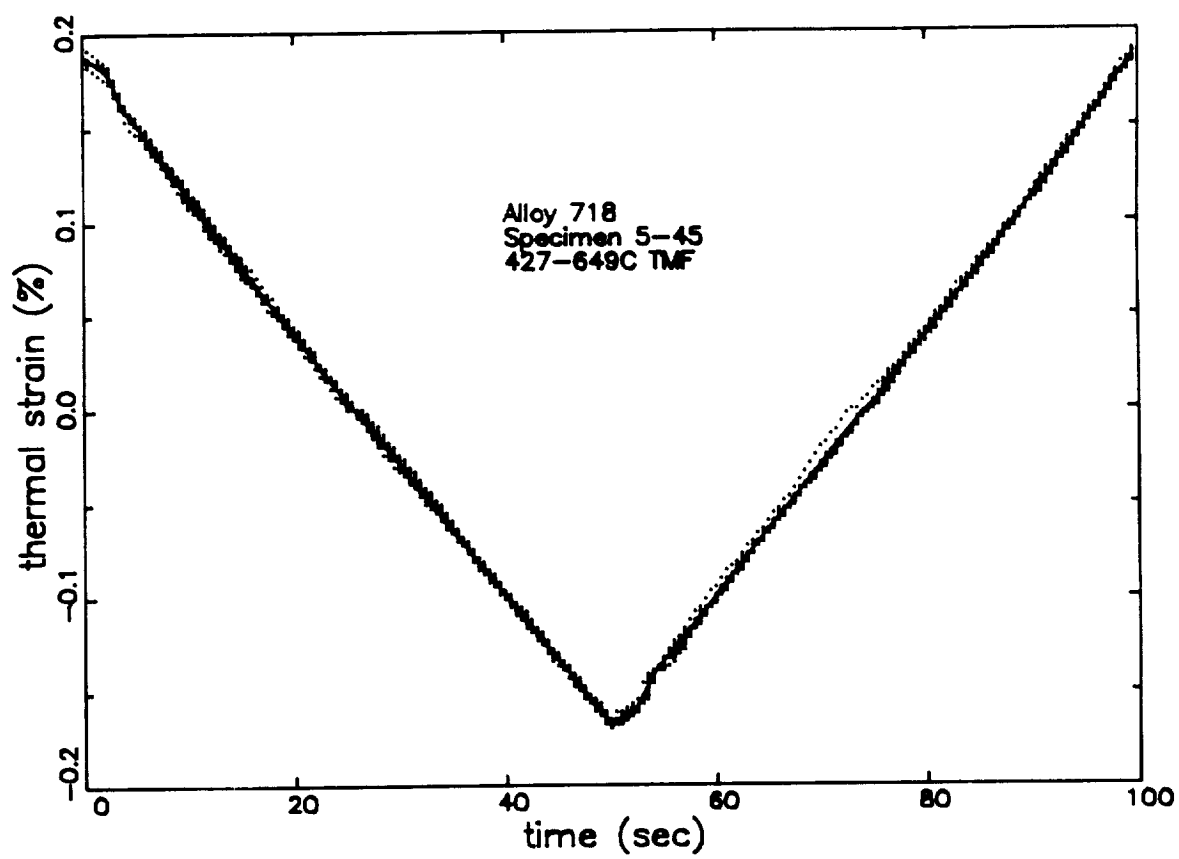


Figure 71: Variation of Thermal Strain during 427 to 649°C (800 to 1200°F) Thermal Cycling of a Buttonhead SEN Specimen.

line connects the locus of the average of nine thermal strain measurements. These data show that this thermal strain is very reproducible. A similar operation was performed for both the back face and crack mouth displacements. The average strains from the control and back face extensometers are shown as a function of temperature in Figure 72. Although there is a slight difference in strain, the slopes of these data are very similar. A linear regression was performed through these data to determine the thermal expansion coefficient which will be used in the finite element analysis of these specimens. The software permits calculation of either total strain or mechanical displacements. The mechanical displacements were calculated by subtracting the average thermal displacement of a given extensometer from the total displacement measured by the same extensometer.

TMF tests were conducted over two temperature ranges: 427 to 649°C (800 to 1200°F) and 538 to 649°C (1000 to 1200°F). The variation of temperature and mechanical strain with time had a triangular wave shape. The thermal-mechanical cycling was performed with both in-phase (maximum strain at maximum temperature) and out-of-phase (maximum strain at minimum temperature) cycling.

5.8 Modified Compact Specimen

The alternate crack growth specimen was a modified compact specimen. Figure 73 shows the drawing of this specimen. This specimen was designed based on a compact-type keyhole notched specimen used in an SAE testing program⁽⁴²⁾. This specimen is bolt-loaded while the more conventional ASTM-recommended compact specimen is pin-loaded. The use of bolt loading permits the use of compressive loads without discontinuities in displacements at near zero loads. The specimen is bolted in clevises which attach to a buttonhead grip by means of a Morse bearing. This provides a rotation point outside the plan of the specimen.

The testing technique for the compact specimen was very similar to that previously described for the buttonhead SEN specimens. The compact specimen

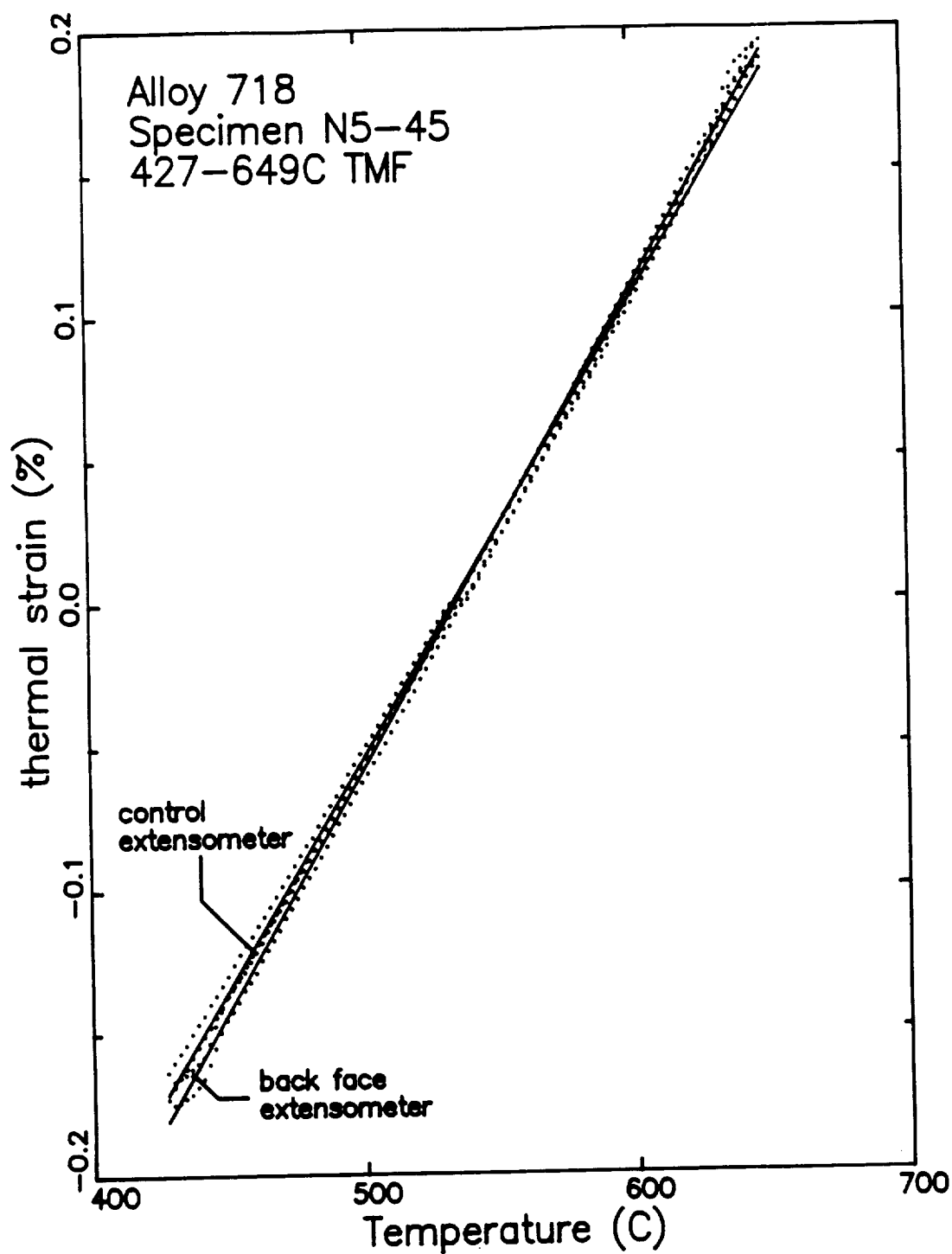
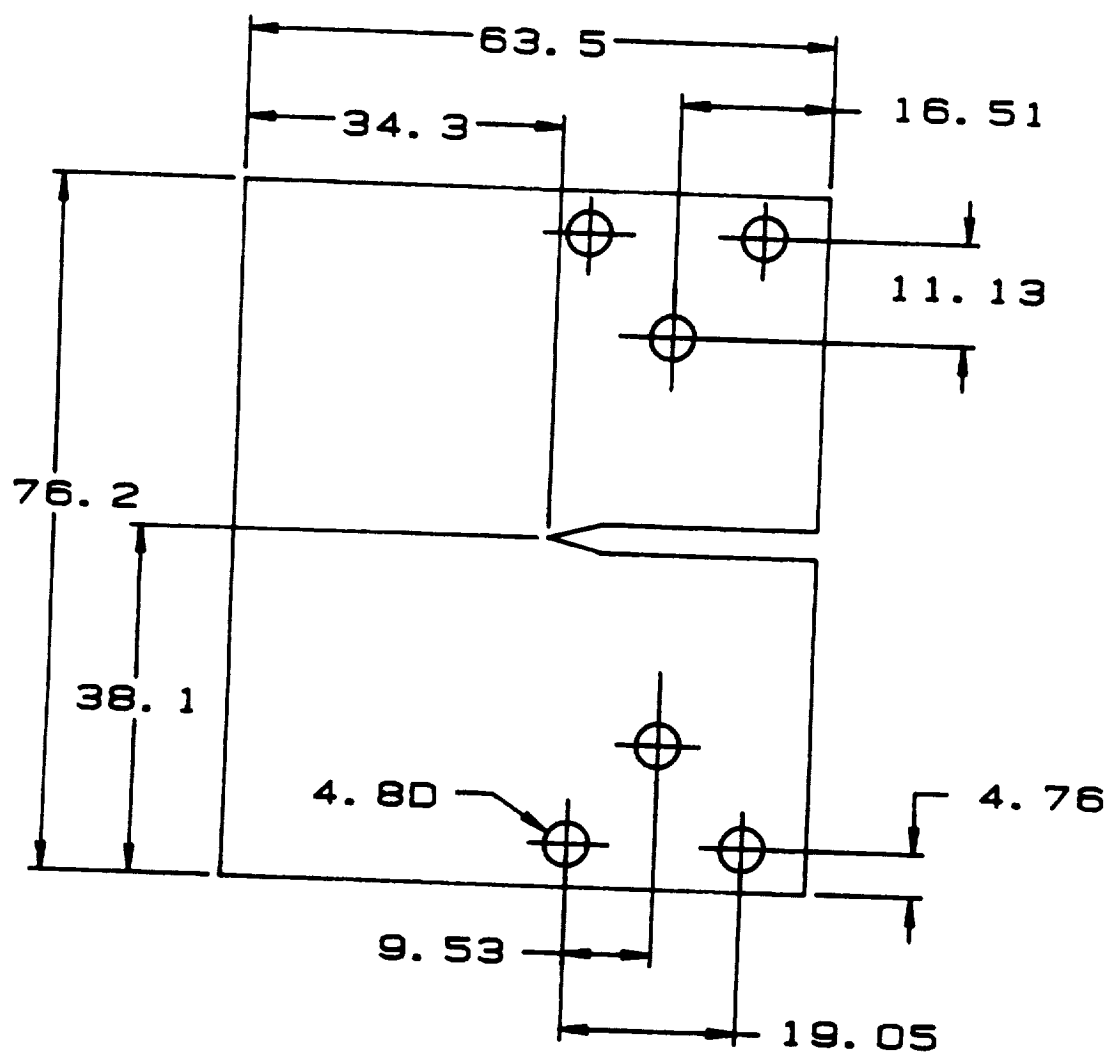


Figure 72: Comparison of the Thermal Strains Measured With the Controlling and Back Face Extensometers during 427 to 649°C (800 to 1200°F) Thermal Cycling of a Buttonhead SEN Specimen.



Dimensions are millimeters.

Figure 73: Drawing of Modified Compact Specimen.

was tested in displacement control with the control extensometer contacting the specimen on the plane of the center loading bolt. The back face and CMOD displacements were also measured. The gage length of the control and back face extensometers was 12.7 mm (0.5 inch) while the CMOD extensometer had a gage length of 8.89 mm (0.35 inch). The displacement and load data were monitored using the ETS data acquisition system. Crack lengths were monitored using the same potential drop system used for the buttonhead SEN specimens.

The crack growth data were calculated using a seven point sliding polynomial technique. The plan size (H/W) of the compact specimen shown in Figure 73 is 0.47 which is different from the 0.4 plan size used in the ASTM-recommended specimen. The modified compact geometry and test technique results in some deviations from the ASTM recommended K-solution. One is caused by the movement of the rotation point and the other is caused by the change in plan size. Both of these factors were addressed in a boundary collocation analysis reported by Srawley and Gross⁽⁴³⁾. They considered various plan sizes as well as different ways to distribute the loads near the loading holes. The following discussion will restrict itself to the two plan sizes modeled by Srawley and Gross⁽⁴³⁾ which bracket the plan size of the modified compact specimen (H/W = 0.4 and 0.5). The influence of load distribution on the K solution diminished with increasing crack length. This effect was less than 0.4 percent for crack length to width (a/W) ratios of 0.3 or greater. Therefore, only a/W ratios in excess of 0.3 (a = 14.1 mm or 0.56 inch) were used in this investigation.

Srawley and Gross proposed a K-solution of the form

$$K = P/B \frac{(2W + a)}{(W - a)^{3/2}} f(a/W) \quad (5.2)$$

where they listed the values of $f(a/W)$ for values of a/W in increments of 0.1. The values of $f(a/W)$ for intermediate plan sizes (H/W) were determined by linear interpolation. This approach was verified by comparing the results of the interpolated K-solution with that reported^(44,45) for the Manjoine test

specimen^(46,47). This should provide an excellent comparison because the plan size of the Manjoine specimen ($H/W = 0.466$) is close to that of the modified compact specimen and because the Manjoine specimen does not have free rotation like the pin-loaded geometry. For a/W ratios from 0.3 to 0.8, the interpolated and Wilson^(44,45) K-solutions agree within 5 percent. If the comparison is made for a/W ratios between 0.3 and 0.7, the agreement is within 1.5 percent. This excellent agreement suggests that the linear interpolation scheme can be used to accurately represent the influence of plan size on the K-solution.

Several type of regression analyses were performed on the interpolated values of $f(a/W)$ for the plan size of the modified compact specimen. The following expression

$$f(a/W) = 1.187 (a/W) - 0.3758 \quad (5.3)$$

had a correlation coefficient in excess of 0.99 and predicted the interpolated values of $f(a/w)$ within 2 percent for a/W ratios from 0.3 to 0.8. The K solution used to analyze the modified compact data was that described by Srawley and Gross (Equation 5.2) using Equation 5.3 to represent $f(a/W)$.

6.0 EXPERIMENTAL RESULTS OF ISOTHERMAL SEN CRACK PROPAGATION TESTS

This section of the report will describe the results of the isothermal crack growth rate tests performed during this investigation. The testing apparatus and data reduction procedures were described in Section 5.0. In summary, buttonhead single edge notch (SEN) specimens were tested in strain (displacement) control. The displacement was controlled in the center of the gage section and the displacements were monitored at the back face and across the crack mouth (CMOD). The crack length was monitored using a DC potential drop technique and the load and displacements were recorded using an automated data acquisition system.

6.1 Test Matrix

Table 13 lists the planned test matrix for the isothermal crack propagation tests. Duplicate tests were planned for each condition listed in Table 13. The strain ranges selected for the crack propagation tests are 0.50, 1.15, and 1.70%. The higher two ranges were used to determine the cyclic constitutive properties. As shown previously (Figure 30), they will result in plastic strain ranges of approximately 0.2% and 0.7% at 538°C (1000°F). The 0.5% strain range resulted in nominally elastic cycling. Most of the crack growth tests were cycled with zero mean strain ($A_{\epsilon} = \infty$). With this A_{ϵ} ratio, tests were performed at 427, 538, 593, and 649°C (800, 1000, 1100, and 1200°F) at all three strain ranges. The influence of mean strain was evaluated at all four temperatures using A_{ϵ} ratios of 1.0 and -2.0. A_{ϵ} ratios of 1.0 and -2.0 correspond to zero and negative mean strains or displacements, respectively. The strain range for the $A_{\epsilon}=1.0$ tests was 1.15%, the same at the intermediate value for the $A_{\epsilon}=\infty$ baseline tests, but the strain range for the $A_{\epsilon}=-2.0$ tests was reduced to prevent buckling of the specimens. The strain ranges listed in Table 13 were modified as the test program proceeded to eliminate buckling and to avoid excessively long tests.

TABLE 13: Isothermal SEN Crack Propagation Test Matrix

Temperature (°C)	Temperature (°F)	Strain Range(s)	A_{ϵ}
427	800	0.0050, 0.0115, 0.0170	∞
538	1000	0.0050, 0.0115, 0.0170	∞
593	1100	0.0050, 0.0115, 0.0170	∞
649	1200	0.0050, 0.0115, 0.0170	∞
427	800	0.0115	1.0
538	1000	0.0115	1.0
593	1100	0.0115	1.0
649	1200	0.0115	1.0
427	800	0.0093	-2.0
538	1000	0.0093	-2.0
593	1100	0.0093	-2.0
649	1200	0.0093	-2.0

6.2 Crack Morphology

Table 14 summarizes the isothermal crack propagation tests which were successfully performed. Also listed in the table are specimens which experience buckling during the initial loading or after a few cycles. The isothermal tests were performed at two different times. The first campaign were the first tests performed. The second campaign was performed after completion of the thermal gradient and TMF crack propagation tests. In the first campaign the CMOD gage was suspended and was susceptible to movement. During the second campaign the gage attachment was adjusted to eliminate lateral movement of the CMOD gage.

The last column in Table 14 lists the crack morphology. A flat morphology refers to cracks which propagate normal to the loading axis of the specimen with no indication of out of plane cracking. Specimens which buckled failed within the first few loading cycles. A shear crack morphology refers to a specimen where the crack initially grows normal to the loading axis, then starts forming shear lips at the edge of the specimen, and gradually the fracture surface is inclined across the thickness of the specimen. Examination of Table 14 shows that occurrence of shear failures increased with increasing strain range and decreasing temperature. It is interesting to note the close correlation between the occurrence of shear crack growth and the conditions which cause serrated yielding in the constitutive property tests.

The variation of the CMOD with cycles of specimen N4-3 previously presented in Figure 68 showed a transition in CMOD which becomes highly negative. This specimen was also one of those which experienced shear crack growth. Examination of several of the first campaign tests showed that specimens which grew in shear also had the transition or shift in the CMOD data. The CMOD transition was not observed for the tests which did not experience shear crack growth as shown in Figures 74 through 76. Figures 74 and 75 show the variation of CMOD at maximum displacement, minimum displacement, crack opening, and crack closing for tests with A_{ϵ} of ∞ and a

Table 14: Summary of Isothermal SEN Crack Propagation Tests

Specimen Number	Temperature (°C)	A_{ϵ}	Strain Range(%)	Campaign	Crack Morphology
N4-1	427	∞	0.50	1	flat
N5-7	427	∞	0.75	2	shear
N5-44	427	∞	0.75	2	shear
N4-19	427	∞	1.15	1	shear
N5-26	427	∞	1.15	1	shear
N4-37	427	∞	1.70	1	shear
N4-45	427	∞	1.70	2	buckled
N4-11	427	1.0	1.15	2	shear
N5-34	427	1.0	1.15	2	shear
N4-28	427	-2.0	0.93	2	shear
N4-31	538	∞	0.50	1	flat
N5-8	538	∞	0.75	2	flat
N5-14	538	∞	0.75	2	flat
N4-3	538	∞	1.15	1	shear
N4-44	538	∞	1.15	2	shear
N5-6	538	∞	1.15	2	shear
N5-42	538	∞	1.15	1	shear
N4-12	538	∞	1.70	1	shear
N5-33	538	∞	1.70	1	shear
N4-22	538	1.0	1.15	2	shear
N4-20	538	-2.0	0.93	2	buckled
N4-40	538	-2.0	0.93	2	flat
N5-17	538	-2.0	0.93	2	shear
N4-23	593	∞	0.50	1	flat
N5-22	593	∞	0.50	1	flat
N4-42	593	∞	1.15	1	flat
N5-4	593	∞	1.15	1	flat
N4-14	593	∞	1.70	1	shear
N5-31	593	∞	1.70	1	shear
N4-33	593	1.0	1.15	2	shear
N5-12	593	1.0	1.15	2	shear
N4-6	593	-2.0	0.93	2	flat
N5-39	539	-2.0	0.93	2	flat
N4-8	649	∞	0.50	1	flat
N4-9	649	∞	0.75	2	flat
N4-26	649	∞	1.15	1	flat
N5-19	649	∞	1.15	1	flat
N4-15	649	∞	0.0150	1	flat
N4-10	649	∞	1.70	1	buckled
N5-11	649	∞	1.70	1	buckled
N5-23	649	1.0	1.15	2	flat
N4-17	649	-2.0	0.93	2	flat
N5-28	649	-2.0	0.93	2	flat

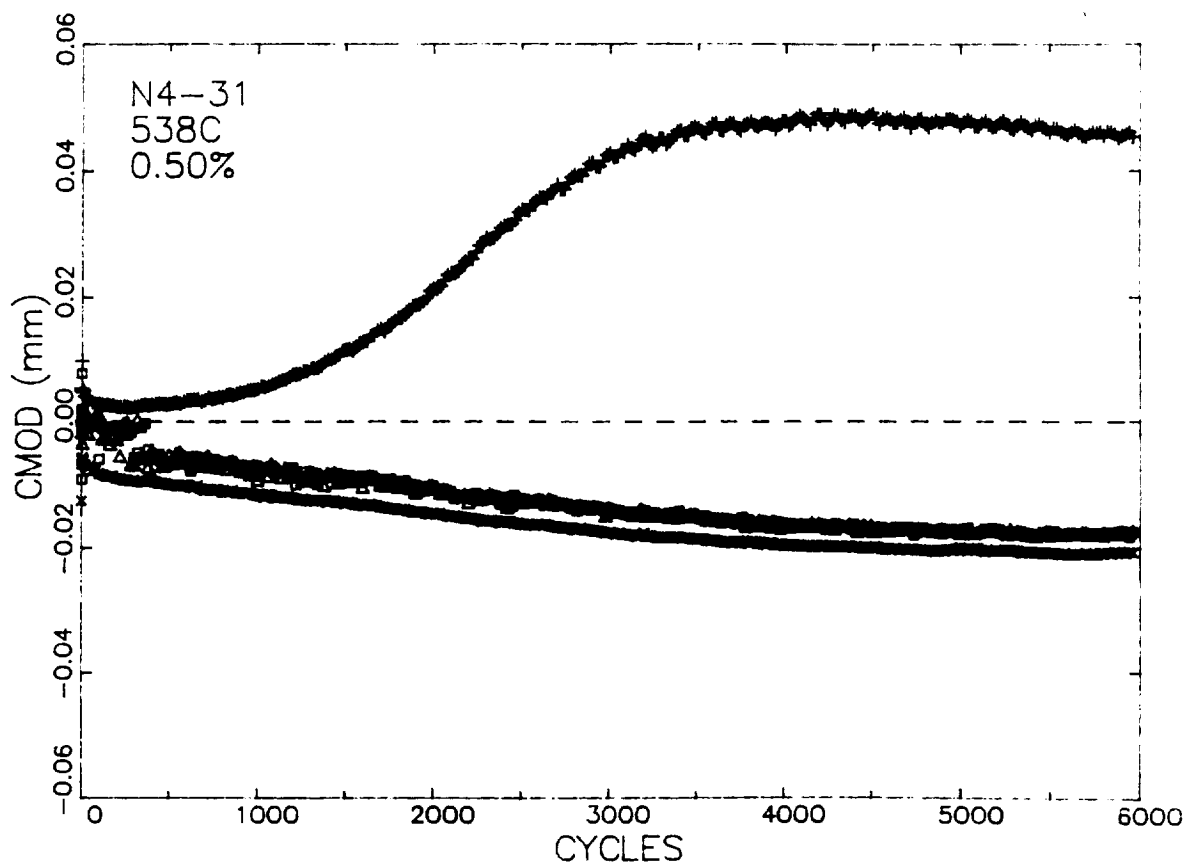


Figure 74: Variation of Maximum, Minimum, Crack Closure, and Crack Opening Values of Crack Mouth Opening Displacement (CMOD) with Cycles for Specimen N4-31 Tested at 538°C (1000°F) with 0.50% Strain Range and A_e of ∞ .

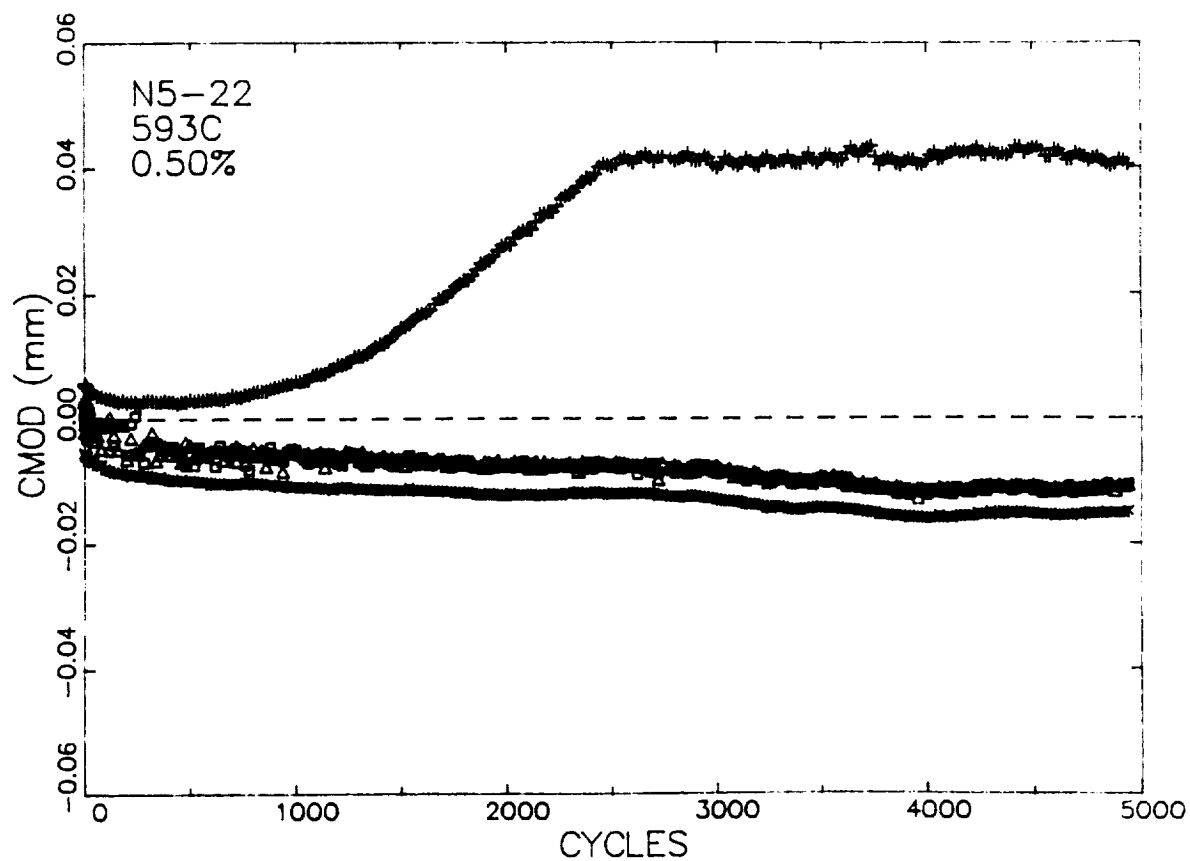


Figure 75: Variation of Maximum, Minimum, Crack Closure, and Crack Opening Values of Crack Mouth Opening Displacement (CMOD) with Cycles for Specimen N5-22 Tested at 593°C (1100°F) with 0.50% Strain Range and A_{ϵ} of ∞ .

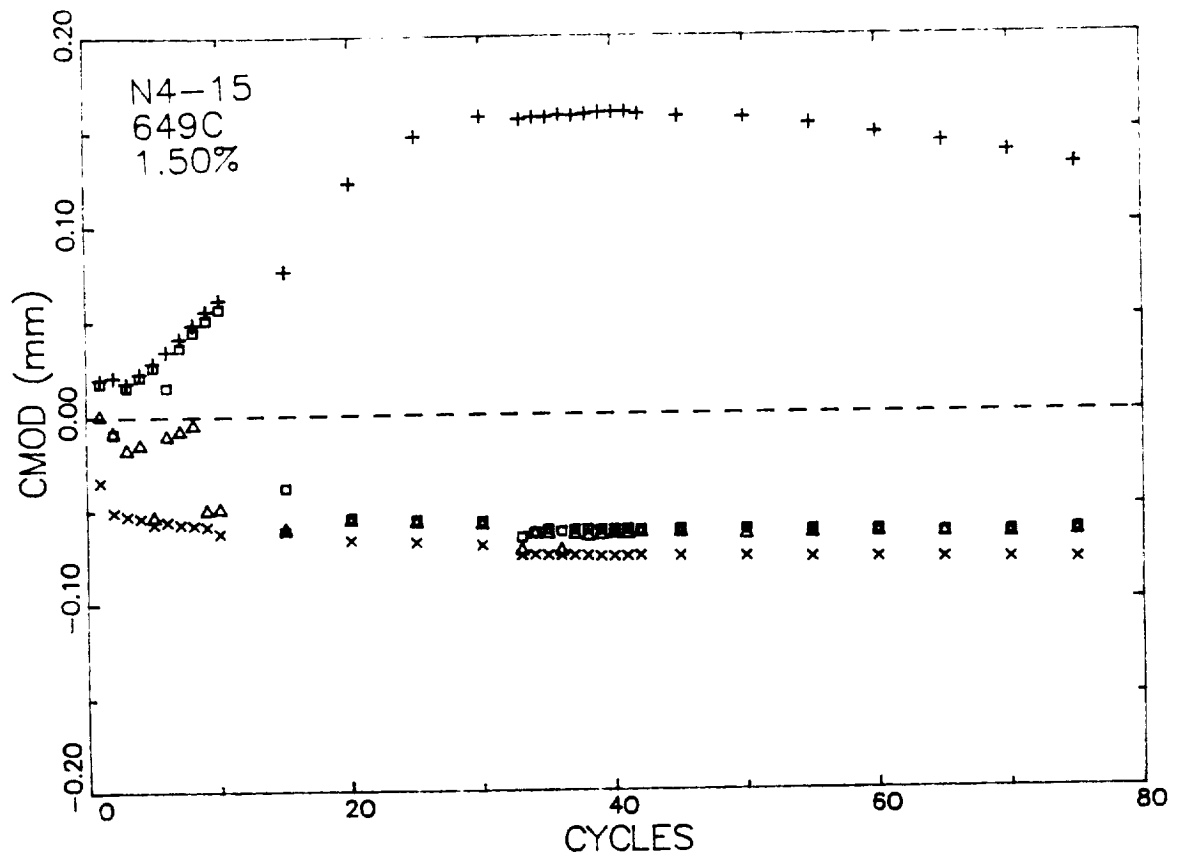


Figure 76: Variation of Maximum, Minimum, Crack Closure, and Crack Opening Values of Crack Mouth Opening Displacement (CMOD) with Cycles for Specimen N4-15 Tested at 649°C (1200°F) with 1.50% Strain Range and A_c of ∞ .

strain range of 0.50% at 538 and 593°C (1000 and 1100°F) respectively. These specimens have the expected trend of increasing CMOD with increasing cycles or crack size. These data also illustrate that the CMOD at crack opening and closing are virtually identical. Figure 76 shows the CMOD data for a 649°C (1200°F) test with an A_c ratio of ∞ and a 1.15% strain range. This strain range corresponds to one higher than the one where the CMOD transition was observed in 538°C (1000°F) tests but slightly lower than the 1.70% strain range where specimen buckling occurred at 649°C (1200°F). It is believed that this behavior results from rotation of the CMOD gage which is caused by out-of-plane specimen displacements induced by the shear crack growth. The attachment method of the CMOD gage was changed for the second isothermal testing campaign which minimized out of plane movement. The CMOD transition was not observed in any of the tests performed in the second campaign further suggesting that the shift in the CMOD measurements was induced by the interaction between shear crack growth and the CMOD gage.

The load-CMOD hysteresis loops determined in tests which experienced the transition behavior appeared to be of the proper shape and were within the calibrated range. These data were assumed to have a mean displacement shift which did not adversely affect the measurement of the point in the loading cycle where crack opening and closing occurred. As a result, the CMOD range rather than a specific value of the data were used to compare the experimental CMOD data with finite element predictions.

6.3 Fracture Mechanics Analysis

The intent of the crack propagation tests was to obtain data to be used for evaluation of the P-I integrals. These data were also used to qualitatively examine the applicability of conventional linear elastic fracture mechanics (LEFM) to correlate these data. It was anticipated that LEFM would not adequately correlate these data since the amount of plasticity greatly exceeds the conditions of small scale yielding; however LEFM analysis can be used to qualitatively assess the influence of temperature and strain range on the crack growth rates.

It is not obvious how to analyze these displacement controlled tests using LEFM. The 538°C (1000°F) tests performed during the first testing campaign were used to investigate the ability of two K-based parameters for correlating the crack growth data. The first parameter was the range of K (ΔK) which is computed using the stress range between the compressive and tensile load peaks. The second parameter is the value of K at maximum load (K_{max}) which is recommended by ASTM for tests with compressive loads⁽³⁹⁾ and completely ignores any damage which may occur at negative loads. The first campaign 538°C tests were performed with a mean strain of zero ($A_e = \infty$) and include a single tests with strain ranges of 0.50 and 1.70% and duplicate tests with a strain ranges of 1.15%.

Figure 77 shows the variation in crack growth rate as calculated using a seven point sliding polynomial technique with crack length. The crack growth rates increase initially, pass through a maximum, and finally diminish with increasing crack length. These tests were run in remote displacement control and experienced changes in both load range and mean load as the crack grew. The degree of load drop was so rapid that the value of K_{max} also passes through a maximum as shown in Figure 78. Under a constant load control mode, the value of maximum K and crack growth rate would always increase with crack length. The decrease in load results from the change in specimen compliance as the crack grows. This becomes especially pronounced after the crack tip position extends past the mid-width of the specimen ($a = 5$ mm or 0.2 inch).

The variation of crack growth rate with ΔK and K_{max} is shown in Figures 79 and 80, respectively. These figures show that the selected LEFM parameters do not correlate the crack growth data for the different strain range tests. This confirms that these tests will be good cases for evaluating path-independent integrals under elastic-plastic crack growth conditions. Comparison of the nominally elastic, 0.5% strain range test in Figure 80 show that there is a unique relationship between crack growth rate and K_{max} even after these values pass through a maximum. This was not observed for ΔK in Figure 79. For nominally elastic crack growth, the

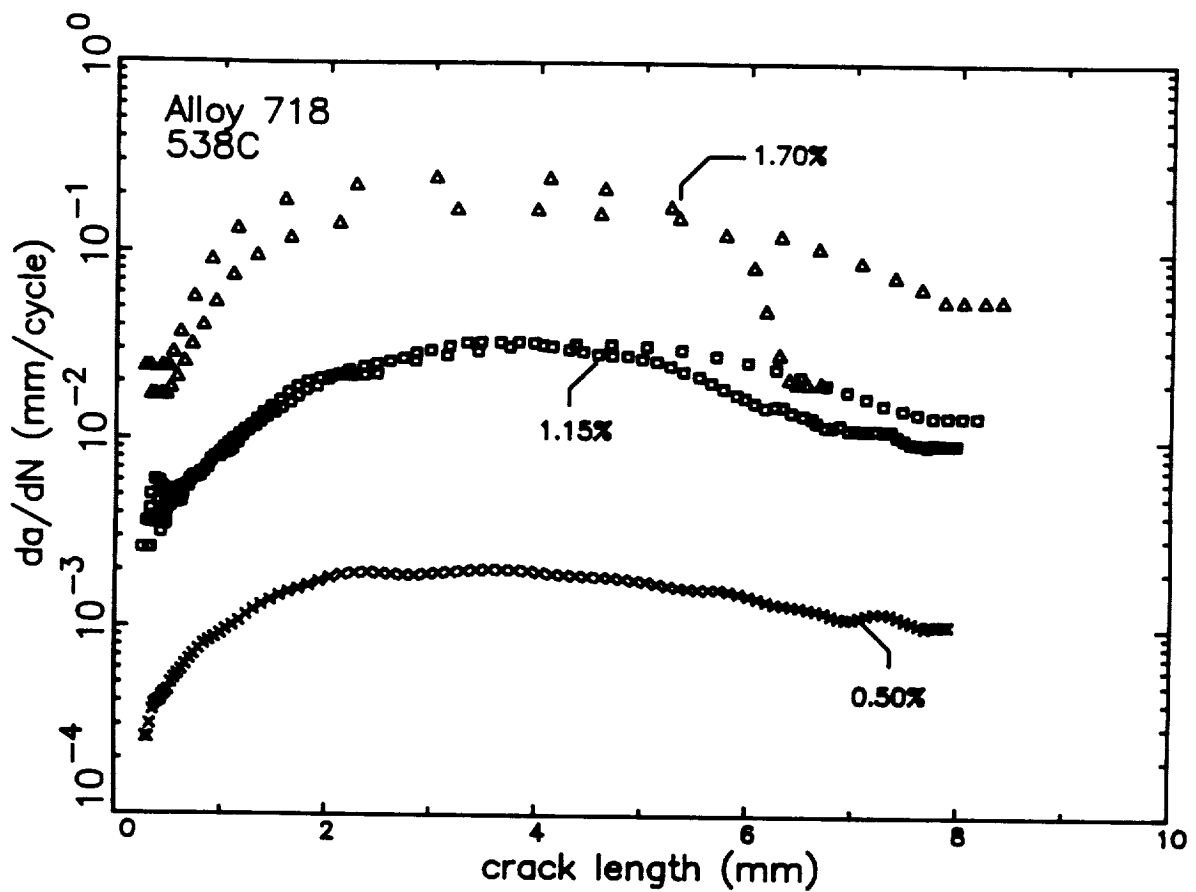


Figure 77: Variation of Crack Growth Rate with Cycles in 538°C (1000°F) Displacement Controlled SEN Tests.

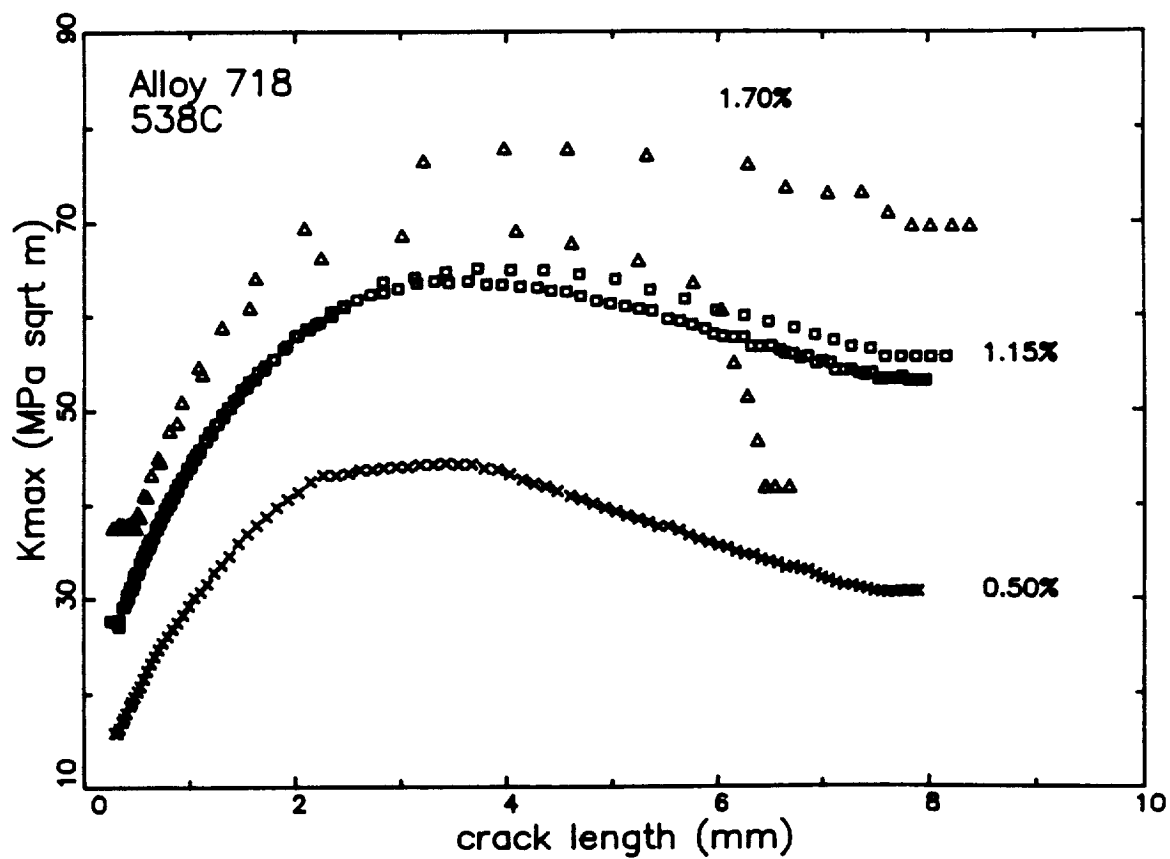


Figure 78: Variation of K_{max} with Cycles in 538°C (1000°F)
Displacement Controlled SEN Tests.

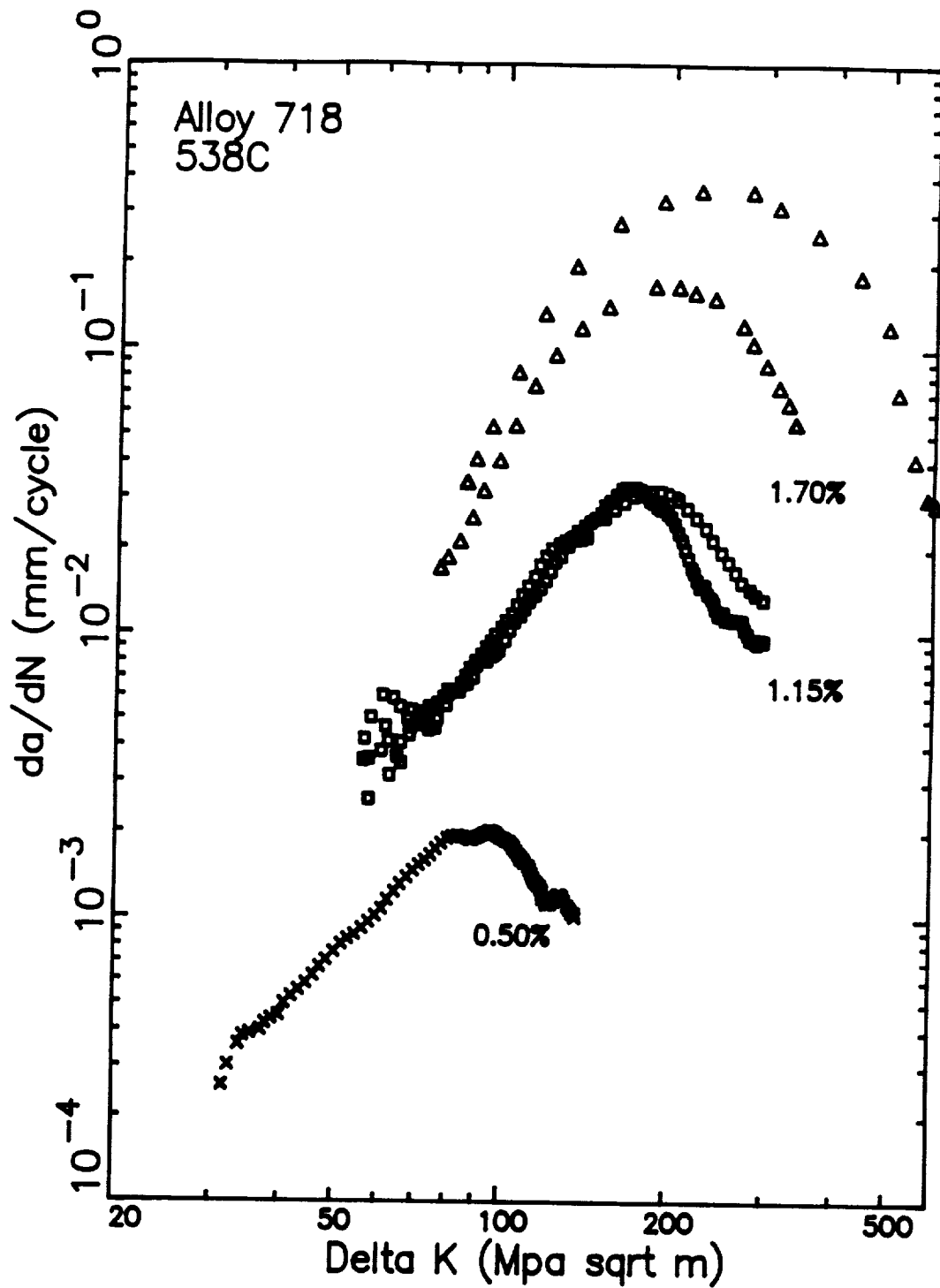


Figure 79: Variation of Crack Growth Rate with ΔK in 538°C (1000°F) Displacement Controlled SEN Tests.

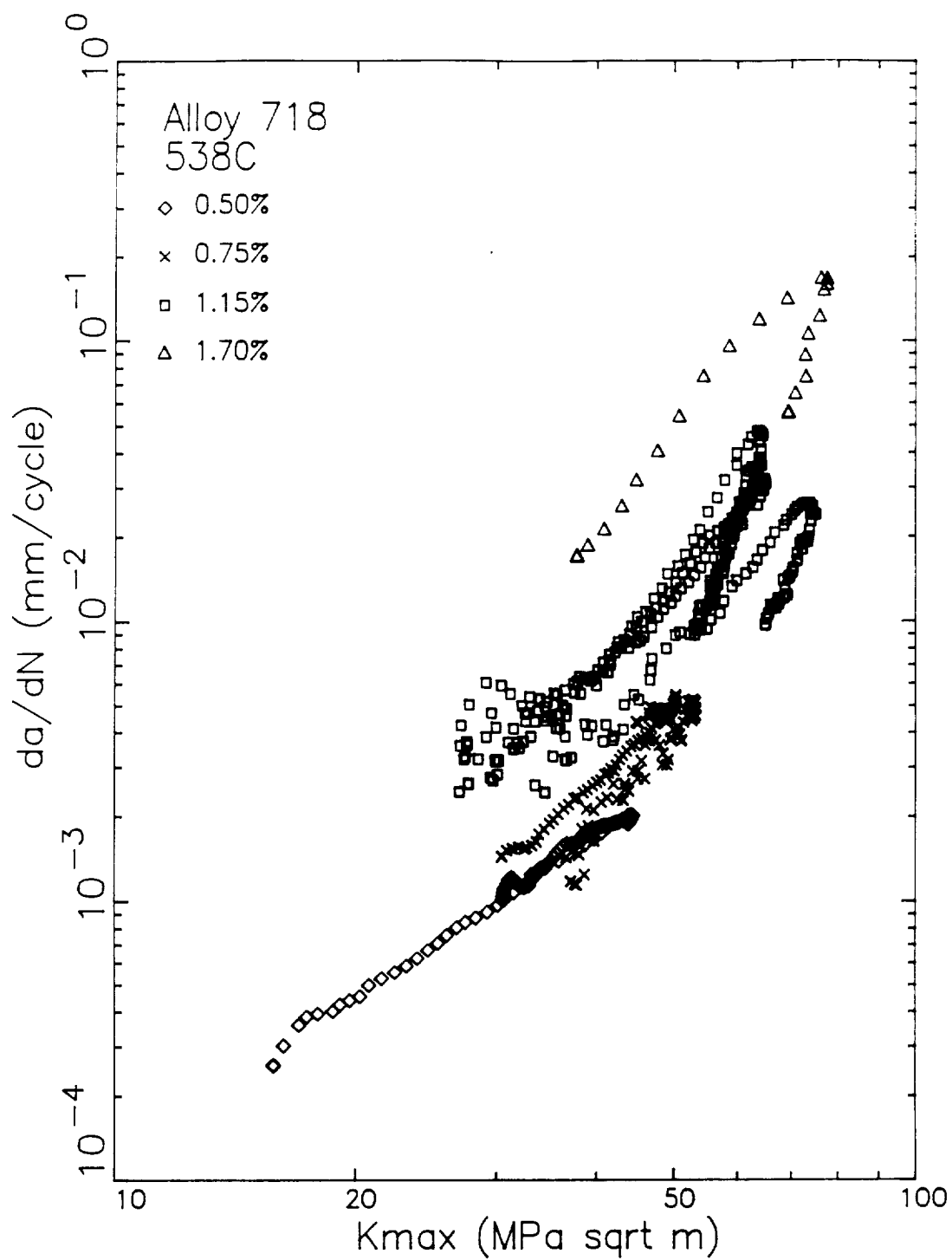


Figure 80: Variation of Crack Growth Rate with K_{max} in 538°C (1000°F) Displacement Controlled SEN Tests.

operational values of K which correlates crack growth data with compressive minimum loads in nickel-base superalloys is very close to K_{\max} ⁽⁴⁸⁾. K_{\max} also correlates the crack growth rates from the higher strain ranges before and after passing through the maximum better than ΔK . The crack growth rate data determined in the other strain controlled tests were analyzed using K_{\max} . The remainder of this section will describe those results.

6.3.1 Results of Zero Mean Strain ($A_{\epsilon}=\infty$) Tests

Figure 81 shows the crack growth data for the $A_{\epsilon}=\infty$ tests performed at 427°C (800°F). As with the data shown in Figure 80, crack growth rate is a multi-valued function of K_{\max} , indicating the necessity of a non-linear fracture mechanics parameter. The tests performed with a strain range of 0.75% had a very small amount of net section cyclic plasticity and had crack growth rates very similar to those with a strain range of 0.50%. This indicates that operational definitions of K or J may be able to treat isothermal cases with very small amounts of cyclic plasticity.

The experimental results for $A_{\epsilon}=\infty$ tests performed at 538, 593, and 649°C (1000, 1100, and 1200°F) are shown in Figures 82, 83, and 84 respectively. These data all show increasing crack growth rates with increasing strain ranges for a given value of K_{\max} . The acceleration in crack growth rates caused by the cyclic plasticity decreases with increasing test temperature.

6.3.2 Results of Non-zero Mean Strain Tests

All the positive mean strain tests were performed with an A_{ϵ} ratio of 1.0 and a strain range of 1.15%. This type of test is cycled from a strain of zero to a maximum strain of 1.15%. The results of the 1.15% strain range tests performed at 427°C (800°F) with A_{ϵ} ratios of 1.0 and ∞ are shown in Figure 85. There is no observable influence of mean strain in these tests. This result is due, in part, to the K_{\max} treatment of the data used in this figure. Both of these cases have significant plasticity and negative minimum

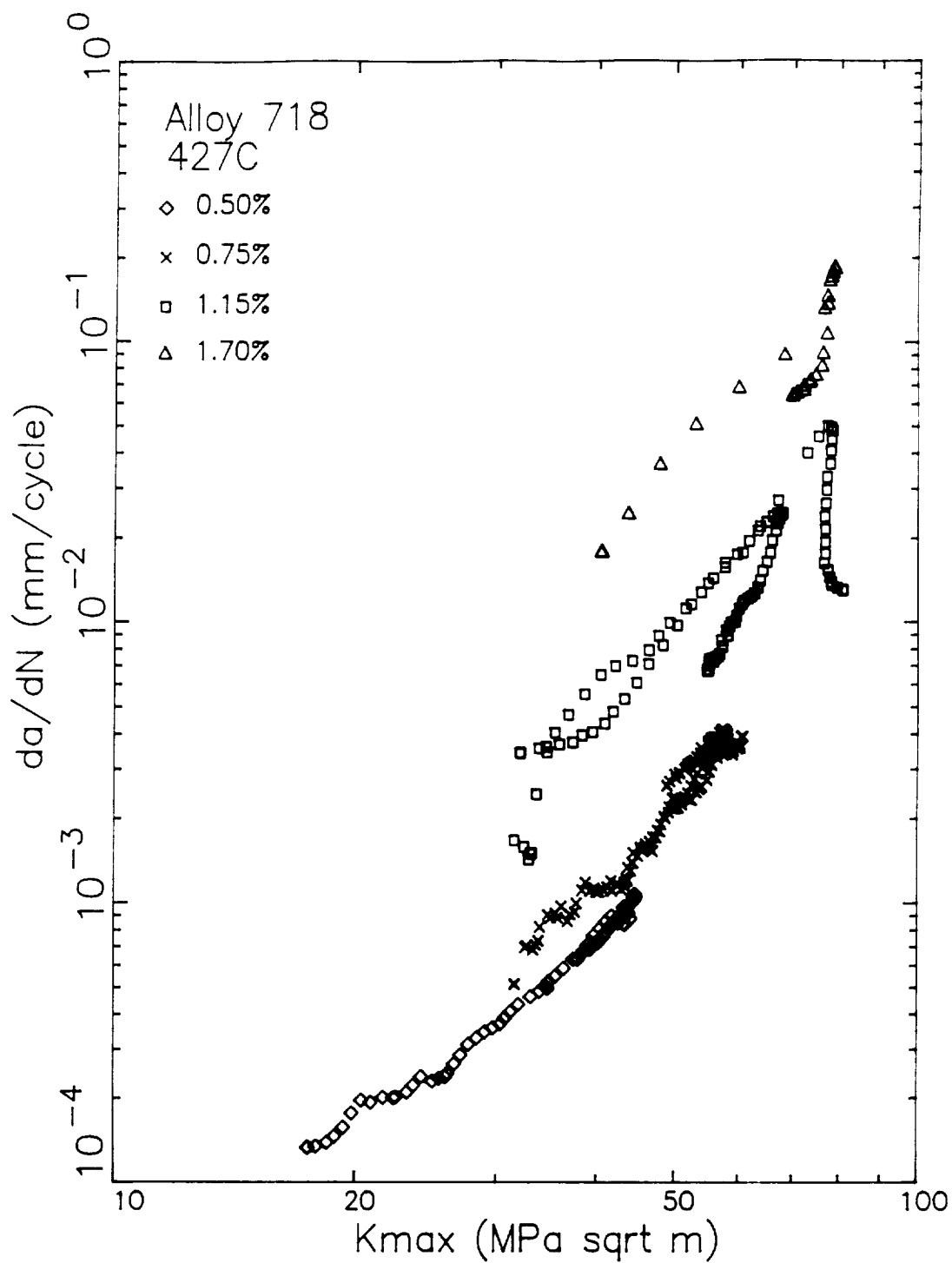


Figure 81: Crack Growth Rates Measured in Alloy 718 SEN Specimens Cycled at 427°C (800°F) with $A_{\epsilon}=\infty$ as a Function of K_{max} and Strain Range.

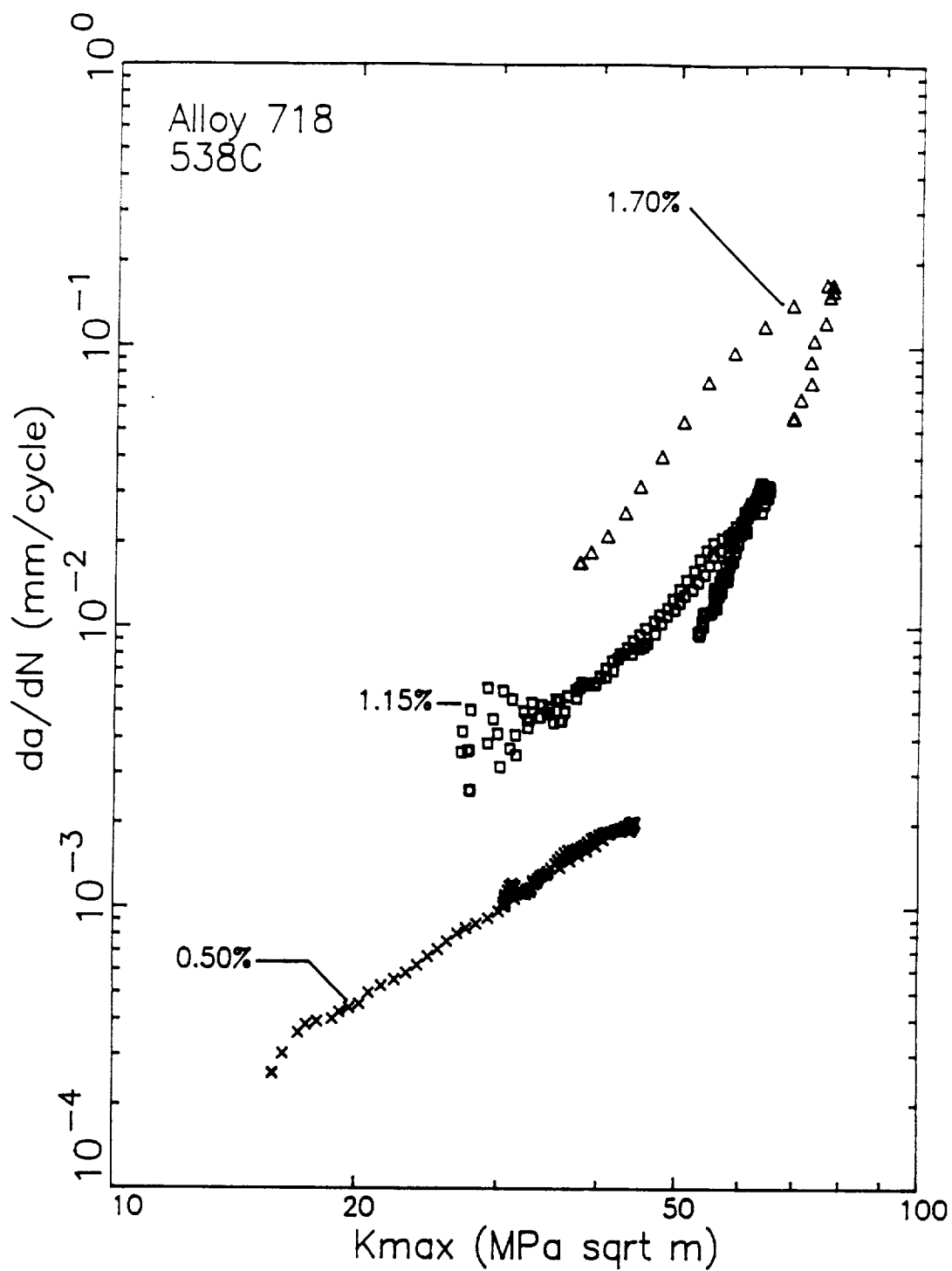


Figure 82: Crack Growth Rates Measured in Alloy 718 SEN Specimens Cycled at 538°C (1000°F) with $A_c = \infty$ as a Function of K_{max} and Strain Range.

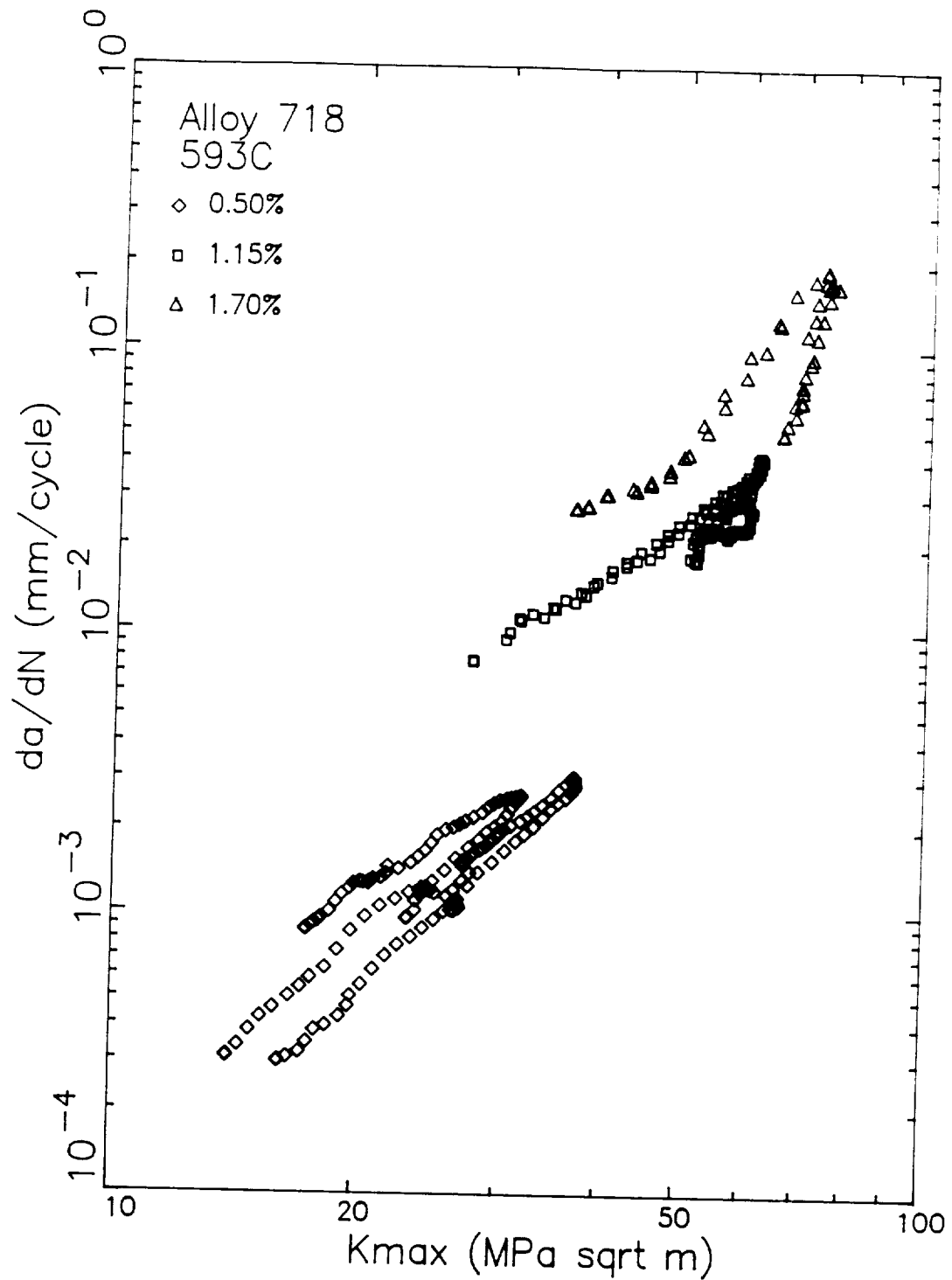


Figure 83: Crack Growth Rates Measured in Alloy 718 SEN Specimens Cycled at 593°C (1100°F) with $A_c = \infty$ as a Function of K_{max} and Strain Range.

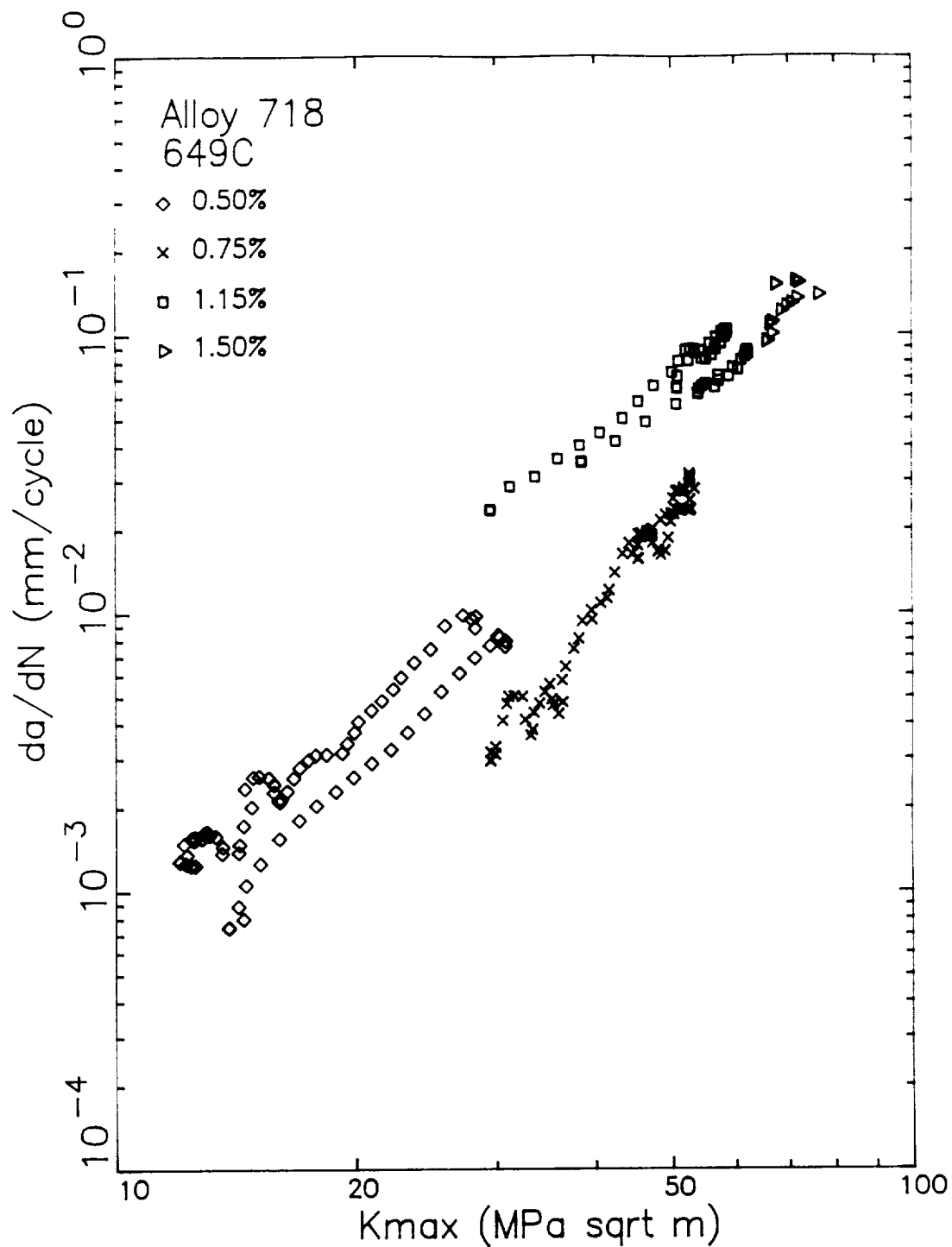


Figure 84: Crack Growth Rates Measured in Alloy 718 SEN Specimens Cycled at 649°C (1200°F) with $A_{\epsilon}=\infty$ as a Function of K_{max} and Strain Range.

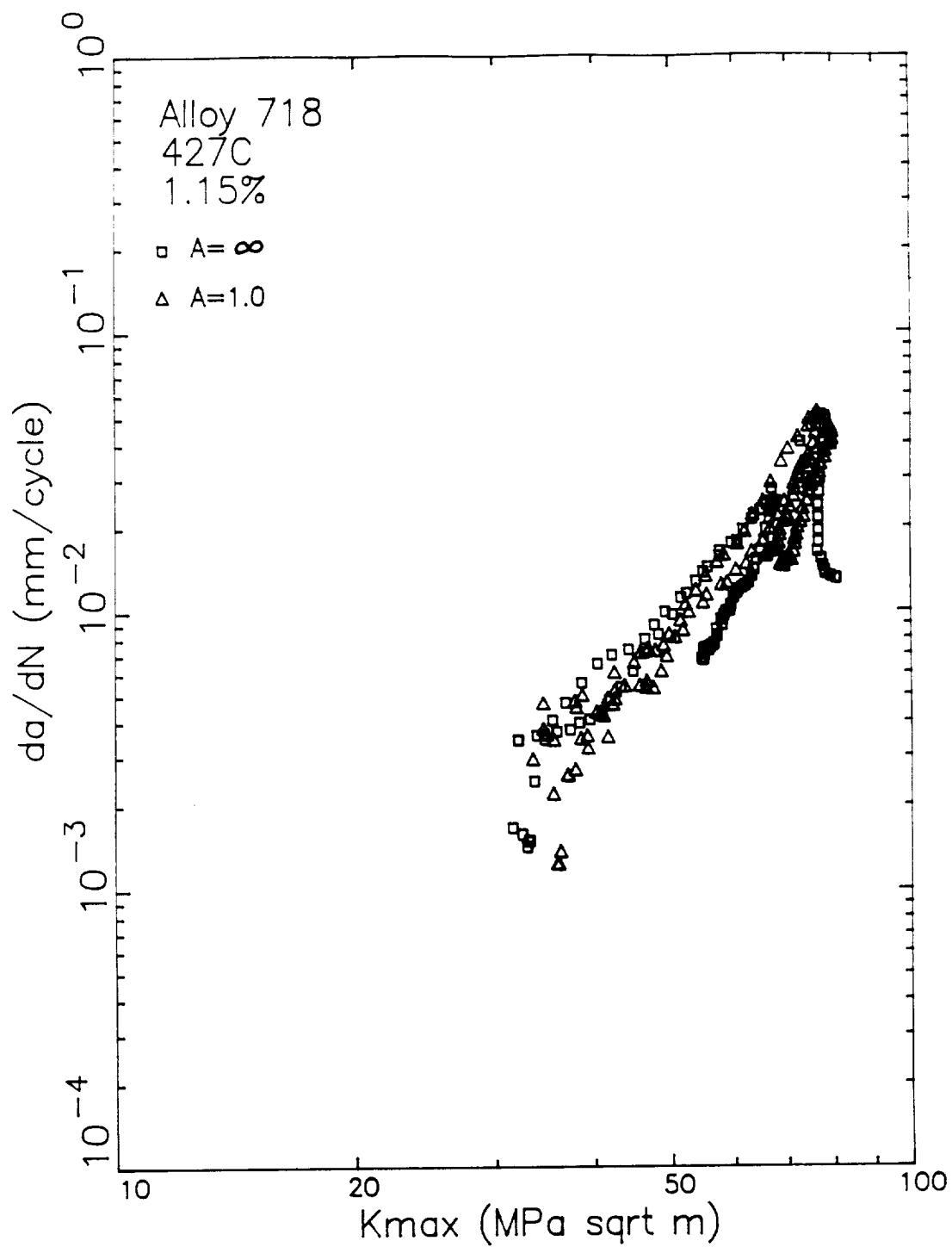


Figure 85: Comparison of Crack Growth Rates Measured Alloy 718 SEN Specimens Cycled at 427°C (800°F) with a Strain Range of 1.15% and A_{ϵ} Ratios of ∞ and 1.0

stresses. The K_{max} parameter considers the magnitude of the positive stresses and ignores the compressive stresses. For a nominally elastic test with negative minimum stress, it would not be expected to see a mean strain effect when plotting crack growth data against K_{max} .

The comparisons of the 1.15% strain range tests performed at the higher temperatures with A_ϵ ratios of ∞ and 1.0 are shown in Figures 86, 87, and 88, respectively. There is not a large influence of mean strain on the crack growth rates but the $A_\epsilon=1.0$ tests had slower crack growth rates at 593 and 649°C. Increasing temperature results in lower cyclic strength and thus higher cyclic plasticity for a fixed strain range. This effect and the overall changes in stress levels with mean displacements may be responsible for this small but possibly significant trend.

Crack growth tests were also performed with an A_ϵ ratio of -2.0 which results in a negative mean strain. The negative mean strain required that the strain range be reduced so that the specimens would not buckle. It was estimated from the $A_\epsilon=\infty$ tests that the minimum strain should not be lower than -0.70%. The combination of this minimum strain and the A_ϵ ratio of -2.0 requires that the strain range be 0.93%. This corresponds to a maximum strain of 0.23%. There were no zero mean strain tests performed at this strain range, so the results of these tests were compared with the $A_\epsilon=\infty$ tests at the nearest strain ranges less than and greater than that used in the negative mean strain tests.

Figure 89 compares the results of the zero and negative mean strain tests performed at 427°C (800°F). The $A_\epsilon=-2.0$ results are bracketed by the $A_\epsilon=\infty$ results. The K_{max} parameter, in part, helps to account for the mean strain effect in a fashion similar to that explained for the positive mean strain results. The data in Figure 89 suggest that there is not a large mean strain effect but do not rule out a more subtle influence.

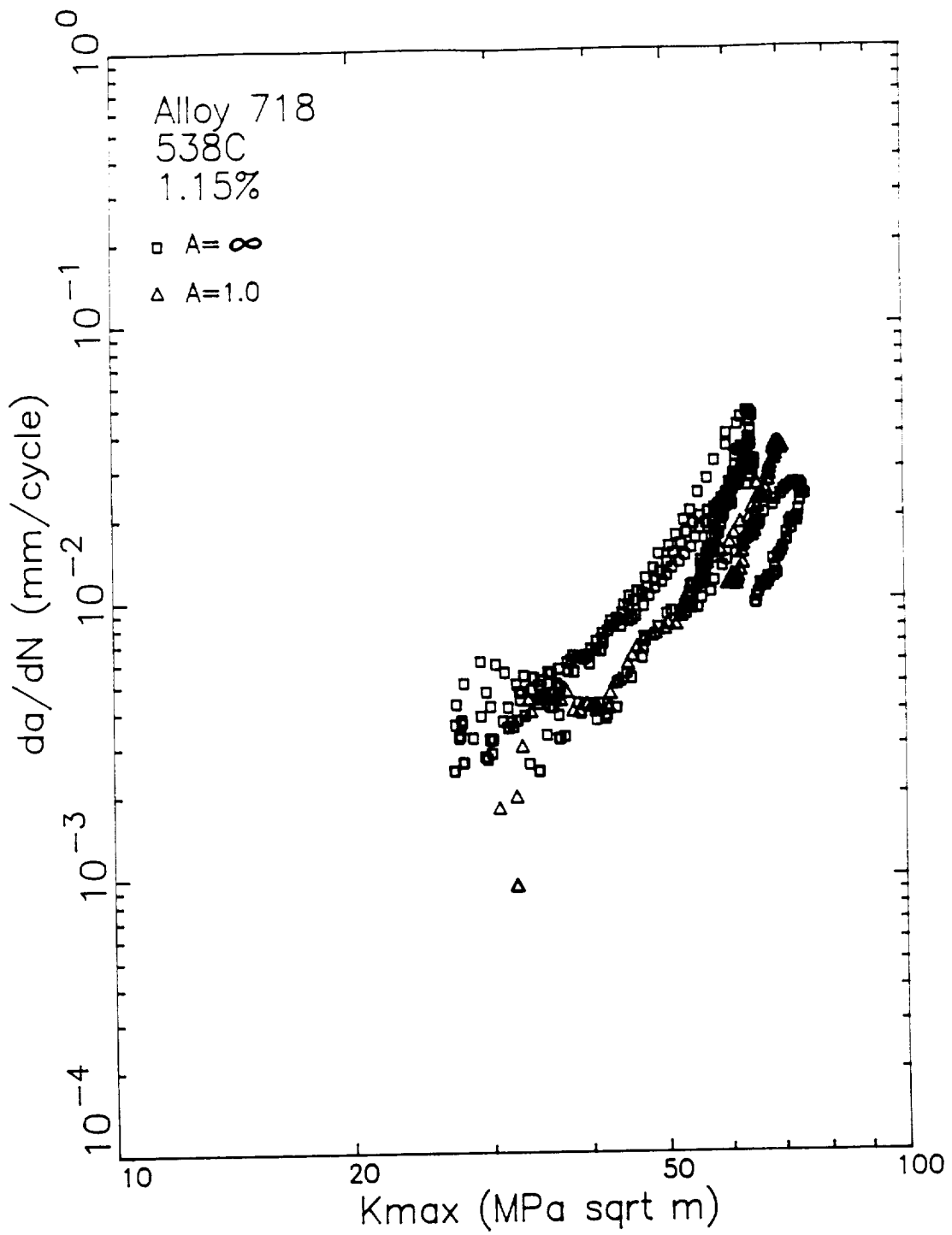


Figure 86: Comparison of Crack Growth Rates Measured Alloy 718 SEN Specimens Cycled at 538°C (1000°F) with a Strain Range of 1.15% and A_c Ratios of ∞ and 1.0.

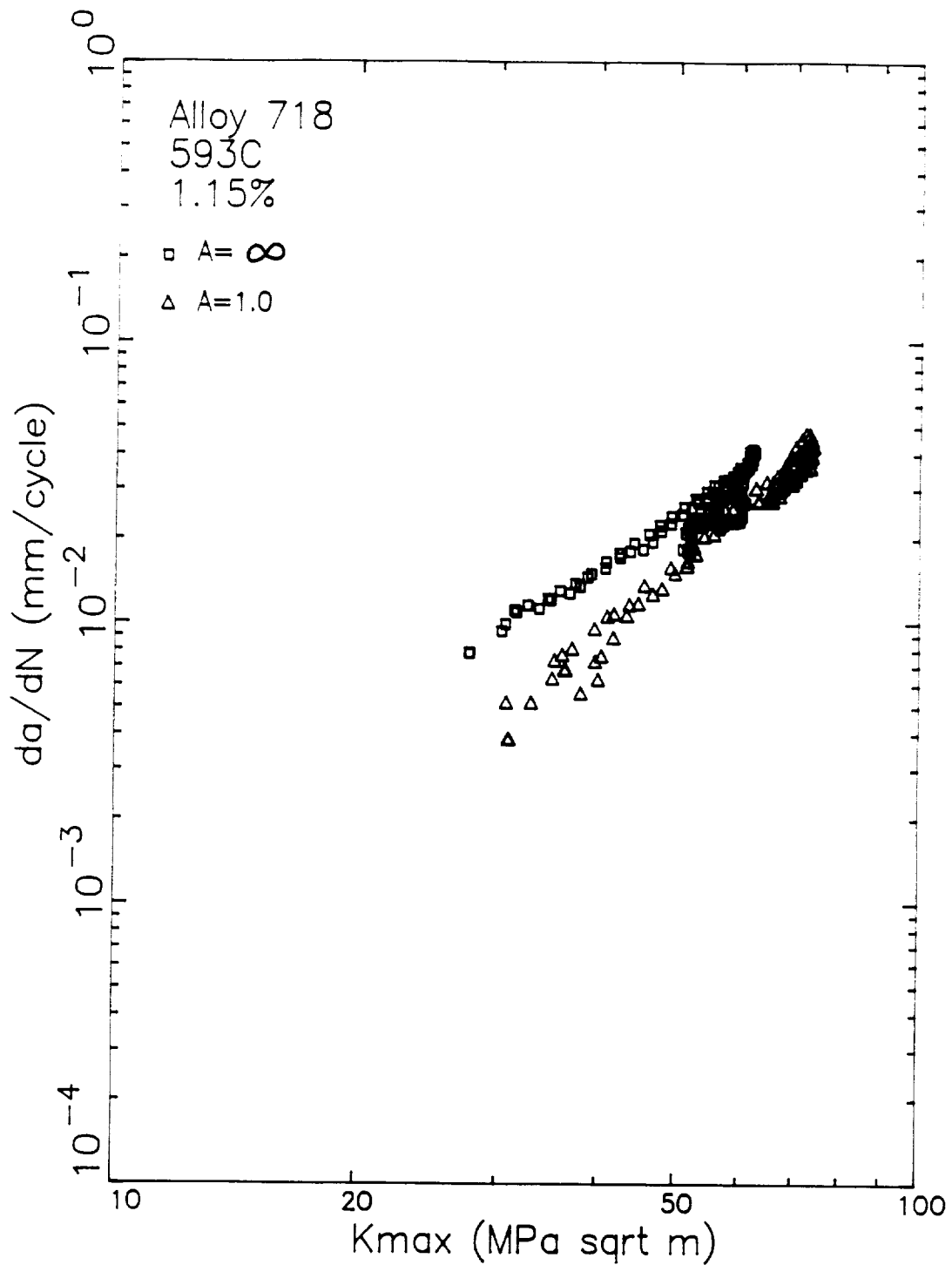


Figure 87: Comparison of Crack Growth Rates Measured Alloy 718 SEN Specimens Cycled at 593°C (1100°F) with a Strain Range of 1.15% and A_e Ratios of ∞ and 1.0.

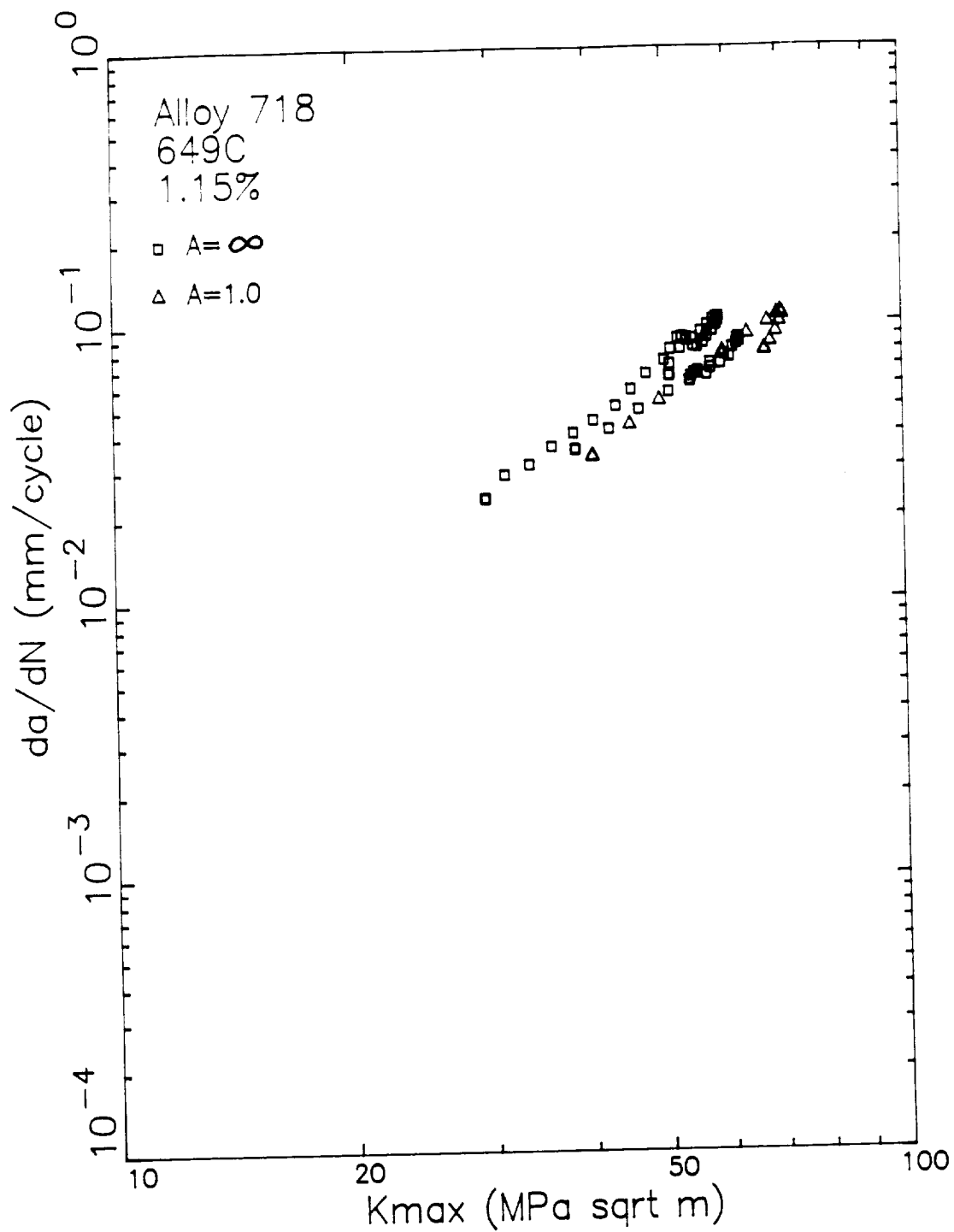


Figure 88: Comparison of Crack Growth Rates Measured Alloy 718 SEN Specimens Cycled at 649°C (1200°F) with a Strain Range of 1.15% and A_e Ratios of ∞ and 1.0

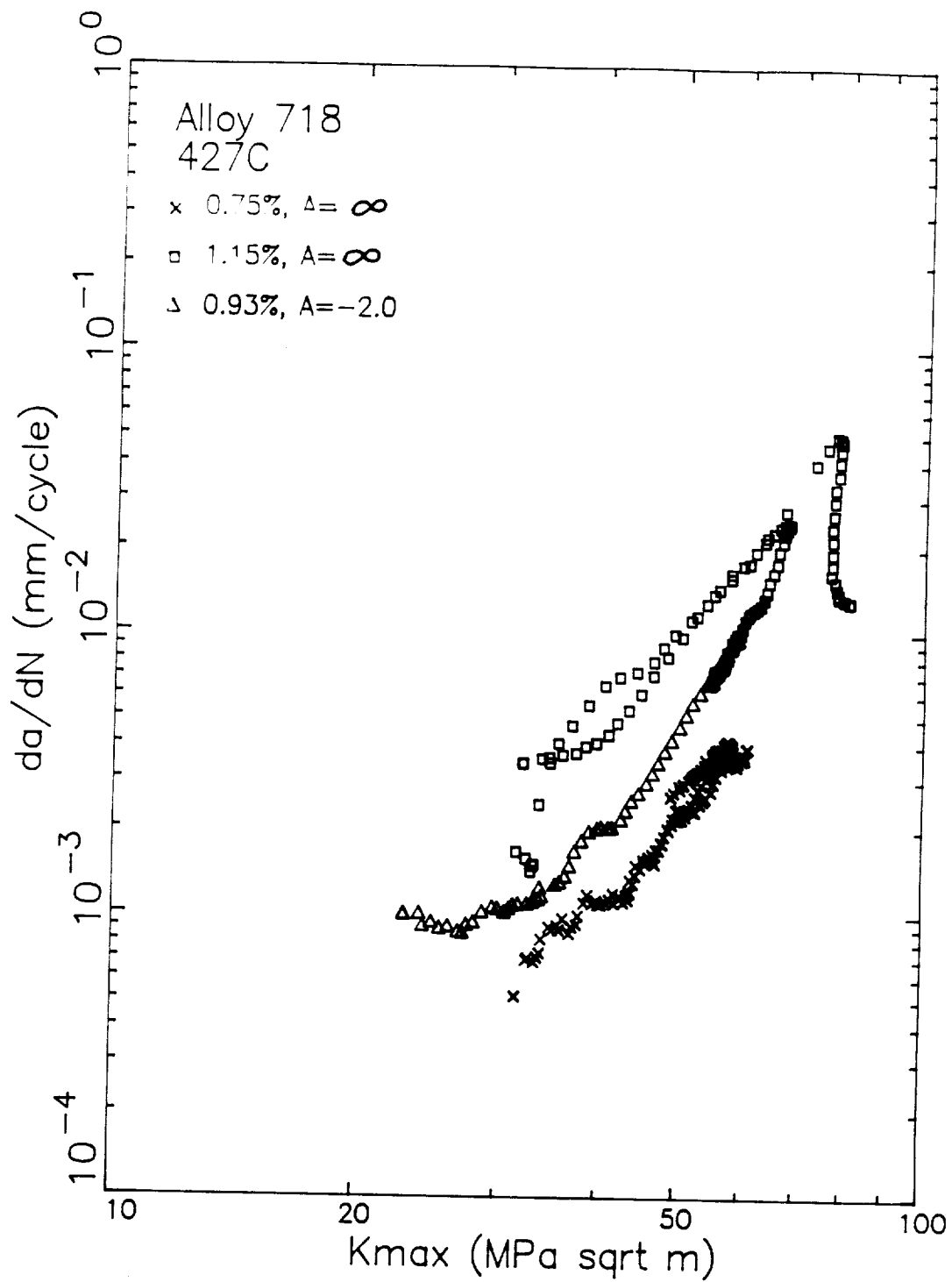


Figure 89: Comparison of Crack Growth Rates Measured Alloy 718 SEN Specimens Cycled at 427°C (800°F) with Similar Strain Ranges and A_e Ratios of ∞ and -2.0.

The comparison of the 538, 593, and 649°C (1000, 1100, and 1200°F) zero and negative mean strain tests are shown in Figures 90, 91, and 92, respectively. The zero mean strain results bracket the $A_e = -2.0$ results indicating no major mean strain effect at the other temperatures.

6.3.3 Influence of Test Temperature

The results of these isothermal crack growth rate tests are to be used to qualitatively interpret the thermal gradient and TMF crack growth tests. These data have been cross-plotted as a function of temperature for fixed displacement (A_e and strain range) conditions to assist in this interpretation. The presence of specimen buckling (Table 14) prevented an exact comparison for all strain ranges at all temperatures.

Figures 93, 94, 95, and 96 show the influence of test temperature on the crack growth rates measured in specimens with an A_e ratio of ∞ for strain ranges of 0.50, 0.75, 1.15, and 1.70%, respectively. Increasing the temperature from 427 to 649°C accelerates the crack growth rates by a factor of approximately 20 for a strain range of 0.50% (Figure 93) when plotted as a function of K_{max} . The relative effect of temperature is diminished as the strain range increased. It is unfortunate that the 1.70% strain range tests conducted at the highest temperature (649°C) buckled, but the data for the temperature range from 427 to 593°C (Figure 96) indicates that there is very little influence of temperature with large amounts of cyclic plasticity. Over this same temperature range, the data for a strain range of 1.15% (Figure 95) shows a 8 fold difference in crack growth rates.

The results of the crack growth rate tests with A_e ratios of 1.0 and -2.0 are compared in Figures 97 and 98, respectively. The tests with a positive mean strain had a strain range of 1.15%. For this condition, increasing the temperature from 427 to 649°C, accelerated the crack growth rates by a factor of approximately 70. A very similar effect was observed for the zero mean strain tests having the same strain range (Figure 95).

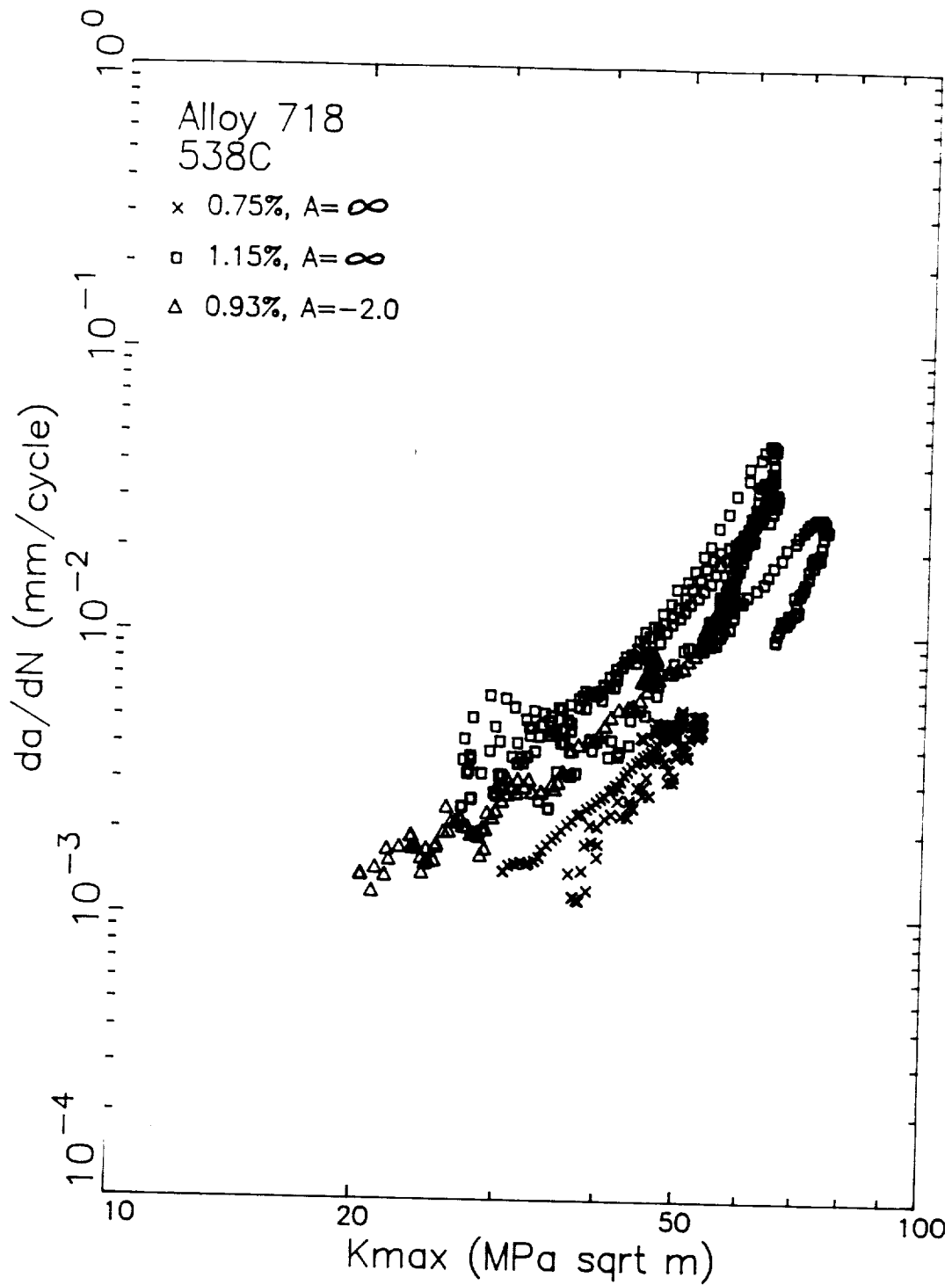


Figure 90: Comparison of Crack Growth Rates Measured Alloy 718 SEN Specimens Cycled at 538°C (1000°F) with Similar Strain Ranges and A_{ϵ} Ratios of ∞ and -2.0.

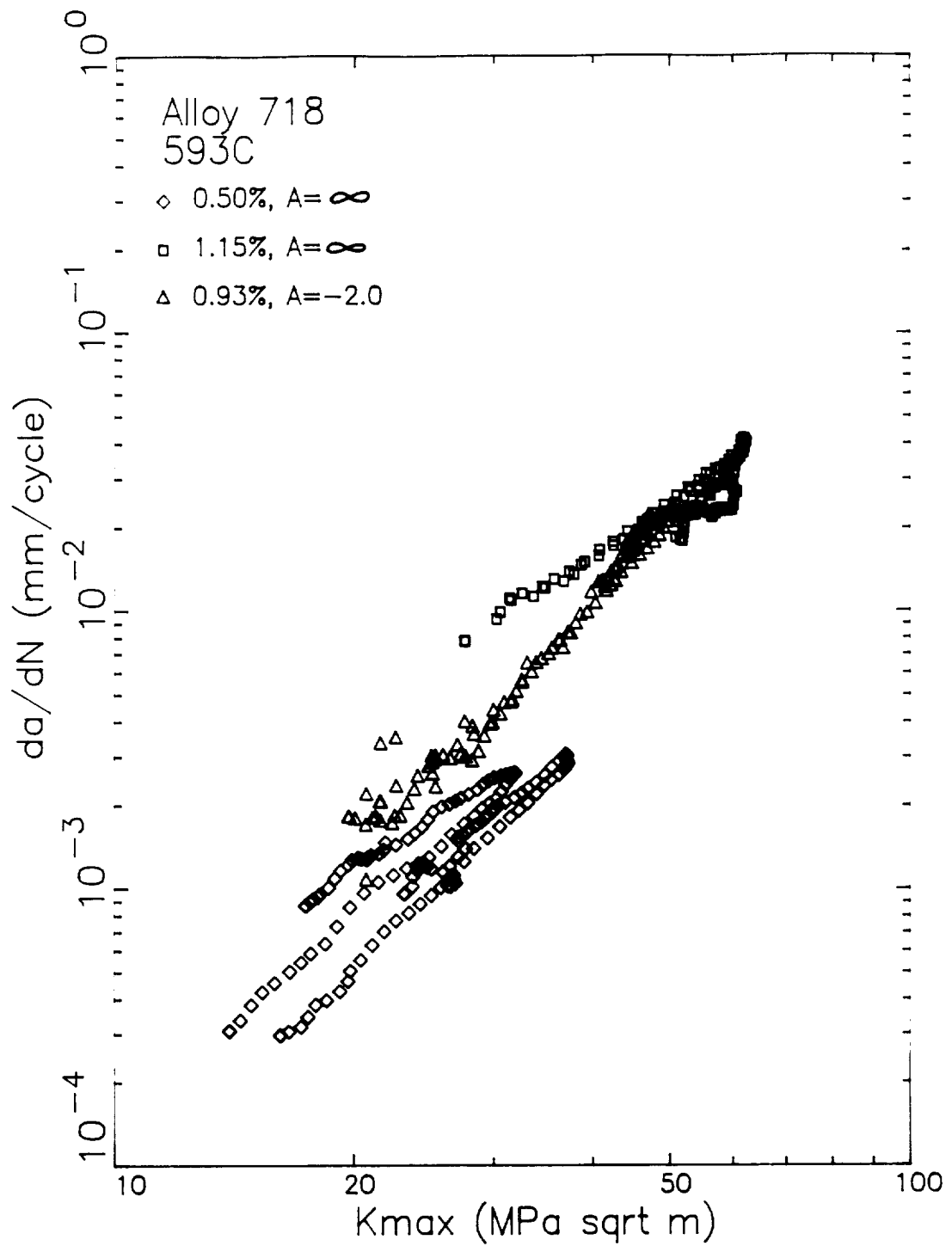


Figure 91: Comparison of Crack Growth Rates Measured Alloy 718 SEN Specimens Cycled at 593°C (1100°F) with Similar Strain Ranges and A_c Ratios of ∞ and -2.0.

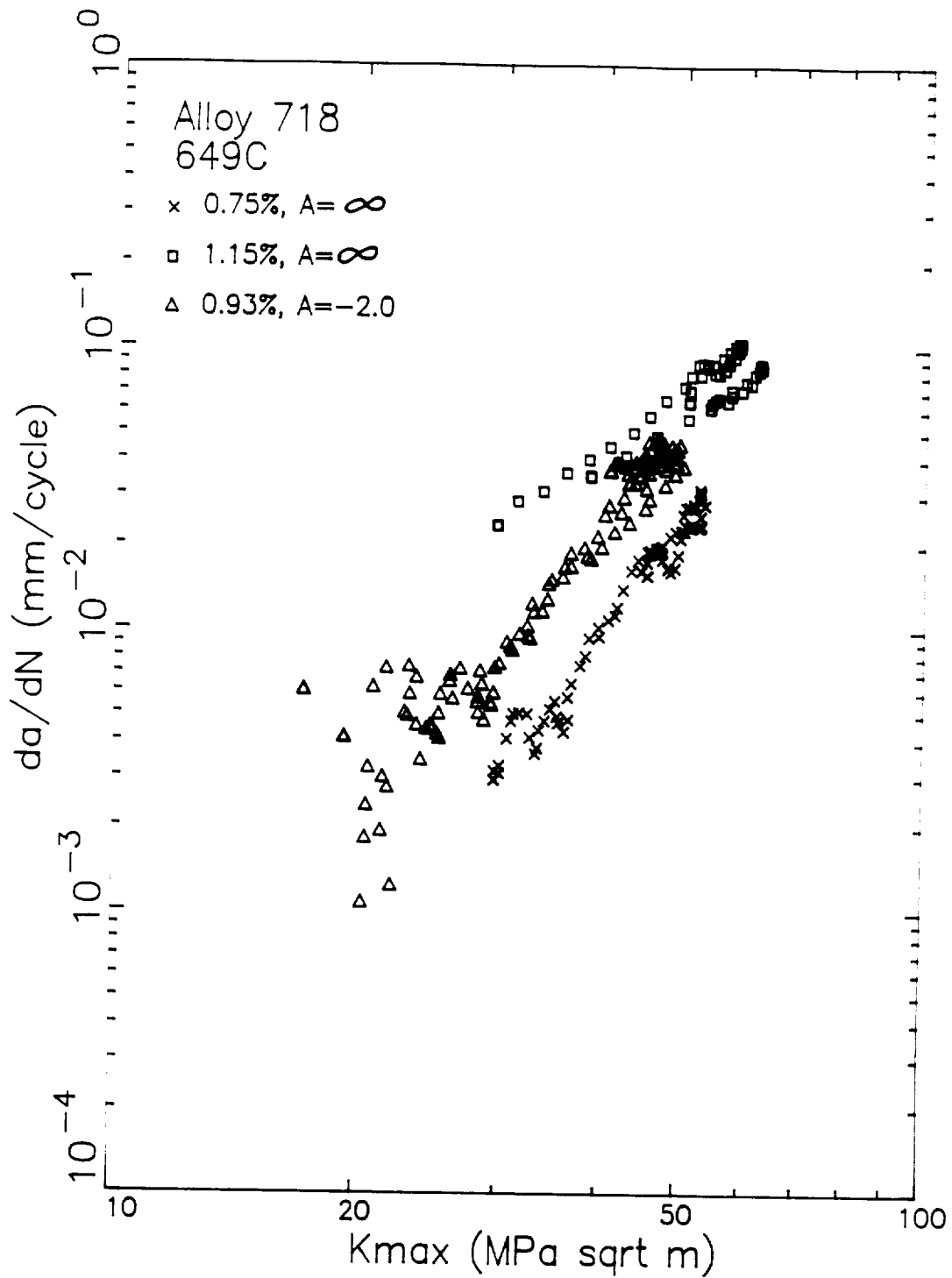


Figure 92: Comparison of Crack Growth Rates Measured Alloy 718 SEN Specimens Cycled at 649°C (1200°F) with Similar Strain Ranges and A_ϵ Ratios of ∞ and -2.0.

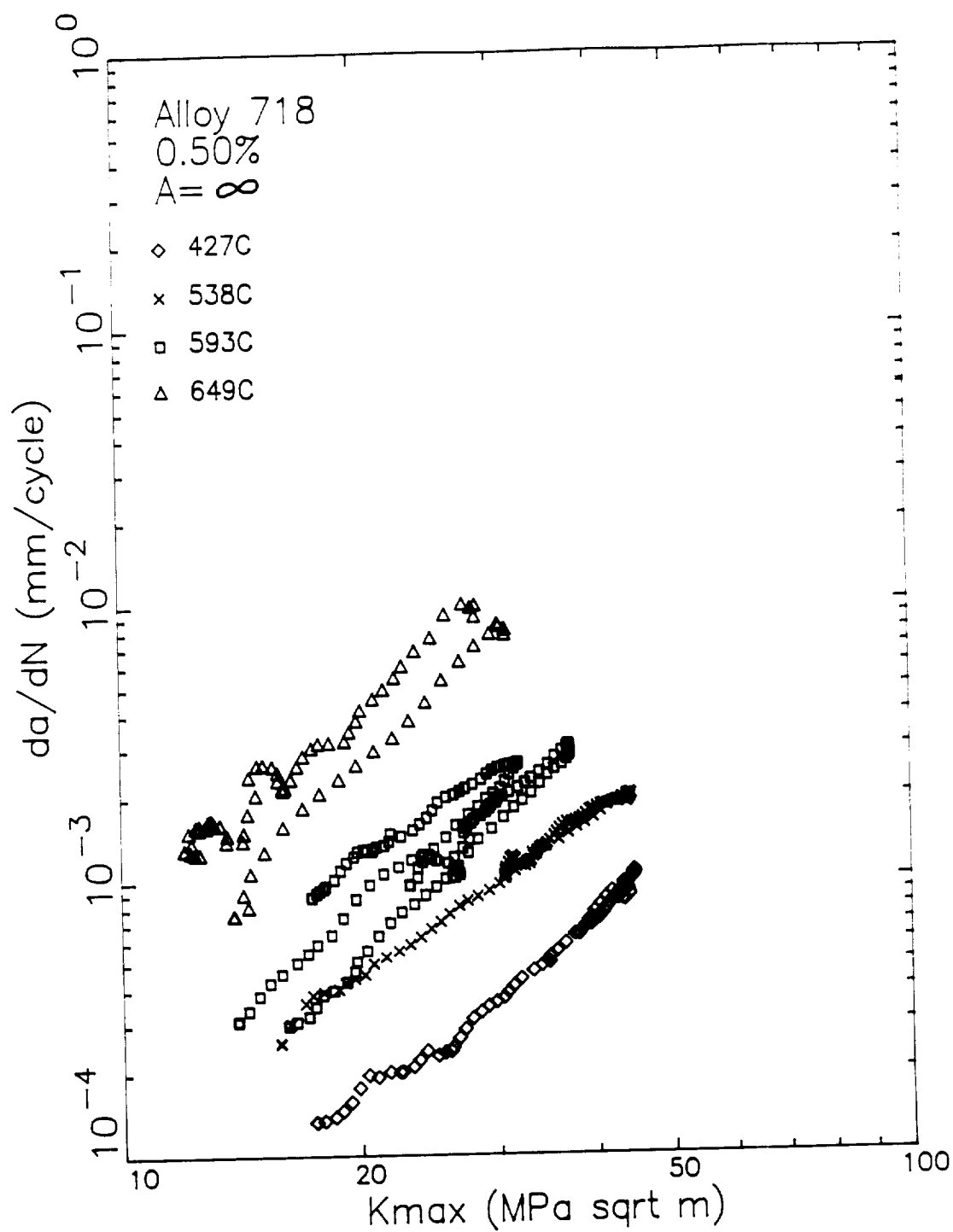


Figure 93: Influence of Test Temperature on the Crack Growth Rates Measured Alloy 718 SEN Specimens Cycled with a Strain Range of 0.50% and an A_e Ratio of ∞ .

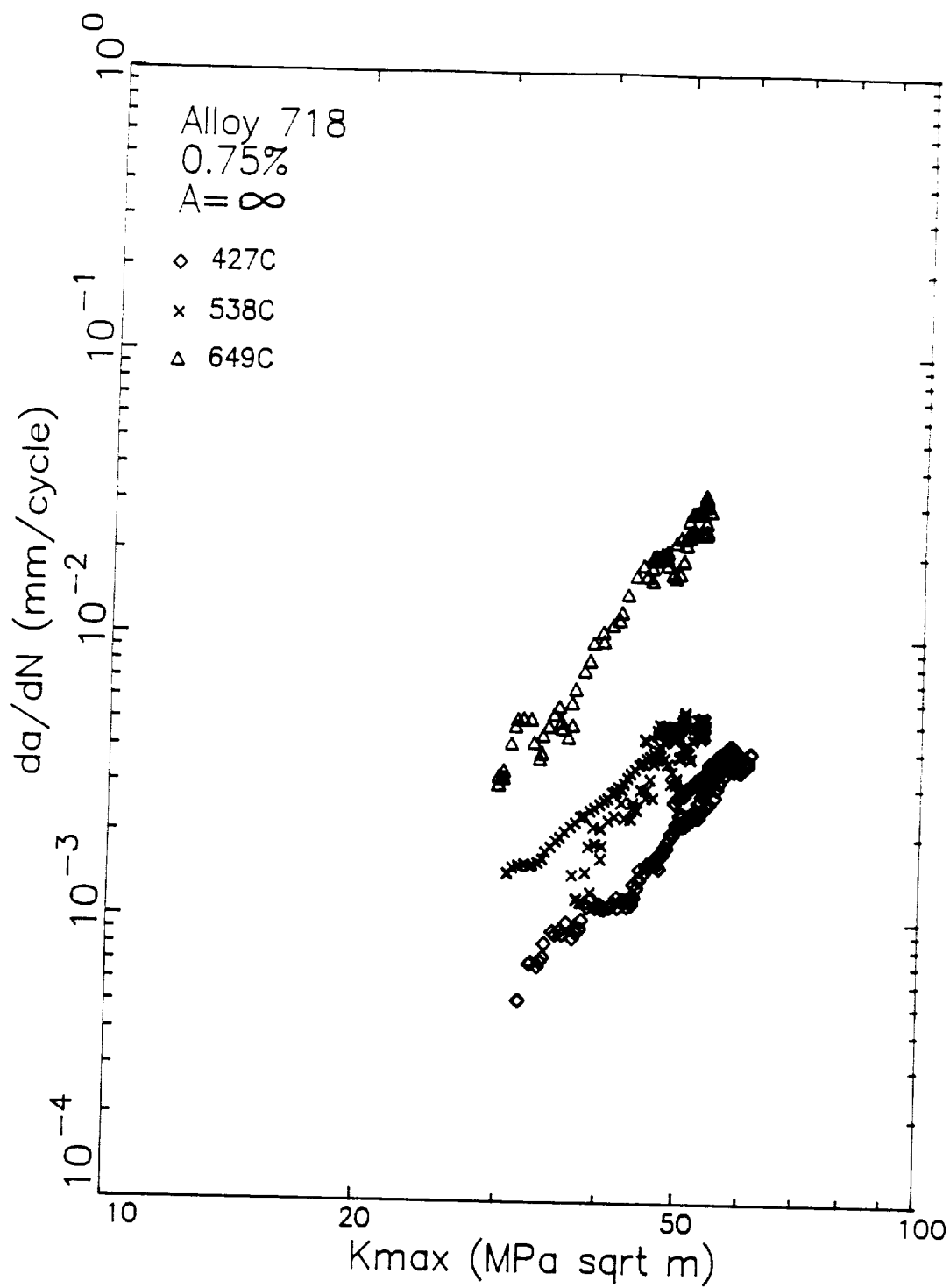


Figure 94: Influence of Test Temperature on the Crack Growth Rates Measured Alloy 718 SEN Specimens Cycled with a Strain Range of 0.75% and an A_{ϵ} Ratio of ∞ .

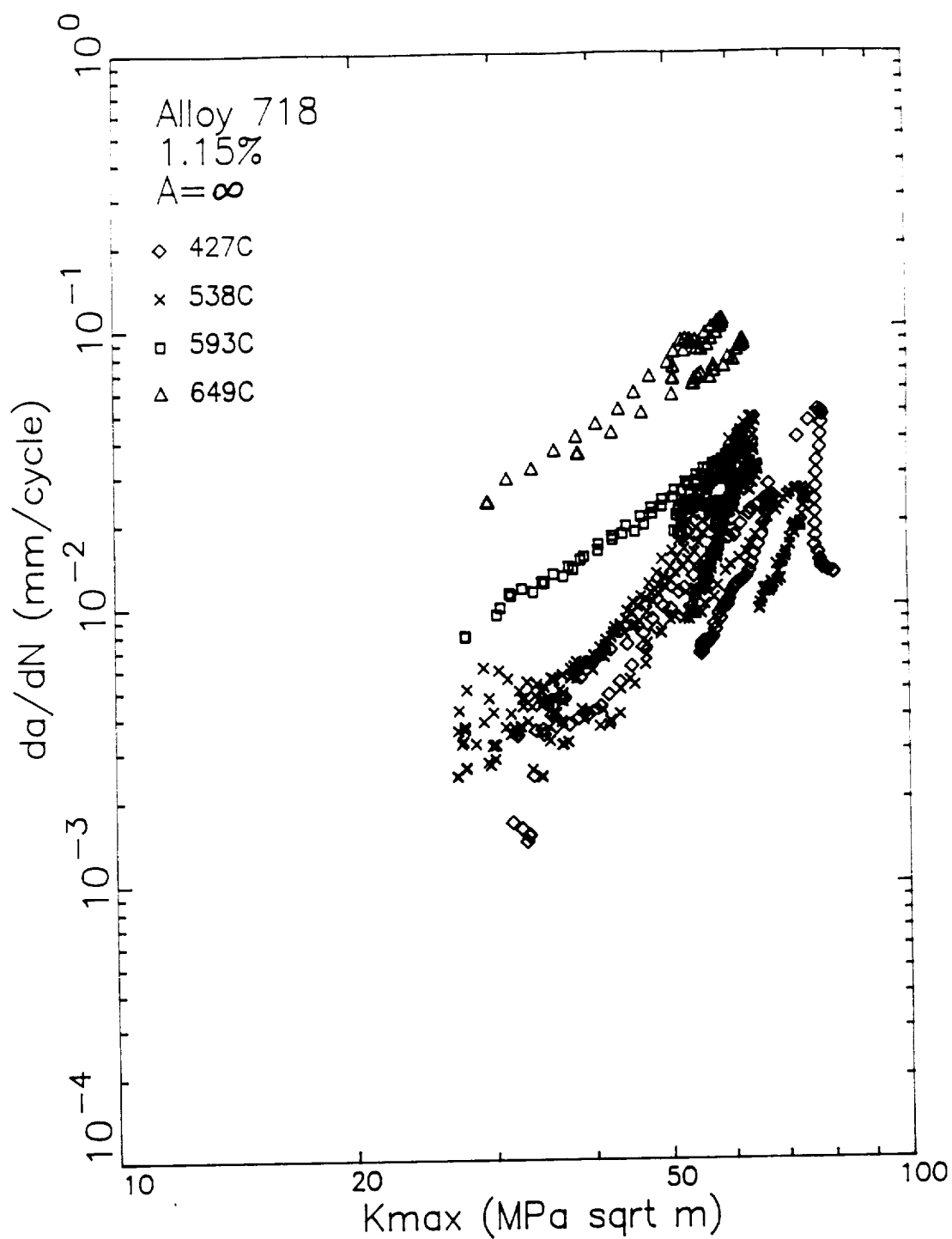


Figure 95: Influence of Test Temperature on the Crack Growth Rates Measured Alloy 718 SEN Specimens Cycled with a Strain Range of 1.15% and an A_e Ratio of ∞ .

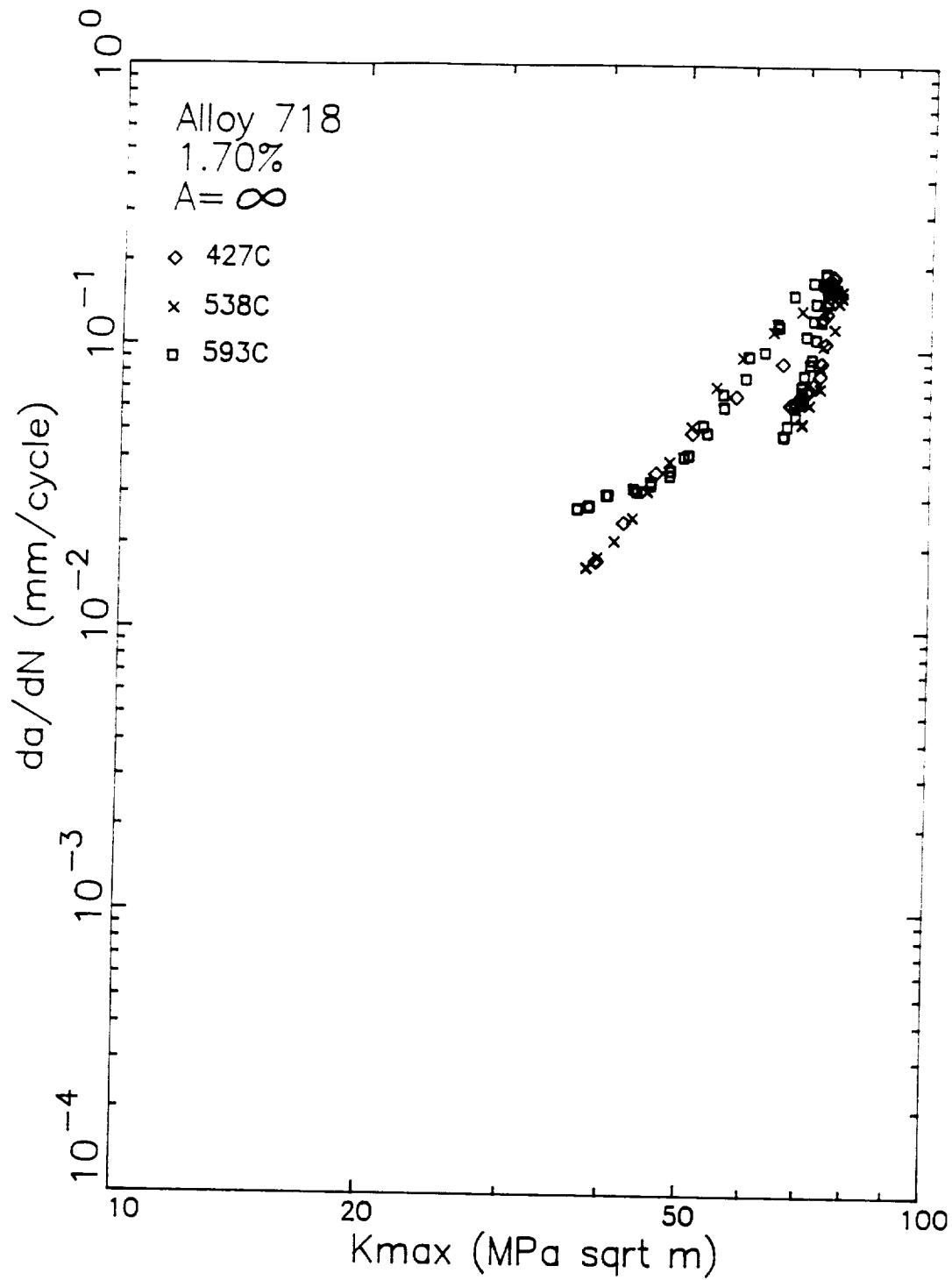


Figure 96: Influence of Test Temperature on the Crack Growth Rates Measured Alloy 718 SEN Specimens Cycled with a Strain Range of 1.70% and an A_c Ratio of ∞ .

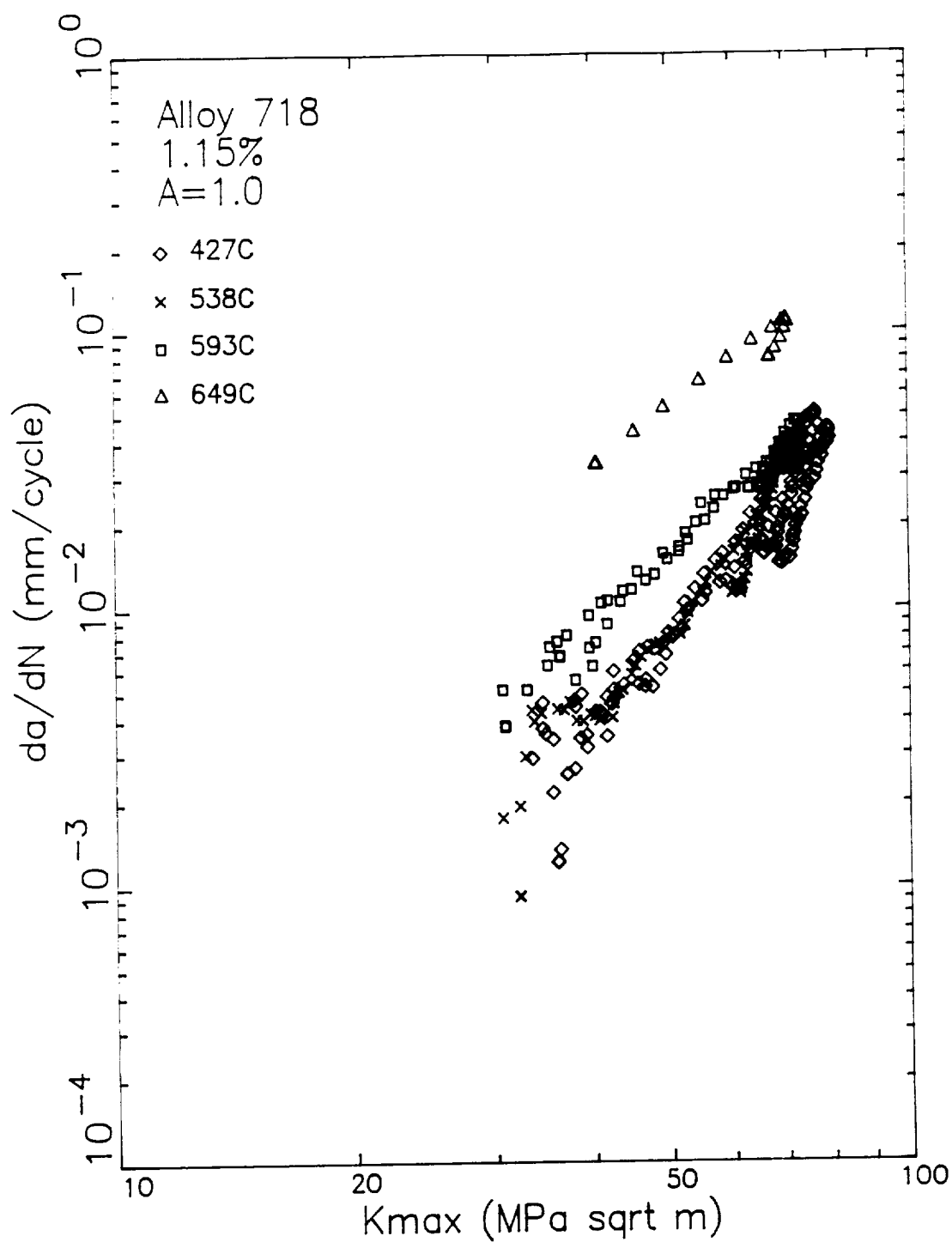


Figure 97: Influence of Test Temperature on the Crack Growth Rates Measured Alloy 718 SEN Specimens Cycled with a Strain Range of 1.15% and an A_e Ratio of 1.0.

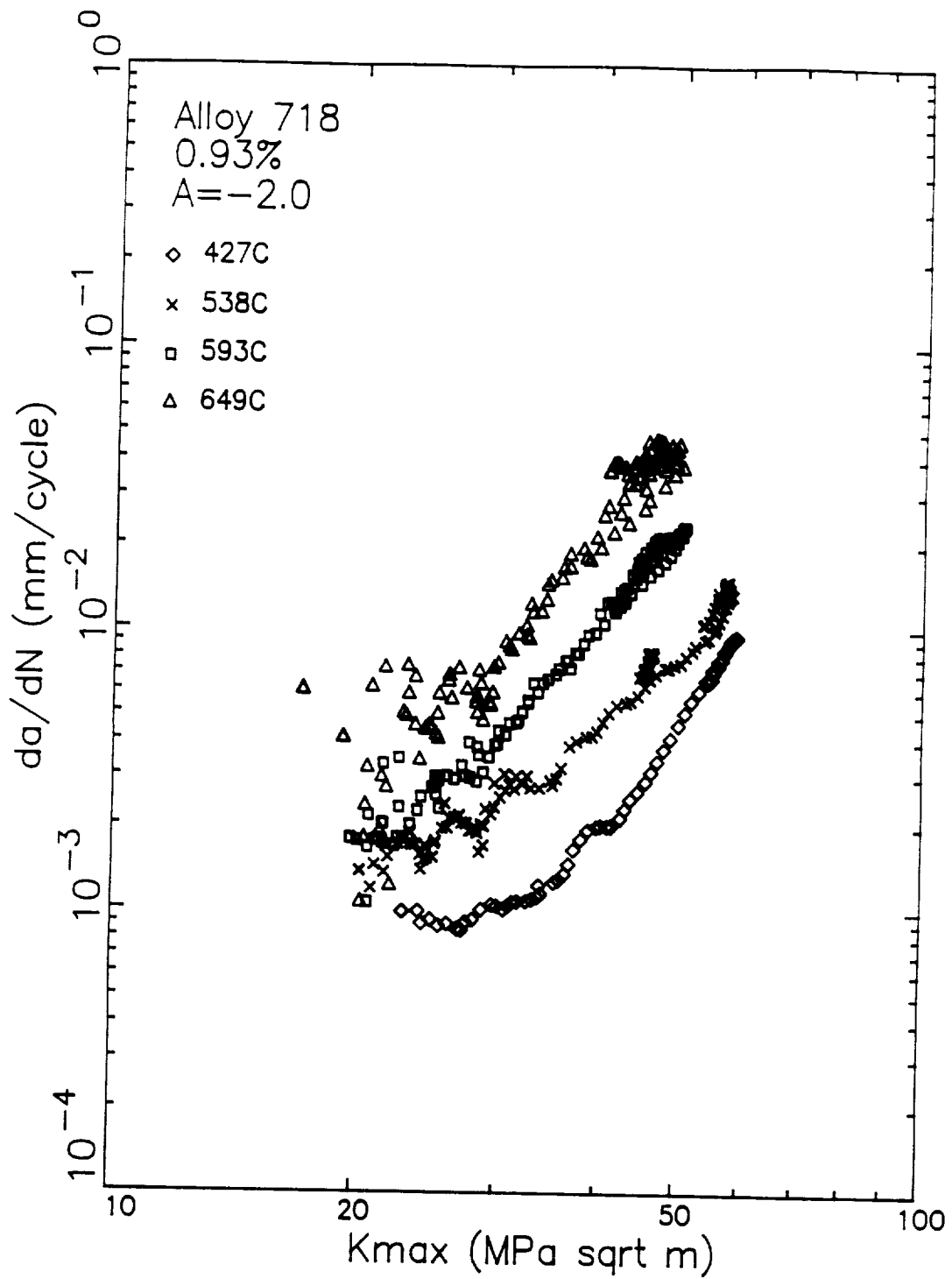


Figure 98: Influence of Test Temperature on the Crack Growth Rates Measured Alloy 718 SEN Specimens Cycled with a Strain Range of 0.93% and an A_{ϵ} Ratio of -2.0.

The same temperature range accelerated the crack growth rates measured in the negative mean strain tests (Figure 98) by a factor of approximately 80. These tests were conducted with a strain range of 0.93%. The relative level of acceleration is on the same order as that observed for zero mean stress tests with strain ranges on 0.75% (Figure 94) and 1.15% (Figure 95).

7.0. ISOTHERMAL FINITE ELEMENT ANALYSIS

7.1. Literature Survey

The application of a finite element method for analysis of crack closure usually involves an enormous amount of computational efforts due to the doubly iterative nature of the problem. The equilibrium must be achieved such that both the material nonlinear behavior and the contact condition of the crack surface are satisfied. The list of available literature in this connection is, consequently, rather short. The papers published in the seventies include Newman et. al.(49-51), Ohji and Ogura(52,53), and Nakagaki and Atluri(54,55).

Newman and Armen(49) analyzed a center-cracked panel (CCP) subjected to cyclic remote stresses using an initial stress method. The constant strain triangular element was used in the model. Newman and Armen(49) increased the load by a small amount and linearized the problem in a loading step. The linearization error and the redistribution of the contact force by closure, opening and crack extension was then taken into account by readjusting the plastic force after solution was obtained for each loading step. They predicted the crack opening stress consistent with Elber's(56) experimental data. Newman(50) reported more extensive work with an improved numerical procedure in which plastic iteration was made in the loading steps. He investigated the effects of mesh size on the crack closing and opening stresses. He also studied the effects of load ratios(50) and the sequence of loading(49,50). In these papers(49,50), no fracture criterion was used and the crack extension was made at the maximum load in each cycle by releasing the crack tip node. In a follow-on paper, Newman(51) used the crack tip strain as the crack growth criterion and examined the effects of mesh size, critical strain, hardening rule and specimen type on the crack growth behavior.

Ohji et. al.(52) analyzed a double-edge V-notched specimen with cracks

emanating at the notch roots. Their results explained the test results of Frost and Dugdale(57) for non-propagating fatigue cracks under completely reversed loading. Ogura and Ohji(53) analyzed a double-edge notched plate under $R=0$ type constant amplitude loading and studied the effects of a single over load, and high-to-low and low-to-high loading sequences. They obtained results analogous to Newman(50). The constant strain triangular elements were used by Ohji, et.al.(52,53).

Nakagaki and Atluri(54) used a hybrid-displacement finite element method with special crack tip elements in which Hutchinson-Rice-Rosengren type singularities are embedded. The circular region of the singular elements at the crack tip, which was connected to the eight noded isoparametric element mesh around, was translated as the crack was extended incrementally, so the amount of crack extension at a time is not related to the mesh size. A stress-based crack growth criterion was adopted in their study. They verified their approach by considering $R=0$ constant and variable amplitude loading(54,55).

Recent work on crack closure analysis has also been reported by Wastberg(58), Blom and Holm(59), Lalor and Sehitoglu(60) and McClung(61). Wastberg(58) investigated crack growth in a compact tension specimen with a cohesive zone at the crack tip and by use of a fracture criterion based on the crack tip force versus crack separation curve. Blom and Holm(59) studied crack growth in a compact specimen for different stress ratios. Lalor and Sehitoglu(60) performed finite element analyses of a crack emanating from a circular hole in a panel. The loads applied on the model were higher than in other papers. They presented results on the behavior of the opening stress as a function of $\sigma_{\max}/\sigma_{ys}$ at different crack lengths under $R=0$ and -1 loading. They also investigated the effects of the state of stress and the hardening exponent. McClung(61) also modeled the crack closure at similar load levels for a similar geometry. Discussions were also made on the effects of mesh design, crack advance scheme, material properties, constitutive model and biaxial stresses on the resulting opening stress. McClung(61) also correlated the crack growth data using closure-modified

parameters such as ΔK_{eff} and ΔJ_{eff} .

7.2. Finite Element Method

The classical incremental theory of plasticity which utilizes the Prandtl-Reuss flow rule, Von Mises yield criteria and the kinematic hardening rule in the strain space is the basis of the constitutive model employed in this analysis. The Besseling's subvolume method⁽⁶²⁾ is used within this constitutive framework.

The numerical scheme of the elastic-plastic finite element analysis used herein is the initial strain method analogous to the method used in Newman^(49,50). For a given load increment the finite element equation of equilibrium at the elemental level can be written as

$$[K] \{\Delta u\} = \{\Delta f\} \quad (7.1)$$

$$\{\Delta f\} = \{\Delta f^a\} + \{\Delta f^\theta\} + \{\Delta f^p\} \quad (7.2)$$

Here, $\{\Delta f^a\}$ is the incremental applied load vector, the stiffness $[K]$, the thermal load vector $\{\Delta f^\theta\}$, and the plastic load vector $\{\Delta f^p\}$ are defined by

$$[K] = \int_V [B]^T [C] [B] dV \quad (7.3)$$

$$\{\Delta f^\theta\} = \int_V [B]^T [C] \{\Delta \epsilon^\theta\} dV \quad (7.4)$$

$$\{\Delta f^p\} = \int_V [B]^T [C] \{\Delta \epsilon^p\} dV \quad (7.5)$$

where the $[B]$ matrix and the elastic properties matrix $[C]$ are found in standard textbooks⁽⁶³⁾ and hence omitted here. The plastic strain and the thermal strain are

$$\{\Delta\epsilon^P\} = \{\Delta\epsilon_{11}^P, \Delta\epsilon_{22}^P, \Delta\epsilon_{33}^P, \Delta\epsilon_{12}^P\} \quad (7.6)$$

$$\{\Delta\epsilon^\theta\} = \alpha\Delta T \{1, 1, 1, 0\}^T \quad (7.7)$$

The prescribed displacement boundary conditions are enforced using penalty constants along the diagonal of the assembled stiffness matrix and replacing the corresponding entries of the force vector by Δu prescribed times the penalty constant.

For analysis of the contact condition of the crack surface, gap elements, which are actually springs with either very high moduli or zero moduli depending on whether the gap is zero or positive, are introduced on the crack plane; see Figure 99. It is noted that gap elements are also located ahead of the crack tip for use in the propagation of the crack. A gap element connects a node on the crack plane to a nonstructural node placed on the line of symmetry as shown in the figure. If the gap becomes negative in the analysis, the high modulus is used for the spring, whereas if the force in the spring becomes tensile while in contact, the modulus is set to zero. If contact occurs, the diagonal entry of the assembled stiffness for the y-directional degree of freedom (d.o.f.) of the crack surface node of the gap element is replaced with the high modulus and the force on the right hand side is set to zero. The original stiffness and the force vector corresponding to the d.o.f. of the crack surface node are saved and later restored to its place if the gap opens up. In computation the modulus of the spring was set equal to the penalty constant for the displacement boundary conditions. The step-by-step analysis procedure for a loading step is given as follows:

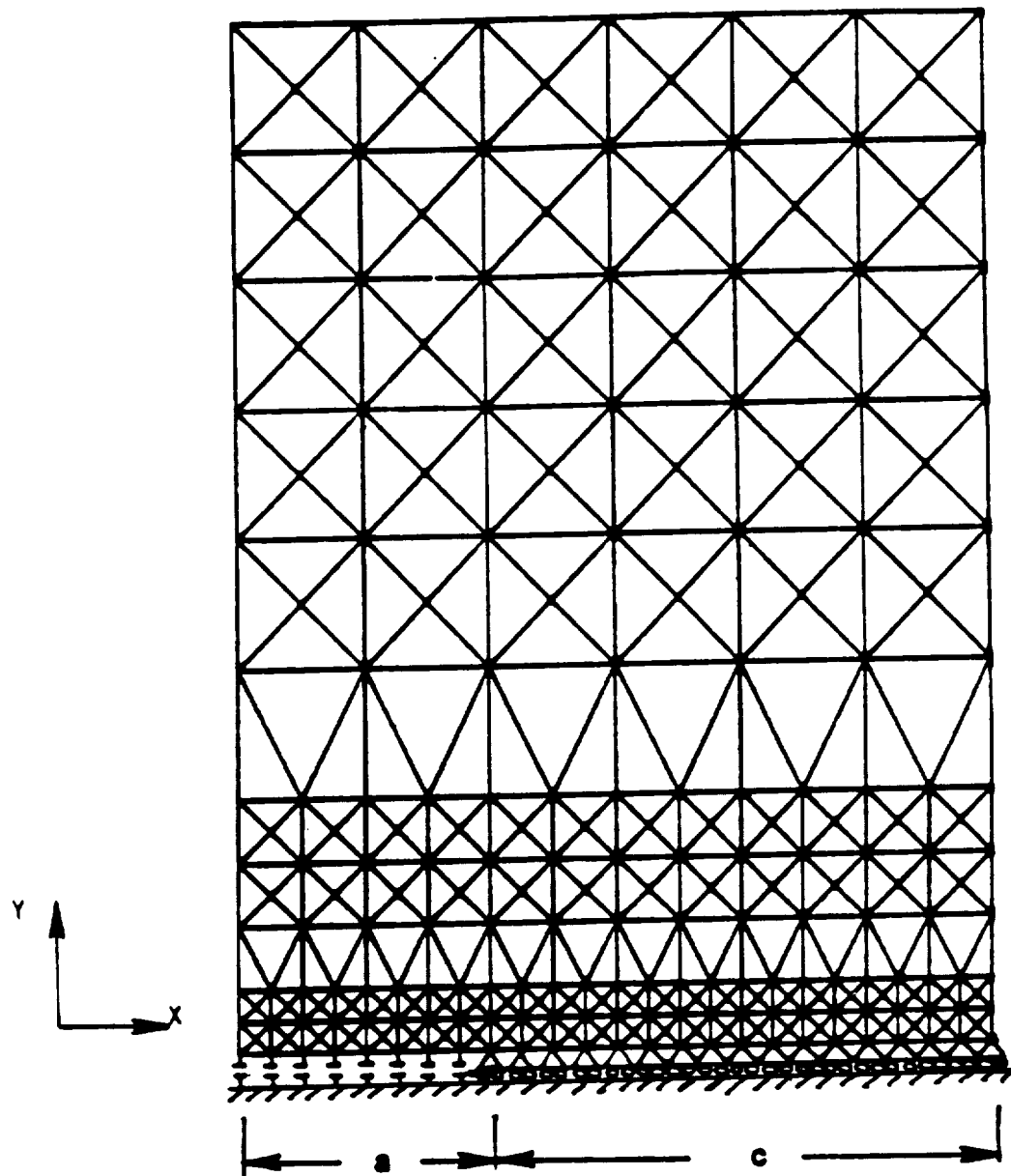


Figure 99: Single Edge Cracked Plate with Gap Elements on the Crack Face.

1. Read the boundary conditions for the loading step.
2. Construct the stiffness (for the first load case) or retrieve the original stiffness saved in a file.
3. Modify the stiffness and the force vector for displacement boundary conditions, and for gap element contact conditions.
4. Solve for the increment of displacement for the incremental elastic force.
5. Compute (or revise) the plastic force and obtain the increment of displacement due to plasticity.
6. Update the total displacement increment and check the contact conditions of gap elements. If there are changes, repeat steps 3 through 5 with modified contact conditions.
7. Check the plasticity convergence criteria. If not converged, go back to step 5.
8. If plastic convergence were achieved and there were no changes in the contact condition, update the field data and write the results in the output file.
9. Go back to step 1 for the next loading step.

The stiffness must be computed in each loading step for TMF cycling where the material properties change with temperature. Notice that the contact conditions of gap elements are examined and revised in the plastic iteration process. This procedure will permit precise assessment of the contact conditions even when the loading step is taken large. For the convergence criteria, the increment of the effective plastic strain defined by

$$\Delta \epsilon_e^P = (2/3 \Delta \epsilon_{ij}^P \Delta \epsilon_{ij}^P)^{1/2} \quad (7.8)$$

was used. It was assumed that the convergence requirement was met if either the absolute value of the change of the effective plastic strain or the percentage change in the two consecutive iterations is smaller than the value given in the input for all the elements in the model.

7.3. Crack Growth and Crack Closure Analysis

7.3.1 Finite Element Model

The finite element model of the single edge notch specimen used in this study is shown in Figure 100. Due to the symmetry of the geometry and the loading condition, only half of the gage length was included in the model. The model consists of 688 constant strain triangular elements and 421 nodes, 33 of which are the nonstructural nodes for the gap elements located on the line of symmetry. The model is 10.16 mm wide, 6.35 mm high and 2.54 mm thick. As discussed earlier, the specimen is subjected to compressive loading at high temperatures. The gage length was taken rather short for possible buckling. As a result, the current model is shorter than other single edge notch specimen models appearing in the literature.

The element size along the crack tip path is certainly a factor which influences the closing and opening behavior of the crack. Obviously, finer crack tip elements permit more residual plastic deformation on the new crack surface as the crack tip nodes are released at the tensile peaks. This will influence the closing stress as Newman⁽⁵⁰⁾ reported for $R=0$ loading.

The size of the mesh along the crack plane in Figure 100 is approximately 0.16 mm. This size is close to the intermediate of the three that Newman⁽⁵⁰⁾ considered. However, the ratio of the mesh to the specimen width is much larger for the present mesh. In other papers^(52,53,60,61), smaller ratios were used for crack closure analysis. The mesh size effect is thought to vary according to the load ratio and the magnitude of loads. Newman⁽⁵⁰⁾ showed that the opening stress was identical for the three meshes he used for $R=0$ loading with a maximum stress equal to half of the yield stress, but it varied at lower stresses. Recently, McClung⁽⁶¹⁾ suggested that mesh sizes less than 5% of the plastic zone size at the maximum load is necessary for accurate determination of the crack closure behavior. He assumed that the crack length is incremented by one mesh each time. In this study, the crack length is incremented by two meshes in each cycle to save

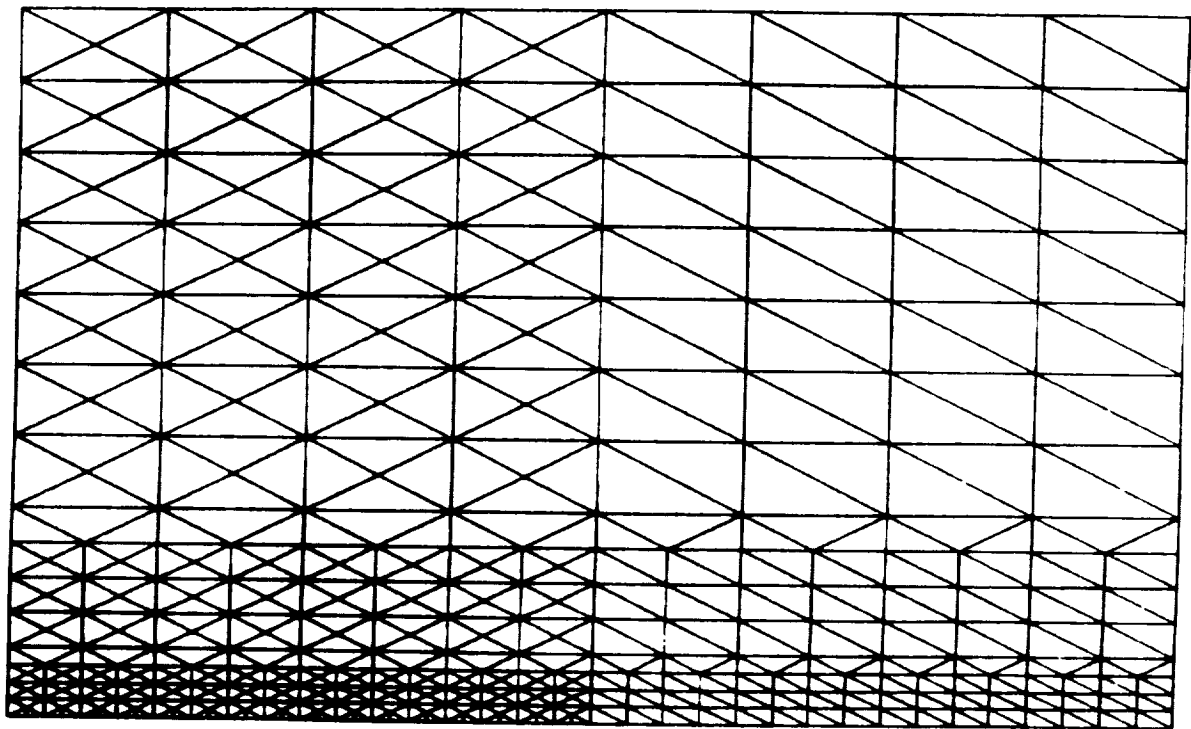


Figure 100: Finite Element Model of the Gage Section of Single Edge Notch Specimen.

the computational time. Therefore, the mesh size should be smaller than 2.5% of the plastic zone size. His work was reported after the completion of the analysis in this program, so the plastic zones for the three control strain ranges analyzed in this study have been compared with the mesh sizes along the crack plane. The plastic zone sizes are shown later in this section along with the results of the finite element analyses. For the strain ranges of 1.15% and 1.7%, the whole crack ligament was in the plastic zone at most of the crack lengths in the analysis. The ratio of the crack length increment to the plastic zone size was in the range of 3.2 to 4.5% in these cases, thus satisfying McClung's criterion. This criterion was not satisfied for the case of 0.5% strain range. The ratio in this case was greater than 14.5%. Nevertheless, the results of this analysis appear to be in good agreement with experimental data and we believe that the mesh is also acceptable for this case.

It is also noted, although a minor aspect, that the small separation of the initial crack surface from the line of symmetry due to EDM machining was neglected since the effects will diminish as the crack propagates.

7.3.2. Analysis Procedure

The finite element analysis was carried out for three specimens subjected to 0.5%, 1.15% and 1.7% total strain ranges as measured by the controlling extensometer.

The analysis of crack growth to be discussed herein is two-tiered. The first part is crack growth simulation wherein the crack tip advances into the material incrementally in each cycle. The purpose is to produce a plastic wake on the newly created crack surface. This analysis will be called a "crack growth simulation". The second part is a cyclic hysteresis loop analysis at constant crack lengths, which is aimed at investigating the crack closing and opening behavior. This analysis will be called a "crack closure analysis". In both analyses the state of stress is assumed to be plane stress. In view of the highly plastic deformation under the loading in

consideration, the plane stress state is believed to be much closer to the real test condition than the plane strain state. The plane stress state will become more prevalent as the crack propagates, and thus the uncracked ligament is subjected to more extensive plastic deformation.

7.3.3. Crack Growth Simulation

The depth of the EDM starter notch in the SEN test specimens was approximately 0.3 mm. Thus, the initial position of crack tip was positioned at the third node from the left on the crack plane in the model which results in an initial crack length of 0.3175 mm. The material at this stage is assumed to be stress-free. In this analysis, each cycle had three load cases as shown in Figure 101; (1) loading up to the tensile peak in a single step, (2) releasing two nodes at the crack tip resulting in an crack length increase of 0.3175mm, and (3) loading down to the compressive minimum in a single step. The process was repeated until the crack length reached 2.54 mm. At this point another cycle of loading was applied and the analysis was terminated. This procedure required 22 load cases.

The loading steps in this analysis may appear to be too large to adequately characterize the nonproportionality of the crack tip field and the residual plastic deformation wake left behind as the crack grows. The simultaneous release of two nodes does not allow the second node to experience the full severity of the crack tip field. This will also worsen the ability to find accurate opening stress according to McClung's(61) criteria for crack length increment. Some preliminary studies were made to investigate the effects of smaller load steps and release of one rather than two nodes at a time. It was found that the changes were rather small for much increased computational efforts as the procedure became more refined. For instance, the differences in the maximum load, minimum load and the CMOD for 1.15% strain range specimen with a 2.54 mm crack length between a single node and two node release simulations were within 4%. The effects of additional loading steps were also small as will be discussed when presenting the results of the hysteresis loop analysis. In this connection, it is worth

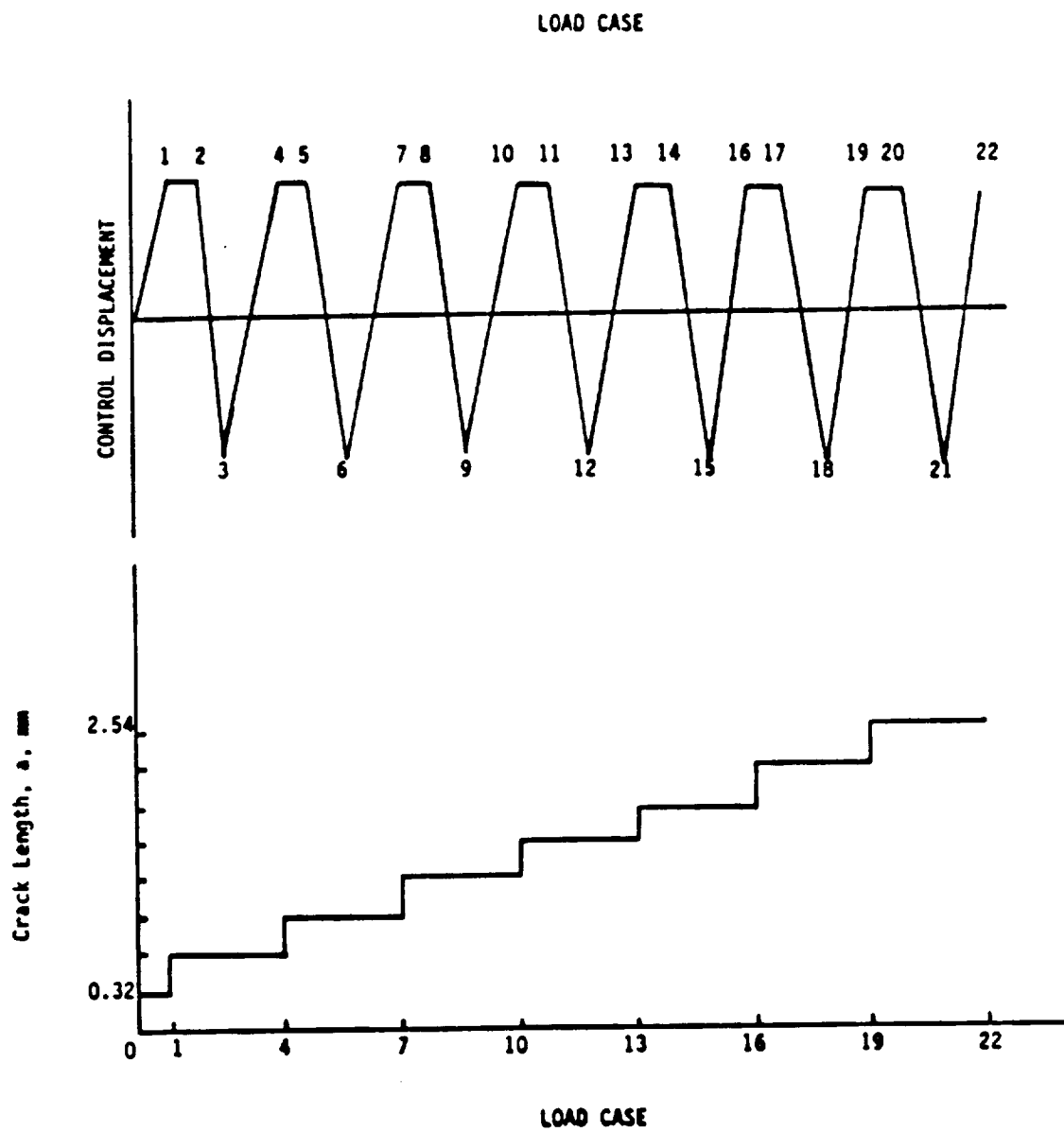


Figure 101: Schematic of Loading Steps in Crack Growth Simulation.

noting the work of Krieg and Krieg⁽⁶⁴⁾ and Schreyer et al.⁽⁶⁵⁾ who investigated the numerical accuracy of an elastic-plastic analysis for various algorithms when one large loading step is taken along a wide range of nonproportional loading paths. For the numerical scheme implemented in the present study, which is essentially the elastic predictor-radial corrector method, and for the loading conditions analyzed, it is expected from these papers that satisfactory results will be obtained without subdividing the loading steps. Furthermore, considering errors which could attribute to other factors, such as discretization and the constitutive relation itself, the procedure to be taken here is well justified.

7.3.4 Crack Closure Analysis

This analysis can be performed at crack lengths associated with any cycles appearing in Figure 101. Due to the cost involved in the analysis we have considered only two crack lengths here, 0.95 mm and 2.54mm. The same crack lengths were used for all three specimens. These crack lengths were selected to analyze situations with significant differences in the crack length, crack growth rate and the extent of deformation. For both crack lengths, the fatigue cycle was divided into ten loading steps. The loading steps are indicated by solid triangles in Figure 102. These include the tensile and compressive peaks, the closing and opening points experimentally observed. Notice also two load cases close to the closing point and the opening point. These load cases are necessary to examine the closing and opening behavior, but not necessarily precisely identify the closing and opening stresses. This could be accomplished by adding a few more load cases.

The crack closure analysis was initiated using the results from the crack growth simulation run which corresponded to the appropriate crack length (load case 7 or 22). The starting point of this analysis was the load case where the material has undergone a whole cycle after node release and not the load case immediately following node release. This will most likely result in a more accurate determination of the closure stresses because the

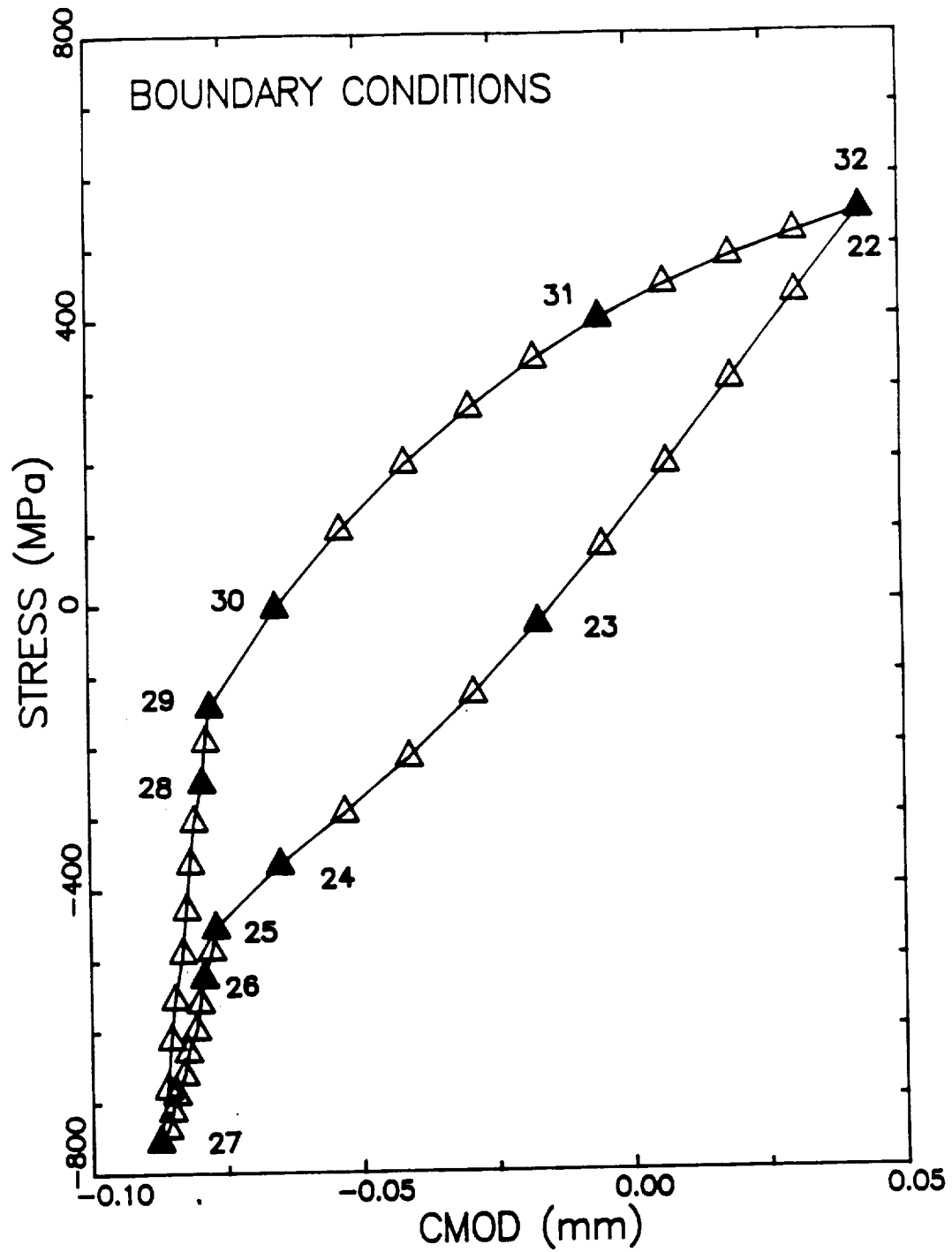


Figure 102: Stress-CMOD Hysteresis Loop Showing Locations of Finite Element Analysis Load Cases.

segment of crack surface most recently created by node release has to be subjected to the contact pressure of crack closing during one simulated fatigue cycle. In most previous investigations, the closure stresses were determined using small unloading steps immediately after the crack tip node was released at the upper peak. The opening stress is nevertheless unaffected since the reverse deformation on the contact area of the crack at the lower peak has already been accounted for.

7.3.3. Boundary Conditions

The boundary conditions in need of discussion are those near the end of the gage section or at the upper boundary of the model. Other boundary conditions are obvious or taken care of internally. The vertical boundary conditions for all the load cases in the two-tier analysis are obtained from the control and backface displacement data measured in the test. The displacement data at the two locations are linearly interpolated and extrapolated to determine the boundary conditions at the nodes on the boundary. The question on the validity of the linearity of the displacement was already raised and discussed in detail in Section 4.0. It was concluded that the linear variation is a reasonable approximation. The lateral boundary conditions on the remote boundary are unknown. However, previous analyses using the results of a full specimen elastic-plastic analysis and zero lateral displacements resulted in rather small changes in the stress intensity factor. Consequently, the lateral displacements at the upper boundary nodes were set to zero. This will give rise to inaccurate shear stress distribution along the boundary, but these stresses are small and the effects will be diminishing with distance from the boundary.

The details of determination of the vertical boundary conditions from the test data are described in the following:

Since the finite element analysis is done in two stages, two sets of boundary conditions are needed. The procedure of determining these will be illustrated for Specimen 4-3, a test performed at 538°C with a strain range

of 1.15% and A_c of ∞ . This is the same specimen used in a previous sections to describe the data analysis procedures.

The boundary conditions for the crack growth simulation analysis were determined by iterating between the available data points. The solid line in Figure 103 shows the variation in crack length (a) with cycle number previously shown in Figure 100. The crack length positions corresponding to the finite element node locations on the crack plane are shown as triangles. The cycle count at these positions was calculated by linear interpolation between the actual data points. In a similar fashion, the maximum and minimum deflections corresponding to the interpolated cycle number were also calculated as shown in Figure 104. The solid lines in this figure were drawn through the maximum and minimum data previously shown in Figures 67 and 69. The data points shown in Figure 104 are the interpolated values which were used as the boundary conditions for the crack growth simulation analysis. A similar interpolation was also performed for loads, crack growth rates, and CMOD values for comparison with those calculated from the finite element analysis.

Figure 105 shows the variation in crack length with cycle number. The triangles indicate the individual data points as determined using the potential drop technique. The darkened points correspond to the cycles where hysteresis loops were obtained on either side of the crack lengths used in the crack closure analysis. A total of 40 sets of boundary conditions were obtained from each cycle. They were determined by placing data points at maximum and minimum deflections, crack closing deflection, and crack opening deflection. Nine other points were placed between each of the following:

- i. minimum and crack opening deflection
- ii. crack opening and maximum deflection
- iii. maximum and crack closing deflection
- iv. crack closing and minimum deflection

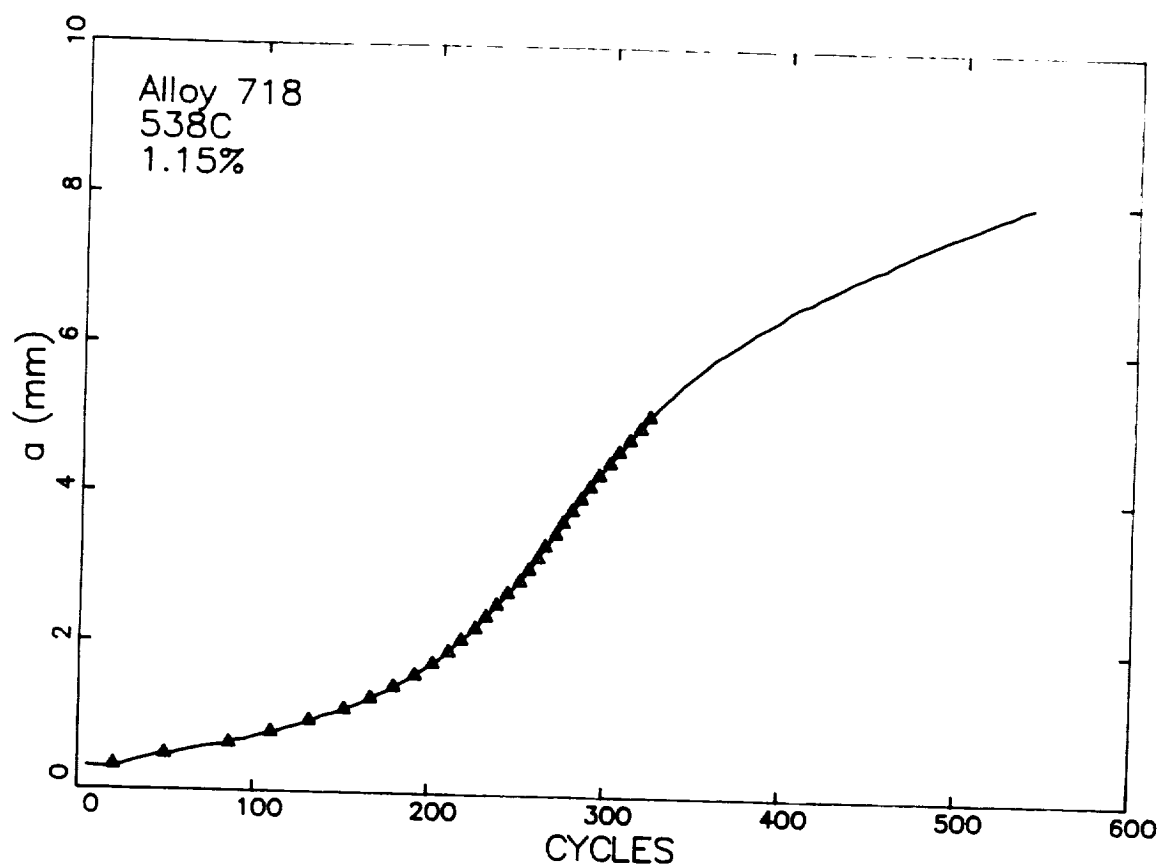
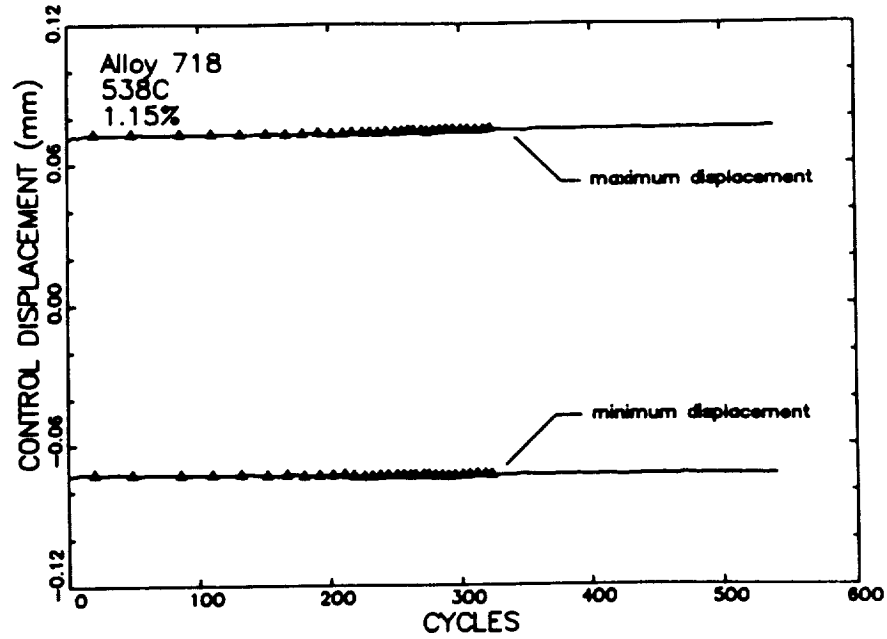
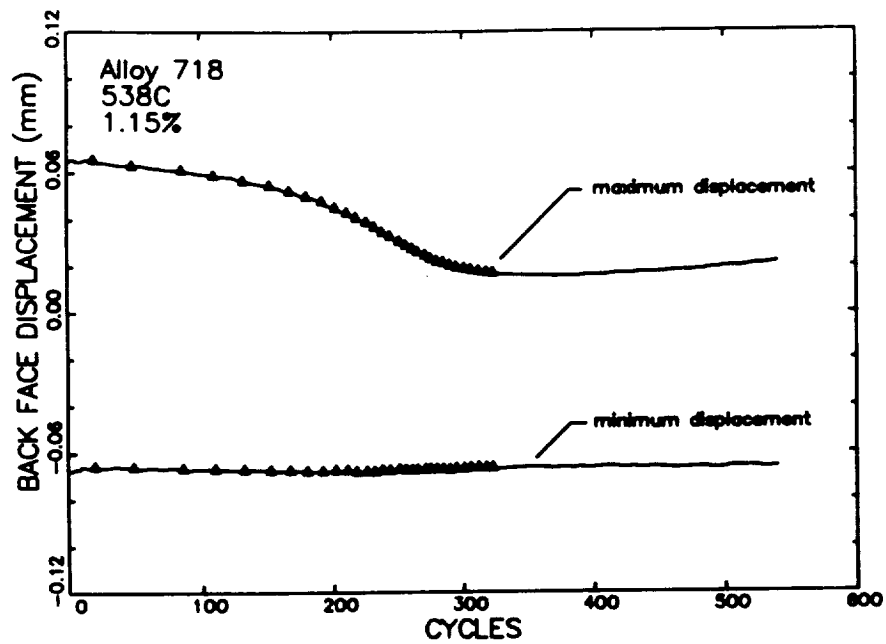


Figure 103: Crack Length as a Function of Cycle - Interpolated for Crack Growth Simulation Analysis



(a)



(b)

Figure 104: Specimen Displacements at (a) Control and (b) Backface Extensometers Used as Boundary Conditions for Crack Growth Simulation Analysis

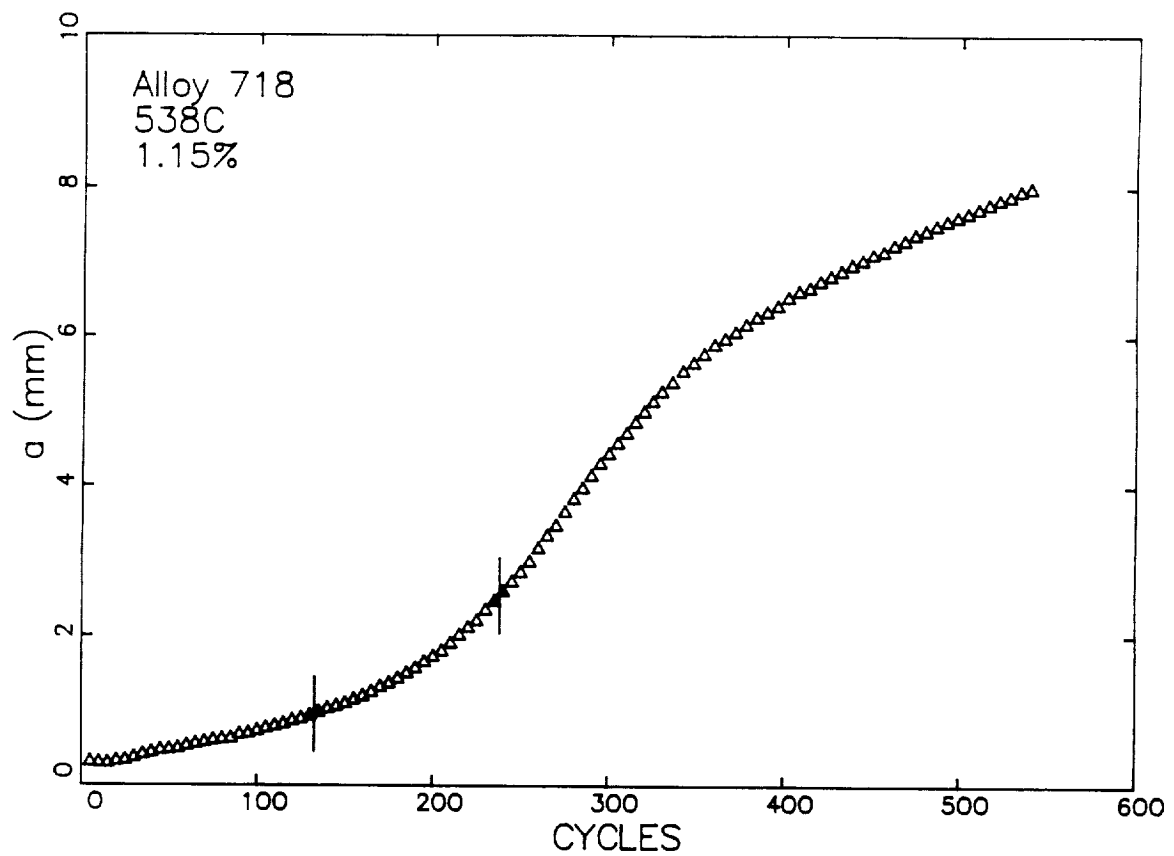


Figure 105: Crack Length as a Function of Cycle and Locations of Two Crack Lengths for Crack Closure Analysis.

The positions of the points were separated by a constant amount of CMOD within each of the four segments listed above.

This procedure was performed for the cycles on each side of the desired crack lengths. As in the case of the boundary conditions for the crack growth simulation, a linear interpolation was performed between the two experimental hysteresis loops. The remote displacements were reported at the same positions in the hysteresis loops. Figure 106 shows the experimental stress-CMOD data from the loops on either side of the desired crack length (x and $+$) and the interpolated data points determined for this case (Δ). This figure illustrates that this approach closely matches the corresponding experimental data.

This procedure has now been repeated for all of the $A_c = \infty$, 538°C crack growth tests. The boundary conditions at 40 points for each hysteresis loop determined in this manner formed the data base for those actually used in the analysis. In the analysis only 10 points were selected among the 40 points as described previously. The 10 load cases are marked by solid triangles in Figure 106.

7.4. Results of Analysis

7.4.1. Crack Growth Simulation

Crack growth simulation of the Alloy 718 SEN tests with three different strain ranges (0.50, 1.15, and 1.70%) were performed using the procedure just described. Figures 107 and 108 show typical examples of the crack surface profile as predicted during the crack growth simulation of the test with the intermediate strain range. The material just behind the crack tip has a cusped morphology due to the residual plastic deformation as the nodes are released (Figure 107). The cusp is obliterated as the material experiences load reversals (Figure 108) and the crack completely closes during the compressive loading. Notice the difference of the crack surface profile from the case of $A_0=1$ loading for which the crack surface remains cusped even

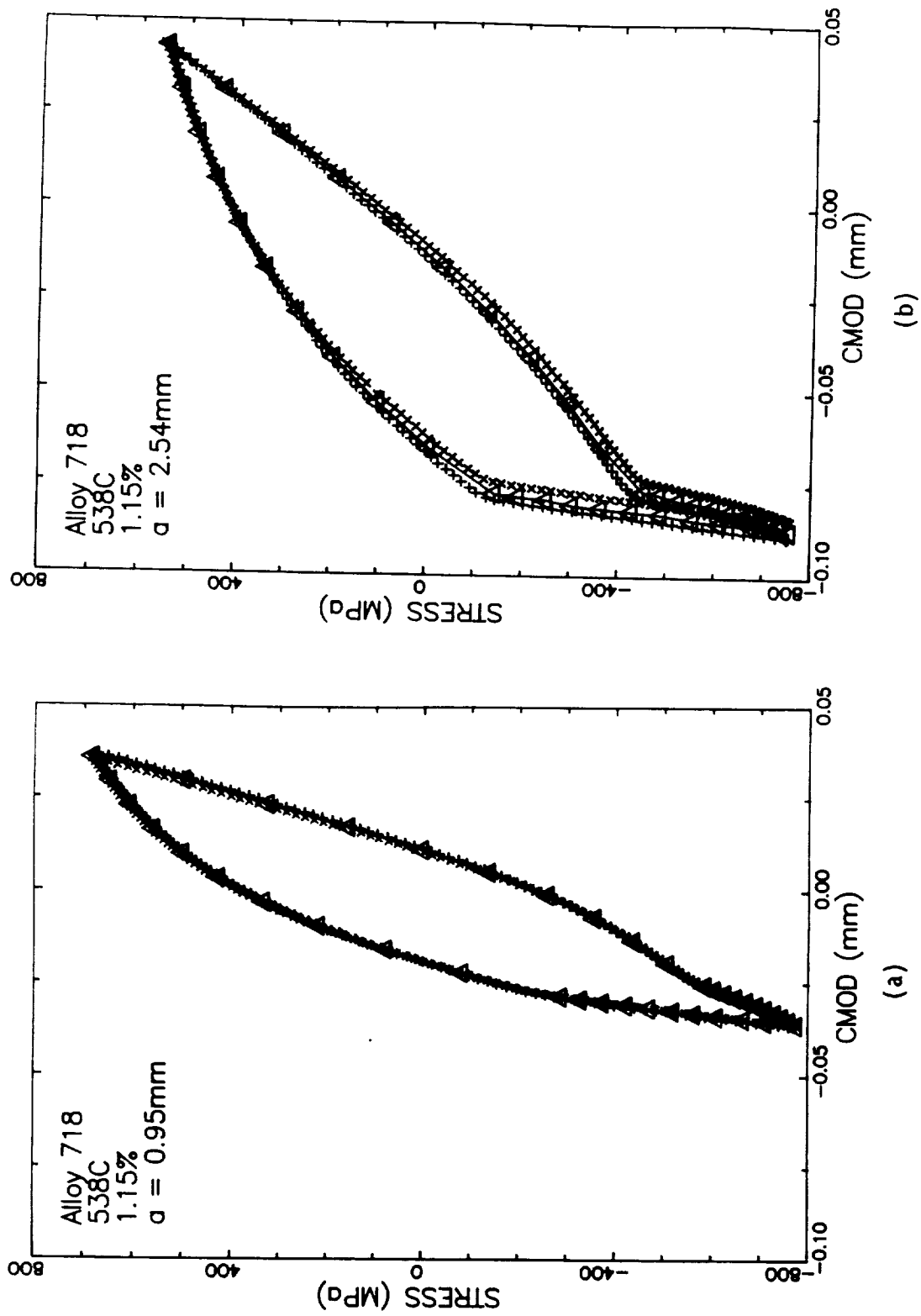


Figure 106: Hysteresis Loops for Crack Lengths of (a) 0.95 mm and (b) 2.54 mm Interpolated for Crack Closure Analysis.

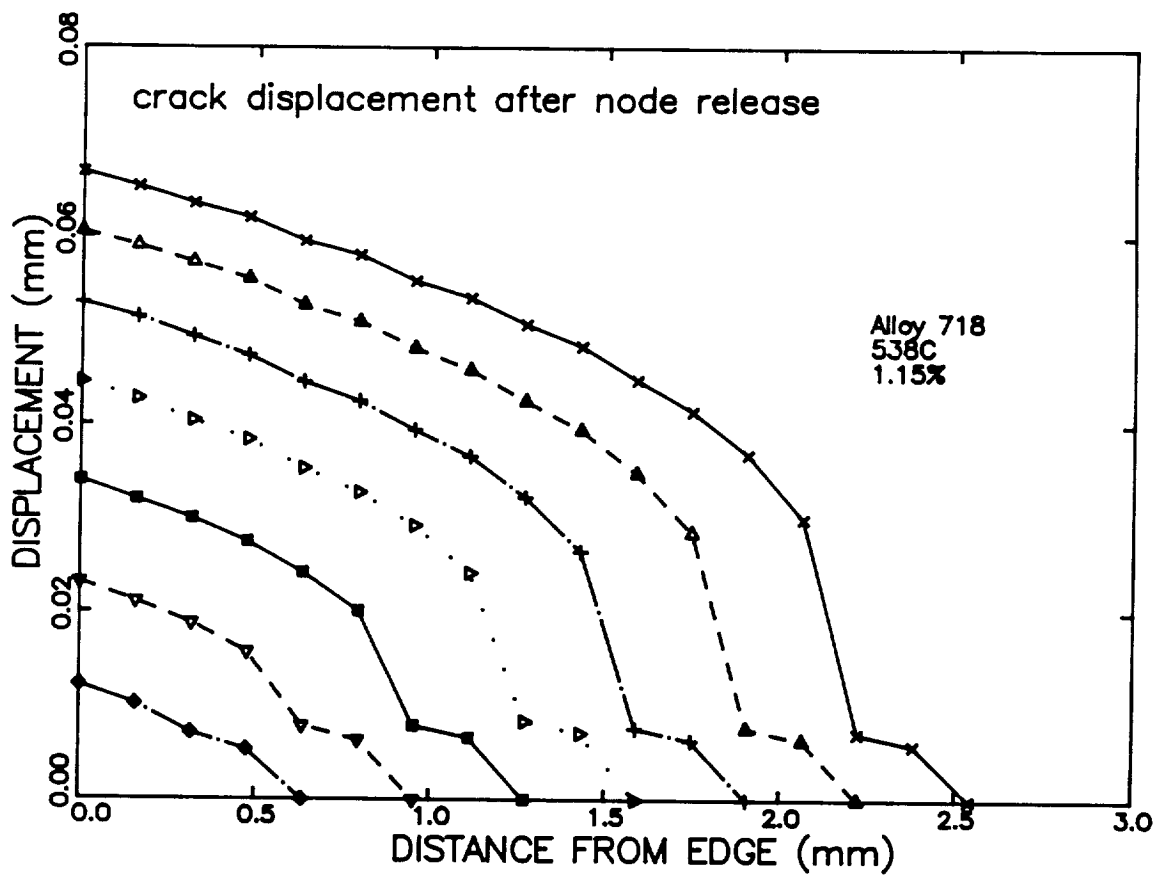


Figure 107: Predicted Crack Surface Displacements After Node Release in a SEN Crack Propagation Analysis of a SEN Specimen Cycled at 538°C (1000°F) and 1.15% Strain Range.

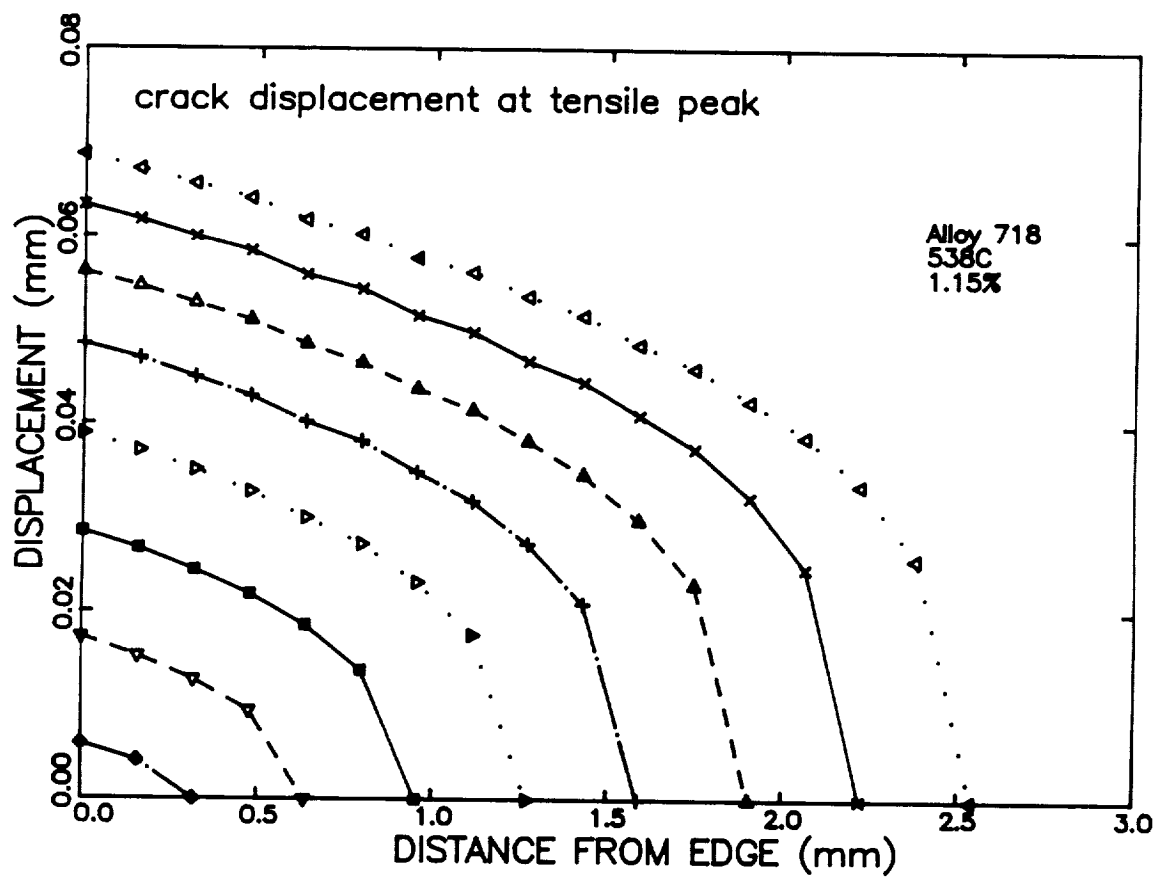


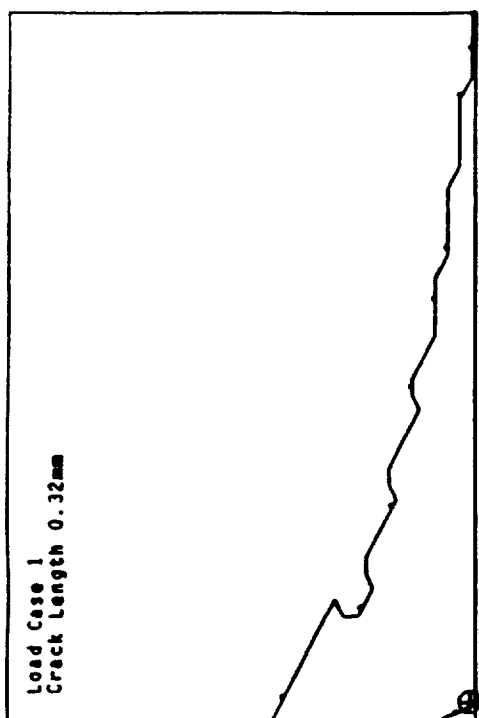
Figure 108: Predicted Crack Surface Displacement at Tensile Peak in a SEN Crack Propagation Analysis of a SEN Specimen Cycled at 538°C (1000°F) and 1.15% Strain Range.

after reloading⁽⁵⁰⁾.

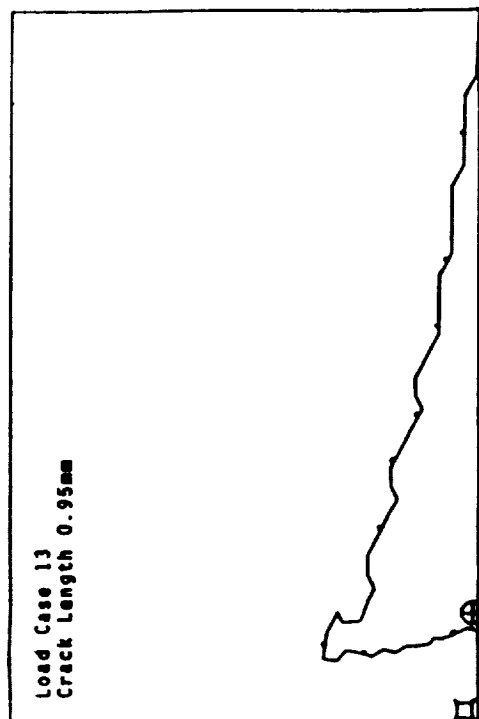
The plastic zones at the tensile peaks are plotted in Figures 109 for the intermediate strain range. The plastic zone became smaller because of load drop, as the crack grew. The plastic zone was oriented backward from the crack tip and spreads over the whole or most of the uncracked ligament at the crack lengths analyzed. For the 1.7% strain range, the plastic zone spreads over the whole specimen and diminished somewhat as the crack propagated. For the 0.5% strain range (nominally elastic case), the initial plastic zone was small but it grew as the crack propagated. The shape of the plastic zone was similar to oval and inclined forward as usually observed in a small scale yielding case. It rotated a little backward and grew fatter with crack propagation.

The average maximum tensile and minimum compressive stress, defined by the total load predicted from the crack growth simulation divided by the cross section area, are plotted in Figure 110 (lines) as a function of crack length for the three strain ranges. The test results (symbols) are also shown in this figure. The correlation seems to be good for all three test conditions. The stress at the tensile peak decreases as the crack becomes longer. This is caused by the increasing contribution of the specimen compliance as the crack propagates under displacement control. The degree of stress drop increased with the amount of plasticity associated. The minimum compressive stress remains relatively constant because at the minimum load the crack is totally closed and the specimen behaves like a uncracked specimen. Notice also in this figure that the stress level at the peaks varies from 75% to 185% of the yield stress (450 MPa) depending on the control strain range and crack length.

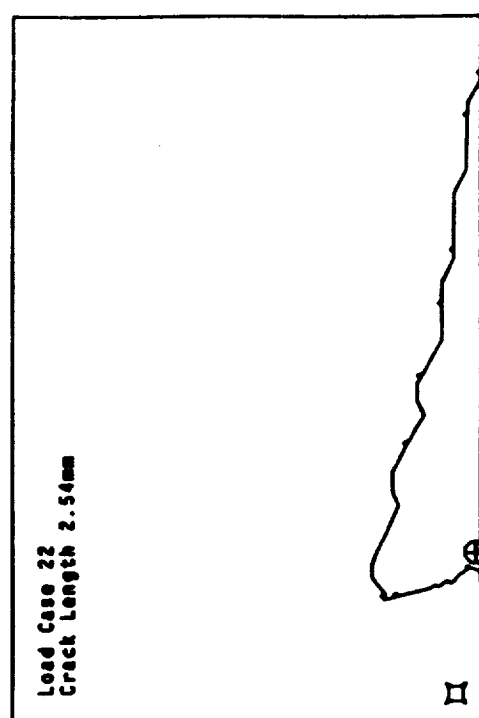
The computed CMOD range (lines) was compared with the test results (symbols) in Figure 111 for the three test conditions. The correlation was again good for the lower strain range specimens, but the quality of the correlation diminishes with increasing strain range.



(a)



(b)



(c)

Figure 109:

Plastic Zones at the Tensile Peaks for 538°C,
1.15% Strain Range, $A_{\epsilon} = \infty$ for Crack Lengths of
(a) 0.3175 mm, (b) 0.95 mm, and (c) 2.54 mm.

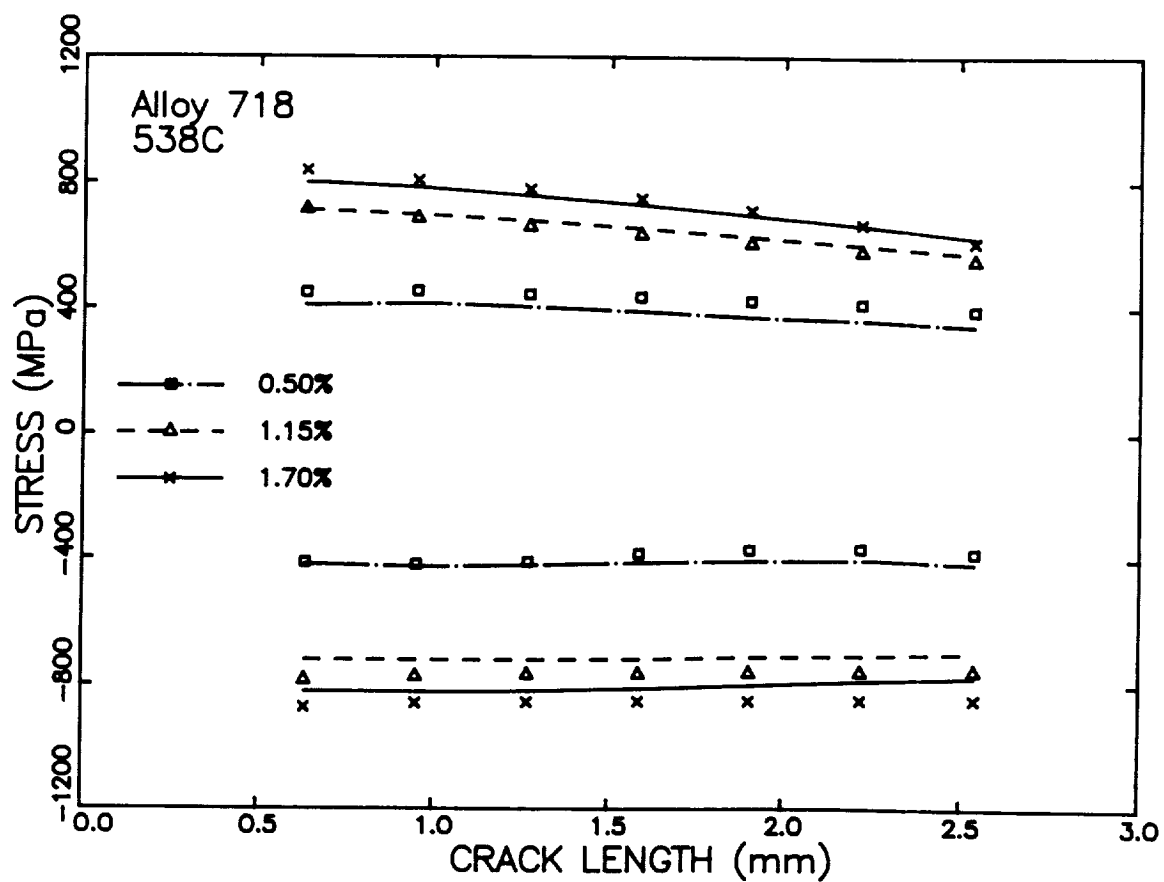


Figure 110: Comparison of Experimental and Predicted Average Cross Section Stresses with Crack Length in a SEN Specimen Cycled at 538°C (1000°F) and 1.15% Strain Range.

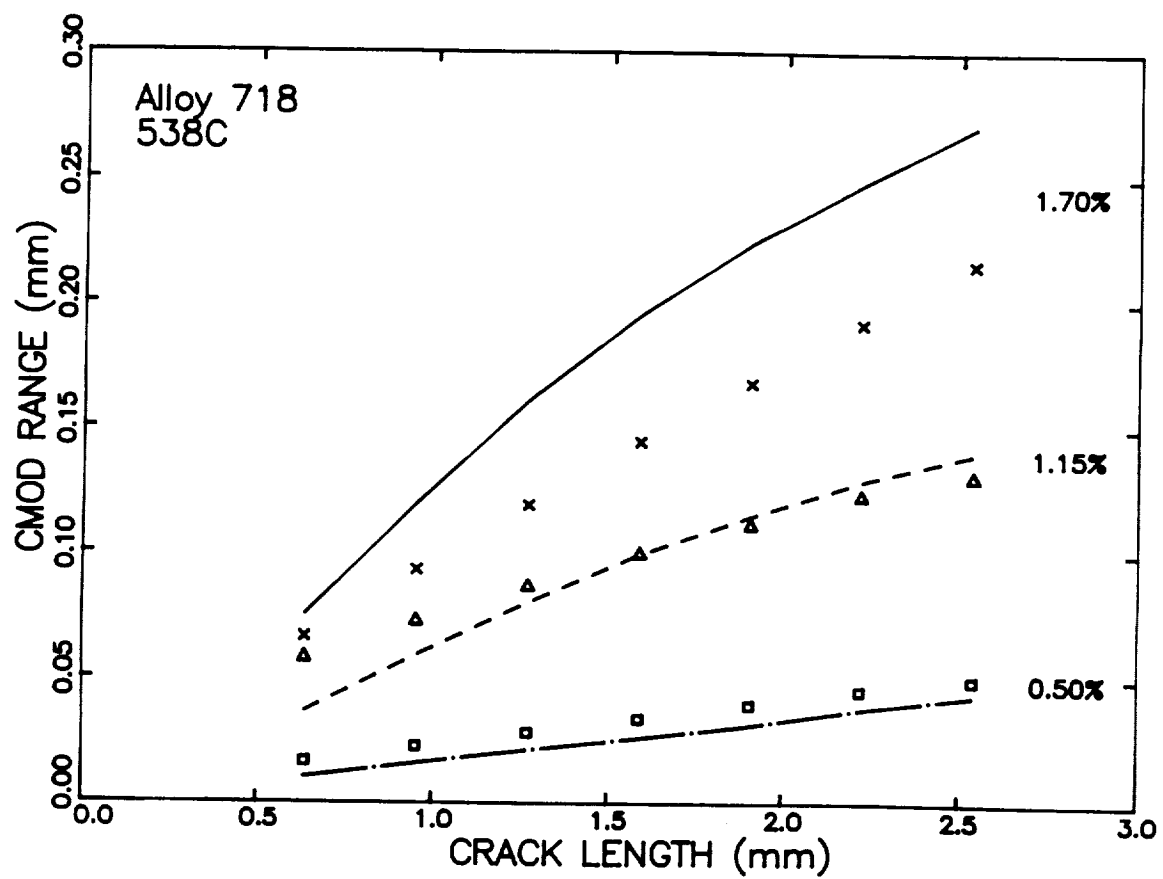


Figure 111: Comparison of Experimental and Predicted CMOD Ranges with Crack Length in a SEN Specimen Cycled at 538°C (1000°F) and 1.15% Strain Range.

7.4.2. Crack Closure Analysis

Crack closure analyses were performed for crack lengths of 0.95mm and 2.54mm for all three strain ranges. Figure 112 shows the crack surface profiles for the load cases in the analysis of a 2.54mm long crack cycled with a 1.15% strain range. The surface profiles at the load cases 26, 27 and 28 are given at the most lower part of the figure, and they are not marked separately because the crack is almost closed for these load cases. The crack was still open at load case 25, which corresponds to the experimentally detected point of crack closure. The first contact was seen at the mouth of the crack in load case 26. This is an interesting observation because crack closure in the experiments was monitored by the displacement at the crack mouth (CMOD). In the analysis of other strain ranges, however, the crack mouth and the near-crack-tip area were simultaneously in contact in the loading step where the first contact appeared. The crack was closed in load case 27 except at the point just behind the crack tip, while it was totally closed in the crack growth simulation run. The near-crack-tip opening was, however, extremely small. The crack was partially closed in load case 28 and it was fully open in load case 29. The crack surface profile of load case 32, the tensile peak, coincided precisely with that of load case 22 which was not shown in the figure. Notice in the figure that the crack surface is slightly wavy due to double node release in the crack growth simulation. The lower peaks in the wave represent the nodes where the crack tip was positioned in the crack growth simulation run. It does not seem that these small ripples affect the closing and opening stresses significantly, nor the irregularity of contact pressure thus created distort the overall crack surface profile to a meaningful extent.

The plastic zones at the tensile peak, the experimental closing and opening points, and the compressive peak are presented in Figure 113 for the intermediate strain range. Notice that the plastic zone at the closing point is significant while it disappeared at the opening point. This indicates that a considerable reverse plastic deformation occurs around the crack tip before the crack starts to close in the reverse loading, however the stresses

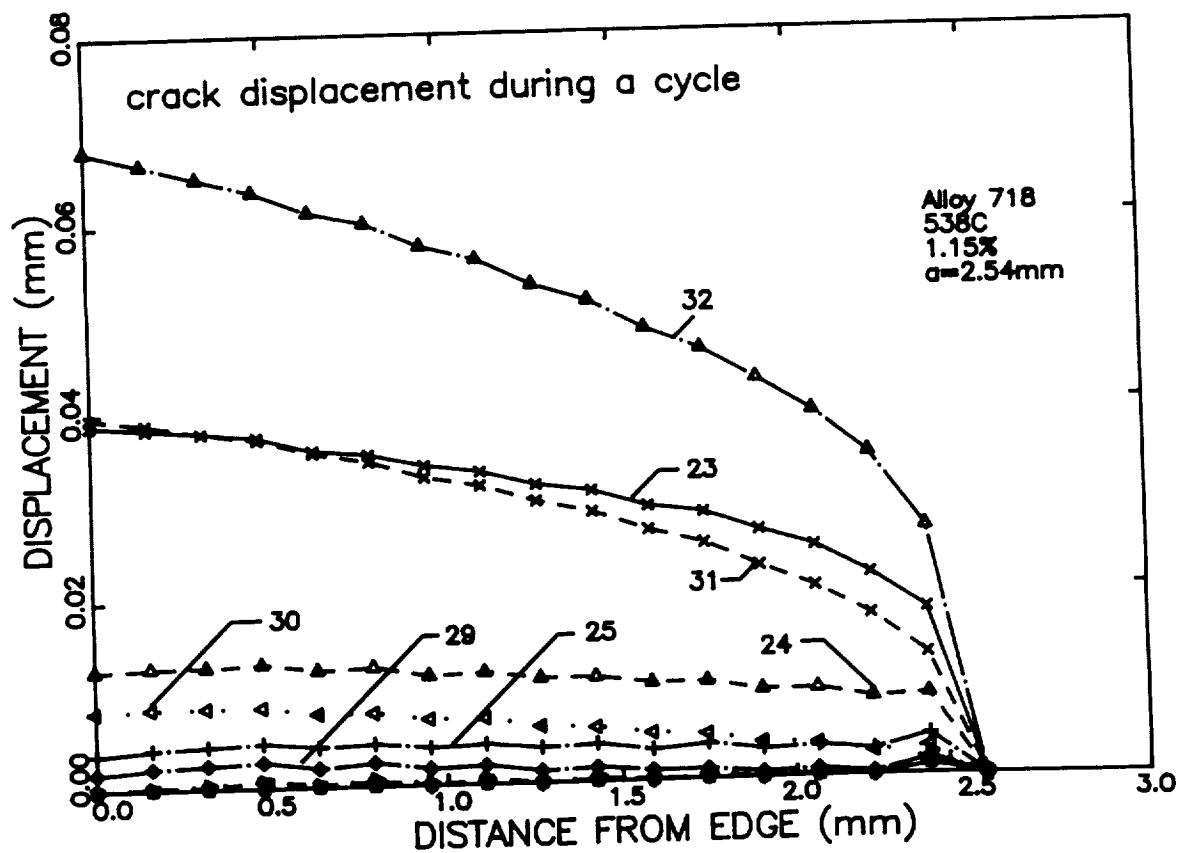


Figure 112: Predicted Variation of Crack Surface Opening During a Loading Cycle of a SEN Specimen with a 2.54 mm Crack Length Cycled at 538°C (1000°F) and 1.15% Strain Range.

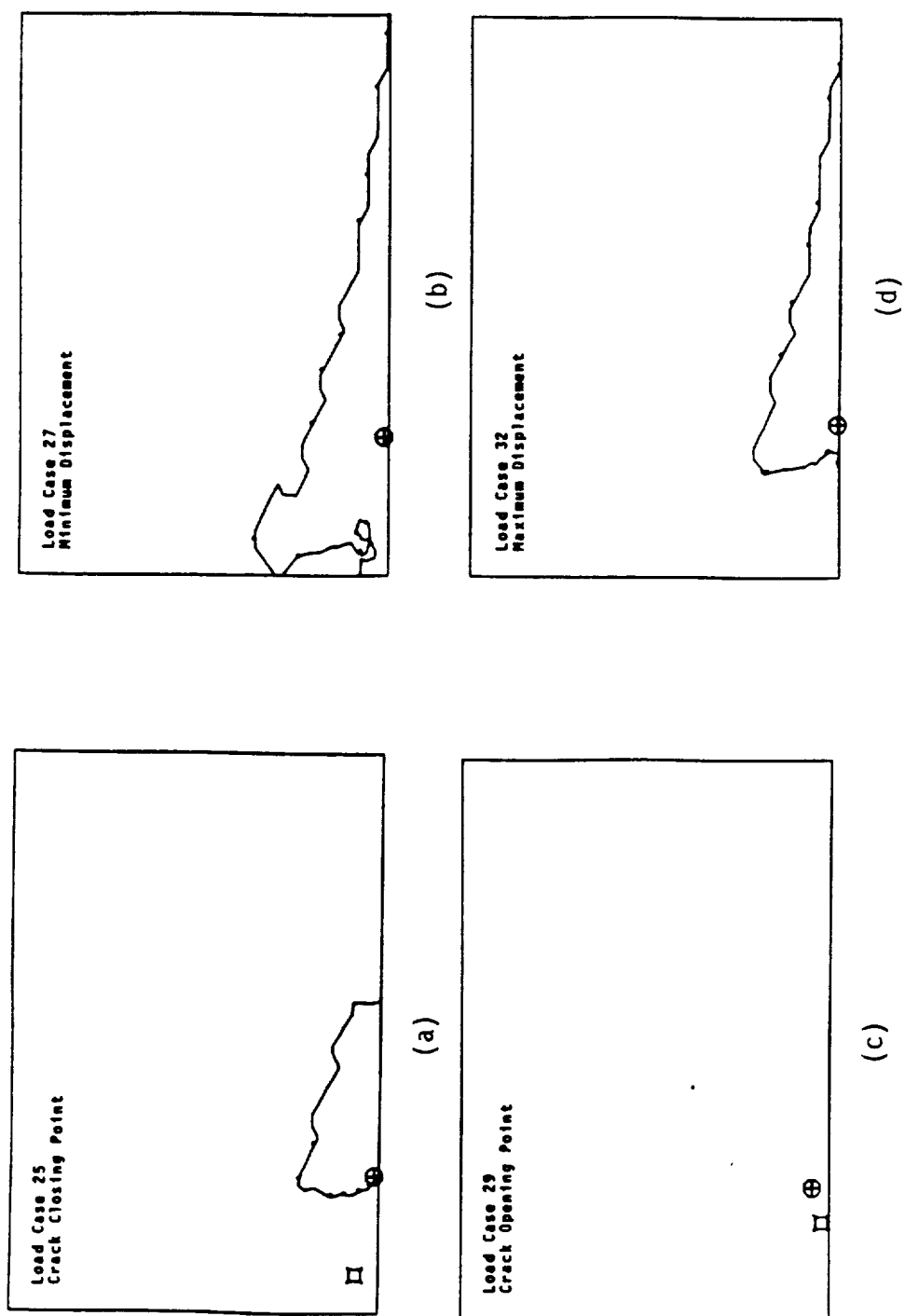


Figure 113: Plastic zones at (a) the Closing Point, (b) the Compressive Peak, (c) the Opening Point, and (d) the Tensile Peak for a SEN Specimen Cycled at 538°C, 1.15% Strain Range, $A_c = \infty$ with a Crack Length of 2.54 mm.

at the compressive peak are much relieved at the opening point. Notice also that the plastic zone is stretched over the crack surface at the compressive peak, meaning that the crack surface is undergone reverse plastic deformation due to contact pressure. For the 1.7% strain range, the plastic zone covered much of the area of the specimen for the four points shown in Figure 113, but to somewhat less extent for the opening point. For the case of 0.5% strain range, the plastic zone at the compressive peak was much smaller than that of the tensile peak and was oriented slightly backward from the crack tip. The plastic zones disappeared at the closing and opening points. The reverse plastic zone on the crack surface at the compressive peak was neither identifiable. It is also noted that the plastic zones at load cases 22 and 32 were virtually identical for all three strain ranges (compare load case 22 in Figure 109 with load case 32 in Figure 113).

The average stress versus CMOD hysteresis loops for the three specimens are shown in Figures 114, 115 and 116. The experimental CMOD data were shifted such that the minimum CMOD measurement and predicted value were equal to compensate the drift of the CMOD measurements as described previously. The stress-CMOD hysteresis loops predicted with the finite element method agree closely with the experimentally measured loops despite various simplifications in the analysis. One can observe the following from the figures:

- The area of the average stress - CMOD hysteresis loop increases as the loading becomes more nonlinear which occurs with increasing displacement ranges and increasing crack length.
- The displacements at the crack closing and opening points are nearly identical for a given hysteresis loop.

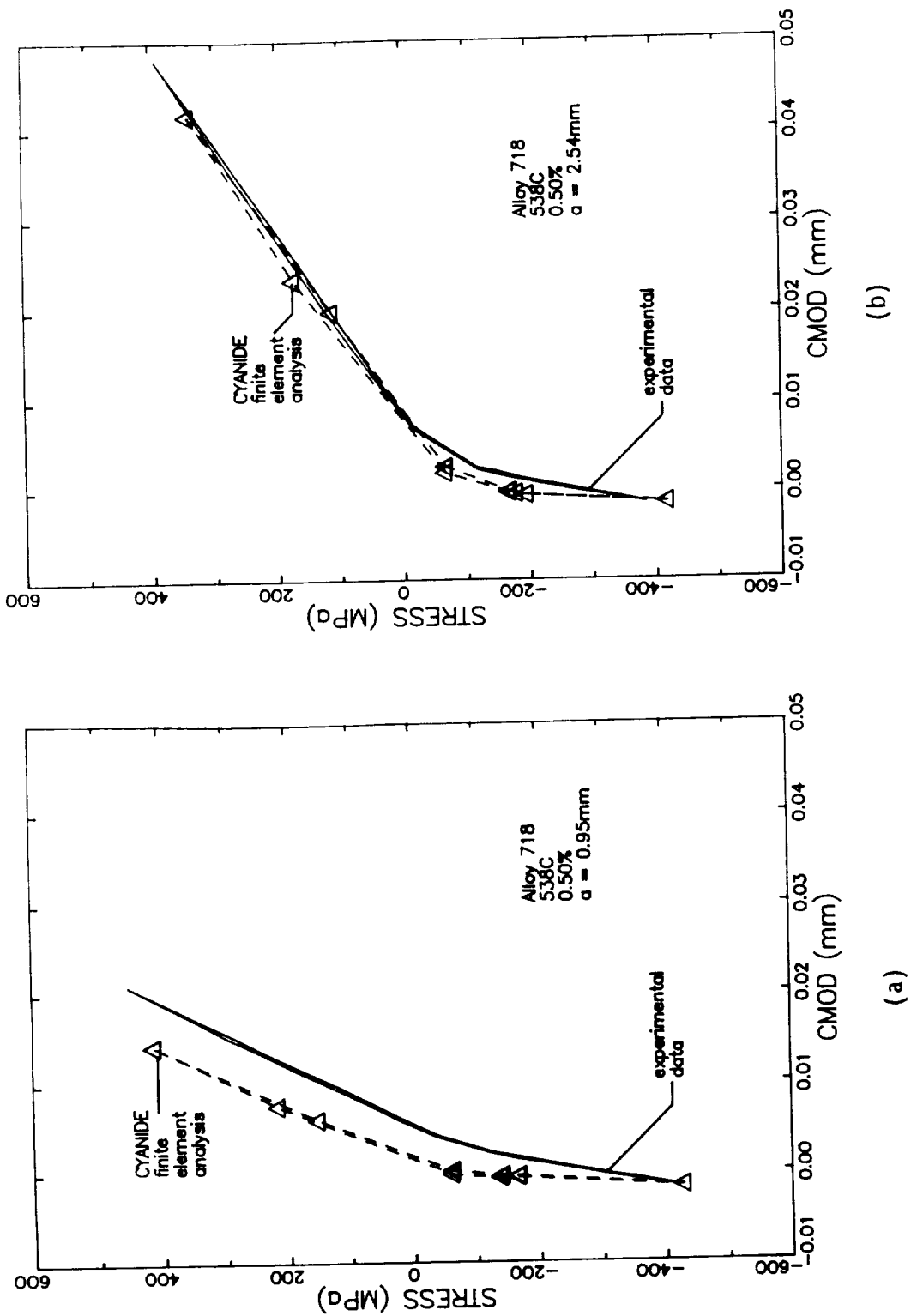
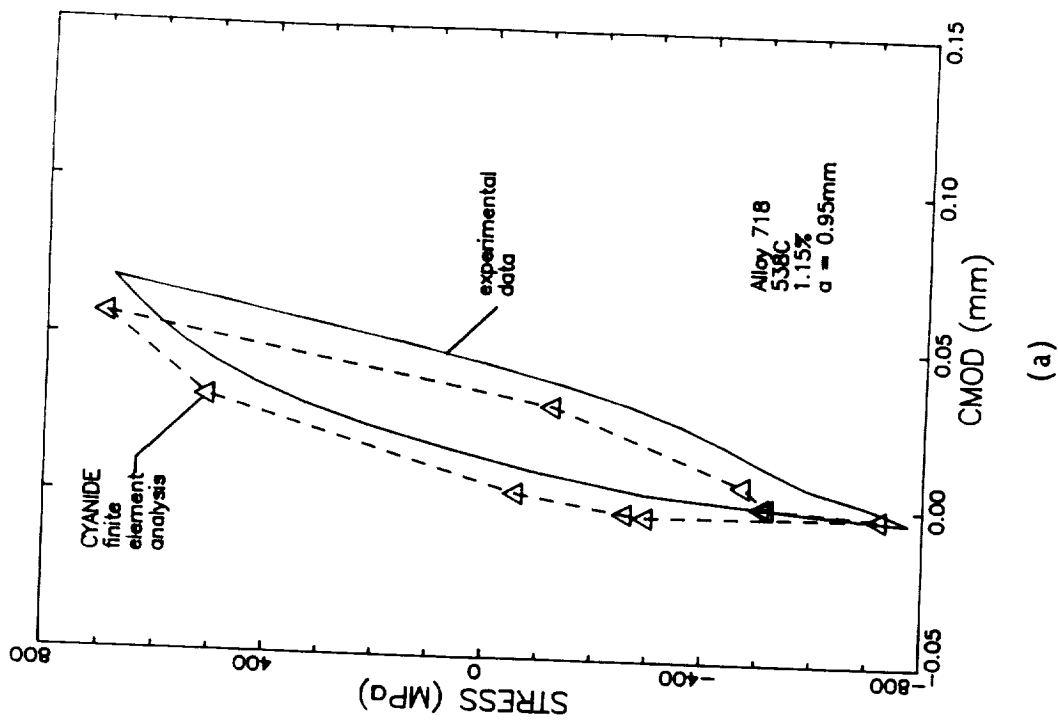
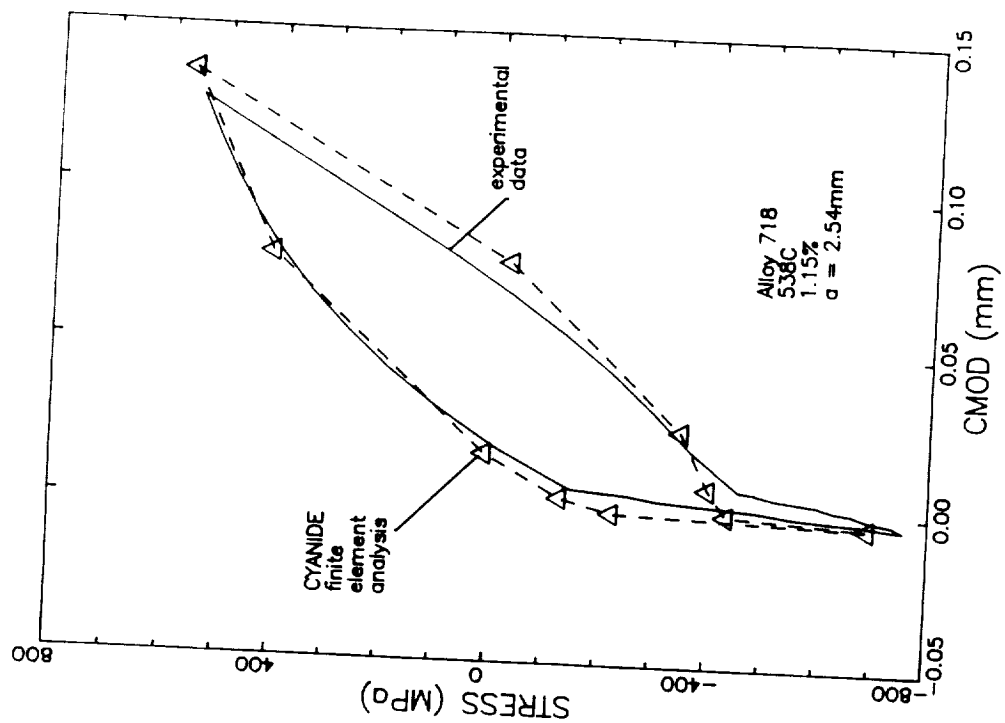


Figure 114: Comparison of Predicted and Experimentally Measured Average Cross Section Stress - CMOD Hysteresis Loops in a SEN Specimen Cycled at 538°C (1000°F) and 0.5% Strain Range with Crack Lengths of (a) 0.95 mm and (b) 2.54 mm.



(a)



(b)

Figure 115: Comparison of Predicted and Experimentally Measured Average Cross Section Stress - CMOD Hysteresis Loops in a SEN Specimen Cycled at 538°C (1000°F) and 1.15% Strain Range with Crack Lengths of (a) 0.95 mm and (b) 2.54 mm.

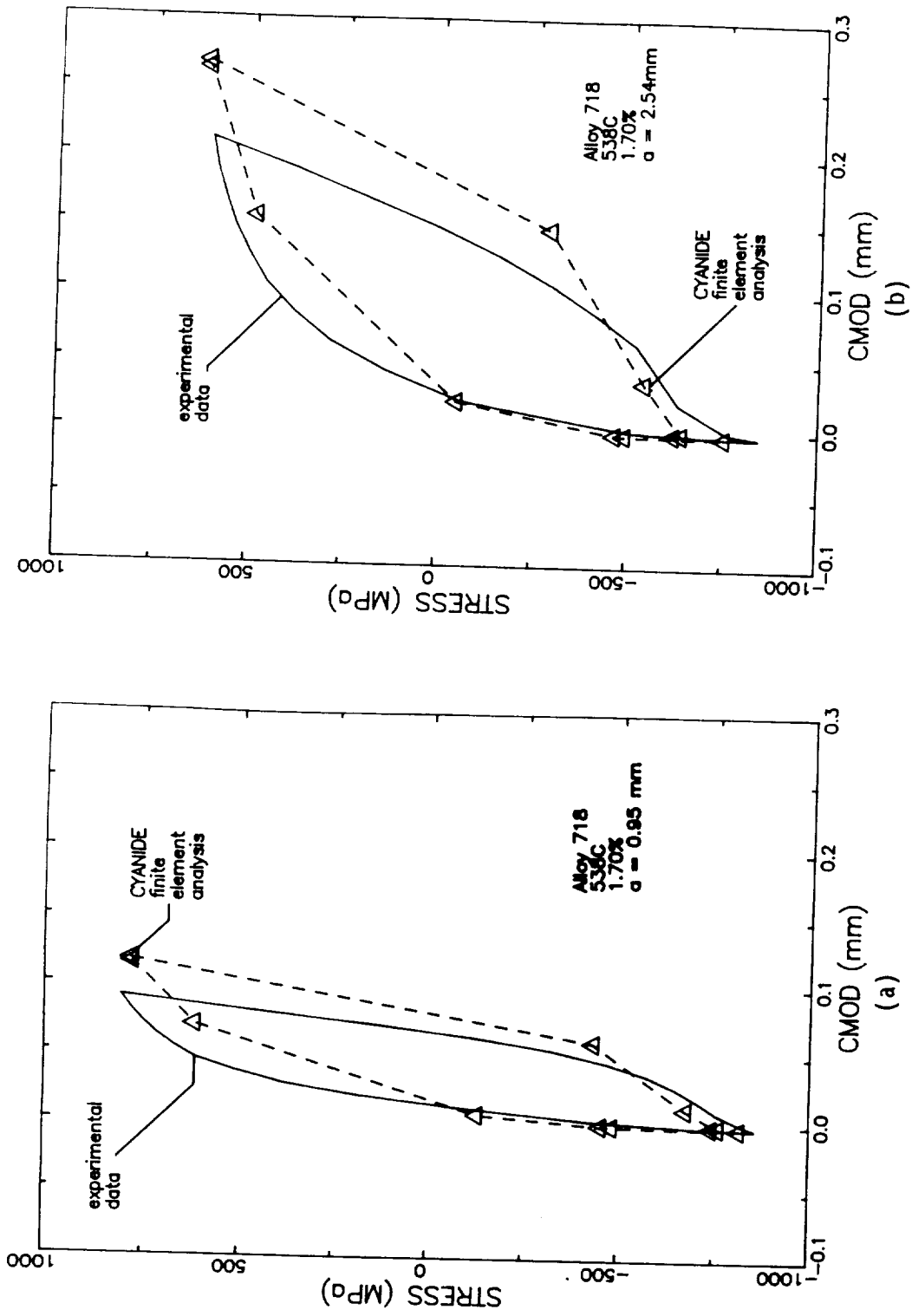


Figure 116: Comparison of Predicted and Experimentally Measured Average Cross Section Stress - CMOD Hysteresis Loops in a SEN Specimen Cycled at 538°C (1000°F) and 1.7% Strain Range with Crack Lengths of (a) 0.95 mm and (b) 2.54 mm.

- The closing stress and the opening stress are compressive for all loading conditions evaluated. The closing stress and the opening stress are approximately equal for the smallest strain range (but the load is still much higher than the load in Newman(50)). As the level of net section plasticity increases, both the closing and opening stresses become more compressive and, within a given hysteresis loop, the closing stress becomes more compressive than the opening stress.
- As the crack propagates, the closing and opening stresses become less compressive. There were no significant changes in the minimum compressive stress. As a result, the portion of the hysteresis loop where the crack was closed became relatively longer with increasing crack length.

The third observation agrees well with the results obtained by other researchers(60,61) for the case of high $A_c = \infty$ remote stresses.

The predicted values of stress and CMOD are nearly identical for load cases 22 and 32 (before and after the multiple load case hysteresis cycle). This provides some substantiation of reliability of numerical results obtained by taking large load steps in the crack growth simulation.

The stress range between the crack opening point and the tensile peak becomes larger as the displacement range increases. This implies that the effect of crack closure on the crack growth rate becomes less significant with increasing plasticity for $A_c = \infty$ loading.

The test data (Figure 66) show that the crack closure and opening loads increase and converge as the crack propagates. Since the maximum load decreases with increasing crack length in these strain control tests, the range of load over which the crack is open decreases drastically as the crack becomes longer. This results in decreasing the ratio of crack opening load range to the total load range as the crack propagates.

Comparison of the predicted and observed hysteresis loops of the stresses and displacements at the positions of the control and backface extensometers was quite good. The only major discrepancy between the experiment and analysis was the prediction of cusps at the closing and opening points; while in the experimental data, the cusps were only slightly visible in the control displacement loops, and virtually nonexistent in the backface displacement loops. It is conjectured that the plane stress assumption in the analysis is related to this deviation.

7.5. Computation of Path-Independent Integrals

The four path-independent (P-I) integrals selected during the P-I integral survey (Section 2.0) were computed by postprocessing the results of finite element analyses for the three strain ranges. The results are presented in the following sections.

7.5.1 Crack Growth Simulation

The paths of computation are shown in Figure 117. The paths were taken away from the remote boundary to avoid possible effects of the assumed boundary conditions. However, the most outer path was taken far enough such that possible inaccuracies in the near-tip field due to neglecting the singularities at the crack tip do not create significant errors in the values of the P-I integrals. The left sides of the paths were taken along the front edge of the specimen, so that the crack tip is always located inside of the paths during propagation. The numerical results showed path-independence of the integrals. The values of P-I integrals at different crack lengths are tabulated in Tables 15, 16 and 17. The J^* integral is plotted as a function of crack length in Figure 118 as an example. The values of P-I integrals were somewhat sensitive to the tolerance for plastic iteration used in the finite element analyses, but the variation was not large enough to affect any conclusions on the crack growth rate as a function of ΔJ_X (Here, ΔJ_X implies the range of any of the four P-I integrals being considered). In the tables, the ΔT_p^* and ΔT_p integrals are for the intervals from the compressive peak to

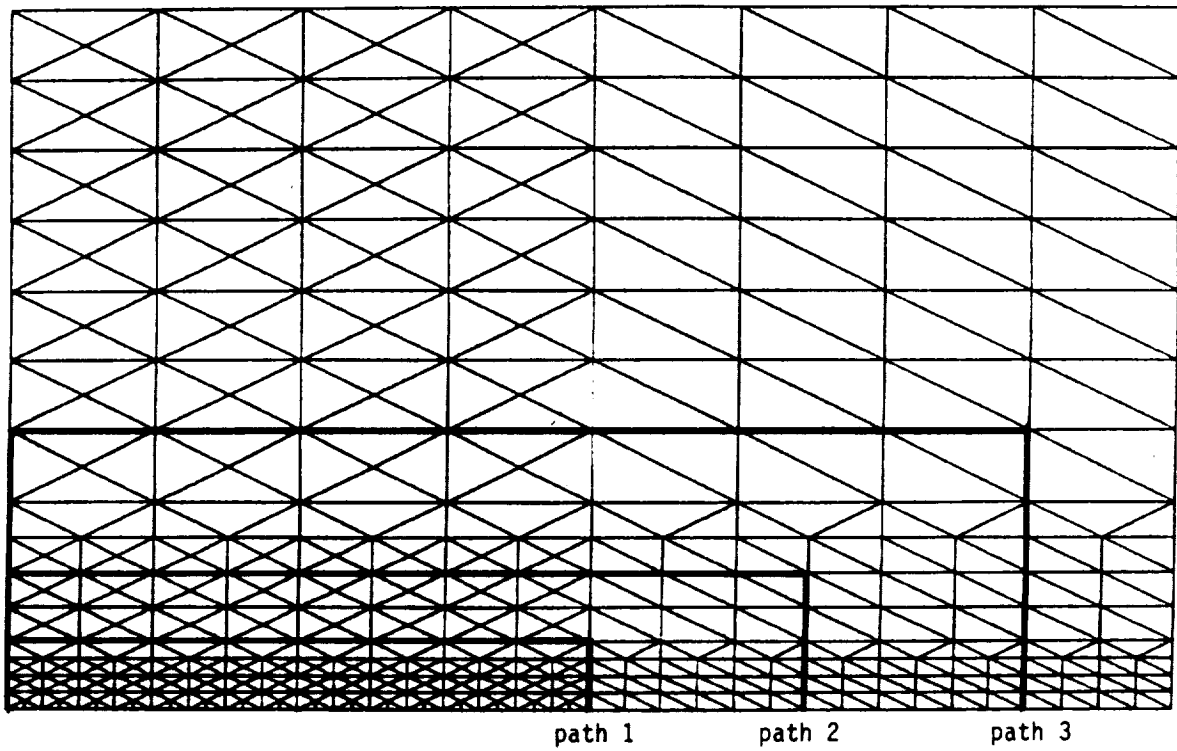


Figure 117: Integration Paths for Crack Growth Simulation Analysis.

Table 15: P-I Integral Values at Different Crack Lengths of SEN Specimen
N4-31 (538°, $A_c = \infty$, 0.50% Strain Range)

Crack length (mm)	Peak (Tensile or Compressive)	J^*	\hat{J} (1.E-3 MPa-m)	ΔT_p^*	ΔT_p
0.3175	T	1.13	1.06	1.13	1.21
0.6350	T	2.54	2.54	2.54	2.80
	C	0.	-0.04		
0.9525	T	3.96	4.02	3.99	4.64
	C	0.1	-0.03		
1.2700	T	4.94	5.14	4.98	6.04
	C	0.	-0.04		
1.5875	T	5.69	5.90	5.75	7.45
	C	-0.01	-0.05		
1.905	T	6.35	6.68	6.46	8.83
	C	-0.03	-0.08		
2.2225	T	7.46	7.81	7.60	10.75
	C	-0.05	-0.10		
2.5400	T	7.96	8.42	8.12	12.04
	C	-0.08	-0.15		

Table 16: P-I Integral Values at Different Crack Lengths of SEN Specimen N4-3 (538°, $A_c = \infty$, 1.15% Strain Range)

Crack length (mm)	Peak (Tensile or Compressive)	J^*	\hat{J} (1.E-3 MPa-m)	ΔT_p^*	ΔT_p
0.3175	T	6.03	5.82	6.03	8.72
0.6350	T	16.58	17.25	16.24	14.01
	C	0.03	0.		
0.9525	T	25.48	26.71	25.27	22.70
	C	0.05	0.03		
1.2700	T	31.96	33.92	32.30	30.33
	C	-0.34	-0.63		
1.5875	T	38.62	40.67	39.07	37.60
	C	-0.59	-1.27		
1.905	T	41.10	43.40	42.49	43.22
	C	-1.49	-2.46		
2.2225	T	44.12	46.32	45.47	46.31
	C	-1.31	-2.53		
2.5400	T	44.26	46.32	45.06	47.88
	C	-1.03	-2.44		

Table 17: P-I Integral Values at Different Crack Lengths of SEN Specimen
N5-33 (538°, $A_c = \infty$, 1.70% Strain Range)

Crack length (mm)	Peak (Tensile or Compressive)	J^*	\hat{J} (1.E-3 MPa-m)	ΔT_p^*	ΔT_p
0.3175	T	27.50	22.68	27.50	57.43
0.6350	T	47.29	48.86	45.94	108.85
	C	-0.29	-0.29		
0.9525	T	74.29	76.76	73.82	130.67
	C	-0.81	-1.20		
1.2700	T	72.00	72.31	74.36	144.08
	C	-0.58	-1.85		
1.5875	T	88.95	88.16	100.81	158.44
	C	-1.05	-2.45		
1.905	T	92.00	92.93	101.12	174.45
	C	-3.12	-2.40		
2.2225	T	97.08	99.32	97.39	175.31
	C	3.99	6.28		
2.5400	T	116.67	124.70	114.31	166.83
	C	2.33	1.66		

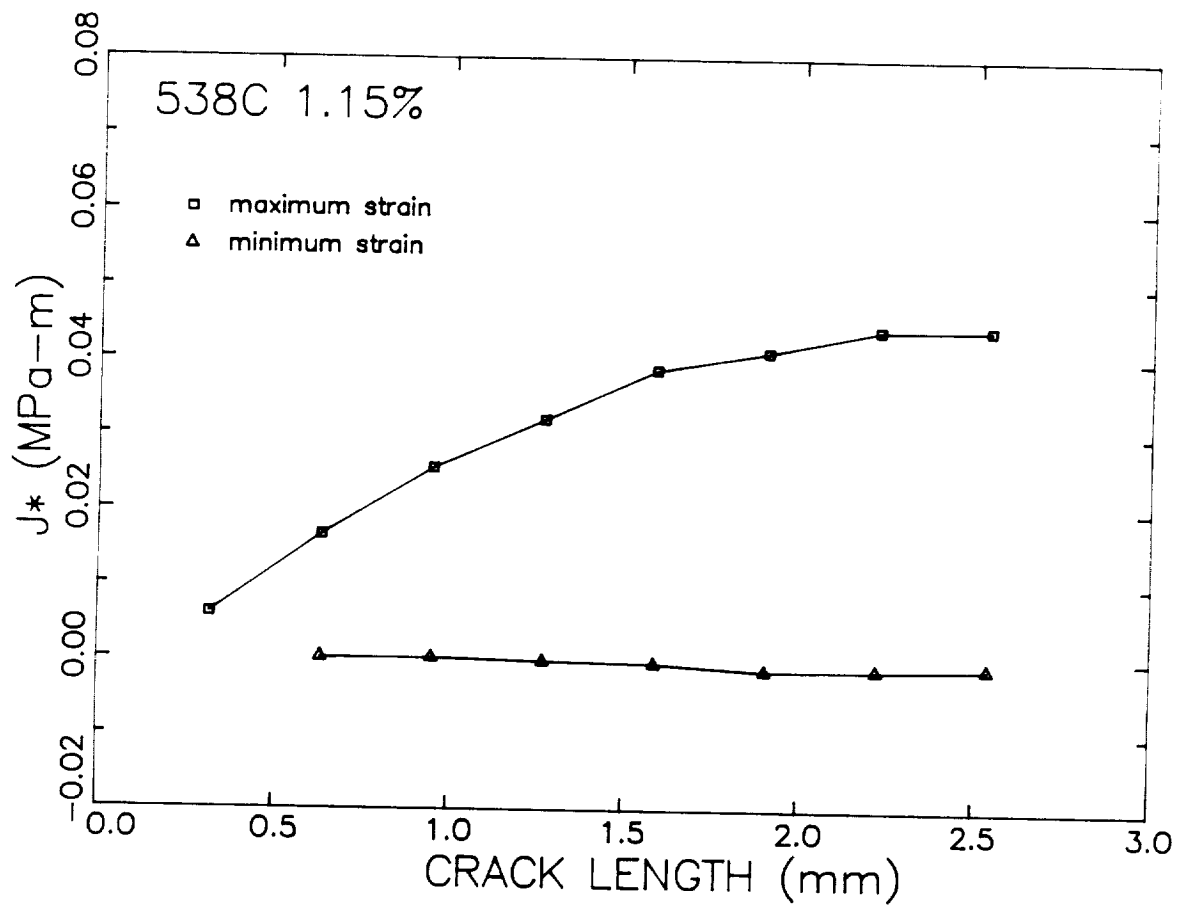


Figure 118: Predicted values of J^* as a Function of Crack Length in a SEN Specimen Cycled at 538°C (1000°F) and 1.15% Strain Range.

the next tensile peak. It is recognized that the increment of the strain energy density in equations (2.7) and (2.8) assumes piecewise linear relation between the stress and strain and therefore the computation of ΔT_p^* and ΔT_p must be made over a series of small load increments. In this respect, the values of ΔT_p^* and ΔT_p computed here are only approximate values. The requirement of small loading steps may be a disadvantage of the ΔT_p and ΔT_p^* integrals compared with J^* and \hat{J} , because more loading steps for accurate computation of T_p^* and T_p usually mean more computational time.

Notice also that the J^* and \hat{J} integrals are negligibly small at the compressive peaks. These integrals increase with crack length at tensile peaks but the rate of increase slows down as the crack grows deeper. This is caused by the decreasing load at longer crack lengths in strain control tests.

7.5.2 Crack Closure Analysis

The crack closure analysis was performed at two crack lengths for each strain range case as mentioned earlier. The paths for 0.95 mm crack and 2.54 mm crack are shown in Figures 119 and 120. Examples of the variation of the P-I integrals with integration paths are given in Figures 121 through 126 and 127 through 132 for 2.54 mm crack, smallest and largest strain range cases, respectively. The equivalent distance from a crack tip means the average distance from the crack tip to the nodes along the path. The numerical results of the P-I integrals showed path-independence to the degree similar to Figures 121 through 132 for most cases. In general, more disturbance in the path-independence was found at higher strain ranges and at the longer crack length where more plasticity effects are involved. The T_p^* and T_p integrals, which are the sums of the respective incremental integrals, varied somewhat more with paths due to the cumulative effect of small variations of ΔT_p^* and ΔT_p with paths. The numerical values in the Figures 125, 126, 131 and 132 are relative to those at Load Case 21; i.e. the summation was made from this point. Integration from the initial point of analysis is unnecessary, because we will only need incremental values, perhaps from the

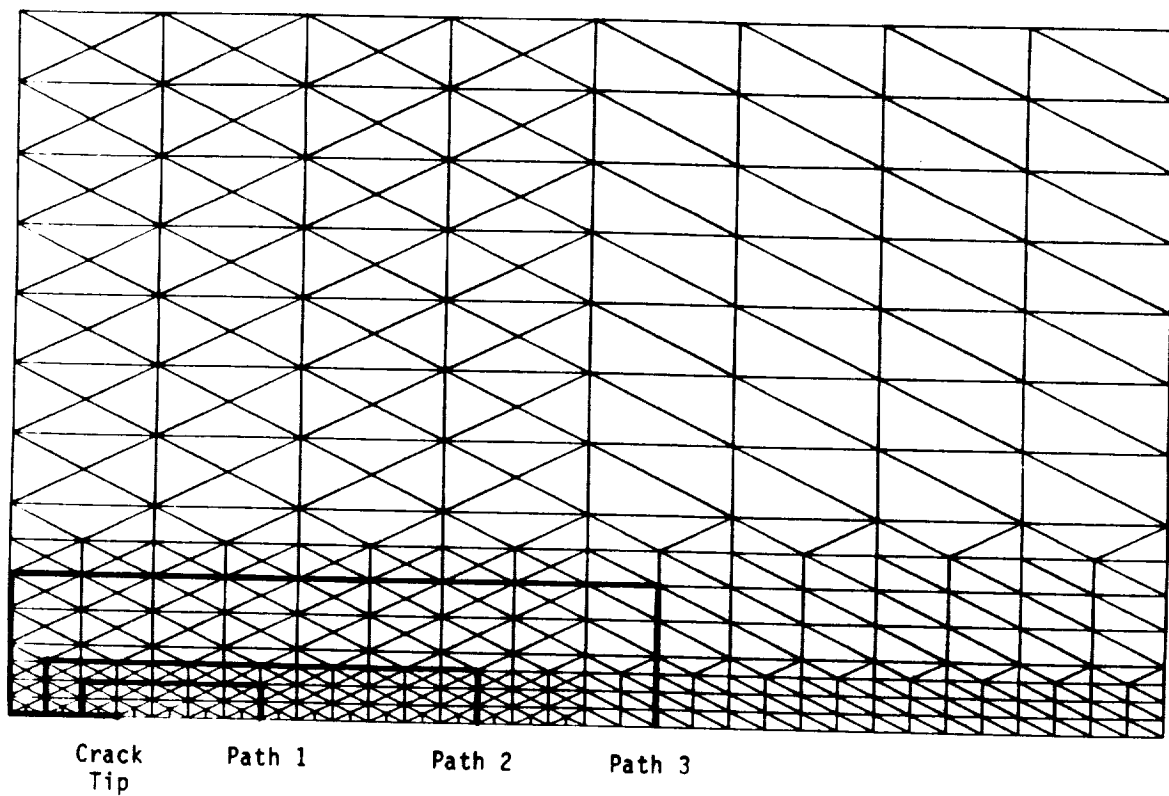


Figure 119: Integration Paths for Crack Closing and Opening Analysis at Crack Length of 0.95mm.

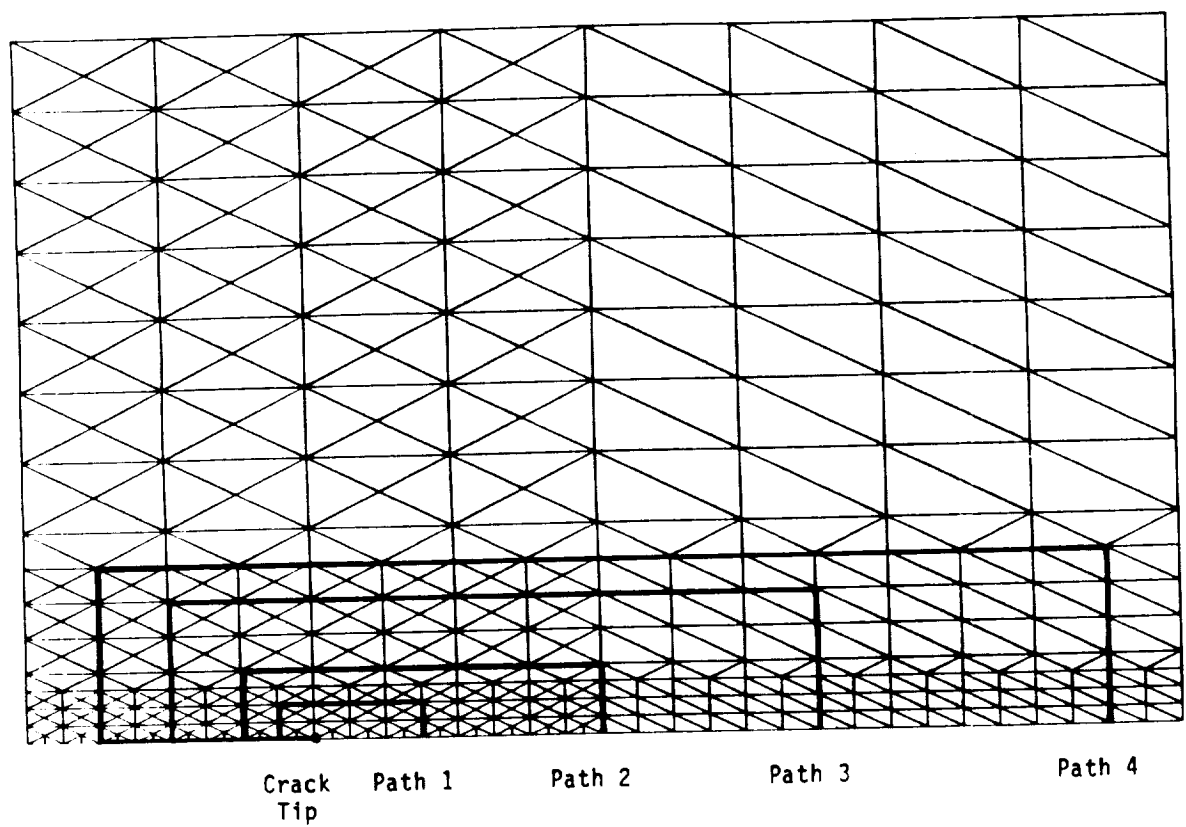


Figure 120: Integration Paths for Crack Closing and Opening Analysis at Crack Length of 2.54mm.

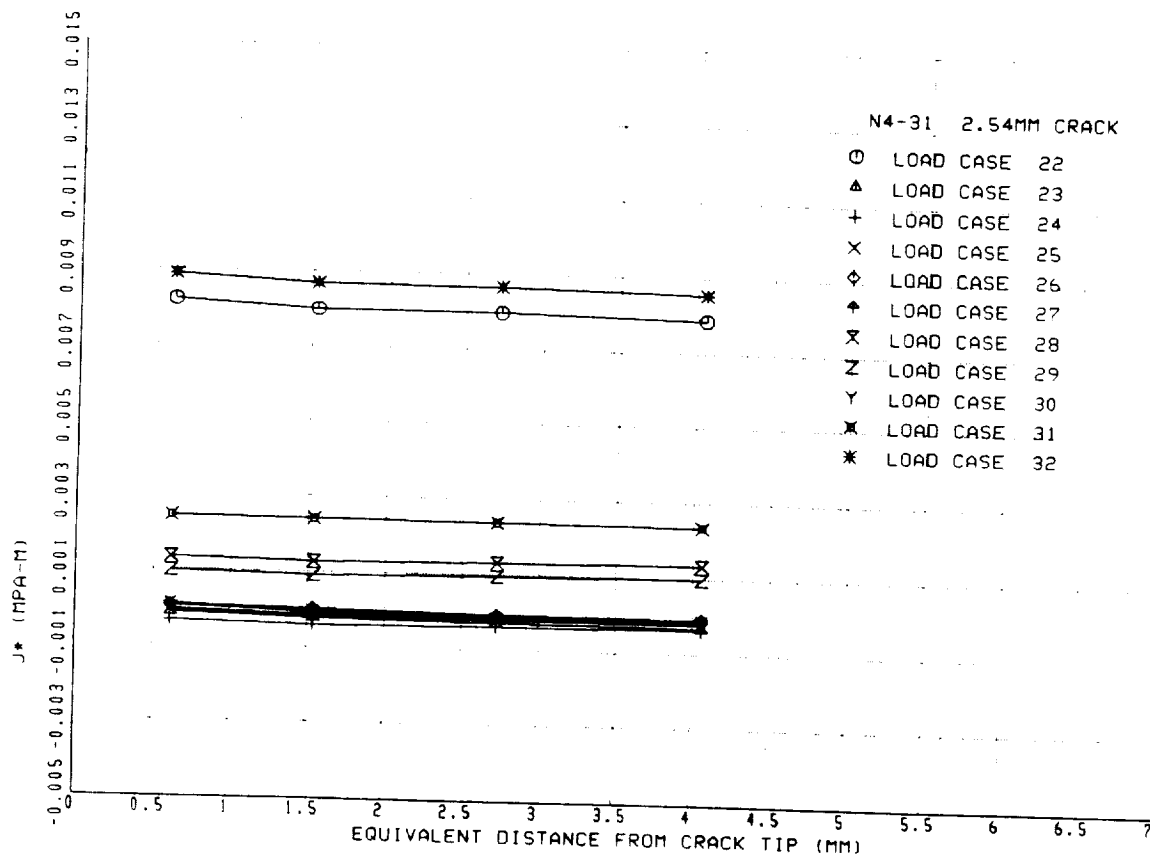


Figure 121: Variation of J^* with Path in a SEN Specimen Cycled at 538°C (1000°F) and 0.5% Strain Range with a Crack Length of 2.54mm.

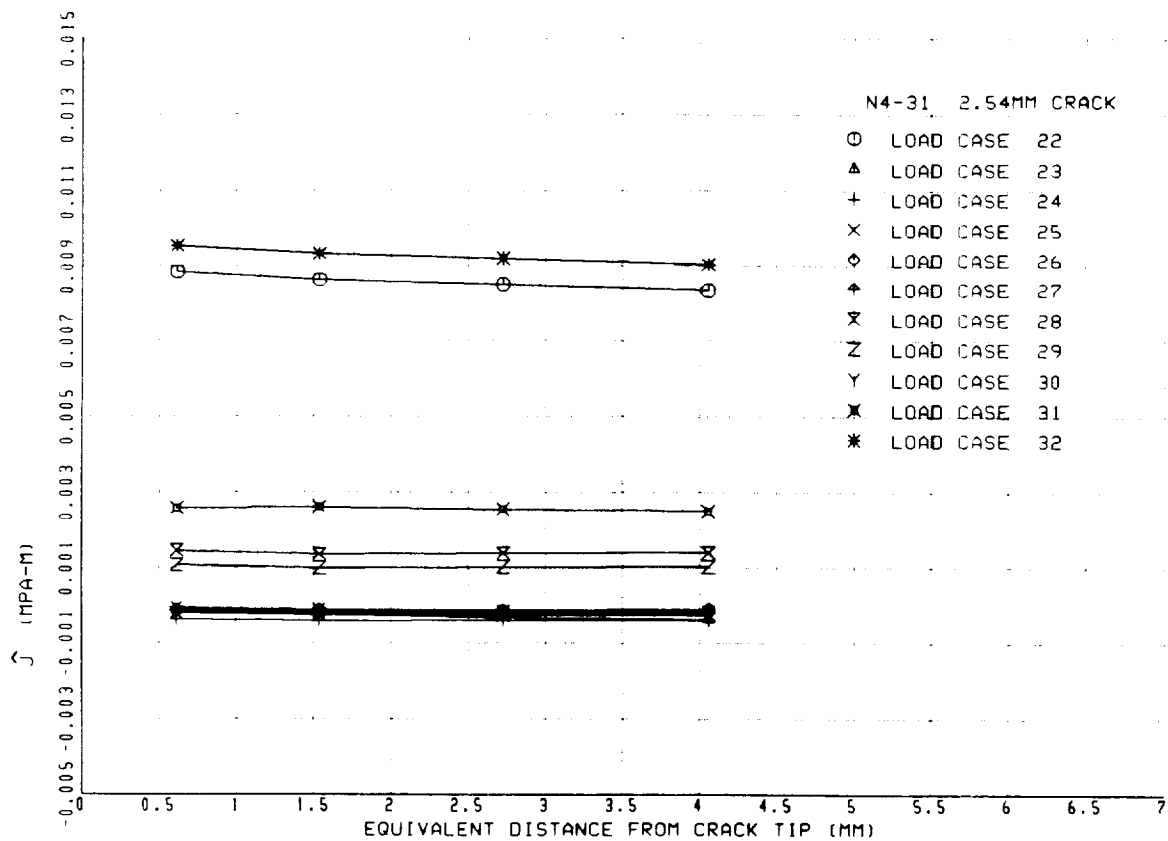


Figure 122: Variation of \hat{J} with Path in a SEN Specimen Cycled at 538°C (1000°F) and 0.5% Strain Range with a Crack Length of 2.54mm.

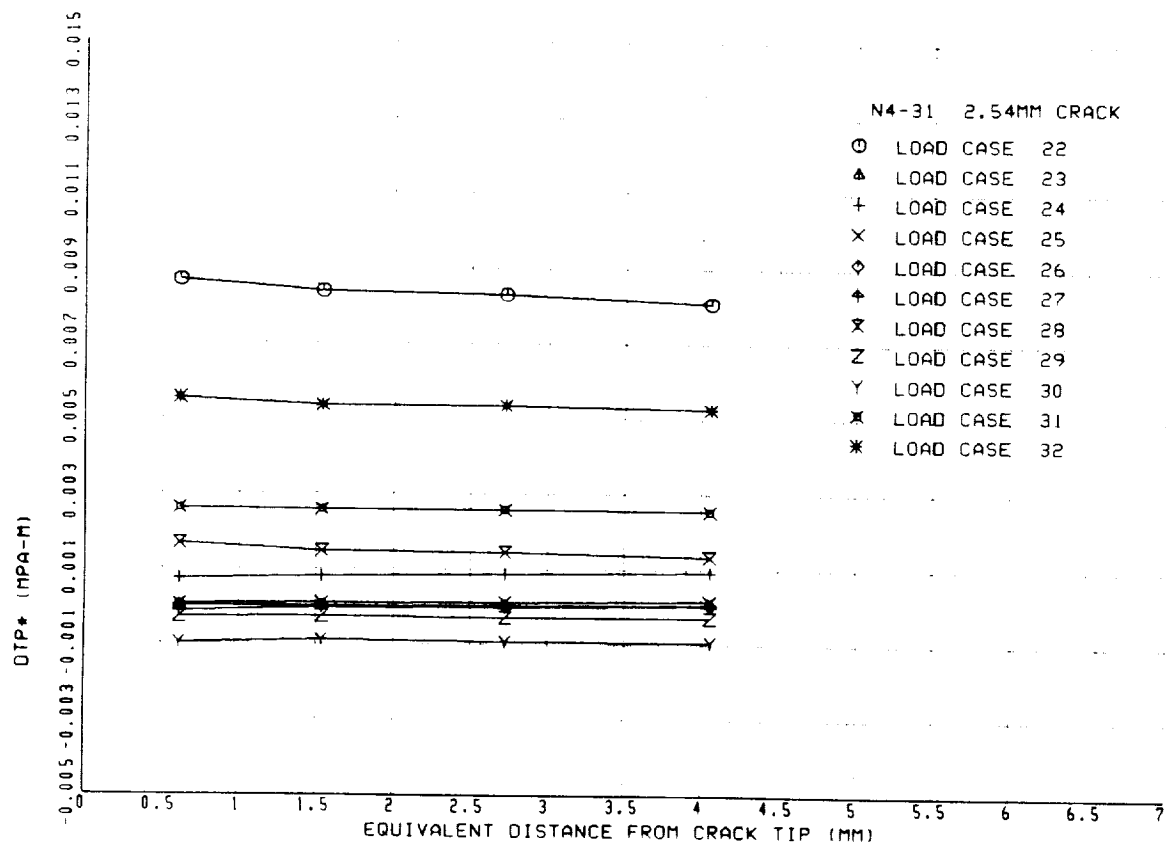


Figure 123: Variation of ΔT_p^* with Path in a SEN Specimen Cycled at 538°C (1000°F) and 0.5% Strain Range with a Crack Length of 2.54mm.

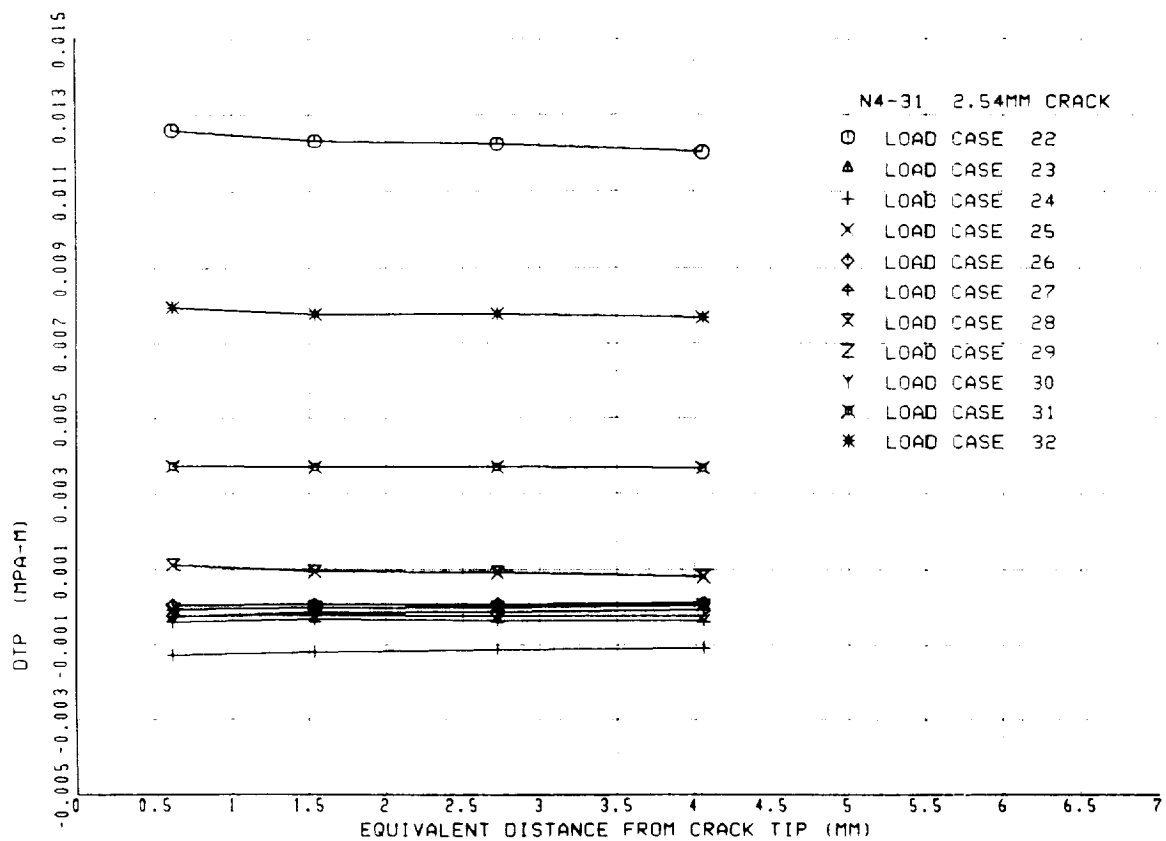


Figure 124: Variation of ΔT_p with Path in a SEN Specimen Cycled at 538°C (1000°F) and 0.5% Strain Range with a Crack Length of 2.54mm.

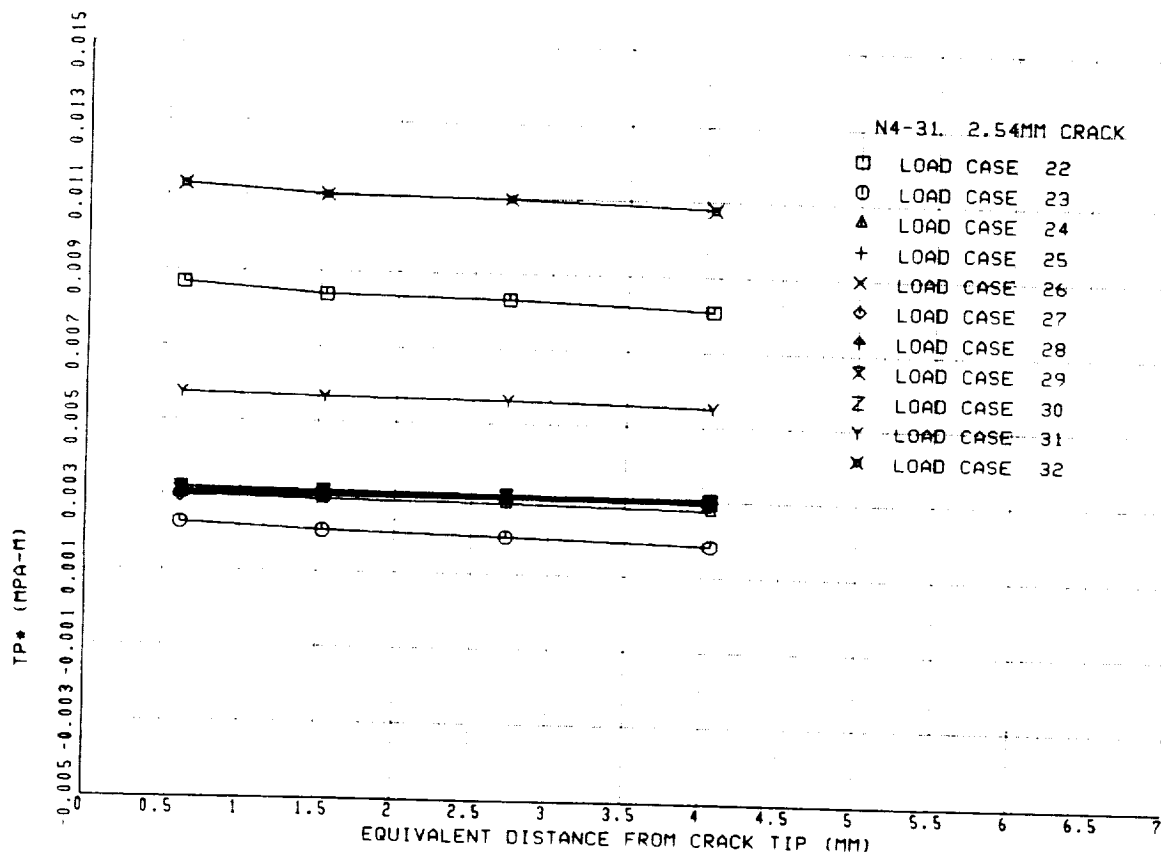


Figure 125: Variation of T_p^* with Path in a SEN Specimen Cycled at 538°C (1000°F) and 0.5% Strain Range with a Crack Length of 2.54mm.

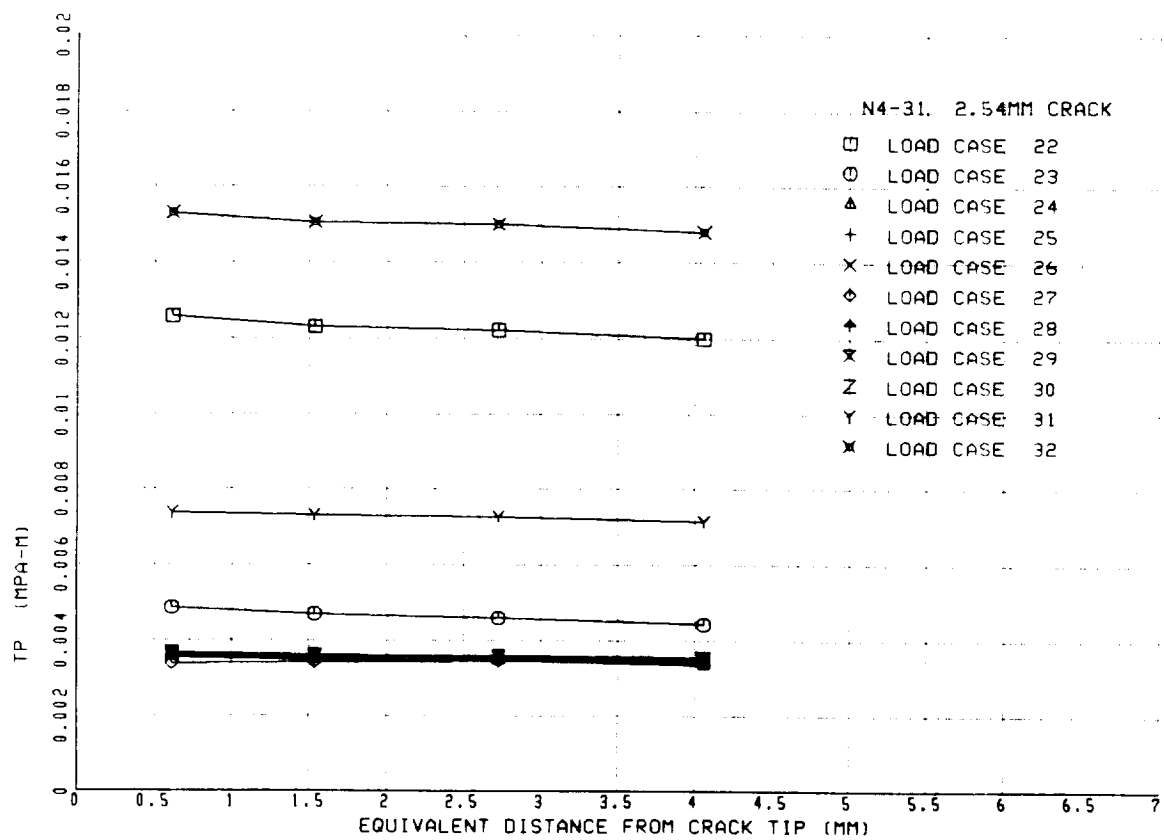


Figure 126: Variation of T_p with Path in a SEN Specimen Cycled at 538°C (1000°F) and 0.5% Strain Range with a Crack Length of 2.54mm.

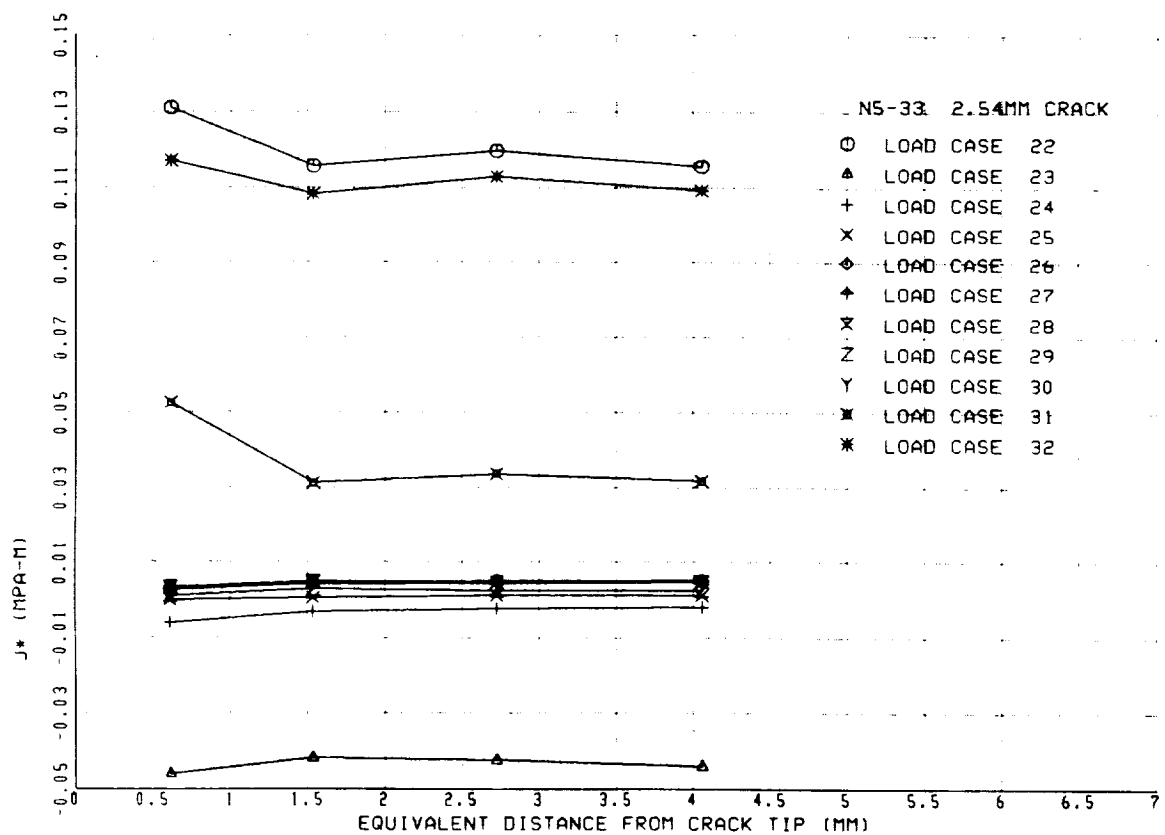


Figure 127: Variation of J^* with Path in a SEN Specimen Cycled at 538°C (1000°F) and 1.7% Strain Range with a Crack Length of 2.54mm.

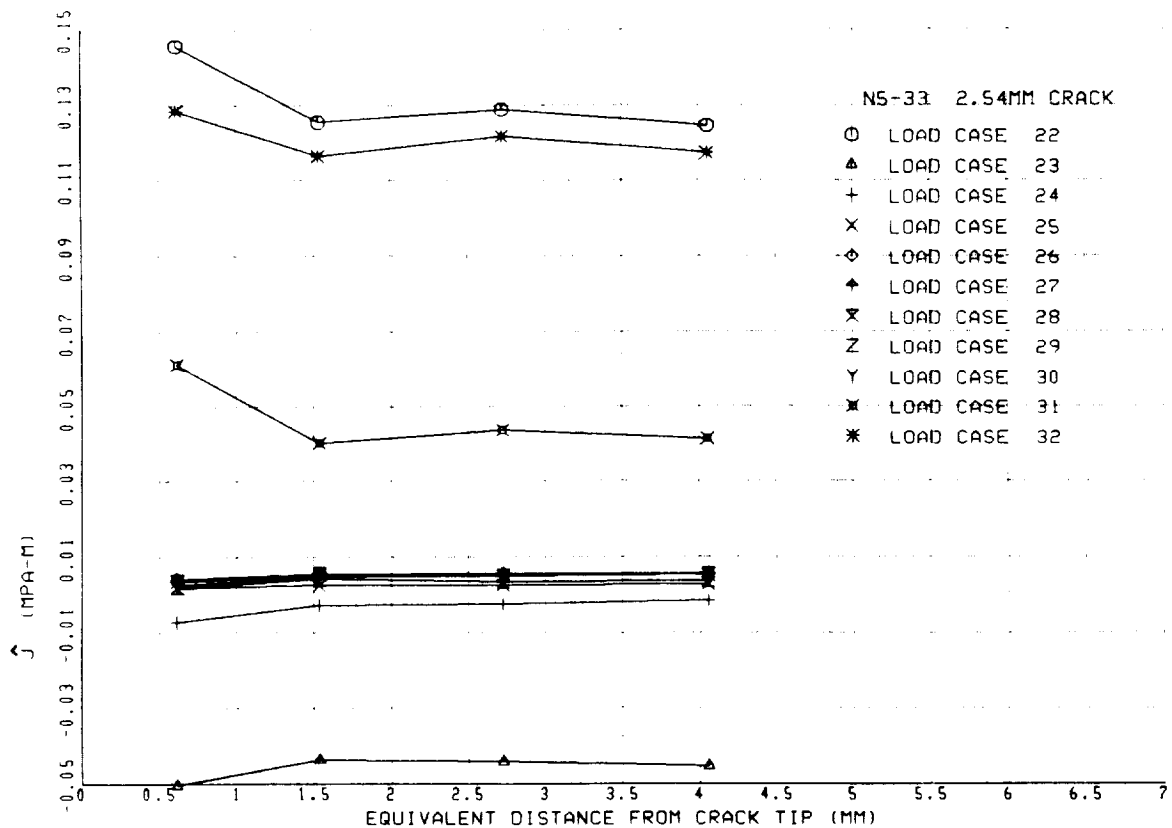


Figure 128: Variation of \hat{J} with Path in a SEN Specimen Cycled at 538°C (1000°F) and 1.7% Strain Range with a Crack Length of 2.54mm.

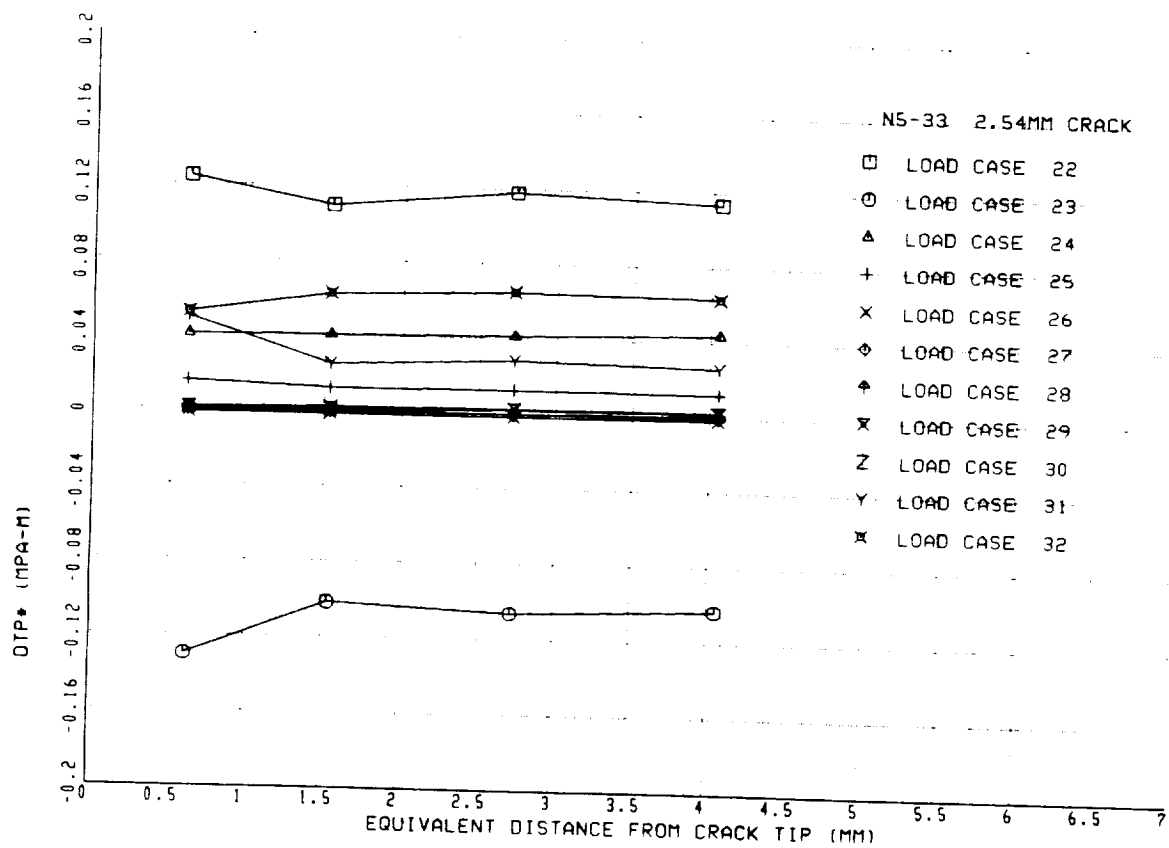


Figure 129: Variation of ΔT_p^* with Path in a SEN Specimen Cycled at 538°C (1000°F) and 1.7% Strain Range with a Crack Length of 2.54mm.

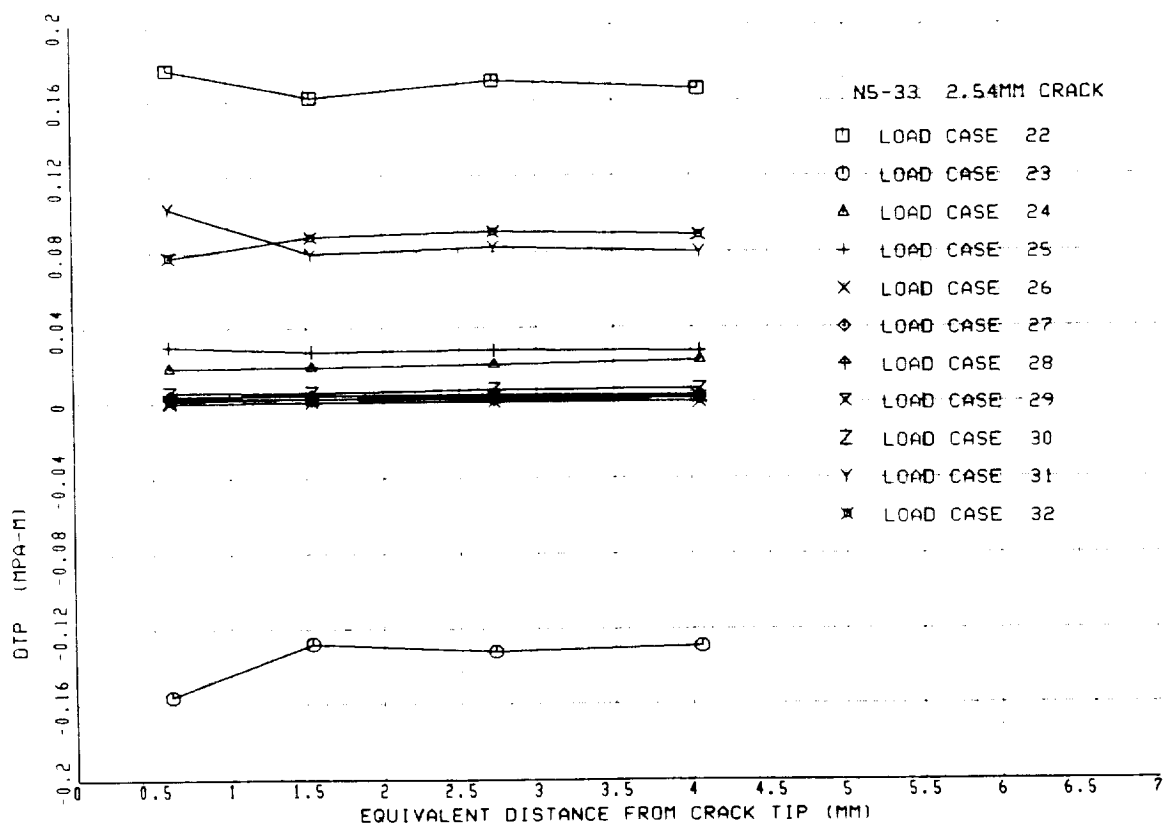


Figure 130:

Variation of ΔT_p with Path in a SEN Specimen Cycled at 538°C (1000°F) and 1.7% Strain Range with a Crack Length of 2.54mm.

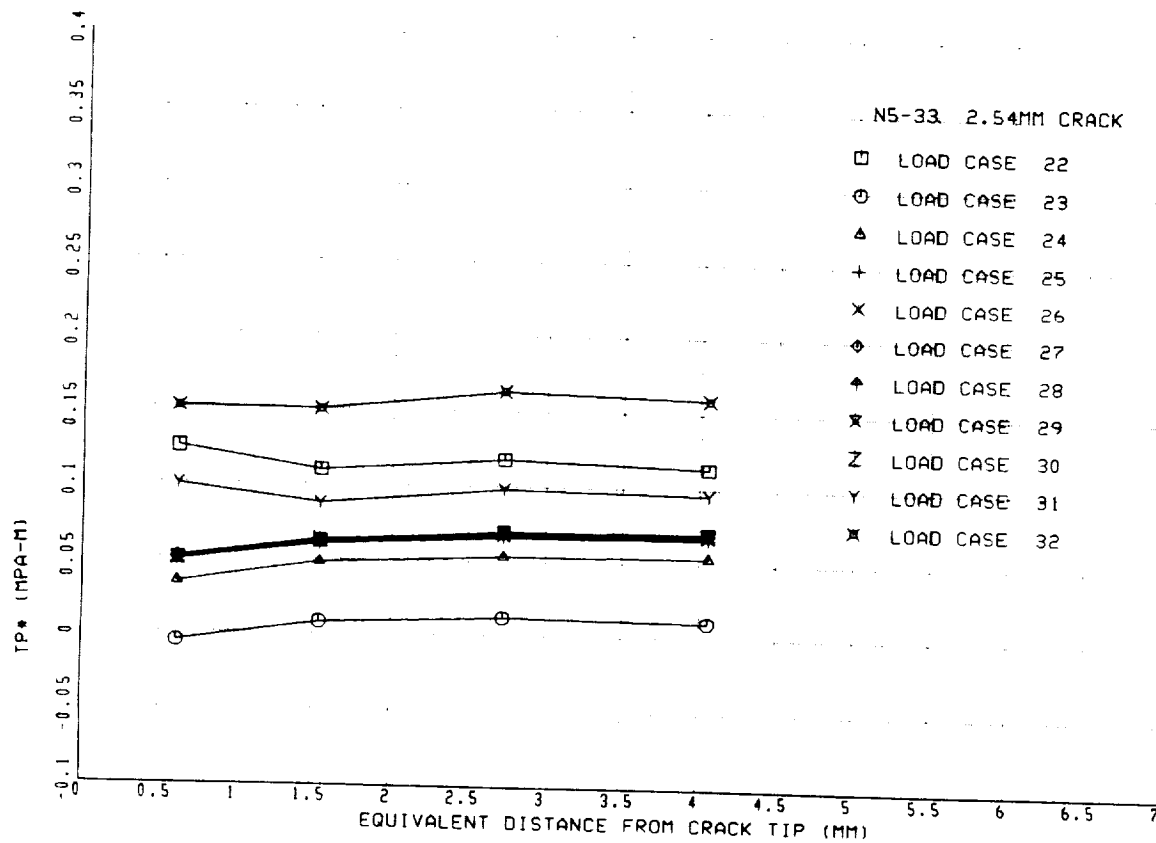


Figure 131: Variation of T_p^* with Path in a SEN Specimen Cycled at 538°C (1000°F) and 1.7% Strain Range with a Crack Length of 2.54mm.

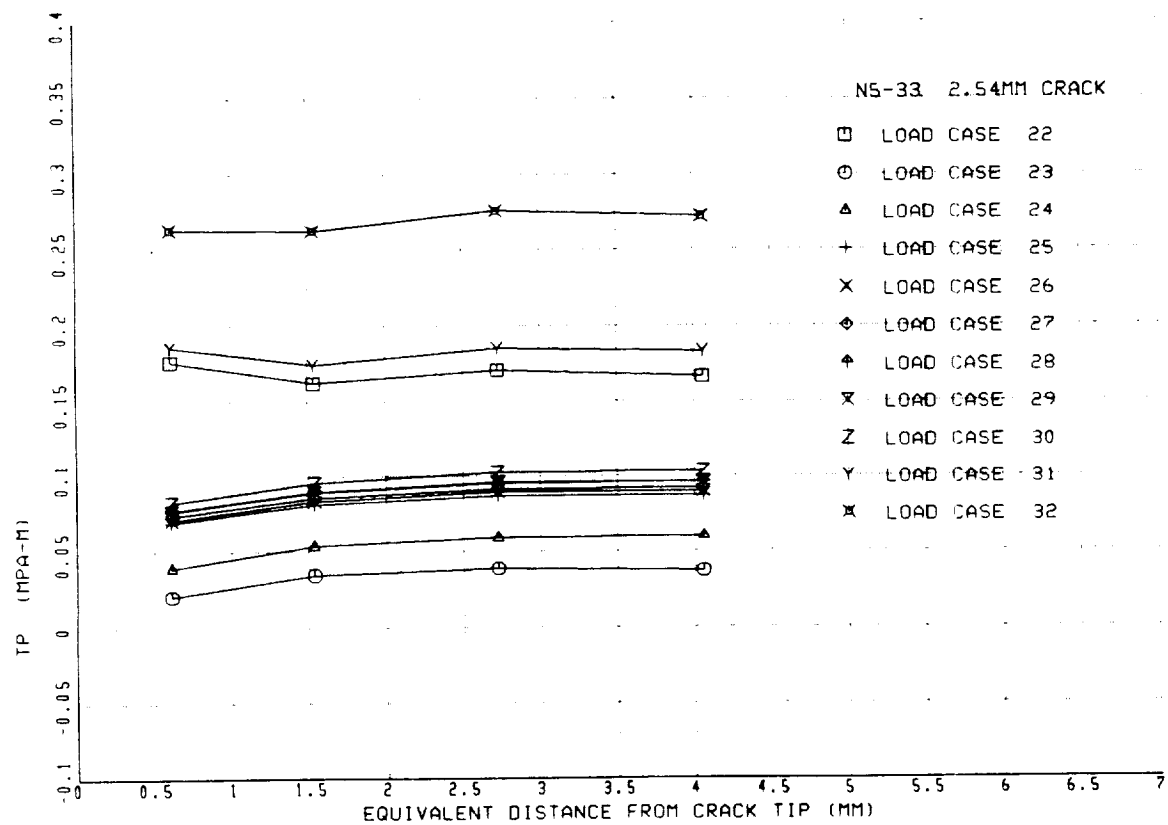


Figure 132: Variation of T_P with Path in a SEN Specimen Cycled at 538°C (1000°F) and 1.7% Strain Range with a Crack Length of 2.54mm.

opening stress to the tensile peak, in implementing these integrals in the crack growth analysis. Notice also in these figures that T_p^* and T_p at Load Case 32 are different from the corresponding values at Load Case 22. One may surmise that this deviation is due to the coarse loading steps in the cycle. However, there exists no proof that the values of these integrals coincide after a cycle even if small loading steps are taken. This must be clarified for these integrals to be useful for practical applications. The increments of T_p^* and T_p from the lower peak to the upper peak were somewhat different between the crack growth simulation and closure analysis results. This difference was up to 26%. The J^* and \hat{J} integrals also showed changes of up to 10% when a cycle was completed; see Figures 121, 122, 127, and 128.

The variation of J^* in a cycle is depicted in Figure 133. Notice that the J^* is very small at the point of crack closing, at the lower peak, and at the crack opening point compared with the value at the upper peak. Notice also that the J^* takes its minimum in the unloading process from the upper peak to the closing point. These two phenomena were common for all four integrals. The numerical data of the P-I integrals are summarized in Tables 18, 19 and 20. These numbers represent the P-I integrals along the largest paths.

7.6. Prediction of Crack Growth with P-I integrals

As reviewed in Section 2.0, the path-independent integrals J^* , \hat{J} , ΔT_p^* and ΔT_p can be applied in the loading situations which include unloading, nonproportional loading, nonuniform temperature and material inhomogeneities. The differences of these integrals between any two loading points in a cycle are also path-independent and can be, directly or indirectly, related to the severity of crack tip deformation. The most meaningful range of these integrals for crack growth prediction is from the opening stress to the maximum stress. These ranges can be found from the crack closure analyses at the two crack lengths for each of the three specimens. The crack growth data at the crack lengths are found from the data in Section 6.0 by interpolation in the manner the boundary conditions are determined. The total number of

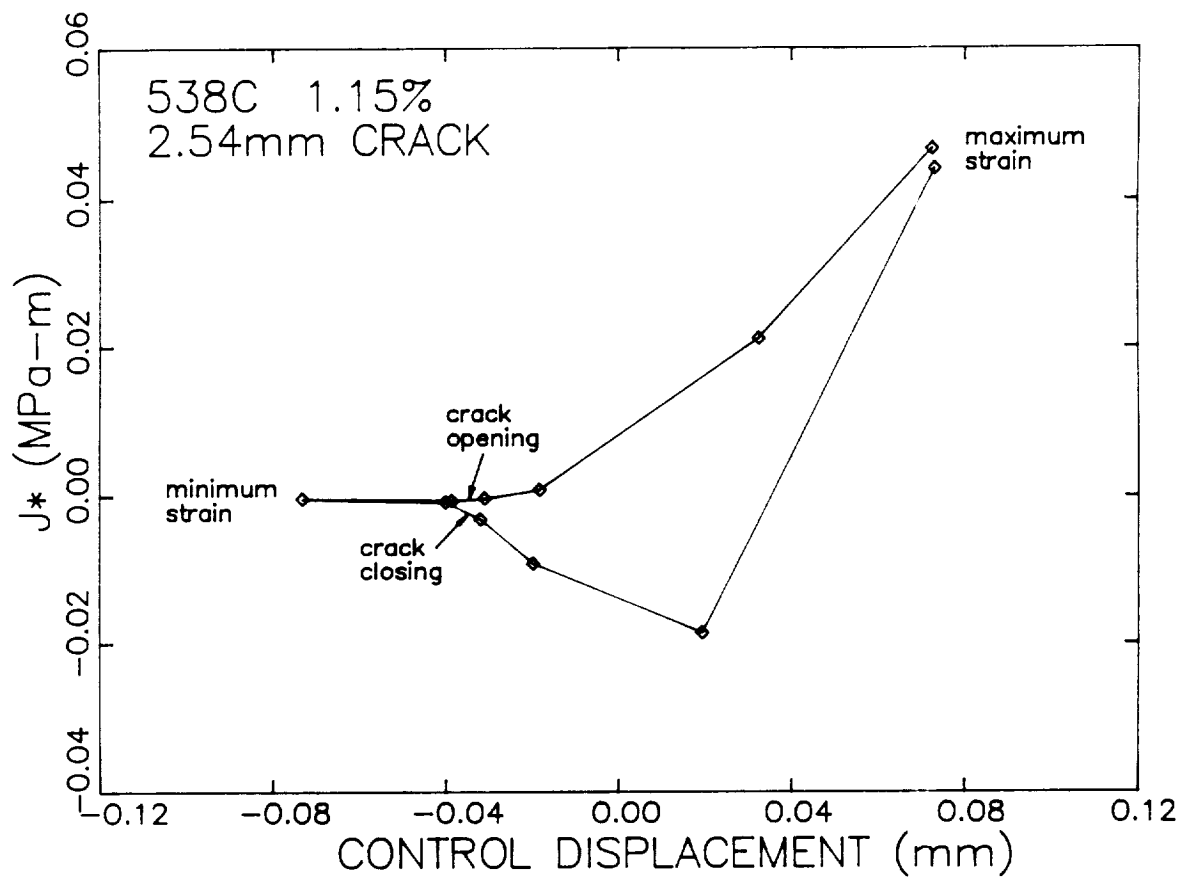


Figure 133: Predicted Values of J^* as a Function of Control Displacement During a Cycle in a SEN Specimen Cycled at 538°C (1000°F) and 1.15% Strain Range with a Crack Length of 2.54mm.

Table 18: Values of P-I Integrals from Crack Closure Analysis of SEN Specimen N4-31 (538°, $A_c = \infty$, 0.50% Strain Range)

Crack length (mm)	Load case	J^*	\hat{J}	ΔT_p^*	ΔT_p
(1.E-3 MPa-m)					
0.95	7	3.88	4.04	3.90	4.55
	8	0.30	0.30	-2.86	-3.07
	9	-0.10	-0.13	-0.14	-0.41
	10	-0.04	-0.06	0.06	0.
	11	-0.04	-0.05	0.	0.
	12	0.	-0.02	0.03	-0.03
	13	0.	-0.01	-0.01	0.05
	14	0.	-0.01	0.	0.03
	15	-0.01	-0.02	-0.01	-0.02
	16	1.08	1.13	1.13	1.29
	17	3.96	4.13	2.40	2.84
2.54	22	7.87	8.34	8.08	12.00
	23	-0.31	-0.38	-6.25	-7.56
	24	-0.35	-0.41	0.93	-1.08
	25	-0.21	-0.26	0.18	0.07
	26	-0.13	-0.18	0.06	0.12
	27	-0.09	-0.10	0.05	-0.06
	28	-0.16	-0.20	-0.08	0.06
	29	-0.11	-0.14	0.06	-0.04
	30	-0.14	-0.16	-0.05	-0.03
	31	2.32	2.48	2.52	3.65
	32	8.50	9.00	5.26	7.66

Table 19: Values of P-I Integrals from Crack Closure Analysis of SEN Specimen N4-3 (538°, $A_c = \infty$, 1.15% Strain Range)

Crack length (mm)	Load case	J^*	\hat{J}	ΔT_p^*	ΔT_p
(1.E-3 MPa-m)					
0.95	7	25.01	26.66	25.03	22.58
	8	-6.21	-6.43	-19.58	-17.55
	9	-2.64	-2.82	4.66	3.38
	10	-0.88	-0.10	1.65	2.39
	11	-0.84	-1.01	0.05	0.09
	12	-0.04	-0.31	1.00	3.47
	13	0.19	0.09	0.15	-3.11
	14	-0.02	-0.11	-0.18	-0.51
	15	-0.19	-0.19	-0.06	-1.94
	16	11.41	12.19	11.33	8.87
	17	26.95	28.63	14.14	18.93
2.54	22	44.03	46.22	45.45	48.27
	23	-18.60	-20.33	-40.77	-30.26
	24	-9.17	-10.17	9.26	-0.11
	25	-3.11	-3.67	5.32	5.81
	26	-0.82	-1.21	2.21	3.77
	27	-0.37	-1.15	0.55	7.54
	28	-0.63	-1.07	-0.29	-5.55
	29	-0.30	-0.62	0.31	-1.30
	30	0.84	0.75	1.42	-0.20
	31	21.17	22.29	19.98	23.78
	32	46.69	49.30	24.45	38.55

Table 20: Values of P-I Integrals from Crack Closure Analysis of SEN Specimen N5-33 (538°, $A_c = \infty$, 1.70% Strain Range)

Crack length (mm)	Load case	J^*	\hat{J}	ΔT_p^*	ΔT_p
(1.E-3 MPa-m)					
0.95	7	73.01	76.59	73.07	129.93
	8	-19.86	-21.26	-59.95	-126.73
	9	-3.46	-4.47	16.79	6.99
	10	-0.20	-1.37	5.79	9.53
	11	-0.12	-1.21	0.11	-0.69
	12	-0.07	-1.14	0.11	-0.69
	13	-0.10	-1.06	-0.22	6.09
	14	-0.03	-0.96	-0.07	0.36
	15	0.12	-0.48	-0.44	5.45
	16	33.01	34.50	32.37	55.29
	17	69.02	72.00	33.54	45.06
2.54	22	115.57	124.40	113.59	166.11
	23	-44.05	-45.41	-102.96	-128.95
	24	-1.84	-1.52	43.73	22.47
	25	1.28	2.92	12.27	27.51
	26	4.93	5.63	2.47	2.65
	27	5.17	5.61	0.62	2.25
	28	4.85	5.28	-0.28	3.78
	29	2.57	3.74	-1.45	0.25
	30	4.74	5.52	2.22	7.10
	31	31.78	41.26	25.83	79.90
	32	109.23	117.09	63.22	88.89

data points on a da/dN versus ΔJ_X plot thus obtained is only six. Notice that the values of the P-I integrals in consideration are very small at the closing stress, at the minimum stress and at the opening stress. Therefore, we can use the difference of the P-I integrals between the maximum stress and the minimum stress as approximate values of the differences between the maximum stress and the opening stress. Since the former values are available from the crack growth simulation at a number of crack lengths for each specimen, we will rather use these data instead of the results obtained in the crack closure analysis. It is recognized that there exist some differences between the data obtained in the two analyses. However, these differences do not shift the data points on a log-log plot of da/dN vs. ΔJ_X to a significant extent.

The da/dN versus ΔJ_X plots are shown in Figures 134, 135, 136 and 137. It is seen that all these P-I integrals are good parameters for predicting crack growth rates for the cases considered. From the Figures 134 through 137 we can write

$$da/dN = C (\Delta J_X)^n \quad (7.9)$$

The coefficient C and the exponent n were calculated using a regression analysis. They are shown in Table 21.

7.7. Discussion

The numerical analysis of crack growth in the highly nonlinear loading regime at high temperatures is not an easy task to carry out because of the computational cost. It was attempted in this report to investigate a somewhat simplified, yet reasonably accurate, approach in conjunction with an experimental program to provide a data base and to validate the numerical results. The simplifications include taking peak-to-peak loading steps and releasing more than one node at a time in crack growth simulation. This approach yielded satisfactory results for the loading conditions considered. A salient feature of the current approach is that the crack closure analysis

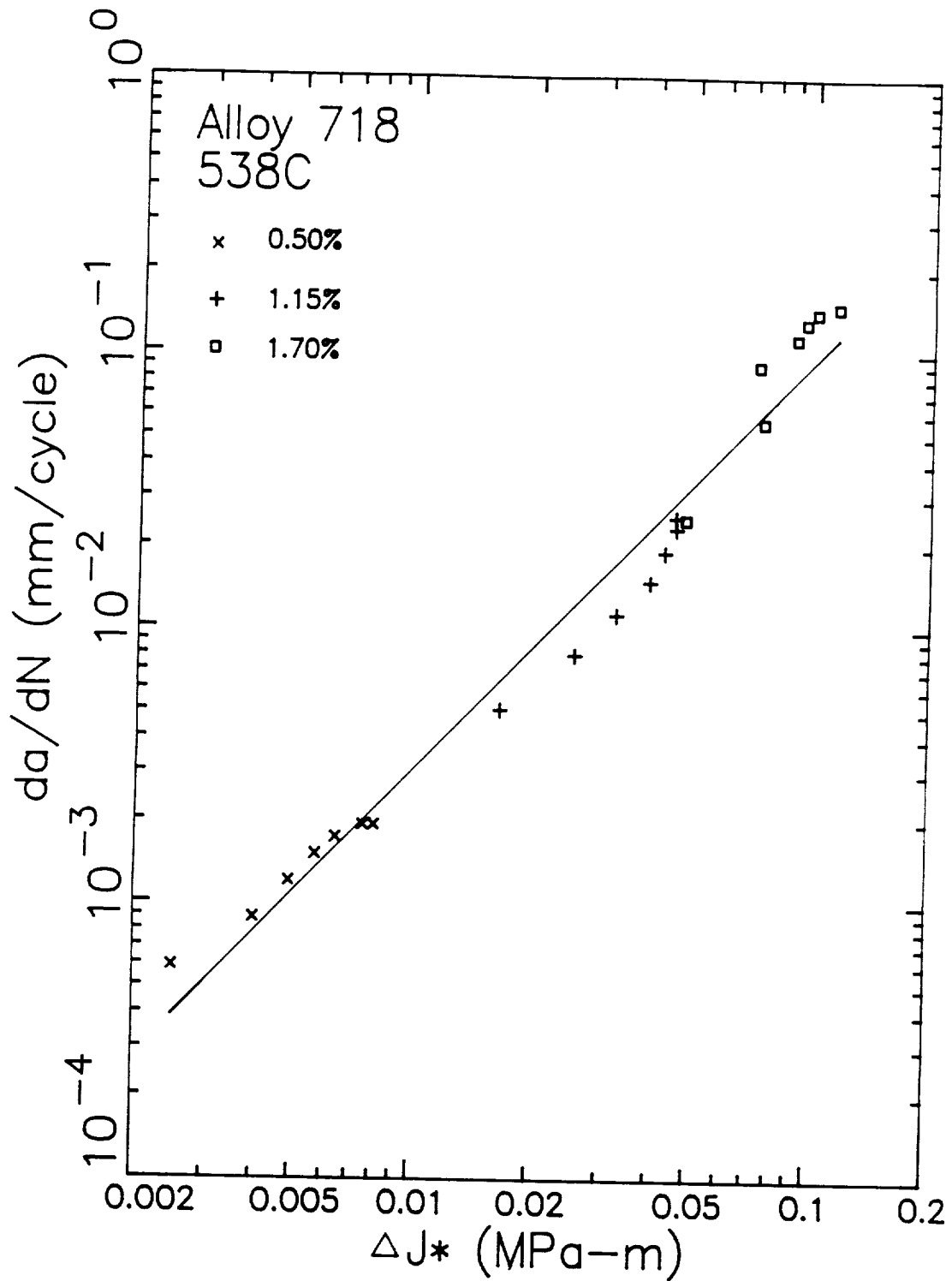


Figure 134: Variation of Crack Growth Rates Measured in Alloy 718 at 538°C (1000°F) with ΔJ^* .

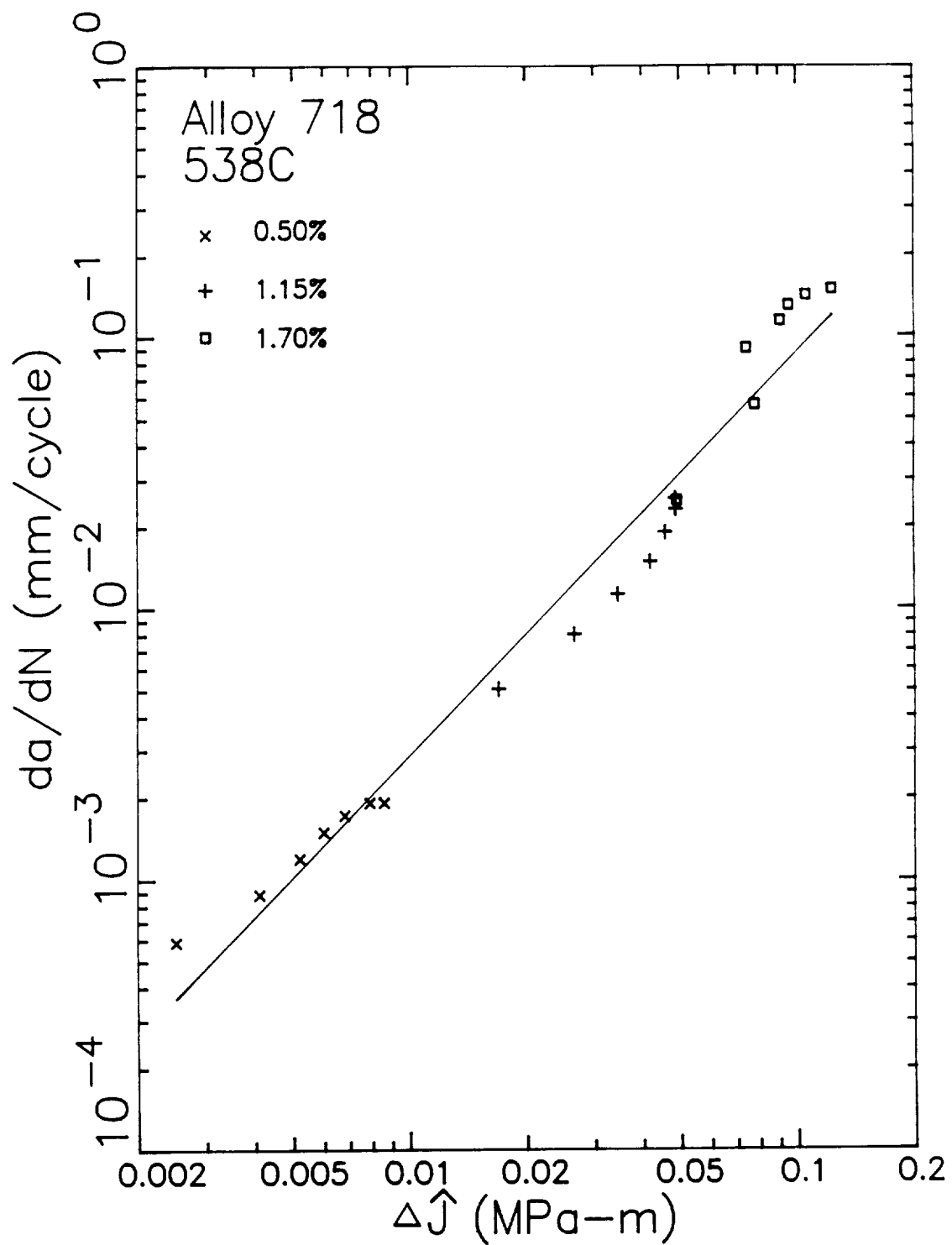


Figure 135: Variation of Crack Growth Rates Measured in Alloy 718 at 538°C (1000°F) with ΔJ .

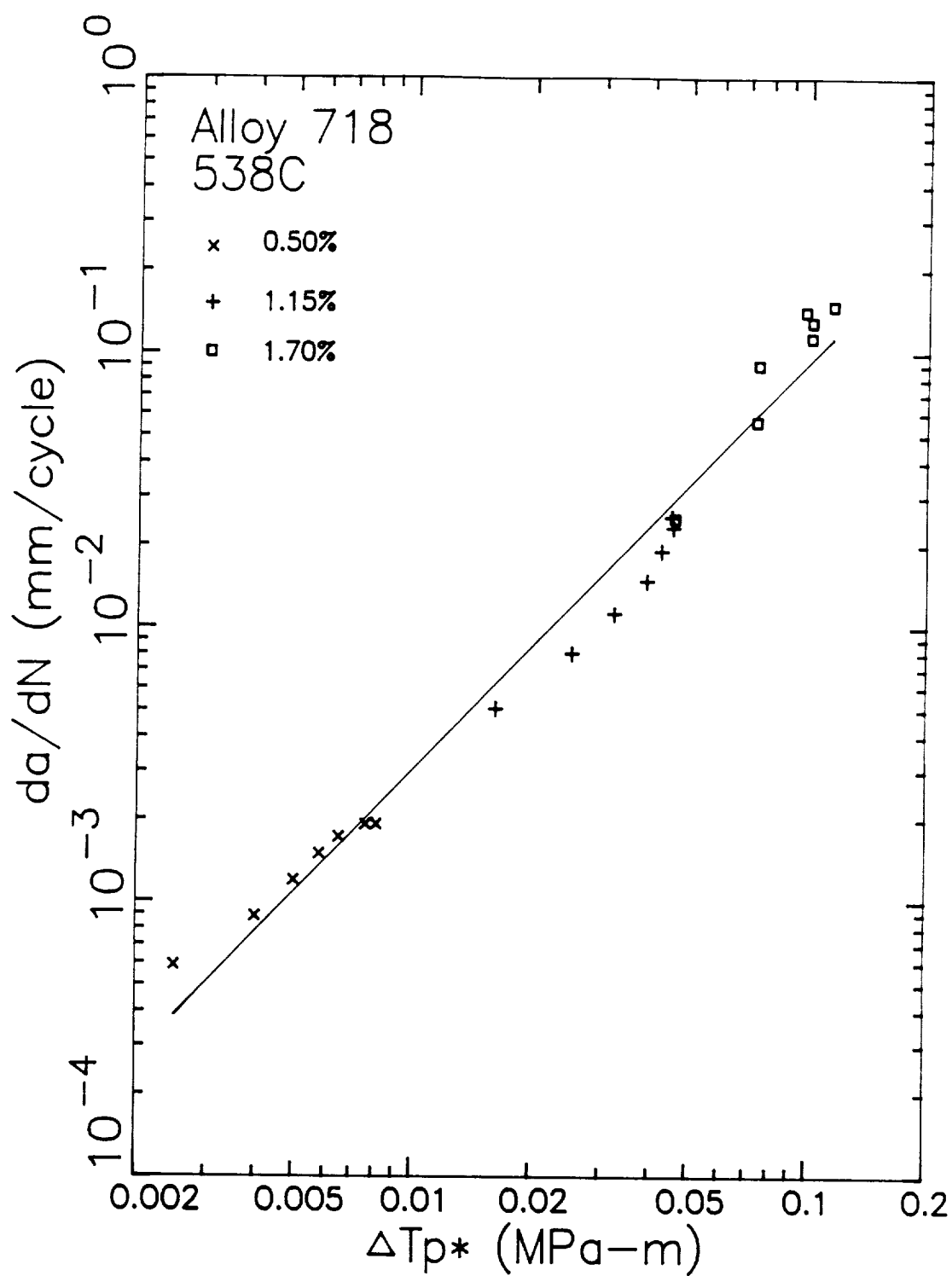


Figure 136: Variation of Crack Growth Rates Measured in Alloy 718 at 538°C (1000°F) with ΔT_p^* .

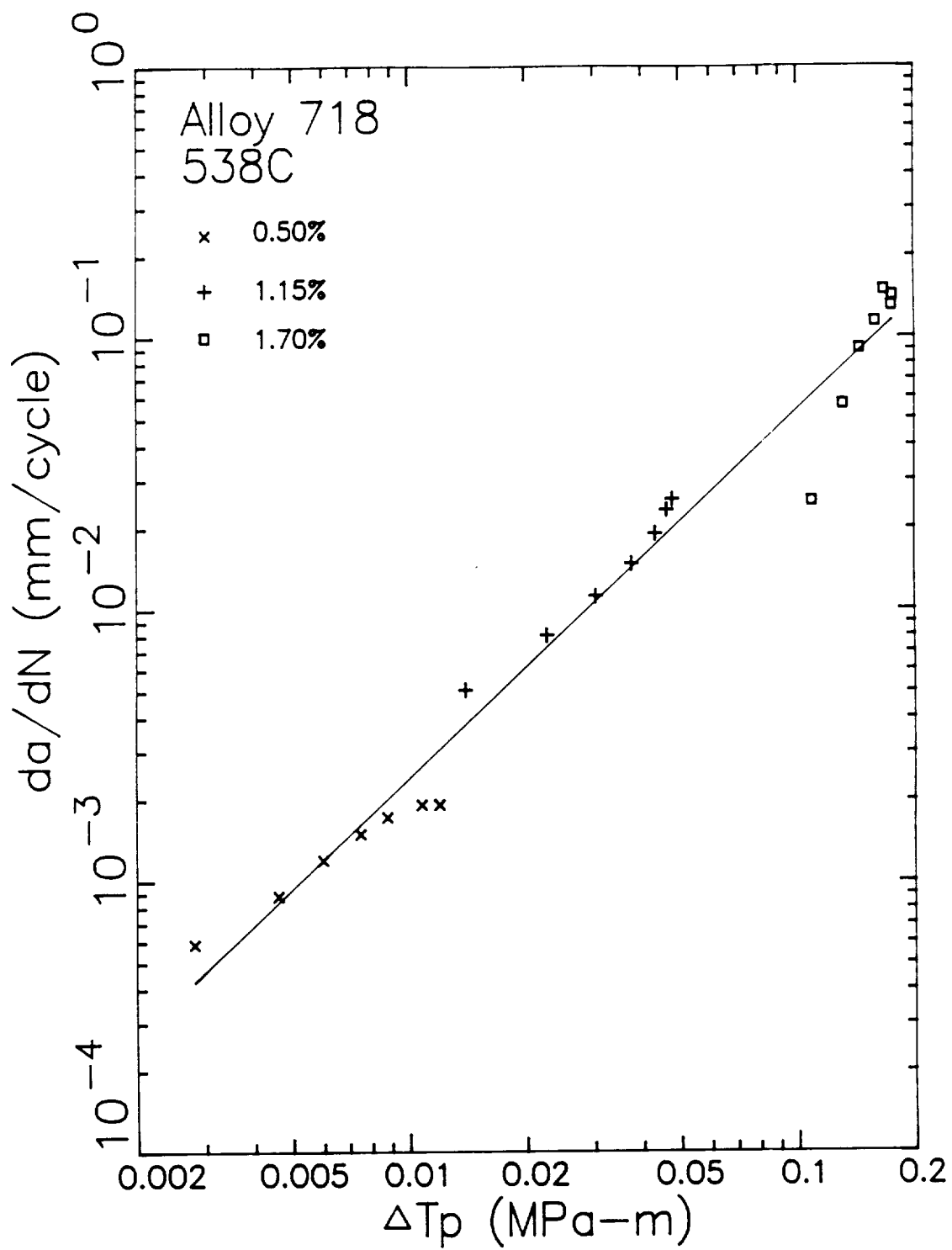


Figure 137: Variation of Crack Growth Rates Measured in Alloy 718 at 538°C (1000°F) with ΔT_p

Table 21: Crack Growth Rate Constants for Path-Independent Integrals

$$da/dN = C (\Delta J_X)^n$$

P-I Integral	C	n
ΔJ^*	2.913	1.490
$\Delta \hat{J}$	2.681	1.486
ΔT_p^*	2.876	1.489
ΔT_p	1.213	1.353

can be performed at any crack lengths by restarting the crack growth simulation run without going through all the cycles by small load increments. The essential feature in the crack growth analysis is to correctly model the crack closing and opening behavior. The method used in this paper proved to be effective in this respect.

The computation of P-I integrals did not pose any particular problem. The computed results of P-I integrals indicated path-independence to acceptable degrees. It must also be stated that, unlike in the J-integral computation, the near field results of a finite element analysis must also carry reasonable accuracy for accurate computation of the area integrals in these P-I integrals. This implies that the finite element mesh must be sufficiently fine inside the integration contour. This is a disadvantage of the new P-I integrals involving area integrals from the computational viewpoint.

The P-I integrals J^* , \hat{J} , ΔT_p^* and ΔT_p proved to be useful crack growth parameters under cyclic loading for the isothermal cases considered herein. The difference of these quantities between the tensile peak and the opening stress point correlated the da/dN data quite well. In view of the consistent trends of the tests results at other temperatures, it is expected that these parameters are viable for all isothermal conditions. However, there is no guarantee that these parameters will be successful in more complicated situations. Effort must continue to validate these parameters for different loading conditions, different temperature conditions and other geometries. Another point which must be noted is that the four P-I integrals almost vanished at the crack closure, crack opening points and at the compressive peak. Consequently, the significance of the crack closing and opening in the crack growth can not be identified for the given loading conditions, since the increments of these integrals from the above three points to the tensile peak are almost identical. Further studies involving mean strain or stress would be necessary to resolve this matter.

In summary, the results obtained in this study, although limited, provide encouragement and motivation to further pursue far-field-based approaches for crack growth prediction under cyclic loading in the highly nonlinear regime.

8.0 CRACK PROPAGATION WITH THERMAL GRADIENT

This section of the report will describe the results and the analysis of the tests performed with a temperature gradient across the width of the buttonhead single edge notch (SEN) specimen. Both monotonic and cyclic tests were performed. The monotonic tests were analyzed using finite element analysis to confirm the linear variation of mechanical strain across the width of the SEN specimen gage length.

8.1 Test Matrix

The experimental techniques used to establish and perform the temperature gradient was described in Section 5.0 and will be summarized here. A temperature gradient from 482 to 649°C (900 to 1200°F) was developed across the width of the SEN specimen (Figure 70) where the crack grew toward the lower temperature. The specimens were tested using the same triple extensometer and data acquisition techniques used for the isothermal tests.

A total of seven SEN specimens were successfully tested with a thermal gradient across the gage section. Duplicate tests were performed under monotonic loading. The remainder of the tests were cycled with zero mean strain ($A_c = \infty$). Duplicate cyclic crack growth tests were performed with strain ranges of 1.15 and 1.70% and a single test was conducted with a strain range of 0.50%.

8.2 Monotonic Tests and Finite Element Analysis

The monotonic tests were performed on specimens which had been precracked to have crack lengths of 1.39 and 1.49 mm (0.0547 and 0.0588 inch). The experimental results will be shown when they are compared to the finite element analyses.

The temperature distribution along the specimen width was nonlinear but for the purpose of the finite element analysis was approximated by three linear segments. The temperature was treated to be 649°C (1200°F) for a distance of 4.45 mm (0.175 inch) away from the edge of the specimen containing the EDM notch. The multilinear temperature distribution then linearly drops to 566°C (1050°F) in the next 3.56 mm (0.14 inch) of the width and, finally, decreases linearly to 482°C (900°F) at the back face of the specimen. This trilinear approximation is shown in Figure 138 along with the experimentally measured temperatures previously shown in Figure 70.

Finite element analyses were performed for a crack length of 1.43mm (0.0563 inch) and the trilinear temperature distribution to determine the nature and magnitude of the stress distribution induced from the temperature gradient. This crack length is close to that in the two monotonic thermal gradient tests and corresponds to a node point in the finite element mesh.

The initial analysis was performed for the pure thermal gradient load case (zero applied load/deflection) and resulted in non-linear variations of stress and displacement. Figure 139 shows the variation of the normal stress variation ahead of the crack tip resulting from the thermal loading. The normal stress has a value of 152 MPa (22 ksi) near the crack tip and it drops sharply to -69 MPa (-10 ksi) at a distance of 4.45 mm (0.175 inch) from the notched edge of the specimen. The stress then gradually increases to 103 MPa (15 ksi) at the back face of the specimen. The positions which correspond to the endpoints of the linear temperature segments also have sharp changes in the normal stress distribution. This normal thermal stress is self-equilibrating in nature since there is no mechanical load applied.

The monotonic temperature gradient tests were analyzed by superimposing the non-linear thermal displacements at the end of the SEN gage section as determined in the pure thermal gradient (zero applied load/deflection) finite element analysis and a linear mechanical contribution inferred from the displacements measured by the control and back face extensometers. These analyses were performed using the same techniques described in Section 7.0

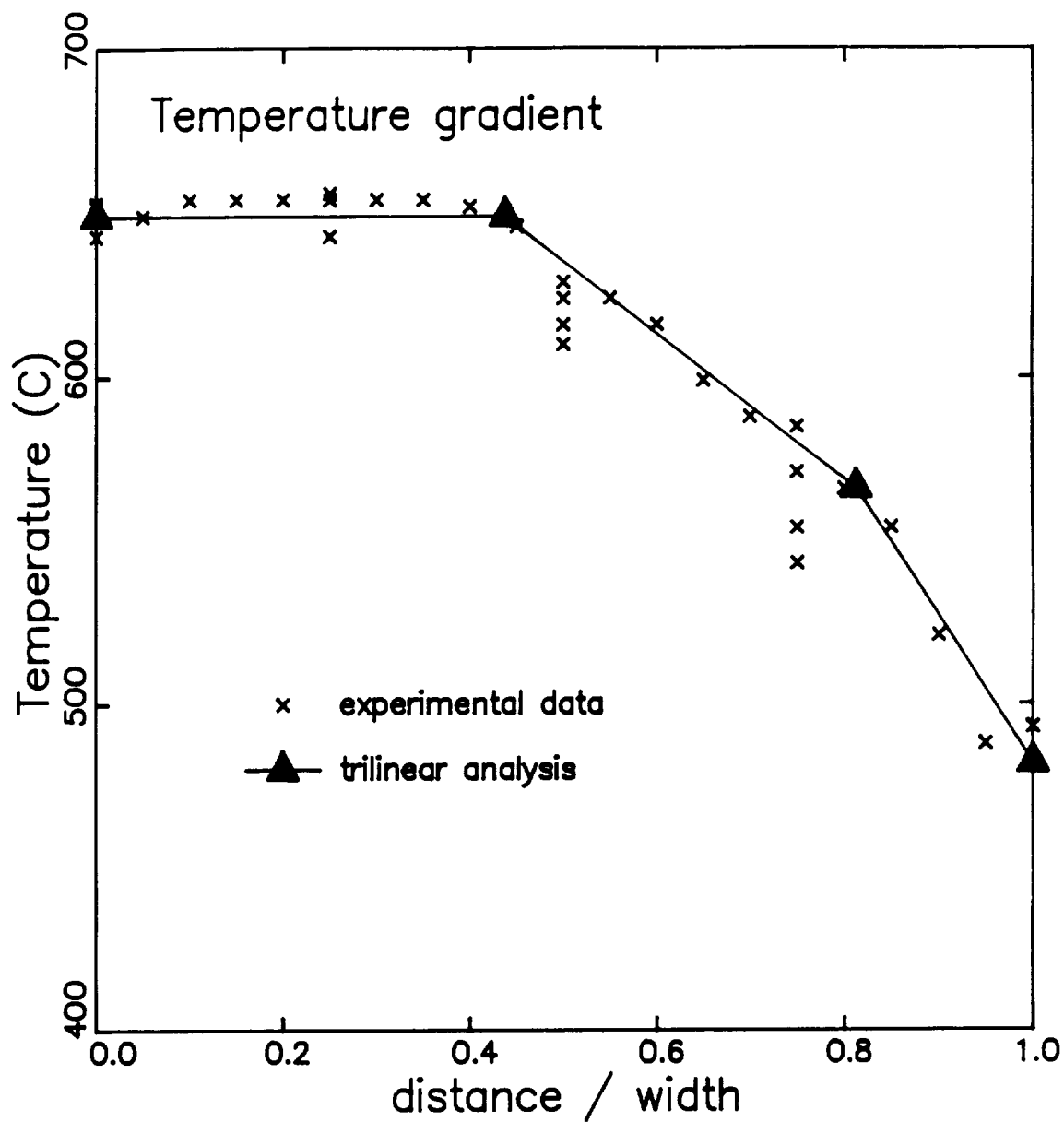


Figure 138: Comparison of Trilinear Approximation and Experimental Data in Alloy 718 Temperature Gradient Tests.

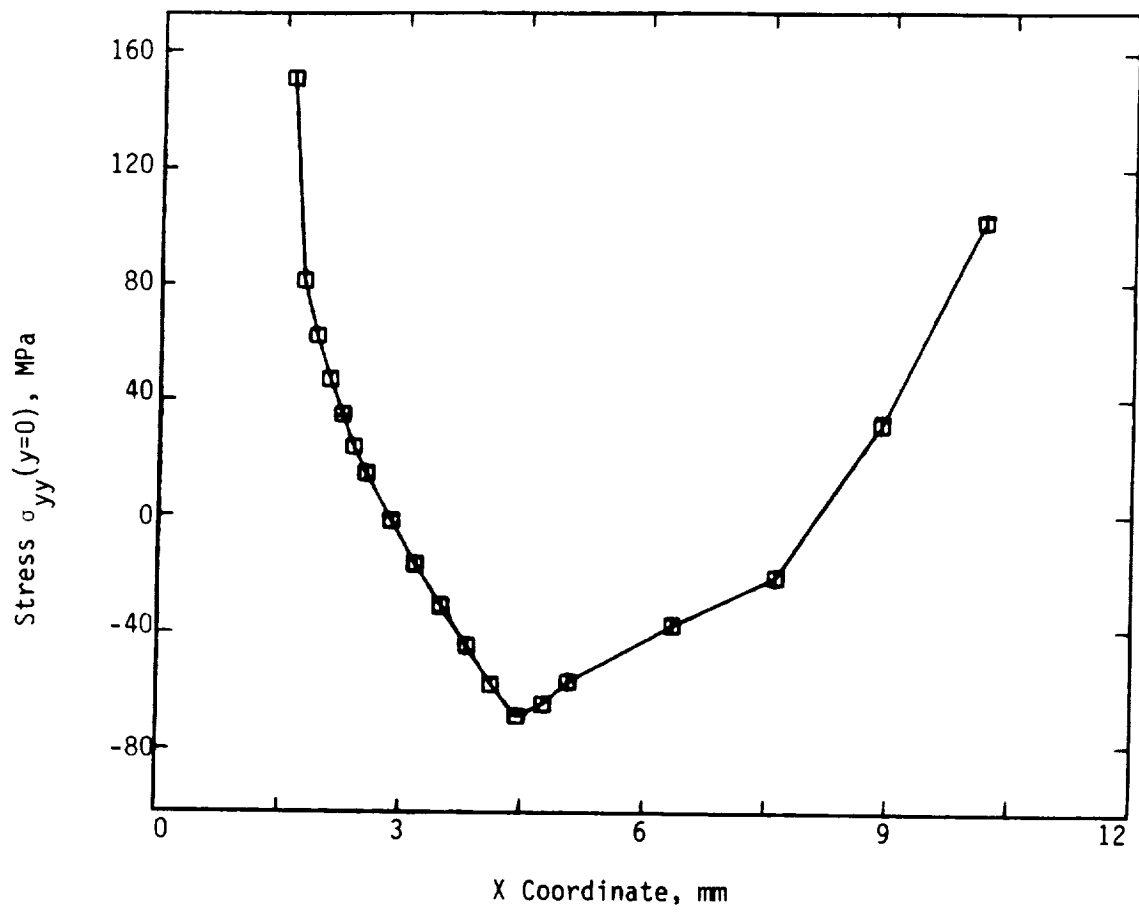


Figure 139: Normal Stress Distribution on the Crack Plane for the Trilinear Temperature Distribution and No Applied Load.

for the isothermal crack growth tests. It was assumed that the crack was stationary and the gap elements were not activated because the loading was not reversed.

The variation of the back face deflection with the mid-width displacement measured by the controlling extensometer are shown in Figure 140. The small "x" symbols show the experimental data from the two tests specimens. These data were used to establish the linear mechanical displacement boundary conditions at the end of the gage section finite element model. The large triangles in this figure show the four displacement values used in the finite element analysis. Figures 141 and 142 compare the experimentally determined and analytically predicted values of gross section stress (load / specimen area) and crack mouth opening displacement (CMOD), respectively, as a function of the control displacement. As shown, the predictions are in excellent agreement with the measurements. These results show that the superposition of the non-linear thermal and linear mechanical displacement variation across the specimen can be used to accurately describe the response of this specimen under temperature gradient conditions.

8.3 Cyclic Temperature Gradient Tests

The result of the cyclic temperature gradient tests are summarized in Table 22. The terms used to describe the crack morphology are the same ones used for the isothermal crack growth tests in Section 6.0. All the cracks grew normal to the axis of the specimen except for those at the highest strain range. The flat morphology was expected for these tests because the temperature at the crack tip for the early part of the test was 649°C (1200°F). The isothermal tests at this temperature had a flat morphology up to the strain level where specimen buckling occurred (Table 14). Buckling occurred in the 649°C isothermal tests with a strain range of 1.70% while at the same strain range, shear cracks grew in the temperature gradient tests. The behavior in the temperature gradient tests may have been induced by the lower temperature in the uncracked ligament. Decreasing the test temperature in the isothermal tests reduced the strain range where shear crack growth was

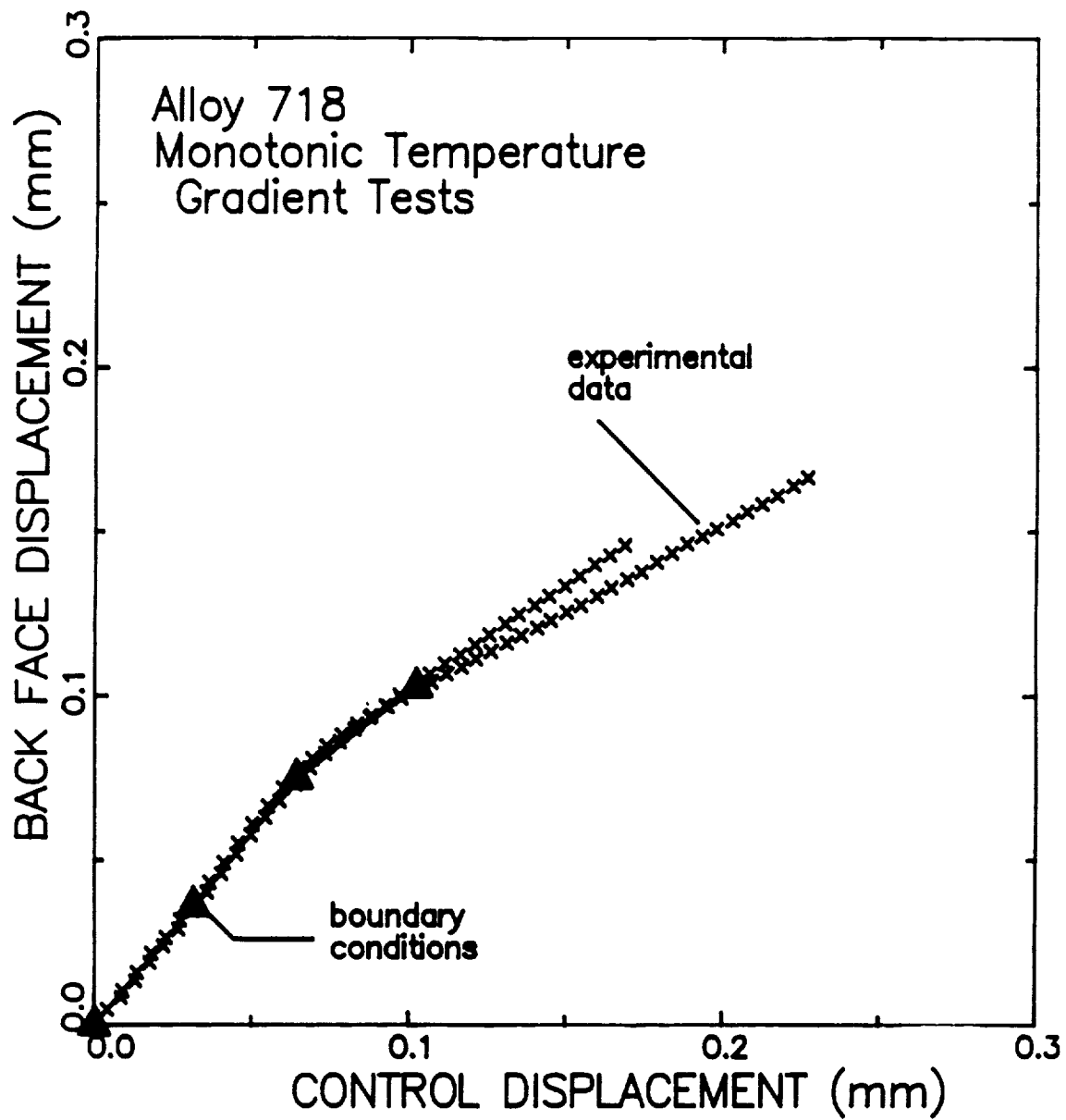


Figure 140: Variation of the Control and Back Face Displacements in Monotonic Temperature Gradient Tests.

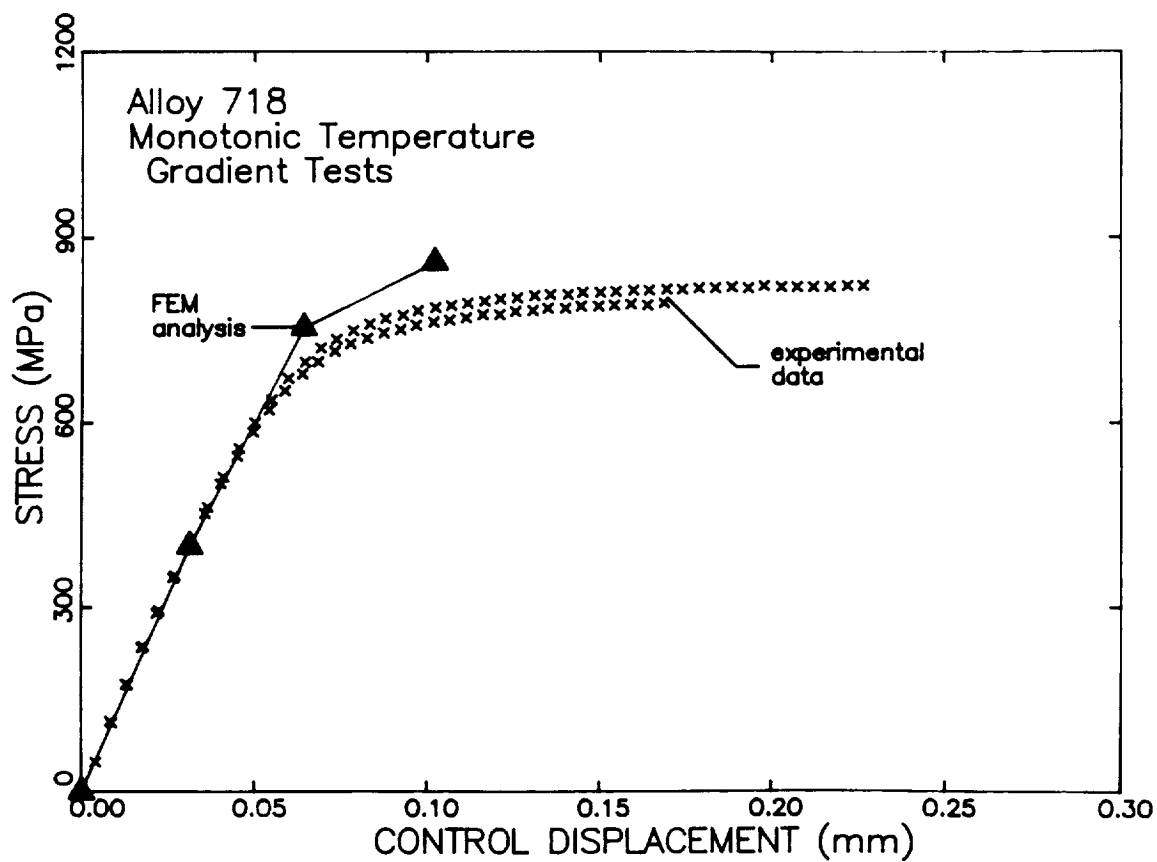


Figure 141: Comparison of the Experimental and Predicted Variation of Average Stress (Load / Specimen Area) With Control Displacement in Monotonic Temperature Gradient Tests.

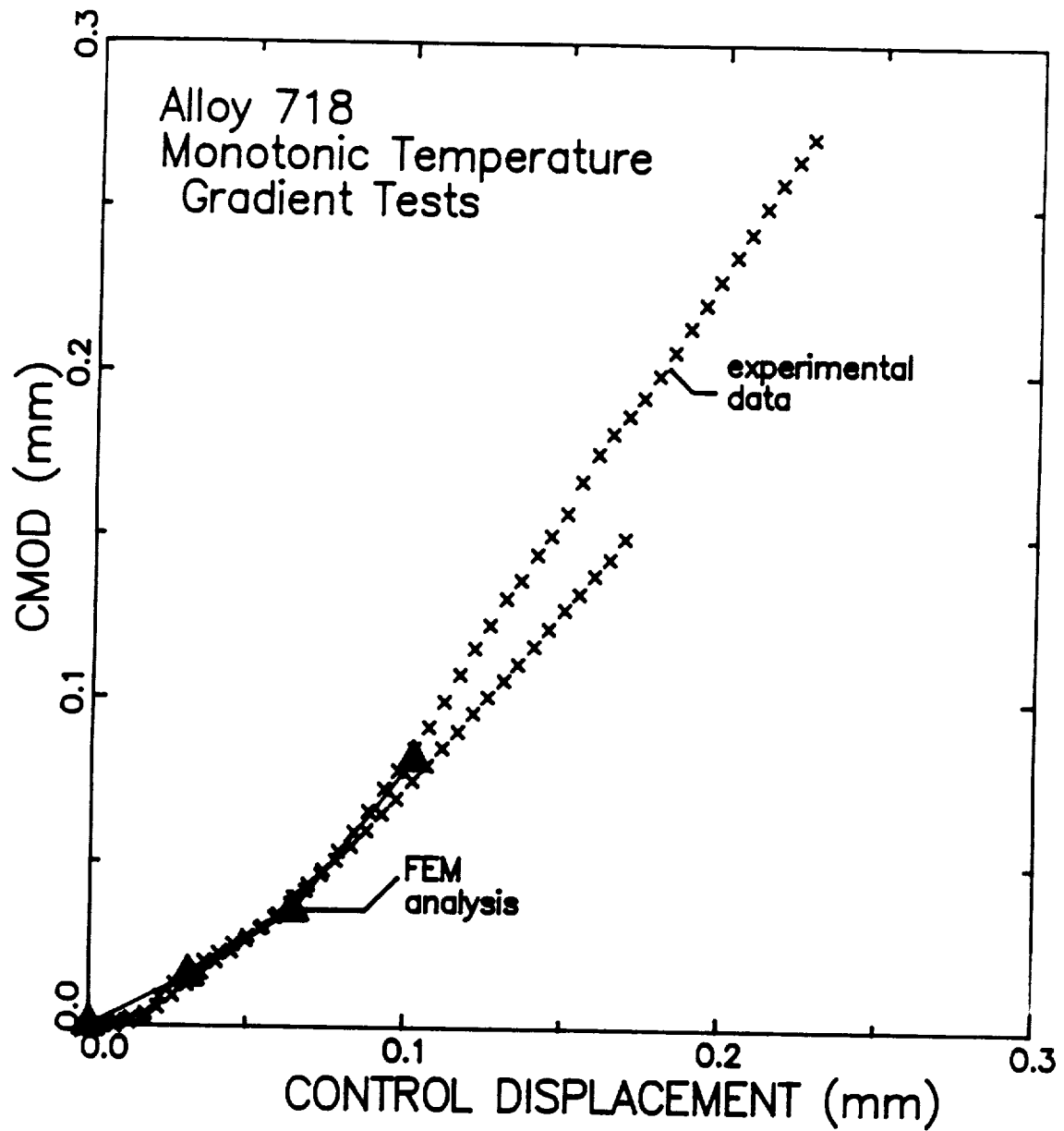


Figure 142: Comparison of the Experimental and Predicted Variation of Crack Mouth Opening Displacement (CMOD) With Control Displacement in Monotonic Temperature Gradient Tests.

Table 22: Summary of Temperature Gradient Crack Propagation Tests

Specimen Number	Strain Range(%)	Crack Morphology
N5-5	0.50	flat
N5-5	1.15	flat
N5-30	1.15	flat
N4-35	1.70	shear
N4-39	1.70	shear

observed. The lower temperature may have also helped to eliminate buckling for the 1.70% strain range because the lower temperature would result in higher flow stresses in the remaining ligament.

The data from the temperature gradient crack growth tests were analyzed using linear elastic fracture mechanics. The measured crack growth rates are plotted in Figure 143 as a function of K_{max} similar to that done for the isothermal crack growth tests. The influence of strain range is a very interesting observation because the 649°C isothermal tests and the in-phase TMF tests, where the maximum stress occurred at 649°C, did not show a significant influence of strain range for a given value of K_{max} . This suggests that the low temperature portion of the specimen which is remote from the crack tip early in the test can have a significant effect on the crack growth behavior. The implication of this result is that it would be difficult to identify an operational definition of a relative simple parameter like K or J which can accurately predict crack growth through an arbitrary temperature gradient.

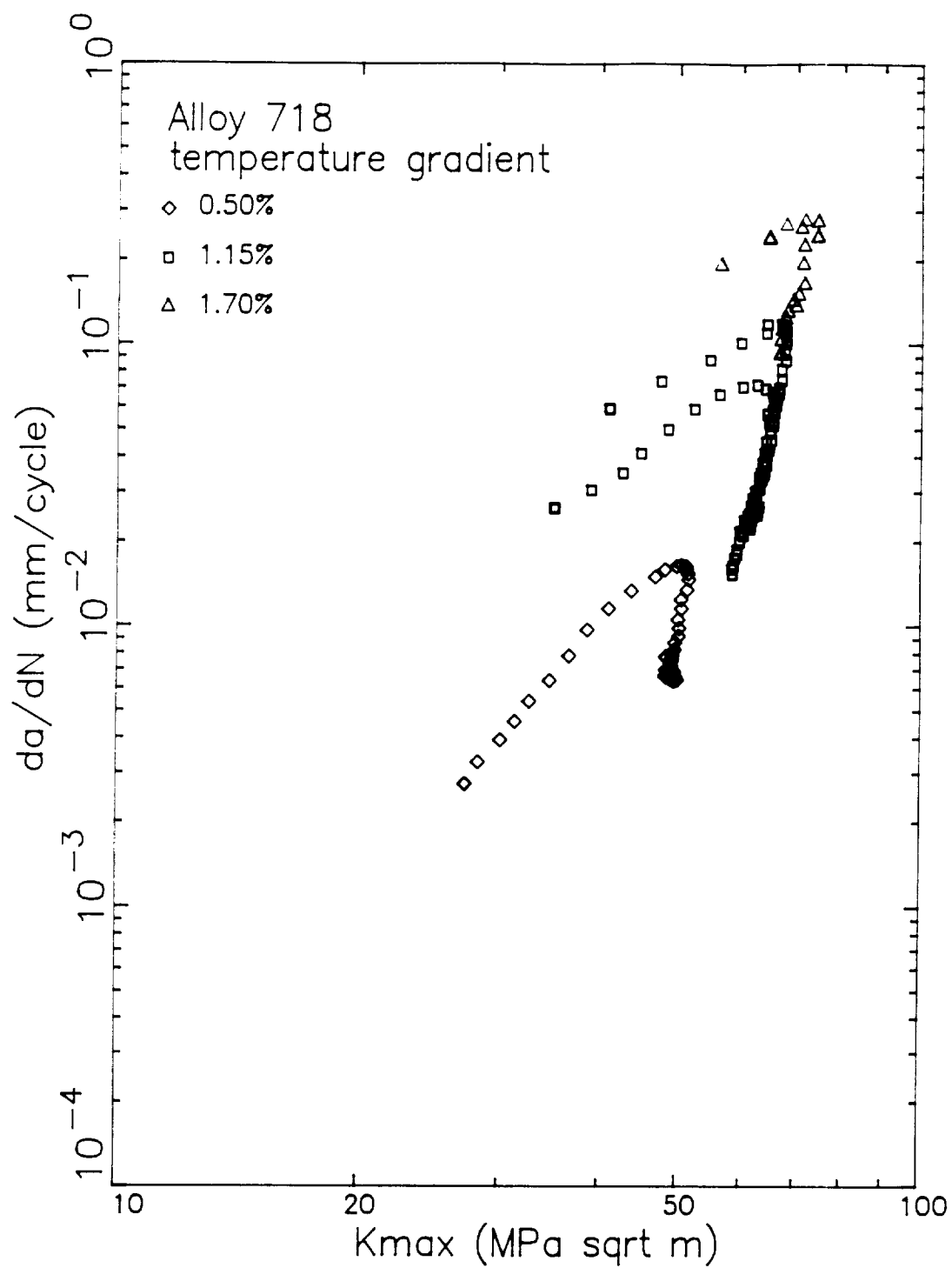


Figure 143: Variation of Crack Growth Rate with K_{max} in the Cyclic Temperature Gradient Tests.

9.0 RESULTS OF VERIFICATION EXPERIMENTS

This section of the report describes the experimental results of the verification tests performed during this program. Two type of tests were conducted - thermal mechanical fatigue (TMF) tests using the buttonhead single edge notch (SEN) specimen and isothermal displacement controlled tests with a modified compact geometry. The results of these tests will be described separately.

9.1 TMF Experiments

The TMF tests were performed in the GEAE EMTL Testing Laboratory using the same triple extensometer and data acquisition technique used for the isothermal SEN tests. The technique used to perform TMF cycling was described in a previous section of this report. For strain ranges less than 1.15%, the specimens were precracked prior to starting the TMF cycling while the cracks in the higher strain range tests were grown from the EDM notch.

9.1.1 TMF Test Matrix

The test matrix for the TMF tests is described in Table 23. The TMF tests were performed over two temperature ranges: 427 to 649°C (800 to 1200°F) and 538 to 649°C (1000 to 1200°F). These temperature ranges were selected because they cover the range of temperatures where isothermal experiments were performed and because there was a larger change in the cyclic stress-strain response at the higher temperatures. The variation of temperature and mechanical strain with time had a triangular wave shape having a period of 100 seconds (0.01 Hz cycling). The thermo-mechanical cycling was performed using both in-phase (maximum strain at maximum temperature) and out-of-phase (maximum strain at minimum temperature) cycling. Examples of in-phase and out-of-phase cycles are illustrated in Figure 144 for the higher temperature range TMF tests. The mechanical strain was cycled at zero mean strain ($A_{\epsilon} = \infty$). The strain ranges reported in Table 23 and throughout this section are only the mechanical portion of the strain.

TABLE 23: TMF Crack Propagation Test Matrix

Temperature (°C)	Temperature (°F)	Mechanical Strain Range(%)	Phase
427-649	800-1200	0.50	In Phase
427-649	800-1200	1.15	In Phase
427-649	800-1200	1.70	In Phase
427-649	800-1200	0.50	Out Phase
427-649	800-1200	1.15	Out Phase
427-649	800-1200	1.70	Out Phase
538-649	1000-1200	0.50	In Phase
538-649	1000-1200	1.15	In Phase
538-649	1000-1200	1.40	In Phase
538-649	1000-1200	0.50	Out Phase
538-649	1000-1200	1.15	Out Phase
538-649	1000-1200	1.40	Out Phase

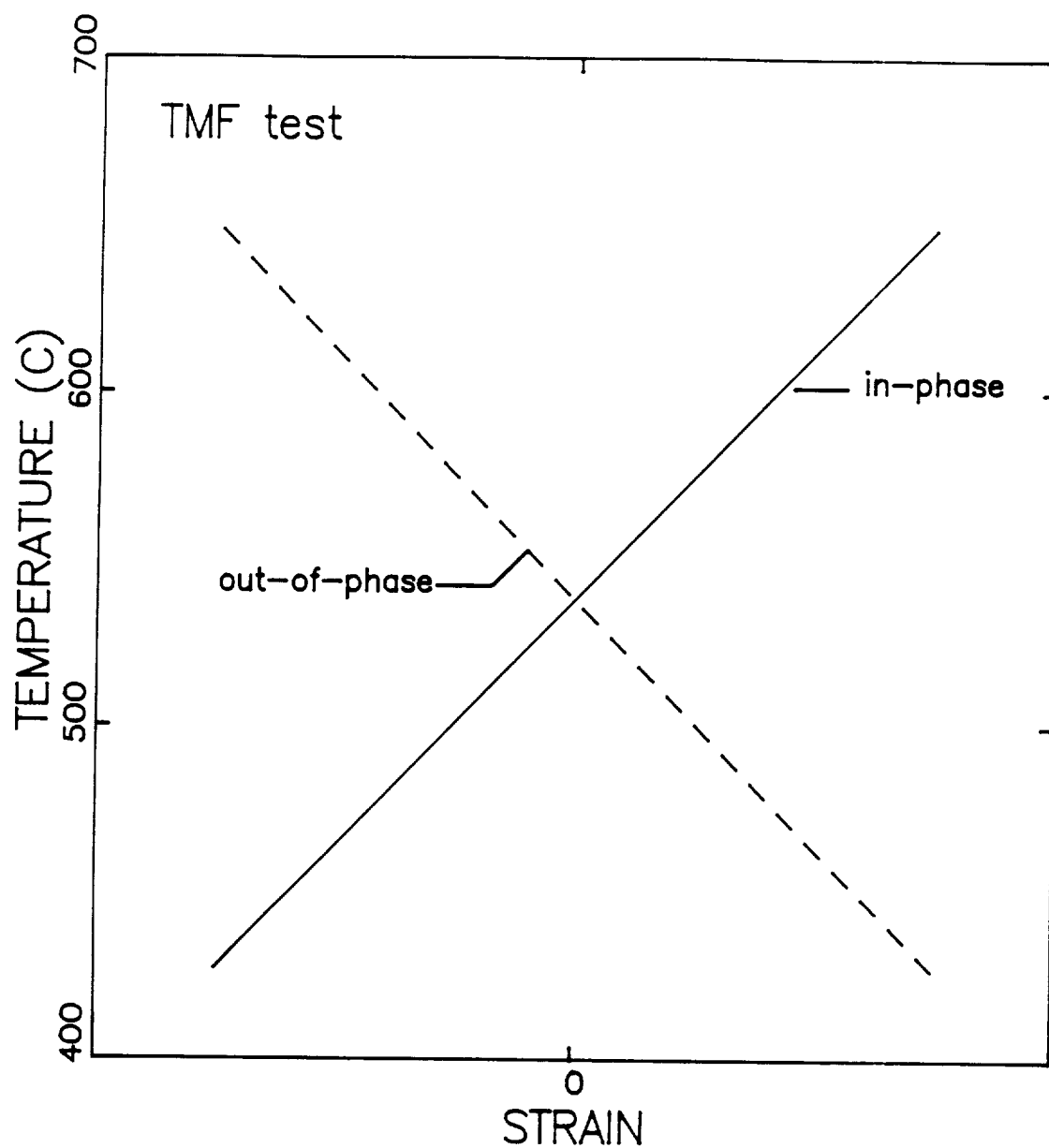


Figure 144: Schematic Figure Showing Variation of Strain with Temperature for In-Phase and Out-of Phase Cycling in 427 to 649°C (800 to 1200°F) TMF Test.

The strain ranges listed in Table 23 were selected from the isothermal test results in an attempt to avoid specimen buckling.

9.1.2 Crack Morphology

Table 24 summarizes the results of the TMF crack growth tests. The crack morphology notation used in this table is the same as that previously used to describe the crack morphology in the isothermal SEN tests. The cracking mode in the TMF tests followed the general trends established from the isothermal tests. The in-phase tests (maximum stress at 649°C) did not experience any shear crack growth up to the strain levels where buckling occurred. This was the same experience observed for the isothermal 649°C tests (Table 14). The out-of-phase tests experience shear crack growth at the higher strain levels. The strain level required to induce shear crack growth was lower in the 427 to 649°C temperature range tests than in the 538 to 649°C temperature range tests. Out-of-phase TMF tests have the maximum stress occurring at the minimum temperature. The TMF shear crack behavior for the two temperature ranges was similar to that observed in the isothermal tests where decreasing test temperature decreased the strain levels required to induce shear crack growth.

9.1.3 Fracture Mechanics Analysis

The crack growth data from the TMF tests has been analyzed using linear elastic fracture mechanics. The crack growth rate data are presented as a function of K_{max} based on the analysis of the isothermal test data.

Figure 145 shows the results from the 427 to 649°C in-phase TMF crack growth rate tests. Comparison of the two 0.50% strain range tests indicates that there is substantially more scatter in TMF tests than in isothermal ones; however, this may be an artifact of the test. The precrack lengths in these two tests were substantially different (0.57 and 0.93 mm) which may, in part, be responsible for the lack of agreement. The test which starts at a lower value of K_{max} or has the higher apparent crack growth rate had the

Table 24: Summary of TMF Crack Propagation Tests

Specimen Number	Temperature Range (°C)	Phase	Strain Range(%)	Crack Morphology
N4-2	427-649	in	0.50	flat
N5-43	427-649	in	0.50	flat
N4-18	427-649	in	1.15	flat
N5-29	427-649	in	1.15	flat
N5-45	427-649	in	1.15	flat
N5-20	427-649	in	1.50	buckled
N4-32	427-649	in	1.70	buckled
N5-13	427-649	in	1.70	buckled
N5-21	427-649	out	0.60	flat
N4-24	427-649	out	0.70	shear
N4-41	427-649	out	1.15	shear
N5-25	427-649	out	1.15	shear
N5-36	427-649	out	1.70	buckled
N4-13	538-649	in	0.75	flat
N5-32	538-649	in	0.75	flat
N4-29	538-649	in	1.15	flat
N5-40	538-649	in	1.15	flat
N4-43	538-649	in	1.30	flat
N5-2	538-649	in	1.40	buckled
N4-36	538-649	out	0.75	flat
N5-9	538-649	out	0.75	flat
N4-7	538-649	out	1.15	shear
N5-41	538-649	out	1.15	flat
N5-3	538-649	out	1.30	shear
N5-24	538-649	out	1.30	shear

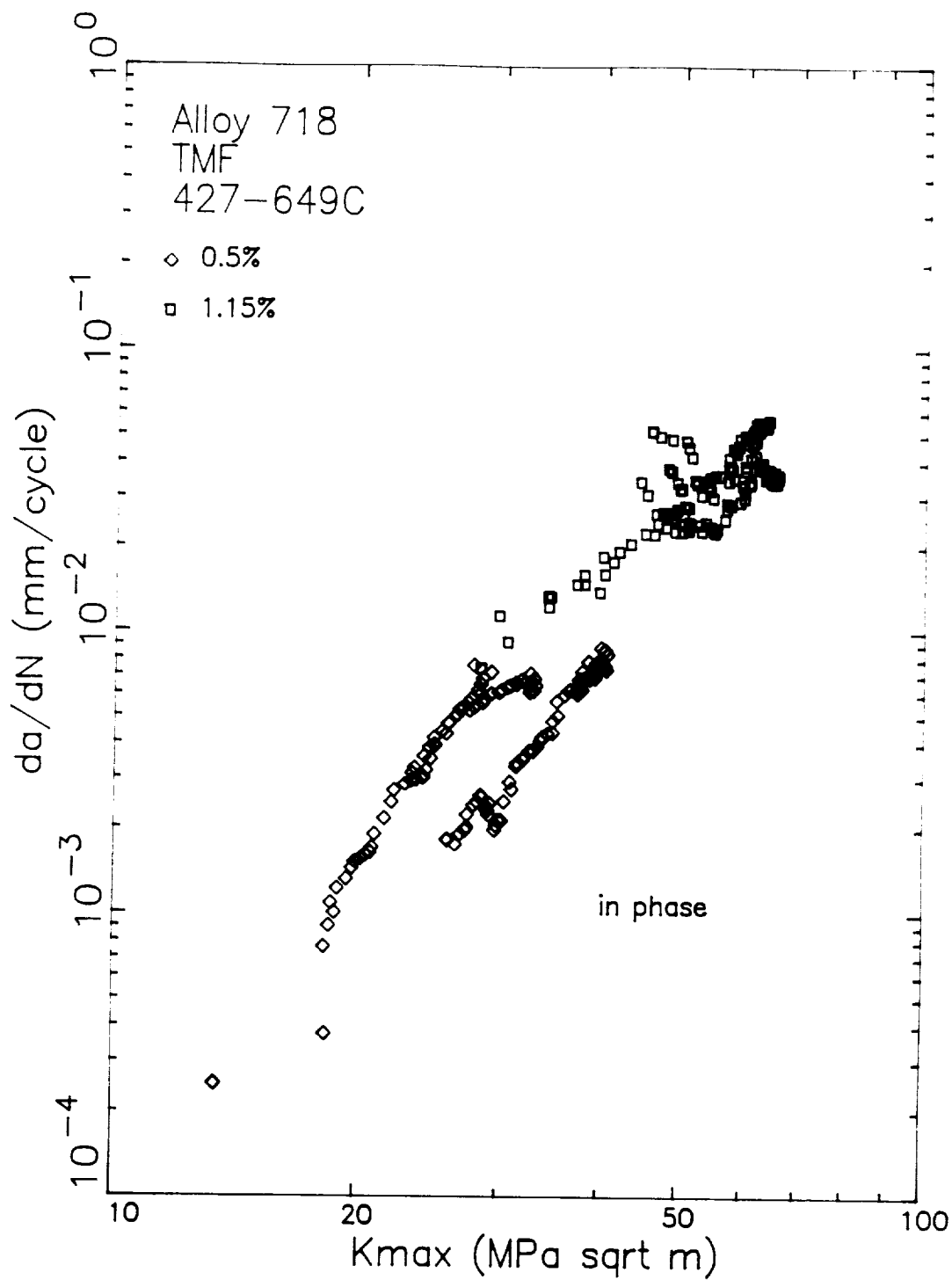


Figure 145: Variation of Crack Growth Rates with K_{\max} for In-Phase TMF Crack Growth Tests Cycles Cycled between 427 and 649°C (800 to 1200°F).

smaller precrack. The best comparison of the test data will be between the short precrack specimen with 0.50% strain range and the higher strain range tests. These results indicate that there is very little influence of strain range on the crack growth rates. This was expected because at 649°C, the temperature at the highest stress in this TMF cycle, a similar conclusion was reached for the isothermal tests (Figure 84).

The results for the out-of-phase 427 to 649°C TMF tests were quite different as shown in Figure 146. In this case increasing the strain range from 0.60 to 1.15% increased the crack growth rates by an order of magnitude. The temperature at the maximum stress for this cycle was 427°C. The isothermal tests at this temperature showed a similar acceleration of crack growth rates with strain range.

The crack growth data from the lower temperature range (538 to 649°C) in-phase and out-of-phase TMF tests are shown in Figures 147 and 148, respectively. As with the higher temperature range tests, the data from the in-phase tests have a much lower strain range sensitivity than the out-of-phase tests. One of the 0.75% strain range tests shown in Figure 147 has an apparent low crack growth rate. The crack in this specimen was grown to a longer crack length and these data were obtained at long crack lengths after the crack growth rate had passed through its maxima. Comparison of the data from the out-of-phase TMF tests shows that there is a smaller effect of strain range in the lower temperature range tests (Figure 148) than for tests with the higher temperature range (Figure 146). This most likely results from the higher temperature (538 vs. 427°C) at maximum stress in the lower temperature range tests. The isothermal test data showed less influence of strain range with increasing temperature.

9.2 Compact Specimen Results

The modified compact specimen tests were performed in the GEAE EMTL Testing Laboratory using the triple extensometer and data acquisition technique described in Section 5.0. All the compact specimens tests were

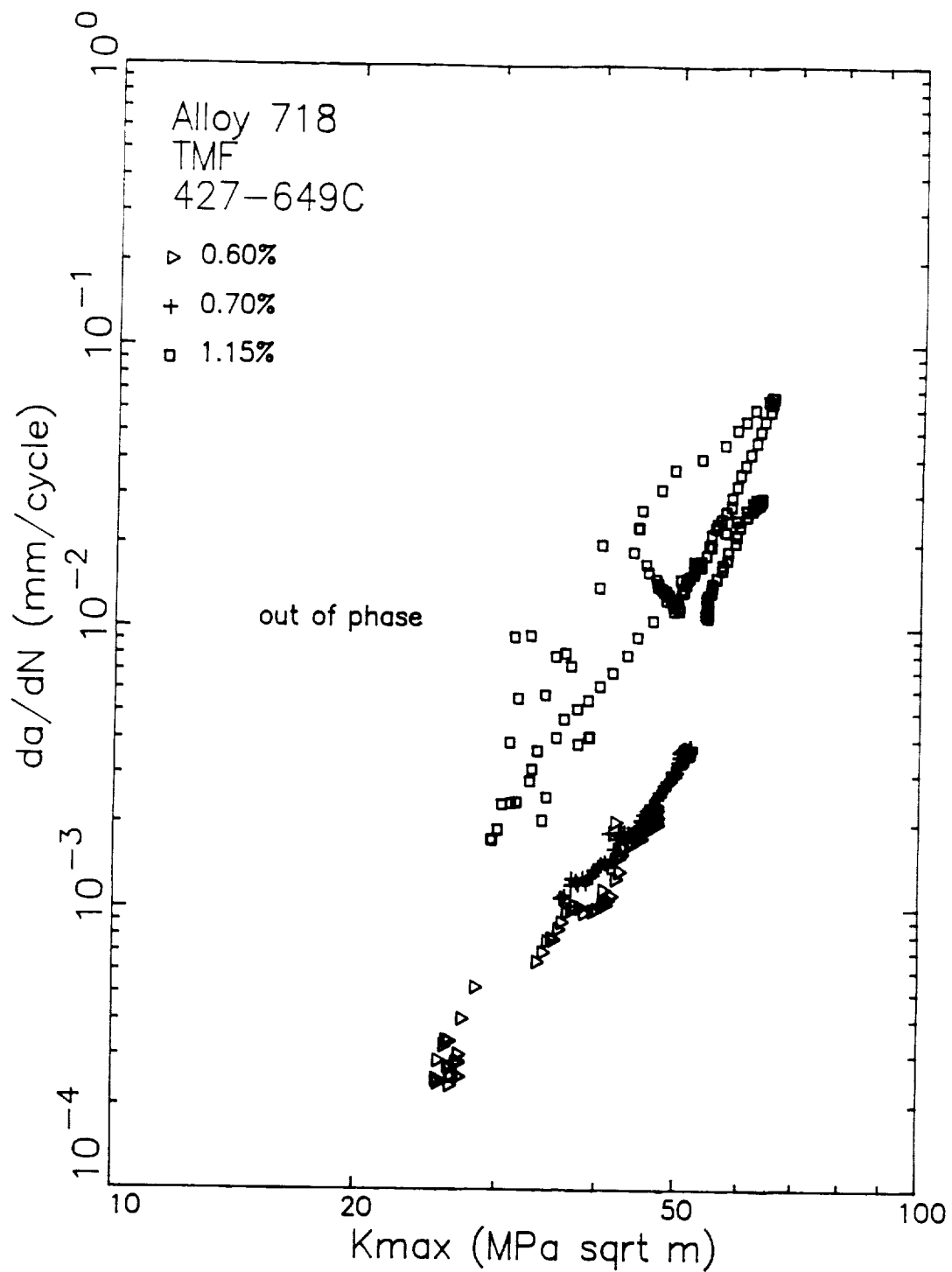


Figure 146: Variation of Crack Growth Rates with K_{max} for Out-of-Phase TMF Crack Growth Tests Cycled between 427 and 649°C (800 to 1200°F).

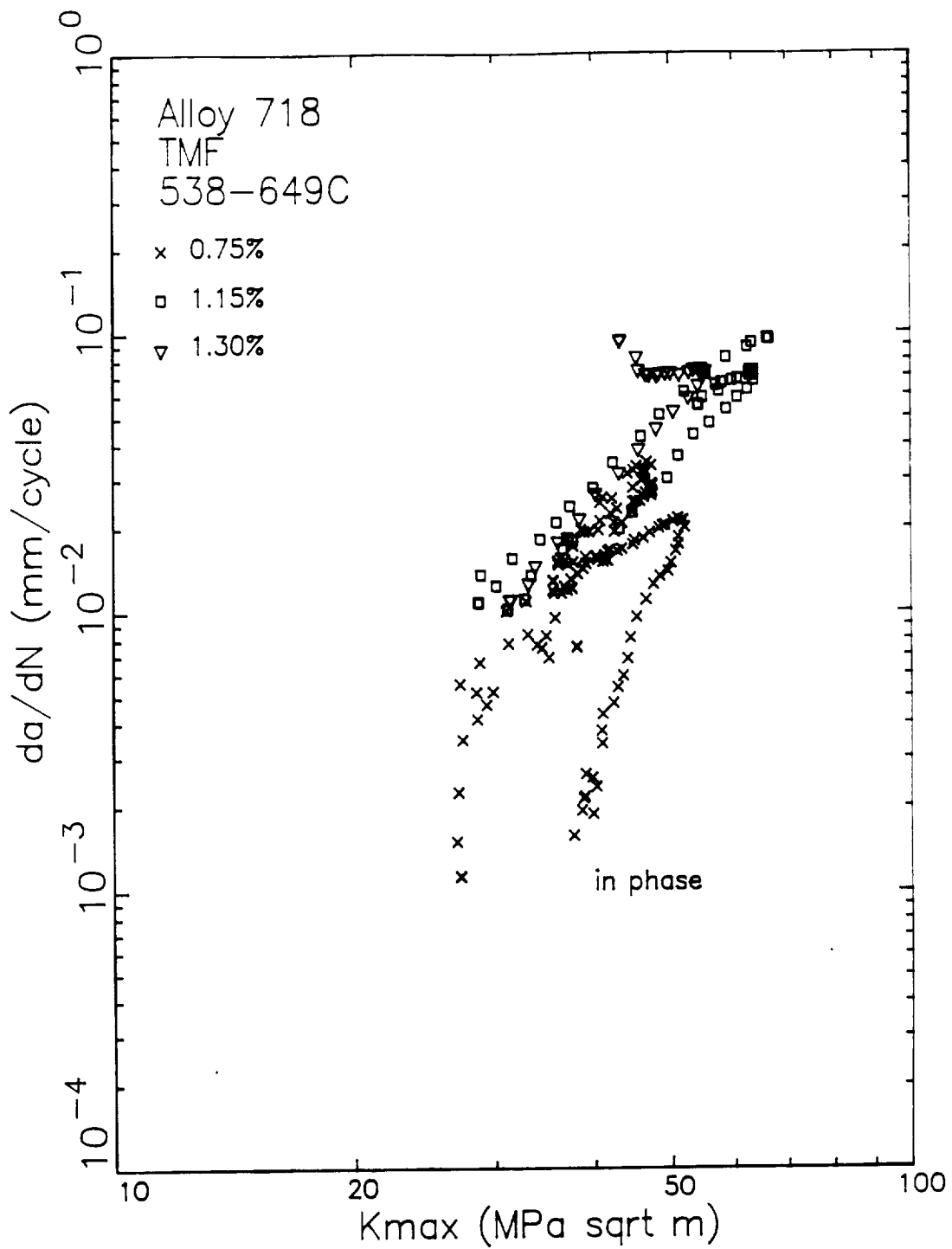


Figure 147: Variation of Crack Growth Rates with K_{max} for In-Phase TMF Crack Growth Tests Cycles Cycled between 538 and 649°C (1000 to 1200°F).

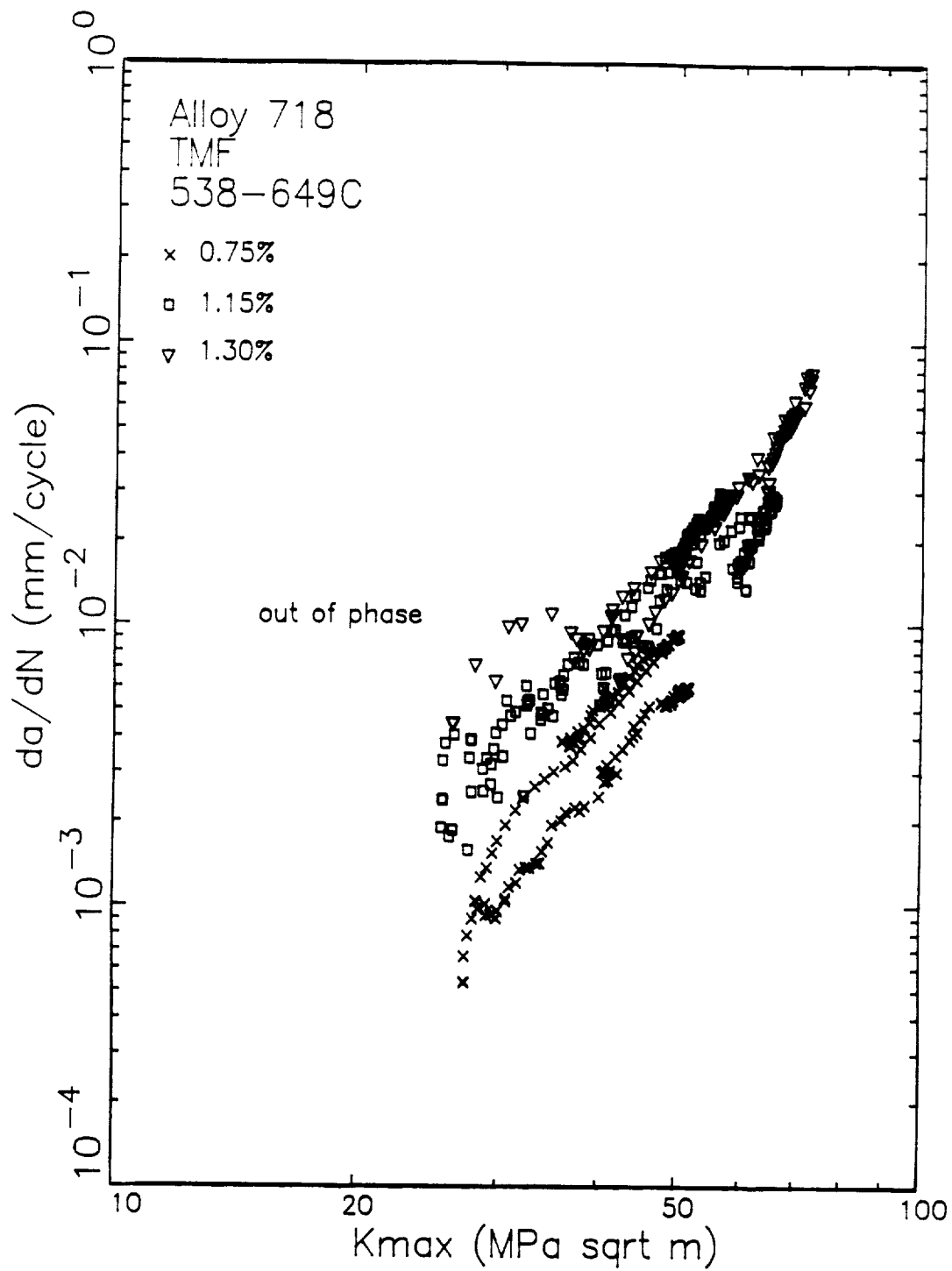


Figure 148: Variation of Crack Growth Rates with K_{max} for Out-of-Phase TMF Crack Growth Tests Cycles Cycled between 538 and 649°C (1000 to 1200°F).

performed isothermally in strain or displacement control with a mean strain of zero ($A_{\epsilon}=\infty$) and a frequency of 0.01 Hz (100 second cycle). Difficulties were encountered in performing tests above 538°C (1000°F) because the Morse bearing did not freely rotate at the elevated temperatures. A total of seven tests were performed at 427 and 538°C. The strain ranges were selected to provide maximum loads values which resulted in the range of K_{max} values obtained during the isothermal SEN tests. The specimens were precracked at room temperature and 10 Hz prior to start of the elevated temperature displacement control test. The large plan size of the modified compact specimen resulted in a much smaller change in crack growth rate for a given number of cycles relative to the SEN specimen. Each specimen was cycled for approximately one day at elevated temperature prior to stopping the test and breaking the specimen.

9.2.1 Modified Compact Displacement Results

The modified compact specimen was used in this investigation to compare the behavior of cracks under tension and bending fields. The modified compact specimen tests were performed to examine more extreme bending fields. As shown in Sections 4 and 5 there was bending present in the SEN specimens, but the maximum displacements at both the front and back faces of the specimen occurred at the maximum load. As expected this was not the case for the modified compact specimen. Figure 149 shows the three load-displacement records measured in compact Specimen N3-16. This test was performed at 538°C with a strain range of 2.4%. When these hysteresis loops were taken, The crack length was approximately 18.5 mm (0.72 inch). At the point of maximum load, both the control and CMOD extensometers were at their maximum value of displacement. The displacement at the back face of the specimen at maximum load was the smallest value measured during a cycle. This clearly illustrates that the modified compact geometry has a much higher degree of bending than the SEN specimen. The load-displacement trends shown in Figure 149 are typical for all the modified compact specimens tested in this investigation.

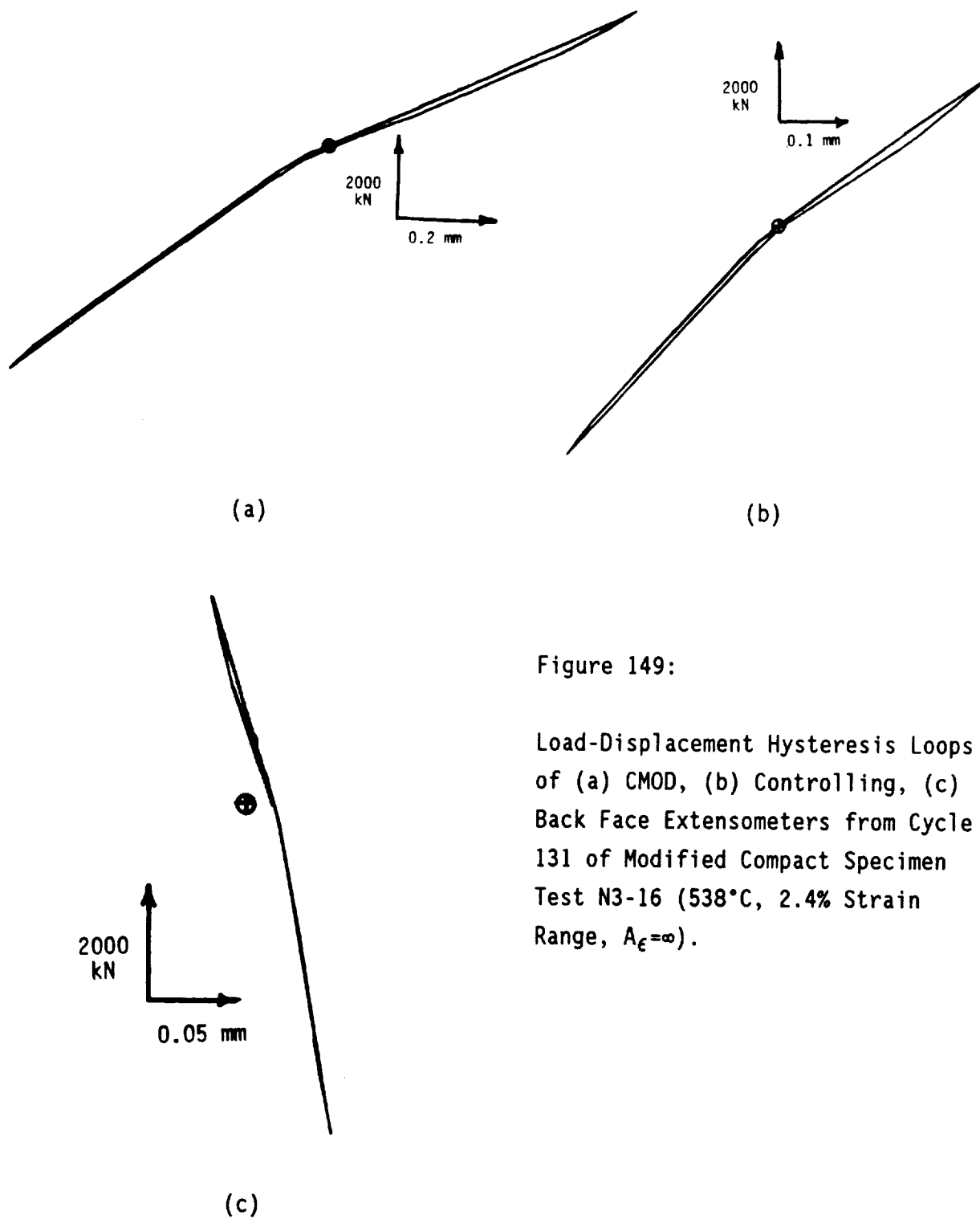


Figure 149:

Load-Displacement Hysteresis Loops of (a) CMOD, (b) Controlling, (c) Back Face Extensometers from Cycle 131 of Modified Compact Specimen Test N3-16 (538°C, 2.4% Strain Range, $A_\epsilon = \infty$).

9.2.2 Fracture Mechanics Analysis

The analysis of the modified compact specimens was performed in a fashion similar to the analysis of the isothermal SEN data except that the K-solution described in Section 5.8 for this specimen geometry was used. The cracks in these specimens grew a distance of less than 1.25 mm (0.05 inch). Over this range in crack lengths there was a relatively small change in K_{max} . Therefore the results of each specimen are characterized by a single value of K_{max} and crack growth rate (da/dN). The value of K_{max} is calculated from the average of K_{max} during each test. The reported values of da/dN are the increment of crack growth during the test divided by the number of cycles. These results are listed in Table 25.

These results are compared with the results from the 427 and 538°C isothermal SEN tests in Figures 150 and 151, respectively. The modified compact specimen results are shown as large triangles. The open triangles are from the compact specimen tests with crack lengths of approximately 18 mm while the closed triangles represent the data from the longer crack length (approximately 30 mm) tests. In both cases the small crack length test results correlated closely with the results of the 0.50% strain range SEN tests which experience nearly elastic cycling. The longer crack length compact specimen data was significantly higher.

It is not possible to determine the causes of this shift in crack growth data until a more complete analysis of the modified compact specimen geometry has been completed.

Table 25: Results of Modified Compact Specimen Crack Propagation Tests

Specimen Number	Temperature (°C)	Strain Range (%)	Initial Crack Length (mm)	Cycles	K _{max} (MPa/m)	da/dN (mm/cycle)
N3-30	427	1.6	17.96	915	26.1	3.11 x 10 ⁴
N3-21	427	2.4	18.47	935	39.2	1.13 x 10 ³
N3-22	427	3.6	31.21	280	20.1	6.17 x 10 ⁴
N3-24	427	5.4	29.67	220	28.7	6.64 x 10 ³
N3-15	538	1.6	18.42	1026	28.0	1.15 x 10 ³
N3-16	538	2.4	18.31	1123	44.2	2.20 x 10 ³
N3-27	538	3.6	31.6	1260	16.5	9.72 x 10 ⁴

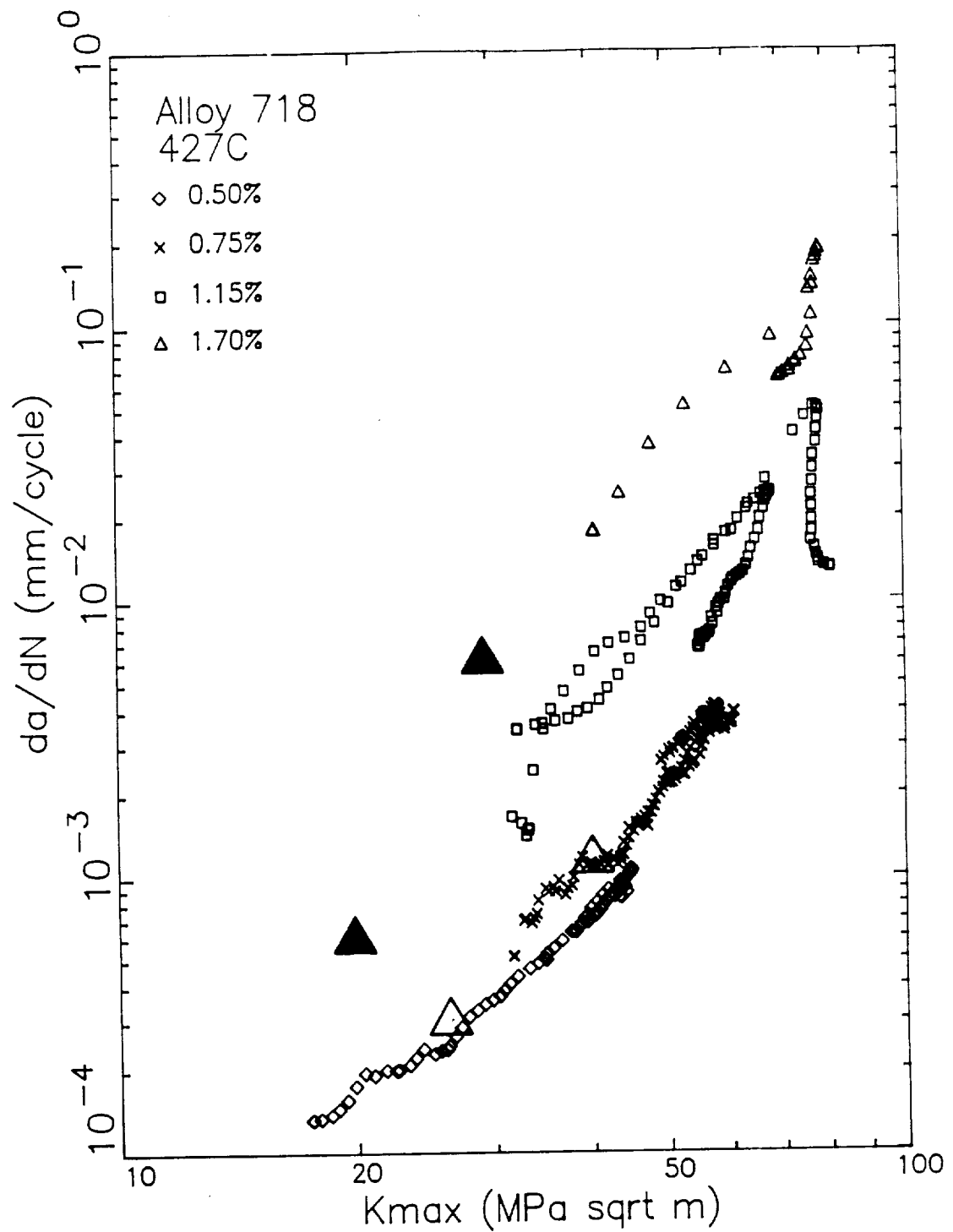


Figure 150: Comparison on Crack Growth Rates in Alloy 718 Measured in Modified Compact (large triangles) and SEN Specimens for $A_{\epsilon}=\infty$ Cycling at 427°C.

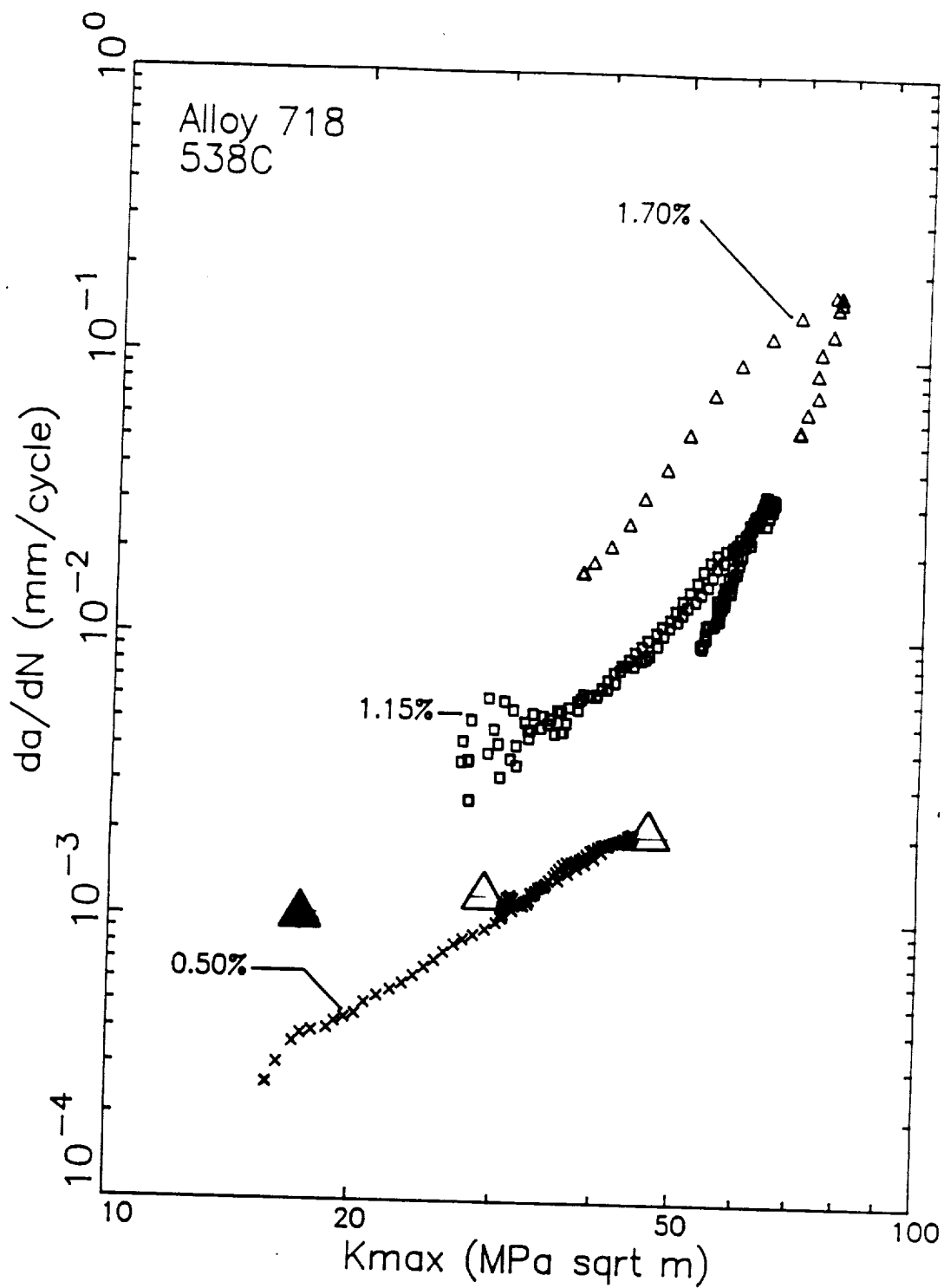


Figure 151: Comparison on Crack Growth Rates in Alloy 718 Measured in Modified Compact (large triangles) and SEN Specimens for $A_c = \infty$ Cycling at 427°C.

10.0 DISCUSSION AND CONCLUSIONS

The results of the current program strongly suggest that significant progress has been made in the development of nonlinear fracture mechanics for application to problems of importance to hot section components of gas turbine engines. This conclusion is based on a thorough analytical and experimental evaluation of crack growth in the developmental activities such as thermo-mechanical fatigue and thermal gradients. This conclusion is based on the detailed work of this program including the following major considerations:

1. A substantial effort was made to develop and verify an experimental and analytical understanding of a buttonhead single edge notch (SEN) specimen. This work featured 3D and 2D finite element analyses of multiple extensometer experiments. This specimen is ideally suited for such studies and it is recommended for future work.
2. A detailed review of nonlinear fracture mechanics P-I integrals was performed. Based on the results of the review, several proposed P-I integrals were selected for detailed evaluation. Theoretically, the selected P-I integrals maintain path-independence for nonproportional loading, unloading after plastic deformation, temperature gradients, and material inhomogeneities. A finite element post-processor was developed for calculating the values of these integrals based on finite element analysis results. Numerical calculations of the proposed P-I integrals were made through finite element analyses which included thermal gradients and reversed cyclic plasticity. The numerical results showed path-independence of these integrals.

3. An extensive experimental study of the crack growth behavior of Alloy 718 was performed which featured elaborate measurements for boundary condition and closure determination. The experiments were conducted using displacement control and two other extensometers were employed to provide the correlative information. The crack growth was monitored using electric potential drop techniques. The test variables included elastic and plastic strain ranges, temperature, thermo-mechanical fatigue, and thermal gradients. The experimental crack growth rates were correlated using linear elastic fracture mechanics (LEFM) parameters ΔK and K_{max} . Neither parameter correlated data because the higher strain range tests were outside the small scale yielding regime.
4. Detailed elastic-plastic finite element analyses were conducted to simulate the crack growth and crack closure at 538°C. The results demonstrated excellent correlation with the experimentally measured closure and opening behavior and showed good agreement with the measured nonlinear load-displacement loops. Based on the excellent agreement, the P-I integral calculations could be made with confidence. The selected P-I integrals all performed well in correlating the effect of nonlinear straining on crack growth. The correlation demonstrated the usefulness of these methods in the regime beyond small-scale yielding.
5. The results of the experiments at other temperatures, by in large, agreed with the results at 538°C. In general, as temperature increased the effect of nonlinear strain on increasing crack growth rates appeared to decrease. The thermo-mechanical test results tended to agree with the isothermal data at the maximum stress level. Further work is required to demonstrate that the P-I integrals could successfully correlate these TMF data. Similarly, more evaluations should be made of the thermal gradient test data.

6. The effect of mean strain on crack growth was as expected. The detailed finite element analyses of the 538°C data, while demonstrating correlation with crack closure, did not address the importance of closure in correlating crack growth data. More work in this regard, perhaps involving the mean strain data, should be performed. The most difficult computational aspect of the current work involved the consideration of closure effects through the build-up of the plastic wake. If this effect could be modeled in simplified ways, the computational complexities would be greatly relieved.
7. For further verifications of the current results, it would be beneficial to analyze the compact tension specimen test data, also generated in this program. This work would demonstrate the geometry sensitivity of the nonlinear methods.
8. To be readily usable, the proposed P-I integral methods should become easier to determine numerically (for example, in a handbook). Additionally, it would be desirable if the P-I integrals had better physical bases.

11.0 REFERENCES

1. Rice, J.R., "A Path-Independent Integral and the Approximate Analysis of Strain Concentration by Notches and Cracks," Journal of Applied Mechanics, Vol. 35, 1968, pp. 379-386.
2. Dowling, N.E. and Begley, J.A., "Fatigue Crack Growth During Gross Plasticity, and the J-Integral", Mechanics of Crack Growth, ASTM STP 590, ASTM, Philadelphia, 1976, pp.82-103
3. Blackburn, W.S., "Path-Independent Integrals to Predict Onset of Crack Instability In An Elastic Material," International Journal of Fracture Mechanics, Vol. 8, 1972, pp. 343-346.
4. Kishimoto, K., Aoki, S., and Sakata, M., "On the Path-Independent Integral-J," Engineering Fracture Mechanics, Vol. 13, 1980, pp. 841-850.
5. Atluri, S.N. Nishioka, T., and Nakagaki, M., "Incremental Path-Independent Integrals in Inelastic and Dynamic Fracture Mechanics," Engineering Fracture Mechanics, Vol. 20, No. 3, 1984, pp. 209-244.
6. Kim, K.S. and Van Stone, R.H., NASA Contract NAS3-23940, GE Aircraft Engines, Cincinnati, Ohio, unpublished research
7. Kim, K.S. and Orange, T.W., "A Review of Path-Independent Integrals in Elastic-Plastic Fracture Mechanics," ASTM STP 945, ASTM, 1988, pp. 713-729.
8. Wilson, W.K. and Yu, I.W., "The Use of the J-Integral in Thermal Stress Crack Problems," International Journal of Fracture, Vol. 15, 1979, pp. 377-387.
9. Gurtin, M.E., "On a Path-Independent Integral for Thermoelasticity," International Journal of Fracture, Vol. 15, 1979, pp. R169-R170.
10. Ainsworth, R.A., Neale, B.K., and Price, R.H., "Fracture Behavior in the Presence of Thermal Strains," Proceedings of Institute of Mechanical Engineers' Conference on Tolerance of Flaws in Pressurized Components, London, 1978, pp. 171-178.
11. McKnight, R.L., "Finite Element Cyclic Thermoplasticity by the Method of Subvolumes", Ph.D. Thesis, University of Cincinnati, 1975
12. Kumar, V., German, M.D., and Shih, C.F., "An Engineering Approach for Elastoplastic Fracture Analysis," EPRI Report NP-1931, Electric Power Research Institute, Palo Alto, CA, July 1981.

13. Yau, J.F., Malik, S.N., Kim, K.S., Van Stone, R.H., and Laflen, J.H., "Elevated Temperature Crack Growth," NASA CR-174957, Annual Report, August 1985.
14. Malik, S.N., Van Stone, R.H., Kim, K.S., and Laflen, J.H., "Elevated Temperature Crack Growth," NASA CR-179601, Annual Report, January 1987.
15. Van Stone, R.H., Krueger, D.D., and Gooden, O.C., "Advanced Cumulative Damage Modeling", AFWAL-TR-88-4146, GE Aircraft Engines, Cincinnati, Ohio 45215, 1988
16. Ramaswamy, V.G., Van Stone, R.H., Dame, L.T., and Laflen, J.H., "Constitutive Modeling for Isotropic Materials", 1985, NASA CR 175004
17. Cook, T.S., ASTM STP 765, ASTM, 1982, pp.269-283
18. Ramaswamy, V.G., GE Aircraft Engines, unpublished research, 1984
19. James, L.A., J. of Eng. Mat. Tech., 1973, pp.254-256
20. Coles, A., Johnson, R.E., and Popp, H.G., J. of Eng. Mat. Tech., 98, 1976, pp. 305-315
21. Sadadnanda, S. and Shahinian, S., Met. Trans., 1978
22. Floreen, S. and Kane, R.H., Met. Trans., 10A, 1979, pp.1745-1751
23. Shahinian, S. and Sadanadna, K., Engineering Aspects of Creep, Vol. 2, 1980, p. 1
24. Nicholas, T., Weerasooriya, T., and Ashbaugh, N.E., "A Model for Creep/Fatigue Interaction in Alloy 718", ASTM STP 905, Fracture Mechanics: Sixteenth Volume, ASTM, 1986, Philadelphia, Pa., pp.167-180
25. Nicholas, T. and Weerasooriya, T., "Hold-Time Effects in Elevated Temperature Fatigue Crack Propagation", ASTM STP 905, Fracture Mechanics: Sixteenth Volume, ASTM, 1986, Philadelphia, Pa., pp.155-168
26. Weerasooriya, T. and Nicholas, T., "Overload Effects in Sustained Load Crack Growth in Inconel 718", Fracture Mechanics: Eighteenth Symposium, ASTM STP 945, ASTM, Philadelphia, 1987, to be published
27. Van Stone, R.H. and Krueger, D.D., "Investigation of Direct Aged Inconel 718 Fatigue Behavior", Contract N00019-82-C-0373, Final Report, GE Aircraft Engines, Cincinnati, Ohio 45215, December 1984

28. Krueger, D.D., Antolovich, Stephen D., and Van Stone, R.H., Met. Trans., 18A, 1987, pp.1431-1449
29. Wright, P.K., Jang, H., and Popp, H.G., "Fatigue and Fracture of Advanced Blade Materials", AFWAL-TR-84-4166, GE Aircraft Engines, Cincinnati, Ohio 45215, February 1985
30. Kumar, V., German, M., and Shih, C. F., "An Engineering Approach for Elastic-Plastic Fracture Analysis," EPRI Report NP-1931 (R.P. 1237-1), Electric Power Research Institute, Palo Alto, CA, 1981.
31. Domas, P.A., Sharpe, W.N., and Yau, J., "Benchmark Notch Test for Life Prediction", NASA CR-1655571, NASA-Lewis Research Center, June 1982
32. Sharpe, W.N., Jr., "Interferometric Strain Measurement" Int. J. Nondestructive Testing, Vol. 3, 1971, pp. 59-76.
33. Sharpe, W.N., Jr., "Applications of the Interferometric Strain / Displacement Gage", Optical Engineering, Vol. 21, 1982, pp. 483-488.
34. Sharpe, William N., Jr. and Ward, Michael, "Benchmark Cyclic Plastic Notch Strain Measurements", J. Eng. Mat. Tech., Vol. 105, 1983, pp. 235-241
35. Gangloff, R.P., Fat. Eng. Mat. and Structures, 4, 1982, pp. 15-31
36. Wilcox, J.R. and Henry, M.F., General Electric Corporate Research and Development, Schenectady, New York, 1982, unpublished research
37. Johnson, H.H., Mat. Res. and Standards, 5, 1965, pp.442-445
38. Krueger, D.D., "Effects of Grain Size and Precipitate Size on the Fatigue Crack Growth Behavior of Alloy 718 at 427°C", M.S. Thesis, University of Cincinnati, 1984
39. "Standard Test Method For Measurement of Fatigue Crack Growth Rates", E647-86a, 1987 Annual Book of ASTM Standards, 03.01, ASTM, 1987, pp. 899-926
40. Harris, D.O., J. Bas. Engineering, 89, 1967, p.49
41. Malik, S.N. and Gilbert, M.S., GE Aircraft Engines, Cincinnati, Ohio 45215, private communication, 1986
42. Tucker, Lee and Bussa, Stephen, Fatigue Under Complex Loading, R.M. Wetzel, Editor, SAE, Warrendale, Pa. 15096, 1977, pp. 1-14
43. Srawley, J.E. and Gross, B., Eng. Frac. Mech., 4, 1972, pp. 587-589

44. Stress Intensity Factors Handbook, Y. Murakami, Editor-in-Chief, Pergamon Press, Oxford, 1987, pp.27-29
45. Wilson, W.K., "Analytical Determination of Stress Intensity Factors for the Manjoine Brittle Fracture Test Specimen", Westinghouse Research Laboratory Report WERL-0029-3, 1965
46. Manjoine, M.J., Trans. ASME, J. Bas. Eng., 87, 1965, pp.293-298
47. Manjoine, M.J., discussion of paper by W.F. Brown, Jr. and J.E. Srawley, ASTM STP 410, 1966, pp.66-70
48. Van Stone, R.H., "Residual Life Prediction Methods for Gas Turbine Components", Materials Science and Engineering, Vol. A103, 1988, pp.49-61
49. Newman, J.C., Jr., and Armen, H., Jr., "Elastic-Plastic Analysis of a Propagating Crack under Cyclic Loading," AIAA Paper No. 74-366, AIAA/ASME/SAE 15th Structures, Structural Dynamics and Materials Conference, April, 1974.
50. Newman, J.C., Jr., "A Finite-Element Analysis of Fatigue Crack Closure," Mechanics of Crack Growth, ASTM STP 590, American Society for Testing Materials, 1976, pp. 281-301.
51. Newman, J.C., Jr., "Finite-Element Analysis of Crack Growth under Monotonic and cyclic Loading," Cyclic Stress-Strain and Plastic Deformation Aspects of Fatigue Crack Growth, ASTM STP 637, American Society for Testing Materials, 1977, pp. 56-80.
52. Ohji, K., Ogura, K., and Ohkubo, Y., "Cyclic Analysis of a Propagating Crack and its Correlation with Fatigue Crack Growth," Engineering Fracture Mechanics, Vol. 7, 1975, pp. 457-464.
53. Ogura, K., and Ohji, K., "FEM Analysis of Crack Closure and Delay Effect in Fatigue Crack Growth under Variable Amplitude Loading," Engineering Fracture Mechanics, Vol. 9, 1977, pp. 471-480.
54. Nakagaki, M., and Atluri, S.N., "Elastic-Plastic Finite Element Analysis of Fatigue Crack Growth in Mode I and Mode II Conditions," NASA-CR-158987, Nov. 1978.
55. Nakagaki, M., and Atluri, S.N., "Elastic-Plastic Analysis of Fatigue Crack Closure in Modes I and II," AIAA Journal, Vol. 18, No. 9, 1980, pp. 1110-1117.
56. Elber, W., "The Significance of Fatigue Crack Closure," Damage Tolerance in Aircraft Structures, ASTM STP 486, American Society for Testing Materials, 1971, pp. 230-242.

57. Frost, N.E. and Dugdale, D.S., J. Mech. Phys. Solids, 5, 182, 1957
58. Wastberg, S., "A Finite Element Analysis of a Crack Growing Under Cyclic Loading," Fatigue of Engineering Materials & Structures, Vol. 6, No. 2, 1983, pp.149-158.
59. Blom, A.F., and Holm, D.K., "An Experimental and Numerical Study of Crack Closure," Engineering Fracture Mechanics, Vol. 22, No. 6, 1985, pp. 997-1011.
60. Lalor, P.L., and Sehitoglu, H., "Fatigue Crack Closure Outside Small Scale Yielding Regime," Presented at ASTM International Symposium on Fatigue Crack Closure, Charleston, S.C., May 1986, to appear in ASTM STP 982.
61. McClung, R.C., "Fatigue Crack Closure and Crack Growth Outside the Small Scale Yielding Regime," Ph.D. Dissertation, Department of Mechanical Engineering and Industrial Engineering, University of Illinois at Urbana-Champaign, IL., 1987.
62. Besseling, J.F., "A Theory of Plastic Flow for Anisotropic Hardening in Plastic Deformation of an Initially Isotropic Material," Report S. 410, National Aeronautical Research Institute, Amsterdam, 1953
63. Bathe, K.J., Finite Element Procedures in Engineering Analysis, Prentice-Hall, Englewood Cliffs, New Jersey, 1982.
64. Krieg, R.D., and Krieg, D.B., "Accuracies of Numerical Solution Methods for the Elastic-Perfectly Plastic Model," Journal of Pressure Vessel Technology, Nov. 1977, pp. 510-515.
65. Schreyer, H.L., Kulak, R.F., and Kramer, J.M., "Accurate Numerical Solutions for Elastic-Plastic Models," Journal of Pressure Vessel Technology, Aug. 1979, pp. 226-234.

